Multiple Sulphur Isotopic Compositions of Archean Records Determined by SHRIMP-SI

Li Liu

January 2019

A thesis submitted for the degree of Doctor of Philosophy of
The Australian National University

Declaration

All the work for this thesis was carried out at the Research School of Earth Sciences, Australian National University between April 2015 and January 2019. This thesis contains no material that has been accepted for the award of any other degree or diploma in any university. To the best of my knowledge, it contains no material previously published or written by another person, except where due reference is made in the text.

Li Liu

Canberra

January 2019

Acknowledgments

During the past four years at the Research School of Earth Sciences, I received a great deal of help from many people.

My Ph.D. research relied heavily on the SHRIMPs, particularly SHRIMP-SI, the great amount of assistance and support given by the members of the SHRIMP group is sincerely appreciated. Firstly, many thanks to my supervisor Prof. Trevor Ireland for providing me with the precious opportunity to conduct Ph.D. research at RSES, for useful discussions on the data and reviews on the drafts. Secondly, I would like to thank Dr. Peter Holden, who is an expert in SHRIMPs with extensive knowledge. Thank you for teaching me how to operate SHRIMPs and reduce the raw data, as well as the patient explanations on the configuration of SHRIMPs, the associated physics and engineering principles, and insightful advice on my research. Thank you for helping to set up and fix the SHRIMPs all the time, even on many weekends. Thirdly, I am grateful to Dr. Bin Fu. Thank you for numerous discussions on the data reduction, operations of SHRIMPs, principles of methods, as well as countless encouragements. Thanks should also go to Dr. Janaina Ávila. Thank you for the supervision during my first Ph.D. year and later lending the sulphides reference materials. Thank you for teaching me how to make good mounts, for the help in sampling in the University of Queensland and quadruple sulphur isotopic composition measurements during the first year. Thanks also to Peter Lanc for the assistance in reducing raw data using POXI-MC and POXI-SC as well as the patient explanations of the software. David Thomson is thanked for fixing the rack of SHRIMP-II, which I accidentally made it stuck.

I would also like to express my gratitude to Associate Prof. John Mavrogenes. Thank you for teaching me how to etch pyrite grains properly, which is of great significance to my research. Thank you also for teaching and guiding me how to design and conduct high-temperature experiments. The useful discussions on the genesis of gold ore deposits, comments on the drafts, and the minerals for establishing the peaks of trace elements are sincerely appreciated.

Thanks to Shane Paxton and Hongtao Gao for teaching me how to use a variety of saws, how to separate individual mineral grains, and the useful guidance in casting some tough materials into mounts. Thanks also go to previous Ph.D. students Morgan Williams and Melanie Sieber for the help in operating SEM. The great deal of help given by David Clark in using the furnace and preparing the silica glass tubes is very much appreciated. Hayden Miller is

thanked for helping to fix the electronics of the furnace, as well as the help when I had trouble in setting the pressure. Dr. Terry Mernagh is also thanked for the help in Raman Spectroscopy operation and data analysis.

I would like to thank Dr. Arthur Hickman from the Geological Survey of Western Australia (GSWA) for teaching me so much knowledge on the geological setting of the Pilbara Craton, the useful information on which drill holes should be sampled, as well as insightful comments on a draft. Many thanks go to Dr. Pascal Philippot from the Institut de Physique du Globe de Paris for the detailed and insightful comments on my mid-term review.

Special thanks go to Prof. Paulo Vasconcelos from the University of Queensland for generously lending the precious drill cores and logging files of the Lamego gold deposit. I am also grateful to the Perth Core Library of GSWA for the approvals of viewing and sampling the drill cores from the Pilbara Craton. Without these drill cores, my research could not have moved on. Many thanks to Monique Brouxhon from the Mineral Exploration Information Branch for the patience and handling of my so many applications of sampling. Thank you also for the kind encouragements when I was in Perth. I am also grateful to the staff of the Perth Core Library. Thank you for the careful loadings and cuttings of so many drill cores, as well as the kindness when I was observing and sampling drill cores there.

The ANU PhD Scholarship, University Research Scholarship (International), Postgraduate Research Scholarship, HDR Fee Remission Merit Scholarship, and ANU Supplementary Scholarship provided by the Australian National University to cover all the tuition fees and living expenses during the past four years are sincerely appreciated. Many thanks also go to RSES for the generous traveling funds.

The Research Trainings provided by the Academic Skills and Learning Centre of ANU are appreciated, which have improved the structure and English of some drafts.

Thanks should also go to many other people at RSES. I would like to thank Dr. Xiaodong Zhang for teaching me so much physics knowledge that helps me greatly in understanding the configuration of SHRIMPs. The help from Prof. Ian Williams and Honorary Associate Prof. Mark Fanning to fix the SHRIMPs when they were not working well is sincerely appreciated. Special thanks go to Associate Prof. Yuri Amelin for giving the useful and insightful advice on my mid-term review. The approval of accessing the lab of Dr. Mark Kendrick for etching

pyrite is also appreciated. I am grateful to Maree Coldrick, the previous Senior Officer of HDR Student Administration, without whose careful work I could not have been able to do a Ph.D. here at RSES. Thanks should go to Josephine Magro for helping to book the flights and hotels before each trip. The patience of Virginia Riddle in handling the scholarship extension is also appreciated. I should also thank Duncan Bolt for fixing the problems of my PC.

I would like to thank my officemates Liane Loiselle and Perinne Tyler, who have provided me with much help in many aspects, research, English, and life. The accompanying and help of other friends (at RSES, University House, and other schools of ANU) during these years are sincerely appreciated. Last but not least, I would like to thank my parents for constant support all the time.

Abstract

Sulphur is intimately involved in environment, life, and mineral deposits. Although an increasing number of studies on the multiple sulphur isotopes of Archean records have been conducted since the discovery of sulphur mass independent fractionation (S-MIF) in Archean metasedimentary rocks, many problems still remain. Two important shortcomings of previous studies are the analytical methods (measuring the sulphur extracted from bulk rock/sulphides) and the lack of investigating the petrogeneses and generations of sulphides. As a result, the obtained data are essentially the compositions of mixed sulphur.

This thesis measures the multiple sulphur isotopic compositions of sulphides using the upgraded SHRIMP-SI (Sensitive High Resolution Ion MicroProbe-Stable Isotopes). Before analyses, the geneses and generations of pyrite are established by the combination of BSE (Back Scattered Electrons) imaging and sodium hypochlorite solution etching.

The first study on the multiple sulphur isotopic composition of pyrite in metasedimentary rocks of 3.2 Ga-2.72 Ga from the Pilbara Craton, Western Australia shows that the strongest S-MIF signal of this Archean interval ($\Delta^{33}S$ of -2.40‰) is larger than previously reported. Additionally, the available samples of this period are still quite limited compared with that of the other Archean intervals. Larger $\Delta^{33}S$ is possible and promising in sulphides with no or poor preservations. The pyrite with more negative $\Delta^{36}S/\Delta^{33}S$ than that of the Archean Reference Array (ARA, -1) displays biological or hydrothermal modifications indicated by deviations from ARA in a trend approximately parallel to the mass dependent biological fractionation or hydrothermal overprints and/or modifications on the primary diagenetic pyrite, respectively.

The second study shows that the barite-associated pyrite from the 3.49 Ga Dresser Formation characterized by considerably negative $\delta^{34}S$ is $\Delta^{33}S$-negative, suggesting sulphate reduction rather than elemental sulphur disproportionation as the earliest sulphur metabolism. However, such correspondences between the $\Delta^{33}S$ sign and sulphur metabolism type require further confirmation. Additionally, the $\Delta^{36}S/\Delta^{33}S$ of the ^{34}S-depleted pyrite exhibits no clear biological deviation trends from the associated barite, indicating that a biological origin is still equivocal.

The third study reveals two generations of pyrite in two typical Neoarchean shale samples, and each generation has two forms of morphology (disseminated grain and nodule). The results show that the multiple sulphur isotopic composition of each generation is similar and the $\Delta^{33}S$ sign is the same rather than dependent on pyrite morphology. The pyrite nodules result from coalescence of the disseminated pyrite grains in the shale matrix.

In the fourth study, the products of desulphidized pyrite and sulphidized metal iron by the released sulphur are both pyrrhotite. The fractionations in $\Delta^{33}S$ and $\Delta^{36}S$ are slight during the conversion, which can be attributed to analytical uncertainty and kinetic mass dependent fractionations. Due to the sensitivity of $\delta^{34}S$ on redox state, $\Delta^{33}S$ can provide additional significant constraints on the sulphur sources of Archean ore deposits.

The fifth study on a typical Neoarchean BIF-hosted gold deposit from the Rio das Velhas Greenstone Belt reveals four generations of pyrite using a combination of etching, BSE imaging, multiple sulphur isotopes, and abundances of gold, selenium, and molybdenum. Generation one shows characteristic negative $\delta^{34}S$, larger $\Delta^{33}S$ and higher concentration of selenium. Generation two is the main gold precipitation stage with the highest gold abundance, and also shows characteristic oscillatory zoning. The widespread S-MIF in the four generations of pyrite suggests that the hydrothermal fluids can be metamorphic fluids, metamorphic fluids reacted with surrounding rocks, and magmatic fluids mixed with metamorphic fluids and/or interacted with wall rocks. Reduction is the most likely trigger of gold precipitation.

Table of Contents

Chapter 1 Introduction

Sulphur is one of the most important elements on the Earth due to the intimate connections with environment, life, and mineral deposits in all evolution stages of the Earth. It is a highly redox-sensitive element with valence varying from -2 to +6, and has four stable isotopes, namely ^{32}S (95.02%), ^{33}S (0.75%), ^{34}S (4.21%), and ^{36}S (0.02%).

Gaseous sulphur-bearing species (mainly SO_2 and H_2S) erupted by volcanoes are important components of the atmosphere, particularly in the Archean, when the volcanic activities are frequent and violent. When the atmospheric oxygen content is high, such sulphur species are oxidized to sulphate, while when the oxygen content is low, which is the case during the Archean, they are photodissociated to elemental sulphur and sulphate by ultraviolet radiation (e.g., Farquhar et al., 2001). These sulphur products are then transported to the ocean via rainfall, and sequestered as sulphides in the sediments eventually.

Sulphur is involved in a variety of dissimilatory (e.g., sulphur oxidation, sulphur/sulphite/sulphate reduction, dimethylsulfoxide reduction) and assimilatory (e.g., synthesis of cysteine, Fe-S clusters, Molybdenum cofactor and 2-thiouridine) microbial metabolisms (e.g., Liu et al., 2012). Protokaryotic bacteria and archaea living on sulphate reduction are among the earliest life forms in the Archean (e.g., Shen et al., 2001).

Sulphur is one of the most important complex ligands of metals (e.g., Vahrenkamp, 1975). Insoluble metals can be dissolved, transported, and concentrated in the form of sulphur-bearing complexes in hydrothermal solutions from source reservoirs, and are then precipitated at deposition spots where the complexes are decomposed.

1 Research background

1.1 The terms of S-MDF and S-MIF

Sulphur mass dependent fractionation (S-MDF) is that the relative variations of isotopic ratios ($^{33}S/^{32}S$, $^{34}S/^{32}S$, and $^{36}S/^{32}S$) scale with the mass difference of the isotopes involved. The isotopic ratios are usually transformed to δ notations. $\delta^{33}S$, $\delta^{34}S$ and $\delta^{36}S$ are the ratios of $^{33}S/^{32}S$, $^{34}S/^{32}S$ and $^{36}S/^{32}S$ standardized relative to V-CDT (Vienna-Canyon Diablo Troilite) following the equation $\delta^{X}S = [(^{X}S/^{32}S)_{unknown}/(^{X}S/^{32}S)_{V\text{-}CDT} - 1] \times 1000$, where X is 33, 34, 36.

S-MDF occurs in both equilibrium and kinetic processes, during which the $\delta^{33}S$-$\delta^{34}S$ and $\delta^{36}S$-$\delta^{34}S$ relationships are approximately linear. The coefficients can be slightly different, depending on the equations chosen for the calculation. However, the most widely used coefficients were calculated based on equilibrium processes, and are 0.515 for $\delta^{33}S$-$\delta^{34}S$ and 1.90 for $\delta^{33}S$-$\delta^{34}S$ (Hulston, 1964; Hulston and Thode, 1965).

Sulphur mass independent fractionation (S-MIF) termed by Zmolek et al. (1999) is essentially a misnomer, since the relative variations of isotopic ratios rely on the mass difference as well. The "independent" is just that the fractionations do not follow the linear relationships of $\delta^{33}S = 0.515\delta^{34}S$ and $\delta^{36}S = 1.90\delta^{34}S$. The discrepances are quantified using $\Delta^{33}S$ ($\delta^{33}S - 1000 \times ((1+ \delta^{34}S/1000)^{0.515}-1)$) and $\Delta^{36}S$ ($\delta^{36}S - 1000 \times ((1+ \delta^{34}S/1000)^{1.90}-1)$)(Farquahar et al., 2013).

1.2 Temporal distribution of S-MIF

S-MIF has mainly been discovered in Archean records[1]. A compilation of the reported data on multiple sulphur isotopic compositions of sulphides and sulphates in Archean records shows an intriguing temporal distribution of $\Delta^{33}S$, and can be subdivided into three intervals: ~3.8-3.2 Ga, ~3.2-2.72 Ga, and ~2.72-2.5 Ga (Fig. 1.1). The S-MIF of ~3.8-3.2 Ga and ~2.72-2.5 Ga is characterized by much larger magnitude of maximum positive $\Delta^{33}S$ (14.3‰ and 14.4‰, respectively) than that of minimum negative $\Delta^{33}S$ (-1.8‰ and -3.9‰, respectively). In contrast, the magnitude of the maximum positive $\Delta^{33}S$ (1.9‰) during ~3.2-2.72 Ga is smaller than that of the minimum negative $\Delta^{33}S$ (-4‰). It is noteworthy that the maximum positive $\Delta^{33}S$ of ~3.2-2.72 Ga is considerably smaller than that of the other two Archean intervals.

Additionally, the $\Delta^{36}S/\Delta^{33}S$ slope displays temporal changes as well. The $\Delta^{36}S/\Delta^{33}S$ of ~3.8-3.2 Ga and ~2.72-2.5 Ga is relatively constant, slightly fluctuating around -1, which has been termed the Archean Reference Array (ARA[2]) by Farquhar et al. (2001). By comparison, the $\Delta^{36}S/\Delta^{33}S$ of ~3.2-2.72 Ga is steeper, and is -1.5 as reported in Farquhar et al. (2007) and Thomazo et al. (2009).

[1] Here, the S-MIF detected in the Paleoproterozoic records (2.5-2.32 Ga, Bekker et al., 2004; Partridge et al., 2008; Guo et al., 2009) and the sulphuric acid aerosols produced in modern stratosphere (Savarino et al., 2003) will not be discussed.

[2] Admittedly, it is still ambiguous whether the ARA should cross the origin. In this thesis, the ARA is a fixed line with an equation of $\Delta^{36}S = -\Delta^{33}S$.

1.3 Processes and mechanisms of producing S-MIF

Through laboratory experiments (photochemical reactions and sulphate reduction) and calculations, four main different processes have been proposed to produce S-MIF: (1) photochemical reactions of gaseous sulphur-bearing species such as SO_2 (e.g., Farquhar et al., 2001) and CS_2 (e.g., Colman et al., 1996), (2) thermochemical sulphate reduction by organic materials such amino acid under hydrothermal conditions (Watanabe et al., 2009), (3) heterogeneous reactions between organic materials and sulphur-bearing aqueous solutions under hydrothermal conditions (Lasaga et al., 2008), and (4) formation of gaseous S_4 and S_8 chains, in which ^{33}S and ^{36}S rarely occur (Harman et al., 2018). So far, no process has been able to fully reproduce the S-MIF signatures preserved in the Archean records. Nevertheless, based on the simultaneous oxygenation of the atmosphere and disappearance of S-MIF in the geological record (e.g., Bekker et al., 2004), as well as the S-MIF detected in the volcanic sulphate produced in modern stratosphere during strong volcanic eruptions (Savarino et al., 2003), the most widely investigated and recognized is photochemical reactions (particularly photolysis) of SO_2.

Through photochemical reaction experiments, measurements of ultraviolet absorption cross sections, and theoretical calculations, three underlying mechanisms of yielding S-MIF during photochemical reactions have been proposed: (1) isotopologue self-shielding (isotopologue abundance dependent; Lyons, 2007; Ono et al., 2013), (2) isotopologue-dependent cross-section structure (Danielache et al., 2008; Endo et al., 2015), and (3) vibrational coupling intersystem crossing (ISC; Whitehill et al., 2013).

1.4 S-MIF and environment

As stated above, the most likely process of producing S-MIF is photochemical reactions (e.g., photolysis) of SO_2 in the atmosphere. Modeling results of Pavlov and Kasting (2002) show that in an atmosphere with oxygen concentration higher than 10^{-5} times the present atmospheric level (PAL), all the sulphur-bearing products from the photochemical reactions would be oxidized to sulphate. Since a certain amount of SO_2 (mass dependent) erupted by volcanoes into the atmosphere is rapidly oxidized to sulphate (mass dependent) without subjected to photolysis, the S-MIF carried by the photochemical products can be dramatically diluted and even removed. The atmospheric oxygen content should be less than 10^{-5} PAL so that the sulphur-bearing species carrying S-MIF will not be oxidized and can be transported to

the oceans via rainfall and later sequestered by sulphides (predominantly pyrite) in the sediments. Based on this principle, S-MIF preserved in the metasedimentary rocks can be an effective and reliable indicator of low oxygen content in the contemporaneous atmosphere.

1.5 Quadruple sulphur isotopes and life

Three main approaches have been used to seek the microorganisms during the earliest stages of the Earth: remains of organisms, biomarkers, and isotopes (Shen et al., 2004 and references therein). In the case of microorganisms living on sulphur metabolisms such as sulphate reduction, neither organism remains nor biomarkers work because of the simple and indistinguishable morphologies and easily modified biomarker molecules, respectively. Therefore, sulphur isotopes are mostly used to explore the earliest sulphur-associated microbes.

Conventionally, $\delta^{34}S$ of sulphide alone is utilized to identify sulphur metabolisms in ancient records. The basis is primarily the large magnitude and/or wide range of fractionation between the products (e.g., sulphides) and initial reactants (e.g., sulphates, sulphur, and sulphites) of microbial experiments with modern microorganisms conducting sulphur-associated metabolisms (Rickard, 2012 and references therein). However, the fractionation in $\delta^{34}S$ is dependent on many factors, including the metabolism rate, substrate type, and species of microbes. For the sulphides preserved in ancient metasedimentary rocks, post-diagenetic modifications can induce mass dependent fractionations in $\delta^{34}S$. Additionally, such fractionations can be produced by abiological processes as well, e.g., thermochemical sulphate reduction and magmatic SO_2 disproportionation (Ohmoto and Goldhaber, 1997). Furthermore, $\delta^{34}S$ is incapable of distinguishing sulphate reduction from sulphur/sulphite/thiosulphate disproportionation due to overlaps in values (Habicht et al., 1998).

In recent years, the connection between quadruple sulphur isotopes and sulphur metabolisms has been established by (1) microbial experiments cultivating sulphur utilizing microorganisms followed by measuring the quadruple sulphur isotopic compostions of the products (e.g., Johnston et al., 2007), and (2) measuring the quadruple sulphur isotopic compositions of natural biogenic pyrite (e.g., pyritized Ammonite and Brachiopods, Ono et al., 2006b). The $\Delta^{36}S/\Delta^{33}S$ of natural biogenic pyrite is -6.85 (obtained by in-situ laser sampling method, Ono et al., 2006b), and that of the products (sulphate-sulphide pairs) from microbial

sulphate reduction[3] is -8.98 (Johnston et al., 2007), both of which are distinct from that of ARA (around -1, Farquhar et al., 2001). In addition to identifying biological activities, quadruple sulphur isotopes are able to distinguish different types of sulphur metabolisms such as sulphate reduction and sulphur/sulphite disproportionation by distinct $^{33}\lambda$ and $^{36}\lambda$ ($^{3x}\lambda$ = (ln(1+ $\delta^{3x}S_{sulphide}$/1000) - ln(1+ $\delta^{3x}S_{sulphate}$/1000))/(ln(1+ $\delta^{34}S_{sulphide}$/1000) - ln(1+ $\delta^{34}S_{sulphate}$/1000)), Johnston et al., 2007). Thus, quadruple sulphur isotopes are a powerful tool for exploring the earliest microorganisms living on sulphur metabolisms.

1.6 Multiple sulphur isotopes and mineral deposits

The two most abundant sulphur isotopes ^{32}S and ^{34}S (i.e., $\delta^{34}S$) of sulphides in ores have long been applied to tracing the sulphur sources of mineral deposits. However, a serious shortcoming of $\delta^{34}S$ as the sulphur tracer is the sensitivity towards redox state. Specifically, fractionations in $\delta^{34}S$ between the sulphides and hydrothermal fluids will occur when other sulphur-bearing species exist, particularly high-valence species such as sulphate (Ohmoto and Rye, 1979). In this case, the $\delta^{34}S$ of sulphides cannot represent that of the bulk original hydrothermal fluids and thus can only provide limited constraints on the sulphur sources.

Ever since the formal report of S-MIF preserved in Archean records (Farquhar et al., 2000), multiple sulphur isotopes ($\delta^{34}S$-$\Delta^{33}S$±$\Delta^{36}S$) have been increasingly utilized to trace the sulphur sources of Archean ore deposits (e.g., Becker et al., 2004; Xue et al., 2013; Selvaraja et al., 2017; LaFlamme et al., 2018). Although the fractionation between the sulphur reservoirs and the sulphur involved into hydrothermal solutions has not been investigated yet, since S-MIF is characteristic of Archean metasedimentary rocks, the signal of S-MIF is a sensitive indicator of the involvement of sulphur from the metasedimentary rocks.

Additionally, sulphur is an important complex ligand of metals, and increases the solubility of metals by forming sulphur-bearing complexes in hydrothermal solutions. Although sulphur reservoirs do not equal metal reservoirs, the sulphur sources can provide constraints on the sources of metals.

[3] The products of sulphides and sulphates were firstly precipitated from the cultures as ZnS and $BaSO_4$, respectively, which were then transformed to Ag_2S for fluorination and measurement for quadruple sulphur isotopes. Both products were normalized to the starting sulphate (Johnston et al., 2007).

2 Research gaps

2.1 Methods

The majority of the multiple-sulphur isotope data in previous studies are obtained by bulk analytical methods. For the bulk rock method, sulphur is firstly extracted from rock powders by acids (e.g., HCl) and other chemical solutions (e.g., $CrCl_2$ solution), and then sequestered as silver sulphide, which is subsequently fluoridated to SF_6 for sulphur isotope ratio measurements by mass spectrometers (e.g., Thomazo et al., 2009; Izon et al., 2015). For bulk sulphide method, the sulphide grains/laminae/nodules are combusted at high temperatures, and then the sulphur isotope ratios are measured using a mass spectrometer or element analyzer (e.g., Baublys et al., 2004; Partridge et al., 2008). The extracted sulphur is pyrite sulphur (Chromium-reducible Sulphur, though a small amount of elemental sulphur can still remain, Hsieh and Shieh, 1997) in most prior studies, and the sulphide grains/laminae/nodules are pure sulphides. However, since the metasedimentary rocks of Archean have usually been subjected to multiple stages of modification after diagenesis, the corresponding data are essentially the sulphur isotopic compositions of mixed sulphur from multiple generations of pyrite or sulphides.

A small proportion of data are obtained by in-situ analysis methods, including in-situ laser fluorination of sulphides and SIMS. Although the sampling is made by in-situ laser fluorination or Cs^+ ion beam bombardment, the same problem as bulk analytical methods can still remain due to the lack of investigation of pyrite generation (as an individual pyrite grain can contain multiple generations of pyrite). Furthermore, for laser method, the sampling area is big and deep (e.g., 400 μm in diameter and 300 μm in depth, Ono et al., 2006b), thus multiple and mixed generations could be expected to be sampled.

2.2 S-MIF in the Archean records

According to the compiled temporal distribution of $\Delta^{33}S$, the period of 3.2-2.72 Ga stands out because of the attenuated magnitudes compared with the preceding and succeeding Archean intervals (Fig. 1.1). Additionally, the $\Delta^{36}S/\Delta^{33}S$ slopes of this period are steeper (Farquar et al., 2007; Thomazo et al., 2009) than that of ARA (around -1, Farquhar et al., 2001). Based on the two important signatures, it has been proposed that the atmosphere of 3.2-2.72 Ga is compositionally different from that of the other periods of Archean. However, it is

noteworthy that the data compiled for this Archean interval were mostly obtained by bulk rock analytical methods (Ohmoto et al., 2006; Ono et al., 2006a; Farquar et al., 2007; Domagal-Goldman et al., 2008; Thomazo et al., 2009; Guy et al., 2012; Izon et al., 2015), and pyrite in metasedimentary rocks of the 2.72 Ga Tumbiana Formation was measured in situ using SIMS (Williford et al., 2016). Additionally, potential for multiple generations of pyrite was not assessed in Williford et al. (2016), thus the sampling could potentially involve mixed sulphur components. Therefore, before concluding a compositionally different atmosphere existed during the period from 3.2 Ga to 2.72 Ga, it is necessary to systematically measure the multiple sulphur isotopic composition of pyrite in 3.2-2.72 Ga metasedimentary rocks in situ using SIMS based on a well-established pyrite generation sequence.

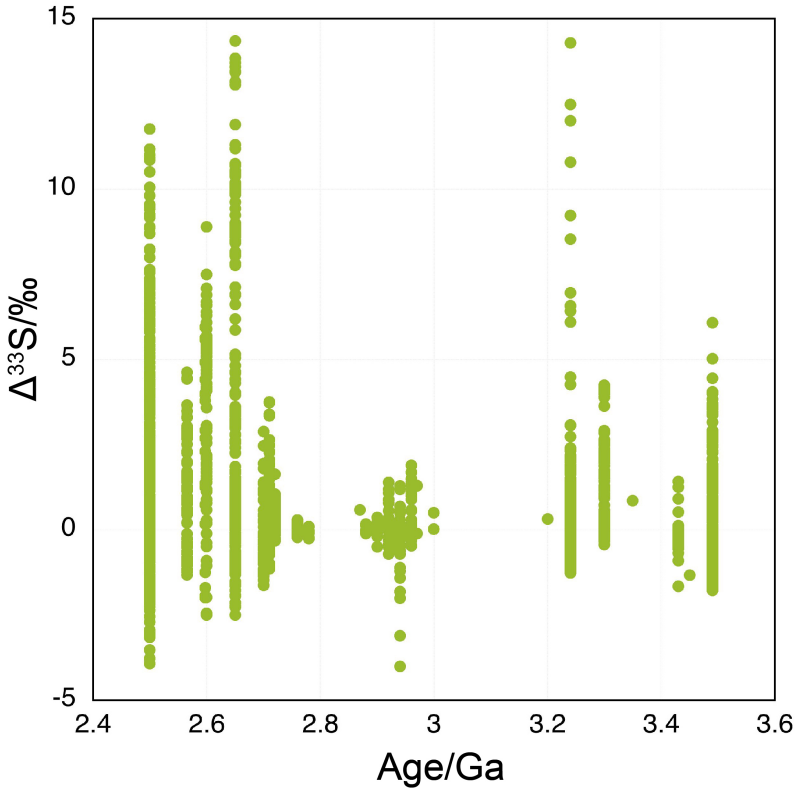

Fig. 1.1 The temporal distribution of $\Delta^{33}S$ in the Archean. Data compiled are from Ono et al., 2003; Ohmoto et al., 2006; Ono et al., 2006a; Farquhar et al., 2007; Kamber and Whitehouse, 2007; Philippot et al., 2007; Kaufman et al., 2007; Domagal-Goldman et al., 2008; Ueno et al., 2008; Ono et al., 2009; Shen et al., 2009; Thomazo et al., 2009; Wacey et al., 2010; Guy et al., 2012; Philippot et al., 2012; Kurzweil et al., 2013; Roerdink et al., 2013; Thomazo et al., 2013; Marin-Carbonne et al., 2014; Zhelezinskaia et al., 2014; Gregory et al., 2015; Izon et al., 2015; Wacey et al., 2015; Williford et al., 2016; Muller et al., 2016. Note that for Wacey et al., 2010 and Guy et al., 2012, only the data of diagenetic sulphides are compiled.

One of the earliest life forms is sulphur-utilizing bacteria or archaea as previous studies have proposed based on the quadruple sulphur isotopic compositions of pyrite and barite from the 3.49 Ga Dresser Formation in the Pilbara Craton, Western Australia. Although both bulk and in-situ methods have revealed considerably depleted ^{34}S (i.e., considerably negative $\delta^{34}S$) in pyrite associated with barite, the former show negative $\Delta^{33}S$ while the latter exhibit positive $\Delta^{33}S$, which led to contrasting conclusions on the earliest sulphur metabolism type, sulphate reduction (Shen et al., 2009; Ueno et al., 2008) or elemental sulphur disproportionation (Philippot et al., 2007). It is necessary to clarify the pyrite generation due to the multiple stages of hydrothermal events forming the chert-barite unit (Van Kranendonk et al., 2008), which, however, were not conducted in previous studies. Additionally, prior experiments on hydrothermal (abiological) reduction of sulphate also produced significant fractionations in $\delta^{34}S$ (Ohmoto and Goldhaber, 1997). Thus it is essential to firstly establish the pyrite generation and then reanalyze the multiple and quadruple sulphur isotopes.

Previous bulk analyses of separated pyrite nodules and disseminated pyrite grains show preservation preference of $\Delta^{33}S$, i.e., negative $\Delta^{33}S$ (sulphate product of SO_2 photolysis) is preserved in nodular pyrite while positive $\Delta^{33}S$ (elemental sulphur product of SO_2 photolysis) is preserved in disseminated pyrite grains (Partridge et al., 2008; Ono et al., 2009). However, the underlying mechanism has not been investigated yet. Additionally, the pyrite generation is also the problem, and thus such preservation preference needs confirmation.

2.3 Application of multiple sulphur isotopes to Archean gold deposits

Although multiple sulphur isotopes have been increasingly applied to tracing the sulphur sources of Archean mineral deposits, it has not been investigated yet how the multiple sulphur isotopes fractionate between the source sulphur reservoir and the sulphur involved in the hydrothermal fluids. Pyrite desulphidation to pyrrhotite and elemental sulphur is an important reaction of releasing sulphur into the hydrothermal fluids (e.g., Phillips and Powell, 2010; Tomkins, 2010). So far only fractionation in $\delta^{34}S$ has been studied (Kajiwara et al., 1981; Yamamoto, 1984; Ripley and Snyder, 2000).

Multiple sulphur isotopic compositions of ore-associated pyrite in Archean gold deposits obtained by prior studies can be divided into two groups: $\Delta^{33}S$ of near zero (Xue et al., 2013) and non-zero (e.g., Selvaraja et al., 2017), which have led to contrasting conclusions on the sulphur sources of this type of mineral deposits (magmatic or metamorphic fluids).

3 Aims and significance

The first aim is to explore larger magnitudes of S-MIF and the causes of more negative $\Delta^{36}S/\Delta^{33}S$ of sulphides in metasedimentary rocks from 3.2 Ga to 2.72 Ga. The significance is that further evidence or constraints can be obtained on whether the atmosphere of this period is compositionally different compared with that of the other Archean intervals.

The second aim is to sort the chronological sequence of pyrite occurring in the chert-barite unit of the 3.49 Ga Dresser Formation, and obtain their multiple sulphur isotopic compositions. The significance is confirming whether microbial sulphate reduction or elemental sulphur disproportionation is the earliest sulphur metabolism form, and further verifying a biological origin for the sulphur forming pyrite depleted in ^{34}S.

The third aim is to obtain the $\Delta^{33}S$ sign of pyrite with different morphology based on a clear pyrite generation. The significance is whether the sign of $\Delta^{33}S$ is dependent on pyrite morphology (nodule and disseminated grain) can be confirmed, and if such dependences do exist, the underlying mechanism can be explored.

The fourth aim is to clarify the quadruple sulphur isotopic fractionation of pyrite desulfidation to pyrrhotite. This investigation has been the first try to reveal the fractionations in $\delta^{34}S$, $\Delta^{33}S$ and $\Delta^{36}S$ between the initial pyrite and products (desulphidized pyrite and liberated sulphur), thus establishing the basis for the application of multiple sulphur isotopes to tracing sulphur sources of Archean ore deposits.

The fifth aim is to clarify the generation of ore-related pyrite of a typical Neoarchean Banded Iron Formation-hosted gold deposit, and acquire high-resolution multiple sulphur isotopic composition and abundance of gold and redox-sensitive trace elements. This study can provide new data on whether the ore-related pyrite of Archean gold deposits contains S-MIF signature, and further constrain the sulphur sources of this type of ore deposits.

4 Outline of the chapters

The main body of the thesis consists of five chapters (Chapter 2 to Chapter 6). Chapter 2 investigates the S-MIF recorded in pyrite of the 3.2-2.72 Ga metasedimentary rocks from the Pilbara Craton, Western Australia. Chapter 3 investigates the $\delta^{34}S$-$\Delta^{33}S\pm\Delta^{36}S$ systematics of

pyrite occurring within the chert-barite unit of the 3.49 Ga Dresser Formation. Chapter 4 investigates the multiple sulphur isotopic compositions of pyrite of different morphology occurring in two typical Neoarchean shale samples. Chapter 5 establishes the basis for the application of multiple sulphur isotopes to tracing the sulphur sources of Archean gold deposits by an experiment of pyrite desulphidation at 675 °C followed by the measurement of quadruple sulphur isotopes. Chapter 6 studies a typical Neoarchean Banded Iron Formation-hosted gold deposit from the Rio das Velhas Greenstone Belt, Quadrilátero Ferrífero using a combination of etching, BSE imaging, multiple sulphur isotopes, and the abundances of gold, selenium and molybdenum.

References

Baublys, K.A., Golding, S.D., Young, E., Kamber, B.S., 2004. Simultaneous determination of $\delta^{33}S_{V\text{-}CDT}$ and $\delta^{34}S_{V\text{-}CDT}$ using masses 48, 49 and 50 on a continuous flow isotope ratio mass spectrometer. Rapid Communications in Mass Spectrometry 18 (22): 2765-2769.

Bekker, A., Holland, H.D., Wang, P.L., Rumble III, D., Stein, H.J., Hannah, J.L., Coetzee, L.L., Beukes, N.J., 2004. Dating the rise of atmospheric oxygen. Nature 427: 117-120.

Colman, J.J., Xu, X., Thiemens, M.H., Trogler, W.C., 1996. Photopolymerization and Mass-Independent Sulfur Isotope Fractionations in Carbon Disulphide. Science 273 (5276): 774-776.

Danielache, S.O., Eskebjerg, C., Johnson, M.S., Ueno, Y., Yoshida, N., 2008. High-precision spectroscopy of ^{32}S, ^{33}S, and ^{34}S sulfur dioxide: Ultraviolet absorption cross sections and isotope effects. Journal of Geophysical Research 113: D17314.

Domagal-Goldman, S.D., Kasting, J.F., Johnston, D.T., Farquhar, J., 2008. Organic haze, glaciations and multiple sulfur isotopes in the Mid-Archean Era. Earth and Planetary Science Letters 269 (1-2): 29-40.

Endo, Y., Danielache, S.O., Ueno, Y., Hattori, S., Johnson, M.S., Yoshida, N., Kjaergaard, H.G., 2015. Photoabsorption cross-section measurements of ^{32}S, ^{33}S, ^{34}S, and ^{36}S sulfur dioxide from 190 to 220 nm. Journal of Geophysical Research: Atmospheres 120 (6): 2546-2557.

Farquhar, J., Bao, H., Thiemens, M., 2000. Atmospheric Influence of Earth's Earliest Sulfur Cycle. Science 289 (5480): 756-758.

Farquhar, J., Cliff, J., Zerkle, A.L., Kamyshny, A., Poulton, S.W., Claire, M., Adams, D., Harms, B., 2013. Pathways for Neoarchean pyrite formation constrained by mass-independent sulfur isotopes. Proceedings of the National Academy of Sciences 110 (44): 17638-17643.

Farquhar, J., Peters, M., Johnston, D.T., Strauss, H., Masterson, A., Wiechert, U., Kaufman, A.J., 2007. Isotopic evidence for Mesoarchaean anoxia and changing atmospheric sulphur chemistry. Nature 449: 706-709.

Farquhar, J., Savarino, J., Airieau, S., Thiemens, M.H., 2001. Observation of wavelength-sensitive mass-independent sulfur isotope effects during SO_2 photolysis: Implications for the early atmosphere. Journal of Geophysical Research 106 (E12): 32829-32839.

Gregory, D.D., Large, R.R., Halpin, J.A., Steadman, J.A., Hickman, A.H., Ireland, T.R., Holden, P., 2015. The chemical conditions of the late Archean Hamersley basin inferred from whole rock and pyrite geochemistry with $\Delta^{33}S$ and $\delta^{34}S$ isotope analyses. Geochimica et Cosmochimica Acta 149: 223-250.

Guo, Q., Strauss, H., Kaufman, A.J., Schröder, S., Gutzmer, J., Wing, B., Baker, M.A., Bekker, A., Jin, Q., Kim, S.T., Farquhar, J., 2009. Reconstructing Earth's surface oxidation across the Archean-Proterozoic transition. Geology 37 (5): 399-402.

Guy, B.M., Ono, S., Gutzmer, J., Kaufman, A.J., Lin, Y., Fogel., M.L., Beukes, N.J., 2012. A multiple sulfur and organic carbon isotope record from non-conglomeratic sedimentary rocks of the Mesoarchean Witwatersrand Supergroup, South Africa. Precambrian Research 216-219: 208-231.

Habicht, K.S., Canfield, D.E., Rethmeier, J., 1998. Sulfur isotope fractionation during bacterial reduction and disproportionation of thiosulfate and sulfite. Geochimica et Cosmochimica Acta 62 (15): 2585-2595.

Harman, C.E., Pavlov, A.A., Babikov, D., Kasting, J.F., 2018. Chain formation as a mechanism for mass-independent fractionation of sulfur isotopes in the Archean atmosphere. Earth and Planetary Science Letters 496: 238-247.

Hsieh, Y.P., and Shieh, Y.N., 1997. Analysis of reduced inorganic sulfur by diffusion methods: improved apparatus and evaluation for sulfur isotopic studies. Chemical Geology 137 (3-4): 255-261.

Hulston, J.R., 1964. Variations in the ratios of the four stable sulphur isotopes in meteorites and their relation to chemical and nuclear effects. Ph.D. thesis, McMaster University.

Hulston, J.R. and Thode, H.G., 1965. Variations in the S^{33}, S^{34}, and S^{36} Contents of Meteorites and Their Relation to Chemical and Nuclear Effects. Journal of Geophysical Research 70 (14): 3475-3484.

Izon, G., Zerkle, A.L., Zhelezinskaia, I., Farquhar, J., Newton, R.J., Poulton, S.W., Eigenbrode, J.L., Claire, M.W., 2015. Multiple oscillations in Neoarchaean atmospheric chemistry. Earth and Planetary Science Letters 431: 264-273.

Johnston, D.T., Farquhar, J., Canfield, D.E., 2007. Sulfur isotope insights into microbial sulfate reduction: When microbes meet models. Geochimica et Cosmochimica Acta 71 (16): 3929-3947.

Kajiwara, Y., Sasaki, A., Matsubaya, O., 1981. Kinetic sulfur isotope effects in the thermal decomposition of pyrite. Geocchemical Journal 15 (4): 193-197.

Kamber, B.S., and Whitehouse, M.J., 2007. Micro-scale sulphur isotope evidence for sulphur cycling in the late Archean shallow ocean. Geobiology 5 (1): 5-17.

Kaufman, A.J., Johnston, D.T., Farquhar, J., Masterson, A.L., Lyons, T.W., Bates, S., Anbar, A.D., Arnold, G.L., Garvin, J., Buick, R., 2007. Late Archean Biospheric Oxygenation and Atmospheric Evolution. Science 317 (5846): 1900-1903.

Kurzweil, F., Claire, M., Thomazo, C., Peters, M., Hannington, M., Strauss, H., 2013. Atmospheric sulfur rearrangement 2.7 billion years ago: Evidence for oxygenic photosynthesis. Earth and Planetary Science Letters 366: 17-26.

LaFlamme C., Sugiono D., Thébaud N., Caruso S., Fiorentini M., Selvaraja V., Jeon H., Voute F. and Martin L. (2018) Multiple sulfur isotopes monitor fluid evolution of an Archean orogenic gold deposit. Geochimica et Cosmochimica Acta 222: 436-446.

Lasaga, A.C., Otake, T., Watanabe, Y., Ohmoto, H., 2008. Anomalous fractionation of sulfur isotopes during heterogeneous reactions. Earth and Planetary Science Letters 268 (1-2): 225-238.

Liu, Y., Beer, L.L., Whitman, W.B., 2012. Sulfur metabolism in archaea reveals novel processes. Environmental Microbiology 14 (10): 2632-2644.

Lyons, J.R., 2007. Mass-independent fractionation of sulfur isotopes by isotope-selective photodissociation of SO_2. Geophysical Research Letters 34 (22): L22811.

Marin-Carbonne, J., Rollion-Bard, C., Bekker, A., Rouxel, O., Agangi, A., Cavalazzi, B., Wohlgemuth-Ueberwasser, C.C., Hofmann, A., McKeegan, K.D., 2014. Coupled Fe and S isotope variations in pyrite nodules from Archean shale. Earth and Planetary Science Letters 392: 67-79.

Muller, É., Philippot, P., Rollion-Bard, C., Cartigny, P., 2016. Multiple sulfur-isotope signatures in Archean sulfates and their implications for the chemistry and dynamics of the early atmosphere. Proceedings of the National Academy of Sciences 113 (27): 7432-7437.

Ohmoto, H., and Goldhaber, M., 1997. Applications of sulfur and carbon isotopes in ore deposit research, in Barnes, H.L., ed., Geochemistry of Hydrothermal Ore Deposits: New York, Wiley, p. 517-611.

Ohmoto, H., and Rye, R.O., 1979. Isotopes of sulfur and carbon, in Barnes, H.L., ed., Geochemistry of Hydrothermal Ore Deposits: New York, Wiley, p. 509-567.

Ohmoto, H., Watanabe, Y., Ikemi, H., Poulson, S.R., Taylor, B.E., 2006. Sulphur isotope evidence for an oxic Archaean atmosphere. Nature 442: 908-911.

Ono, S., Beukes, N.J., Rumble, D., 2009. Origin of two distinct multiple-sulfur isotope compositions of pyrite in the 2.5 Ga Klein Naute Formation, Griqualand West Basin, South Africa. Precambrian Research 169 (1-4): 48-57.

Ono, S., Whitehill, A.R., Lyons, J.R., 2013. Contribution of isotopologue self-shielding to sulfur mass-independent fractionation during sulfur dioxide photolysis. Journal of Geophysical Research: Atmosphere 118 (5): 2444-2454.

Ono, S., Beukes, N.J., Rumble, D., Fogel, M.L., 2006a. Early evolution of atmospheric oxygen from multiple-sulfur and carbon isotope records of the 2.9 Ga Mozaan Group of the Pongola Supergroup, Southern Africa. South African Journal of Geology 109 (1-2): 97-108.

Ono, S., Wing, B., Johnston, D., Farquhar, J., Rumble, D., 2006b. Mass-dependent fractionation of quadruple stable sulfur isotope system as a new tracer of sulfur biogeochemical cycles. Geochimica et Cosmochimica Acta 70 (9): 2238-2252.

Partridge, M.A., Golding, S.D., Baublys, K.A., Young, E., 2008. Pyrite paragenesis and multiple sulfur isotope distribution in late Archean and early Paleoproterozoic Hamersley Basin sediments. Earth and Planetary Science Letters 272 (1-2): 41-49.

Pavlov, A.A., and Kasting, J.F., 2002. Mass-Independent Fractionation of Sulfur Isotopes in Archean Sediments: Strong Evidence for an Anoxic Archean Atmosphere. Astrobiology 2 (1): 27-41.

Phillips, G.N., and Powell, R., 2010. Formation of gold deposits: a metamorphic devolatilization model. Journal of Metamorphic Geology 28 (6): 689-718.

Philippot, P., Van Zuilen, M., Lepot, K., Thomazo, C., Farquhar, J., Van Kranendonk, M.J., 2007. Early Archaean Microorganisms Preferred Elemental Sulfur, Not Sulfate. Science 317 (5844): 1534-1537.

Philippot, P., van Zuilen, M., Rollion-Bard, C., 2012. Variations in atmospheric sulphur chemistry on early Earth linked to volcanic activity. Nature Geoscience 5: 668-674.

Rickard, D., 2012. Sulfidic Sediments and Sedimentary Rocks. In Developments in Sedimentology, Amsterdam, Elsevier 65: 1-766.

Ripley, E.M., and Snyder, K., 2000. Experimental sulfur isotope studies of the pyrite to pyrrhotite conversion in a hydrogen atmosphere. Economic Geology 95 (7): 1551-1554.

Roerdink, D.L., Mason, P.R.D., Whitehouse, M.J., Reimer, T., 2013. High-resolution quadruple sulfur isotope analyses of 3.2 Ga pyrite from the Barberton Greenstone Belt in South Africa reveal distinct environment controls on sulphide isotopic arrays. Geochimica et Cosmochimica Acta 117: 203-215.

Savarino, J., Romero, A., Cole-Dai, J., Bekki, S., Thiemens, M.H., 2003. UV induced mass-independent sulfur isotope fractionation in stratospheric volcanic sulfate. Geophysical Research Letters 30: 2131.

Selvaraja, V., Caruso, S., Fiorentini, M.L., LaFlamme, C.K., and Bui, T.H., 2017. Atmospheric sulfur in the orogenic gold deposit of the Archean Yilgarn Craton, Australia. Geology 45 (8): 691-694.

Shen, Y., and Buick, R., 2004. The antiquity of microbial sulfate reduction. Earth-Science Reviews 64 (3-4): 243-272.

Shen, Y., Buick, R., Canfield, D.E., 2001. Isotopic evidence for microbial sulphate reduction in the early Archaean era. Nature 410: 77-81.

Shen, Y., Farquhar, J., Masterson, A., Kaufman, A.J., Buick, R., 2009. Evaluating the role of microbial sulfate reduction in the early Archean using quadruple isotope systematics. Earth and Planetary Science Letters 279 (3-4): 383-391.

Thomazo, C., Ader, M., Farquhar, J., Philippot, P., 2009. Methanotrophs regulated atmospheric sulfur isotope anomalies during the Mesoarchean (Tumbiana Formation, Western Australia). Earth and Planetary Science Letters 279 (1-2): 65-75.

Thomazo, C., Nisbet, E.G., Grassineau, N.V., Peters, M., Strauss, H., 2013. Multiple sulfur and carbon isotope composition of sediments from the Belingwe Greenstone Belt (Zimbabwe): A biogenic methane regulation on mass independent fractionation of sulfur during the Neoarchean? Geochimica et Cosmochimica Acta 121: 120-138.

Tomkins, A.G., 2010. Windows of metamorphic sulfur liberation in the crust: Implications for gold deposit genesis. Geochimica et Cosmochimica Acta 74 (11): 3246-3259.

Ueno, Y., Ono, S., Rumble, D., Maruyama, S., 2008. Quadruple sulfur isotope analysis of ca. 3.5 Ga Dresser Formation: New evidence for microbial sulfate reduction in the early Archean. Geochimica et Cosmochimica Acta 72 (23): 5675-5691.

Vahrenkamp, H., 1975. Sulfur Atoms as Ligands in Metal Complexes. Angewandte Chemie International Edition 14 (5): 322-329.

Van Kranendonk, M.J., Philippot, P., Lepot, K., Bodorkos, S., Pirajno, F., 2008. Geological setting of Earth's oldest fossils in the ca. 3.5 Ga Dresser Formation, Pilbara Craton, Western Australia. Precambrian Research 167 (1-2): 93-124.

Wacey, D., McLoughlin, N., Whitehouse, J., Kilburn, M.R., 2010. Two coexisting sulfur metabolisms in a ca. 3400 Ma sandstone. Geology 38 (12): 1115-1118.

Wacey, D., Noffke, N., Cliff, J., Barley, M.E., Farquhar, J., 2015. Micro-scale quadruple sulfur isotope analysis of pyrite from the ~3480 Ma Dresser Formation: New insights into sulfur cycling on the early Earth. Precambrian Research 258: 24-35.

Watanabe, Y., Farquhar, J., Ohmoto, H., 2009. Anomalous Fractionations of Sulfur Isotopes During Thermochemical Sulfate Reduction. Science 324 (5925): 370-373.

Whitehill, A.R., Xie, C., Hu, X., Xie, D., Guo, H., Ono, S., 2013. Vibronic origin of sulfur mass-independent isotope effect in photoexcitation of SO_2 and the implications to the early earth's atmosphere. Proceedings of the National Academy of Sciences of the United States of America 110 (44): 17697-17702.

Williford, K.H., Ushikubo, T., Lepot, K., Kitajima, K., Hallmann, C., Spicuzza, M.J., Kozdon, R., Eigenbrode, J.L., Summons, R.E., Valley, J.W., 2016. Carbon and sulfur isotopic signatures of ancient life and environment at the microbial scale: Neoarchean shales and carbonates. Geobiology 14 (2): 105-128.

Xue, Y., Campbell, I., Ireland, T.R., Holden, P., Armstrong, R., 2013. No mass-independent sulfur isotope fractionation in auriferous fluids supports a magmatic origin for Archean gold deposits. Geology 41 (7): 791-794.

Yamamoto, M., 1984. Sulfur isotope effects in the thermal breakdown of pyrite. Earth and Planetary Science Letters 69 (2): 335-340.

Zhelezinskaia, I., Kaufman, A.J., Farquhar, J., Cliff, J., 2014. Large sulfur isotope fractionations associated with Neoarchean microbial sulfate reduction. Science 346 (6210): 742-744.

Zmolek, P., Xu, X., Jackson, T., Thiemens, M.H., Trogler, W.C., 1999. Large Mass Independent Sulfur Isotope Fractionations during the Photopolymerization of $^{12}CS_2$ and $^{13}CS_2$. The Journal of Physical Chemistry A 103 (15): 2477-2480.

Chapter 2 Investigation into the ca. 3.2-2.72 Ga Sulphur Mass Independent Fractionation Recorded in the Pilbara Craton, Western Australia

Abstract: The sulphur mass independent fractionation (S-MIF) of ca. 3.2-2.72 Ga is distinct from that of the other Archean periods because of the dampened magnitude and more negative $\Delta^{36}S/\Delta^{33}S$. However, the available samples of this period are limited owing to poor or no preservations. Additionally, the majority of the data were obtained by bulk rock analytical methods, which are essentially the sulphur isotopic compositions of mixed sulphur components due to multiple stages of post-sedimentation overprints and modifications. This study systematically measured the multiple sulphur isotopic composition of pyrite in metasedimentary rocks of ca. 3.2-2.72 Ga from the Pilbara Craton, Western Australia, where the best-preserved Archean records occur, using the upgraded SHRIMP-SI, combined with pyrite genesis and generation investigation by BSE imaging and NaOCl etching. The results show that $\Delta^{33}S$ of this Archean interval varies from -2.40‰ to 0.79‰. Such a range is inconsistent with any experiment of producing S-MIF so far, where the magnitude of the maximum positive $\Delta^{33}S$ is considerably larger than that of the minimum negative $\Delta^{33}S$. Since the products carrying positive $\Delta^{33}S$ from photochemical reactions of SO_2 are inclined to be preserved in deep marine environments, nevertheless, the available samples are mostly of shallow water environments. Larger magnitudes of $\Delta^{33}S$ are promising in unavailable samples. In the $\Delta^{33}S$-$\Delta^{36}S$ plot, the data of the diagenetic pyrite of the 2.72 Ga Tumbiana Formation, the 2.93 Ga Mosquito Creek Formation and the 2.78 Ga Mt. Roe Basalt deviate from the Archean Reference Array (ARA) in a trend similar to biological fractionation and microbial sulphate reduction. The data of the other pyrite of 2.93 Ga Mosquito Creek Formation and 2.78 Ga Mt. Roe Basalt deviate from the ARA as well, which can be attributed to hydrothermal modifications.

1. Introduction

Sulphur mass independent fractionation (S-MIF), where the fractionations between the isotopic ratios of $^{34}S/^{32}S$, $^{33}S/^{32}S$ and $^{36}S/^{32}S$ during a reaction deviate from the isotope mass difference proportionality, is characteristic of Archean records. The magnitude of S-MIF is quantified using $\Delta^{33}S$ ($\delta^{33}S - 1000 \times [(1 + \delta^{34}S/1000)^{0.515} - 1]$) and $\Delta^{36}S$ ($\delta^{36}S - 1000 \times [(1 + \delta^{34}S/1000)^{1.90} - 1]$). The temporal distribution of S-MIF in the Archean and Paleoproterozoic is intriguing: the largest S-MIF occurs between 2.7 Ga and 2.5 Ga, with $\Delta^{33}S$ ranging from -3.9‰ to +14.4‰, followed by Paleoarchean, with $\Delta^{33}S$ varying from -1.8‰ to +14.3‰, and then the attenuated S-MIF from ca. 3.2 Ga to 2.72 Ga, with positive $\Delta^{33}S$ up to merely +1.9‰ and negative $\Delta^{33}S$ up to -4‰, whereas S-MIF after 2.5 Ga diminishes dramatically, with $\Delta^{33}S$ mostly of less than ±0.5‰ (Fig. 2.1).

The most likely processes of producing S-MIF are photochemical reactions of SO_2, based on the simultaneous disappearance of S-MIF in the geological records and significant increase in the atmospheric oxygen concentration (e.g., Bekker et al., 2004), the relative consistence between the quadruple sulphur isotopic composition of photochemical products and that of the Archean records (e.g., Farquhar et al., 2001), and the S-MIF detected in the volcanic sulphate produced in modern stratosphere (e.g., Savarino et al., 2003). Modeling results based on SO_2 photolysis have shown that the preservation of S-MIF requires low oxygen content in the atmosphere, probably less than 10^{-5} times the present atmospheric level (PAL; Pavlov and Kasting, 2002) and abundant reducing gases such as methane (Zahnle et al., 2006). On these grounds, some authors have suggested that the atmosphere from ca. 3.2 Ga to 2.72 Ga was oxidized (Ohmoto et al., 2006; Ono et al., 2006a). However, such viewpoints are contrary to the conclusion derived from the concentrations of redox-sensitive elements (e.g., U, Mo, Cr, Se) in the metasedimentary rocks of this period (Yang et al., 2002; Wille et al., 2013). Other authors, alternatively, hold the opinion that the atmosphere was still anoxic during this unique period, except that the atmospheric composition was different based on the characteristic more negative $\Delta^{36}S/\Delta^{33}S$ ratios (e.g., Farquhar et al., 2007). While others, taking the

contemporaneous glaciation into account, propose the presence of an organic haze to explain the muted S-MIF (Domagal-Goldman et al., 2008). Nevertheless, a detailed study on the ca. 2.9 Ga Witwatersrand succession of South Africa by Guy et al. (2012) suggests that the dampened S-MIF observed is the result of dilution by mass-dependent sulphur from a crustal source.

The analytical methods used in previous studies on the ca. 3.2 to 2.72 Ga samples are mostly based on bulk rock or sulphides (Kiba method-extracted sulphur or chromium (II)-extracted sulphur). Even for chromium-reducible sulphur (CRS, composed primarily of pyrite sulphur), a single pyrite grain in Archean metasedimentary rocks can contain more than one generation of pyrite, not to mention different pyrite grains, therefore, the data represent the multiple sulphur isotopic compositions of mixed sulphur components. The Paleoarchean and Late Neoarchean sulphides (mainly pyrite) have been extensively measured in situ using SIMS, and the results show larger maximum magnitudes of S-MIF (e.g., Philippot et al., 2007; Philippot et al., 2012; Kamber and Whitehouse, 2007; Williford et al., 2016) compared to those obtained by bulk sulphur analytical methods (e.g., Ono et al., 2003; Ueno et al., 2008; Kaufman et al., 2007; Izon et al., 2015). In comparison, pyrite in metasedimentary rocks of ca. 3.2 to 2.72 Ga has rarely been measured in situ for multiple sulphur isotopic composition. Additionally, the genesis of pyrite measured has only been addressed in a reconnaissance examination in a few previous studies (e.g., Guy et al., 2012). Hence, before coming to the conclusion of a compositionally different atmosphere in the Mesoarchean, it is necessary to re-measure the multiple sulphur isotopic compositions of pyrite in metasedimentary rocks of this period in situ based on well-established pyrite genesis and generation sequence.

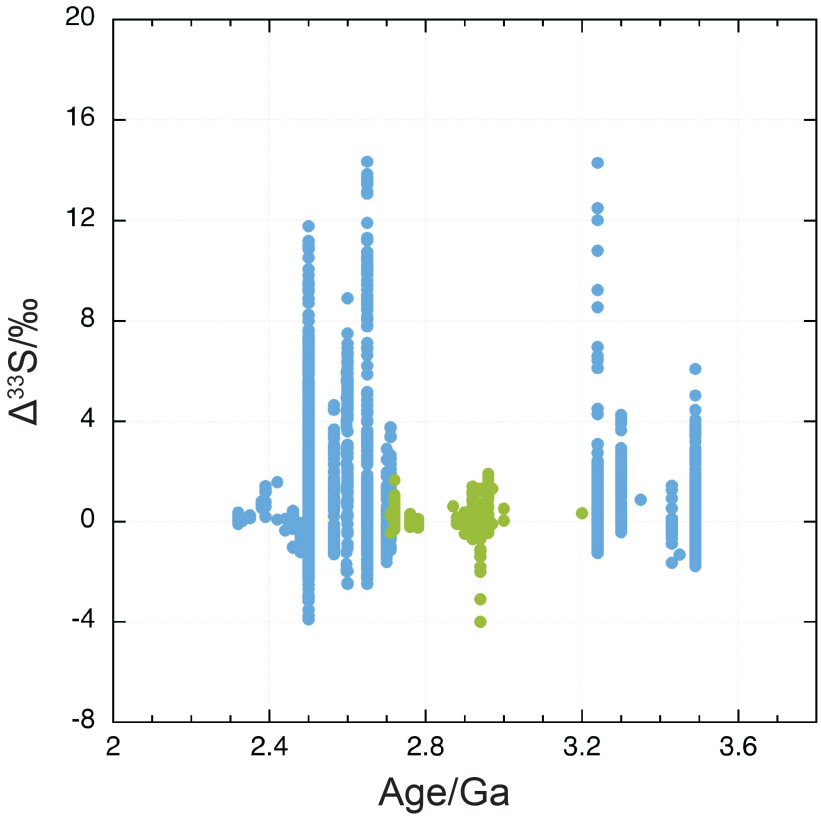

Fig. 2.1 The temporal distribution of S-MIF in the Archean and the early Paleoproterozoic. Data compiled include Ono et al., 2003; Bekker et al., 2004; Ohmoto et al., 2006; Ono et al., 2006a; Farquhar et al., 2007; Kamber and Whitehouse, 2007; Philippot et al., 2007; Kaufman et al., 2007; Domagal-Goldman et al., 2008; Partridge et al., 2008; Ueno et al., 2008; Guo et al., 2009; Ono et al., 2009; Shen et al., 2009; Thomazo et al., 2009; Wacey et al., 2010; Guy et al., 2012; Philippot et al., 2012; Kurzweil et al., 2013; Roerdink et al., 2013; Thomazo et al., 2013; Marin-Carbonne et al., 2014; Zhelezinskaia et al., 2014; Gregory et al., 2015; Izon et al., 2015; Wacey et al., 2015; Williford et al., 2016; Muller et al., 2016. Note that for Wacey et al., 2010 and Guy et al., 2012, only the data of diagenetic sulphides are compiled. $\Delta^{33}S$ in Bekker et al., 2004 is recalculated following $\Delta^{33}S = \delta^{33}S - 1000 \times [(1 + \delta^{34}S/1000)^{0.515} - 1]$.

This study investigated the multiple (triple and quadruple) sulphur isotopic compositions of pyrite in metasedimentary rocks of ca. 3.2 to 2.72 Ga from the Pilbara Craton, Western Australia using the upgraded SHRIMP-SI (Sensitive High Resolution Ion MicroProbe-Stable Isotope). Before the analyses, pyrite genesis and generation were studied by a combination of

BSE (Back-scattered electron) imaging and NaOCl solution etching. The aims of this study are to seek larger magnitude of S-MIF, confirm and explain the more negative $\Delta^{36}S/\Delta^{33}S$.

2. Geological Setting

The Pilbara Craton is located in the northwest of Western Australia and consists of the northern Pilbara and the southern Fortescue and Hamersley Basins (Fig. 2.2). The northern Pilbara is composed of 3.80-3.55 Ga basement, 3.53-3.11 Ga granite-greenstone terranes and 3.22-2.93 Ga metavolcanic-sedimentary basins (Hickman, 2012), and is divided into the East Pilbara Terrane (EPT), the Central Pilbara Tectonic Zone (CPTZ), the West Pilbara Terrane (WPT), and other terranes (Van Kranendonk et al., 2002; Pike et al., 2006). The EPT (3.53-3.22 Ga) is a volcanic plateau made up of the Pilbara Supergroup characterized by ultramafic-mafic volcanics, barite deposits, stromatolites and contemporaneous granitic supersuites. The WPT is composed of three terranes: the Karratha Terrane (3.50-3.25 Ga), the Regal Terrane (ca. 3.2 Ga), and the Sholl Terrane (3.13-3.11 Ga). The Regal Terrane further consists of the Regal Formation (3.2 Ga) and the Dixon Island Formation (3.19 Ga).

The basins in east Pilbara include the Soanesville Basin, the Budjan Creek Basin, the Gorge Creek Basin, and the Mosquito Creek Basin. The Soanesville Basin overlying the northwest EPT is composed of the Soanesville Group (3.24-3.19 Ga; Rasmussen et al., 2007). The Budjan Creek Basin (3.2 Ga; Nelson, 2001) overlying the southeast EPT consists of the Budjan Creek Formation and unnamed volcanics. The Gorge Creek Basin is composed of the Gorge Creek Group (3.05-3.02 Ga), which in east Pilbara is made up of the Farrel Quartzite, the Cleaverville Formation, and the Cundaline Formation. The Mosquito Creek Basin (MCB) is located to the southeast of EPT, and trends between east-west and northeast-southwest over an estimated strike length of 400 km (Hickman, 2004). The strata in the MCB are mainly the Nullagine Group, which is composed of the underlying Coondamar Formation (3.2-2.94 Ga) that comprises sandstone, chert, gabbro, and (ultra)mafic volcanics, and the overlying Mosquito Creek Formation (2.97-2.91 Ga; Bagas et al., 2008) that consists of ca. 200 m basal

interbedded conglomerate, turbiditic sandstone, siltstone and shale, and <4-km upper thinly bedded sandstone interbedded with siltstone and shale (Blake, 2001).

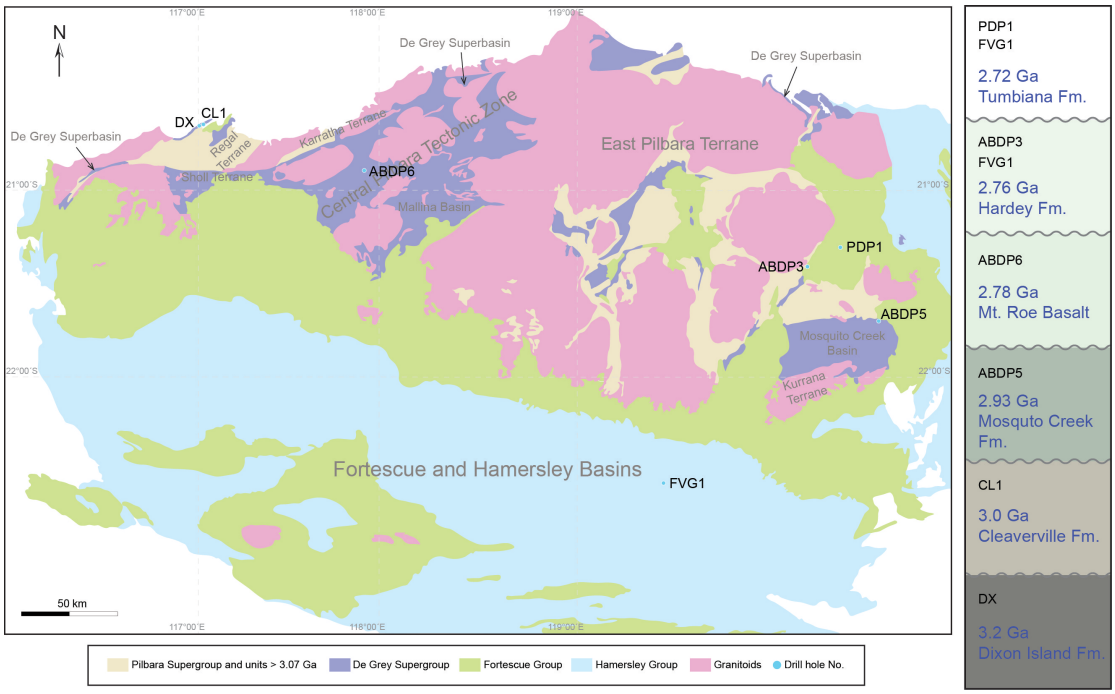

Fig. 2.2 On the left is the simplified geological map of the Pilbara Craton along with the drill hole sites, modified from the 1:50,000 Geology map from GeoView database of the Geological Survey of Western Australia (https://geoview.dmp.wa.gov.au/GeoViews/?Viewer=GeoVIEW). Also included are the terranes and basins outlined in Hickman (2012). On the right is the stratigraphic column of the strata from ~3.2 to 2.72 Ga in the Pilbara Craton.

The basins in the central and western parts of Pilbara include the Nickol River Basin, the Gorge Creek Basin, the Whim Creek Basin, and the Mallina Basin. The Nickol River Basin (3.27-3.25 Ga) overlying the Karratha Terrane is composed entirely of the Nickol River Formation. The Gorge Creek Group (3.05-3.02 Ga) in west Pilbara comprises only BIF (Banded Iron Formation), chert and shale-dominated Cleaverville Formation (Hickman, 2004). The Whim Creek Basin (3.01-2.99 Ga) consists entirely of the Whim Creek Group (Pike and Cas, 2002). The Mallina Basin (2.97-2.94 Ga) is composed of Coonieena Basalt, Cattle Well Formation, Cistern Formation, Rushall Slate, Constantine Sandstone, Bookingarra Formation, and Mallina Formation in west Pilbara, while Lalla Rookh Sandstone in east Pilbara. The

Gorge Creek Basin, Whim Creek Basin, Mosquito Creek Basin, and Mallina Basin have been integrated to the De Grey Superbasin and the corresponding groups to the De Grey Supergroup (Van Kranendonk et al., 2006; Hickman, 2012).

The Fortescue Group is distributed across a total area of around 250,000 km^2 in the four sub-basins (Black, 1993) of the Fortescue Basin, locally reaching a thickness of up to 6.5 km (Thorne and Trendall, 2001). It spans a period of 150 Ma from 2.78 Ga to 2.63 Ga, and is a volcanic-sedimentary succession composed of Bellary Formation, Mt. Roe Basalt, Hardey Formation, Kylena Formation (named as Boongal Formation in the south Pilbara sub-basin), Tumbiana Formation (Pyradie Formation in the south), Maddina Formation (Bunjinah Formation in the south), and Jeerinah Formation. The Mt. Roe Basalt, Kylena Formation, and Maddina Formation consist primarily of continental flood basalt and basaltic andesite (Thorne and Trendall, 2001), and Mt. Roe Basalt also contains some shale interlayers. The three sedimentary units, the Hardey Formation, the Tumbiana Formation, and the Jeerinah Formation, were deposited 2.77 to 2.75 Ga, ca. 2.72 Ga, and 2.69 to 2.63 Ga ago, respectively. The Hardey Formation is composed of fluvial conglomerate and sandstone, as well as lacustrine shale. The Tumbiana Formation comprises two members, Mingah and Meentheena, which are made up of sandstone and volcaniclastics, and shale and stromatolitic limestone, respectively. Jeerinah Formation consists of Woodiana, Warrie, and Roy Hill Shale members.

3. Samples and methods

3.1 Samples

All the samples studied here were drill cores from the Pilbara Craton, Western Australia, and were obtained from the Perth Core Library. Detailed drill core descriptions and the associated drill hole names and locations are listed in Table 2.1.

3.2 Making mounts and etching

Drill cores were firstly observed under a binocular microscope to look for pyrite nodules and disseminated grains, which were marked and cut from drill cores along with the lithological matrix. These chips were subsequently cast into the first batch of mounts, which were polished and then immersed in 8-12.5% NaOCl sodium hypochlorite solution for about two minutes, revealing the internal textures of pyrite. The etched pyrite was observed in reflected light to select the appropriate pyrite for multiple sulphur isotope analysis. Targeted pyrite nodules and grains were cut from the mounts, and were assembled into the second batch of mounts together with the reference materials (Ruttan pyrite and Balmat pyrite) for sulphur isotope measurements. These mounts were again immersed in the sodium hypochlorite solution, followed by reflected light imaging. The etched mounts were subsequently polished with 1-μm diamond paste to remove the oxidized film on the surface, followed by photographing under the microscope.

3.3 SEM analysis

The mounts were thoroughly cleaned (using ethanol, RBS35 detergent, warm water, and deionized water in the ultrasonic bath) and dried (vacuum oven, 60 °C). They were then conductively coated with 10 nanometers of gold or 15 nanometers of aluminium in a Leica ACE 600 sputter coater. After that, the mounts were examined using a JEOL JSM-6400 SEM (Secondary Electron Microscopy) located at the Research School of Earth Sciences, the Australian National University, unraveling the internal textures of pyrite by BSE imaging and confirming the chemical composition of the minerals to be analyzed using EDS (Energy Dispersive Spectroscopy). The operating conditions were 15 kV (acceleration voltage), 1 nA (beam current), and 11 mm (working distance).

3.4 SHRIMP-SI measurement

After SEM examination, the gold or aluminium film was removed firstly by potassium iodide solution or decon90 detergent, respectively and then by 1-μm diamond paste polishing. The mounts were then thoroughly cleaned, followed by drying in the vacuum oven (60 °C) for at least five days to degas. The mounts were then coated with 40 nanometers of gold or 45 nanometers of aluminium for SHRIMP-SI analysis.

The detailed acquisition parameters are summarized in Table 2.2. The primary beam was positive caesium ions generated by a Kimbal Physics IGS5 ion gun. The total acceleration energy of the caesium ion beam from ion gun to the sample surface was 15 keV. Due to the variable size of pyrite grains (individual grains and those constituting pyrite nodules), both big-spot (ca. 27 × 20 μm) and small-spot (ca. 18 × 15 μm) analyses were used.

The secondary negative sulphur ions were focused through an ion extraction system to the source slit with a width of 60 μm. The four sulphur isotope ions ($^{32}S^-$, $^{33}S^-$, $^{34}S^-$, $^{36}S^-$) through mass analyser were collected simultaneously by the multiple collectors (Faraday cups); $^{32}S^-$, $^{33}S^-$ and $^{34}S^-$ ions were measured by current mode with resistors of 10^{11} or 10^{12} Ω, whereas $^{36}S^-$ ion was measured by charge mode using a capacitor of 22 pF (Ireland et al., 2014)(for comparison purposes, a few sessions utilized current mode for $^{36}S^-$ with a resistor of 10^{12} Ω). In order to resolve $^{33}S^-$ and $^{32}SH^-$, a mass resolution of 4000 at 10% peak height was used, which was obtained by a collector slit width of 150 μm.

Each run commenced with rastering the primary beam over an area slightly larger than the spot for five (big-spot analyses) or two (small-spot analyses) minutes, removing the gold/aluminium coat and allowing the sample surface to become conditioned with Cs^+ ions, while an in-line valve between the source chamber and the electrostatic analyzer was closed and base-lines for the electrometers were collected. This was followed by steering the secondary ion beam to maximize the signal of sulphur ions and further stabilize the secondary ion beam through the source slit.

The primary reference material was Ruttan pyrite ($\delta^{34}S$ = 1.2‰, $\Delta^{33}S$ and $\Delta^{36}S \approx 0$) and the secondary reference material was Balmat pyrite ($\delta^{34}S$ = 15.1‰, $\Delta^{33}S$ and $\Delta^{36}S \approx 0$)(Crowe and Vaughan, 1996; Williford et al., 2011; Whitehouse, 2013; Ireland et al., 2014). Each session started with Ruttan pyrite and Balmat pyrite, followed by unknowns as long as the conditions were stable, and then Ruttan pyrite and Balmat pyrite, and so forth. For big-spot analyses, each analytical run comprised four or five sets, and $^{32}S^-$, $^{33}S^-$, $^{34}S^-$ and $^{36}S^-$ were all measured; for small-spot analyses, each analytical run consisted of two or four sets, and only $^{32}S^-$, $^{33}S^-$ and $^{34}S^-$ were measured due to the low signal of $^{36}S^-$. Each set consisted of ten scans, and each scan was made up of ten subcounts.

Sulphur isotope data were reduced using the POXI-MC software developed by the RSES of ANU. The electrometer gains on the individual detectors were not precisely determined. The unknowns were calibrated directly to the reference material such that the relative difference in isotopic composition between unknowns and reference material was determined. The measured ratios of the Ruttan pyrite were then fixed to the Vienna Canyon Diablo Troilite (V-CDT) reference frame.

The measured $^{3x}S^-/^{32}S^-$ ratios are expressed in delta (δ) notation as permil deviations relative to the standard ratios of V-CDT: $\delta^{3x}S_{V\text{-}CDT}$ (‰) = $[(^{3x}S/^{32}S)_{unknown}/(^{3x}S/^{32}S)_{V\text{-}CDT} - 1] \times 1000$, where $(^{3x}S/^{32}S)_{unknown}$ and $(^{3x}S/^{32}S)_{V\text{-}CDT}$ are the $^{3x}S/^{32}S$ ratios of the unknown and V-CDT, respectively. Since Ruttan pyrite was used as the primary reference material in this study, $\delta^{3x}S_{V\text{-}CDT}$ (‰) = $\delta^{3x}S_{V\text{-}CDT}$(Ruttan) + $[(^{3x}S/^{32}S)_{unknown}/(^{3x}S/^{32}S)_{Ruttan} - 1] \times 1000$, where $\delta^{3x}S_{V\text{-}CDT}$(Ruttan) is the $\delta^{3x}S_{V\text{-}CDT}$ value of Ruttan pyrite ($\delta^{33}S_{V\text{-}CDT}$(Ruttan), $\delta^{34}S_{V\text{-}CDT}$(Ruttan), and $\delta^{36}S_{V\text{-}CDT}$(Ruttan) are 0.618‰, 1.2‰, and 2.281‰, respectively, Crowe and Vaughan, 1996; Williford et al., 2011; Whitehouse, 2013; Ireland et al., 2014). $\Delta^{33}S$ and $\Delta^{36}S$ were calculated following the relationships $\Delta^{33}S = \delta^{33}S - 1000 \times [(1 + \delta^{34}S/1000)^{0.515} - 1]$ and $\Delta^{36}S = \delta^{36}S - 1000 \times [(1 + \delta^{34}S/1000)^{1.90} - 1]$, respectively.

4. Results

Two generations of pyrite are distinguished in the shale of the 3.2 Ga Dixon Island Formation based on the images of BSE and etched pyrite. The anhedral first generation constitutes the main body of the pyrite nodules, and the majority shows oscillatory zoning; while the euhedral to subhedral second generation occurs as/within veins, and is homogeneous (Fig. 2.3A, B and C).

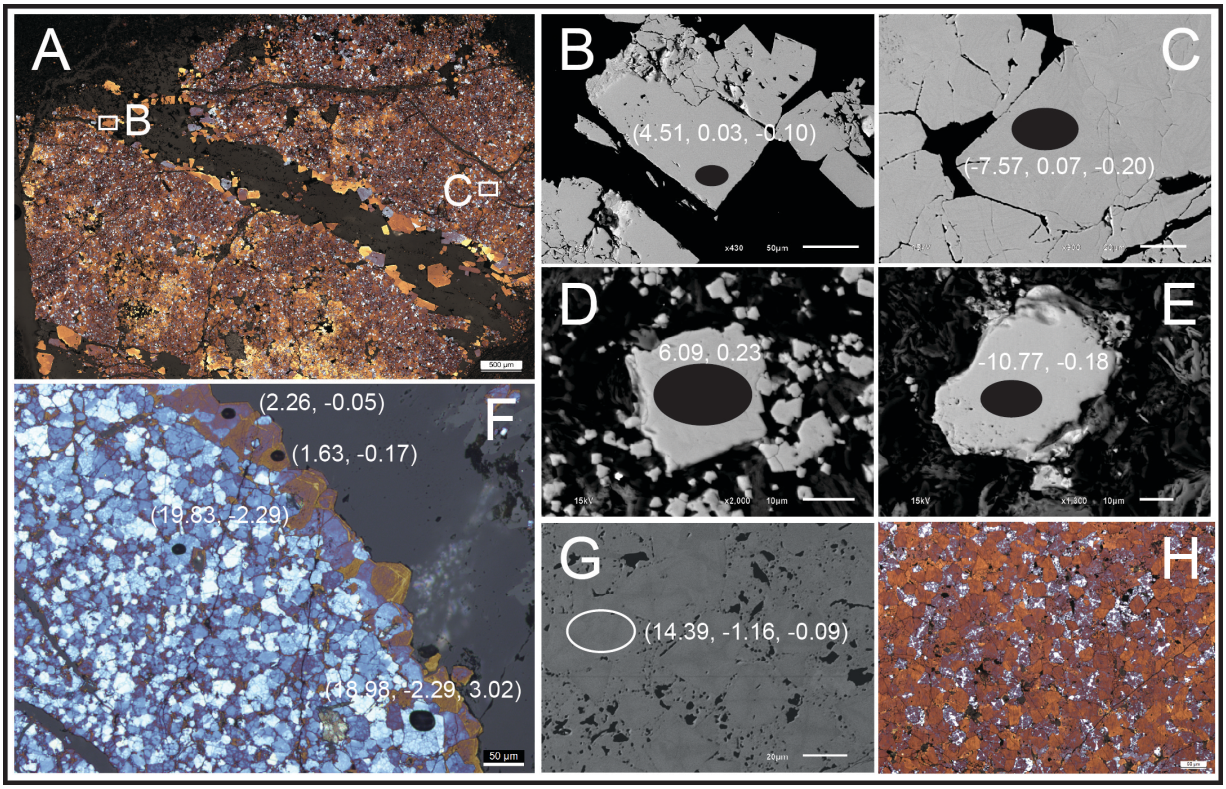

Fig. 2.3 A. A reflected light microphotograph of sodium hypochlorite etched pyrite nodule from the DX_92.22-92.26m (3.2 Ga Dixon Island Formation) shale displaying two generations of pyrite. The earlier generation is the main body of the nodule while the second generation overgrows on the first generation and occurs within the vein. B. A BSE image of a secondary pyrite grain within a vein characterized by euhedral shape, big size, and homogeneous internal texture. C. A BSE image of an earlier generation pyrite grain showing oscillatory zoning. D and E. BSE images of two pyrite grains in the shale of CL1_80.76-80.77m and CL1_104.99-105.00m (3.0 Ga Cleaverville Formation), respectively. F. A reflected light microphotograph of part of an etched pyrite nodule showing two generations of pyrite, from the shale of ABDP5_38.35-38.36m (2.93 Ga Mosquito Creek Formation).

G. A BSE image of part of the nodule from the ABDP5_40.74-40.75m (2.93 Ga Mosquito Creek Formation) shale displaying two generations of pyrite, and the earlier generation pyrite exhibits cross internal texture. H. A reflected light microphotograph of part of an etched pyrite nodule from the ABDP5_40.74-40.75m shale, showing two generations of pyrite and the cross internal texture of the first generation pyrite. The triple/quadruple sulphur isotopic compositions ($\delta^{34}S$, $\Delta^{33}S$, $\Delta^{36}S$) are also shown.

The pyrite grains in the shale of the 3.0 Ga Cleaverville Formation are relatively small in size (only sufficiently large for small-spot analyses). Some of them show oscillatory zoning as well, and some display two generations revealed by core-rim texture (Fig. 2.3D and E).

Three types of pyrite are identified in the shale of the 2.93 Ga Mosquito Creek Formation: diagenetic, hydrothermally modified diagenetic, and secondary. The pyrite nodule in the ABDP5_38.35-38.36m shale consists of diagenetic pyrite and secondary pyrite. The former is homogeneous and constitutes the main part of the nodule while the latter occurs as a rim (Fig. 2.3F). The pyrite nodule in the ABDP5_40.74-40.75m shale is composed of hydrothermally modified diagenetic pyrite and secondary pyrite. The secondary pyrite is porous and overgrows the euhedral to subhedral hydrothermally modified diagenetic pyrite. The hydrothermal modification is identified by the characteristic internal texture revealed by the images of BSE and etched pyrite (Fig. 2.3G and H).

The shale of the 2.78 Ga Mt. Roe Basalt contains diagenetic, hydrothermally modified diagenetic, and secondary pyrite (Fig. 2.4A, B, C and D), while the hydrothermally altered basalt contains only secondary pyrite. The diagenetic pyrite occurs as nodules in the shale of ABDP6_93.43-93.44m and ABDP6_261.63-261.64m, and disseminated grains in the shale of ABDP6_101.21-101.22m and ABDP6_101.40-101.42m. The hydrothermally modified diagenetic pyrite occurs as irregular nodules/laminae in the shale of ABDP6_93.43-93.44m, ABDP6_265.80-265.83m, ABDP6_115.80-115.81m and ABDP6_101.40-101.42m, as well as disseminated grains in the ABDP6_101.40-101.42m shale.

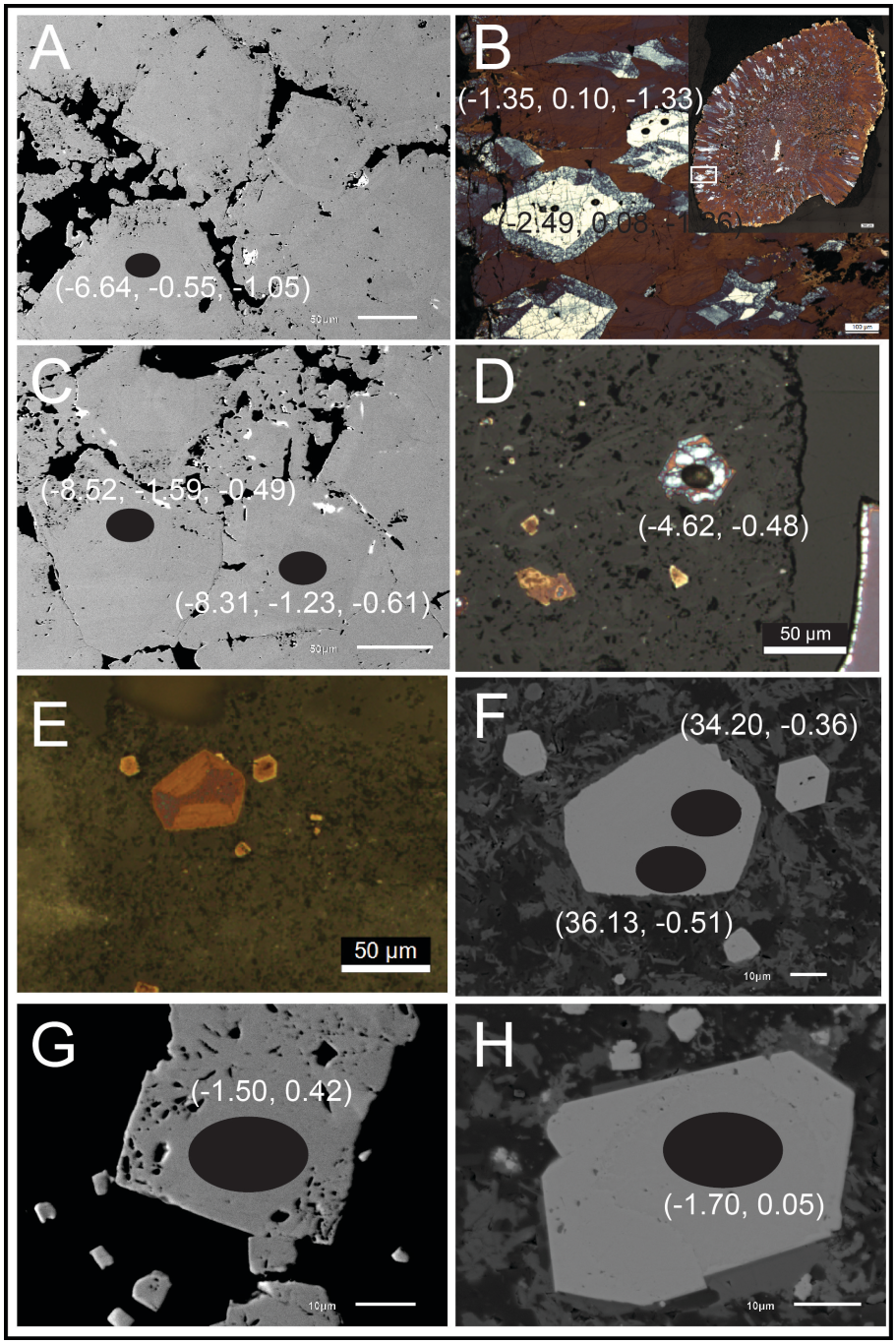

Fig. 2.4 A and C. BSE images of hydrothermally modified diagenetic pyrite of a nodule from the shale of ABDP6_265.80-265.83m (2.78 Ga Mt. Roe Basalt). B. Two reflected light microphotograph of an etched pyrite nodule from the ABDP6_93.43-93.44m shale (2.78 Ga Mt. Roe Basalt). D. A reflected light microphotograph of a diagenetic pyrite grain from the ABDP6_101.40-101.42m shale (2.78 Ga Mt. Roe Basalt). E. A reflected light microphotograph of an etched pyrite in the ooidal sandstone of FVG1_1834.86-1834.87m (2.76 Ga Hardey Formation) displaying two generations of pyrite; The

earlier generation of pyrite can be detrital or diagenetic. F. The BSE image of E. H. A BSE image of a two-generation pyrite grain in the ooidal sandstone of FVG1_1843.86-1843.87m. G. A BSE image of a pyrite grain in the shale of ABDP3_114.060-114.061m (2.76 Ga Hardey Formation). The triple/quadruple sulphur isotopic compositions ($\delta^{34}S$, $\Delta^{33}S$, $\Delta^{36}S$) are also shown.

The pyrite grains in the ooidal sandstone of the 2.76 Ga Hardey Formation generally display two generations of pyrite, and the earlier generation can be detrital or diagenetic (Fig. 2.4E and H). Those in the shale have been mostly modified by later hydrothermal fluids (Fig. 2.4G).

The individual pyrite grains in the PDP1_44.33-44.34m shale of the 2.72 Ga Tumbiana Formation contain up to three generations of pyrite (Fig. 2.5C and D), with the first generation diagenetic and the later two generations hydrothermal. The disseminated pyrite grains in the PDP1_81.00-81.01m shale contain two generations of hydrothermal pyrite, and those in the PDP1_44.08-44.10m shale are all one generation of hydrothermal pyrite. The pyrite nodule in the PDP1_43.15-43.16m shale is composed of two generations of pyrite, and the earlier generation is diagenetic whereas the later generation is hydrothermal (Fig. 2.5A and B).

The multiple sulphur isotope data are listed in Table 2.3. Internal precision is expressed in the value of two standard errors of Ruttan pyrite, and is on average 0.15‰ ($\delta^{34}S$), 0.05‰ ($\Delta^{33}S$), and 0.30‰ ($\Delta^{36}S$) for big-spot analyses, and 0.17‰ ($\delta^{34}S$) and 0.14‰ ($\Delta^{33}S$) for small-spot analyses. Reproducibility is expressed in the value of two standard deviations of Ruttan pyrite in each session, and is on average 0.50‰ ($\delta^{34}S$), 0.13‰ ($\Delta^{33}S$), and 0.39‰ ($\Delta^{36}S$) for big-spot analyses, and 0.58‰ ($\delta^{34}S$) and 0.23‰ ($\Delta^{33}S$) for small-spot analyses.

For the 3.2 Ga Dixon Island Formation, the first generation of pyrite exhibits a wide range of $\delta^{34}S$ (-14.74 to 23.41‰), but a limited range of $\Delta^{33}S$ (-0.77 to 0.19‰) and $\Delta^{36}S$ (-0.40 to 0.41‰). The second generation of pyrite shows two groups of sulphur isotopic compositions.

One group has $\delta^{34}S$ of 4.51 to 13.35‰ and $\Delta^{33}S$ of -0.11 to 0.09‰, and the other group has $\delta^{34}S$ of 5.09‰ and $\Delta^{33}S$ of 2.58‰.

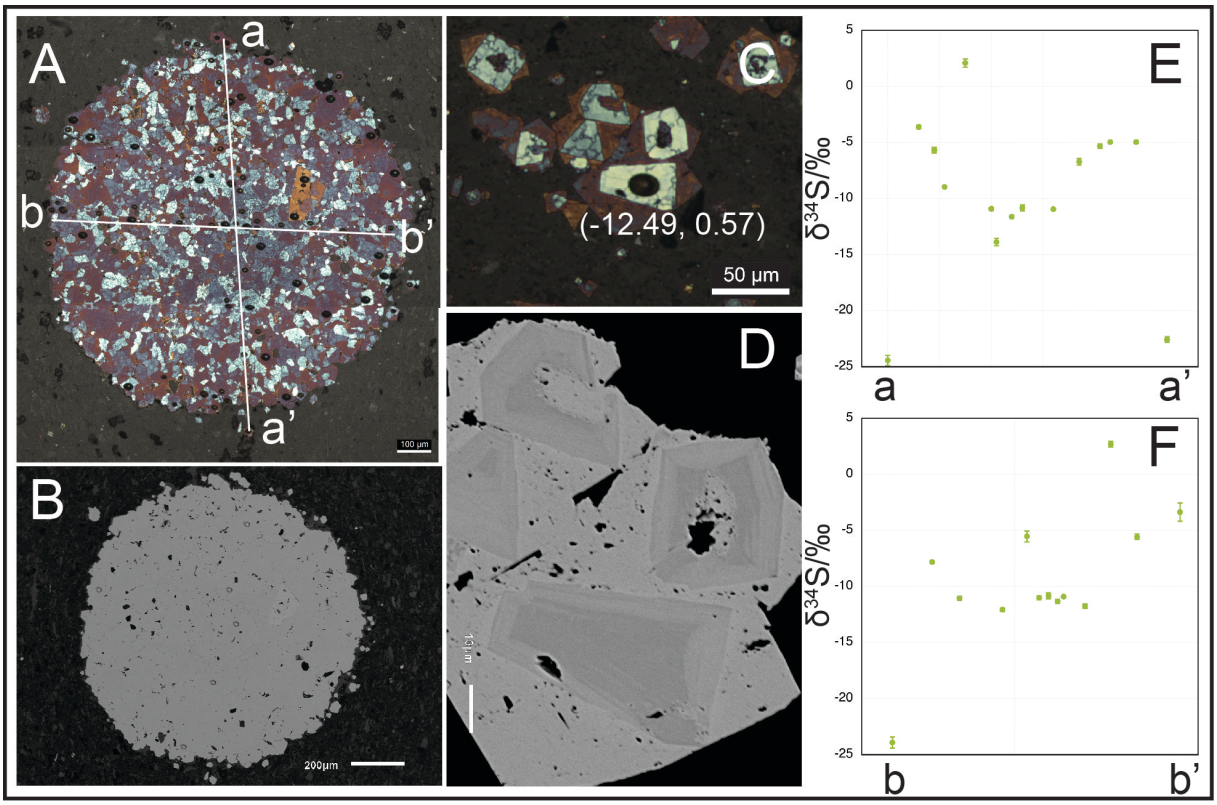

Fig. 2.5 A. A reflected light microphotograph of an etched pyrite nodule in the shale of PDP1_43.15-43.16m (the 2.72 Ga Tumbiana Formation). B. The BSE image of A. C. A reflected light microphotograph of etched pyrite grains in the shale of PDP1_44.33-44.34m, showing three generations of pyrite. D. The BSE image of C. The triple sulphur isotopic composition is also shown. E and F. Two traverses of $\delta^{34}S$ of the pyrite nodule. Error bar is the value of two standard errors.

The pyrite of the 3.0 Ga Cleaverville Formation shows a characteristic wide range of $\delta^{34}S$ (-10.77 to 46.43‰) but a restricted range of $\Delta^{33}S$ (-0.37 to 0.23‰).

For the 2.93 Ga Mosquito Creek Formation, the diagenetic pyrite grains show high positive $\delta^{34}S$ (19.82‰ on average), large magnitudes of negative $\Delta^{33}S$ (-2.35‰ on average), and positive $\Delta^{36}S$ (3.17‰ on average). The hydrothermally modified pyrite grains display moderate positive $\delta^{34}S$ (13.87‰ on average), moderate magnitudes of negative $\Delta^{33}S$ (-1.19‰

on average), and small magnitudes of positive $\Delta^{36}S$ (-0.29 to 0.42‰). In comparison, the secondary pyrite grains exhibit $\delta^{34}S$ and $\Delta^{33}S$ of near zero.

For the 2.78 Ga Mt. Roe Basalt, the diagenetic pyrite shows $\delta^{34}S$ of -4.62 to 3.66‰, $\Delta^{33}S$ of -0.48 to 0.72‰, and $\Delta^{36}S$ of -1.33 to -1.26‰. The hydrothermally modified diagenetic pyrite exhibits $\delta^{34}S$ of -8.77 to -1.28‰, $\Delta^{33}S$ of -2.11 to 0.20‰, and $\Delta^{36}S$ of -1.57 to 0.49‰. The secondary pyrite has $\delta^{34}S$ of -7.83 to -0.68‰, $\Delta^{33}S$ of -0.29 to 1.99‰, and $\Delta^{36}S$ of -2.15 to -0.32‰.

For the 2.76 Ga Hardey Formation, the earlier generation of detrital or diagenetic pyrite show $\delta^{34}S$ of -1.70 to 34.20‰ and $\Delta^{33}S$ of -0.36 to 0.29‰. The hydrothermally modified diagenetic pyrite has small magnitudes of negative $\delta^{34}S$ (-2.28‰ on average) and positive $\Delta^{33}S$ (0.26‰ on average). The secondary pyrite shows significantly variable $\delta^{34}S$ (-2.82 to 36.13‰) and small magnitudes of $\Delta^{33}S$ (-0.51 to 0.35‰).

For the 2.72 Ga Tumbiana Formation, the diagenetic pyrite in the PDP1_44.33-44.34m shale has $\delta^{34}S$ of -12.49‰ and $\Delta^{33}S$ of 0.57‰, whereas the secondary pyrite has $\delta^{34}S$ of -0.95 to -3.08‰ and $\Delta^{33}S$ of 1.18‰ (on average). The secondary pyrite in the PDP1_81.00-81.01m shale shows a mean $\delta^{34}S$ of -3.72‰ and $\Delta^{33}S$ of 0.35‰. The secondary pyrite in the PDP1_44.08-44.10m shale has a mean $\delta^{34}S$ of -2.42‰ and $\Delta^{33}S$ of 1.74‰. The diagenetic pyrite constituting the pyrite nodule and disseminated in the matrix of the PDP1_43.15-43.16m shale are characterized by a wide range of $\delta^{34}S$ (-25.25 to 2.70‰, -11.93‰ on average), small positive $\Delta^{33}S$ (0.49‰ on average) and larger magnitudes of negative $\Delta^{36}S$ (-1.44‰ on average); while the secondary pyrite in the nodule shows a mean $\delta^{34}S$ of -3.37‰, $\Delta^{33}S$ of 0.90‰, and $\Delta^{36}S$ of -1.81‰.

The $\delta^{34}S$-$\Delta^{33}S$ plot is characterized by the large range of $\delta^{34}S$ from around -30 to around 50‰ (Fig. 2.6). The diagenetic pyrite in the shale of Tumbiana Formation displays considerably negative $\delta^{34}S$, while the pyrite in the shale of Cleaverville Formation and Dixon Island Formation, as well as the detrital or diagenetic pyrite in the sandstone of Hardey Formation

shows highly positive $\delta^{34}S$. The hydrothermally modified diagenetic pyrite in the shale of Mt. Roe Basalt exhibits good linear relationship between $\delta^{34}S$ and $\Delta^{33}S$.

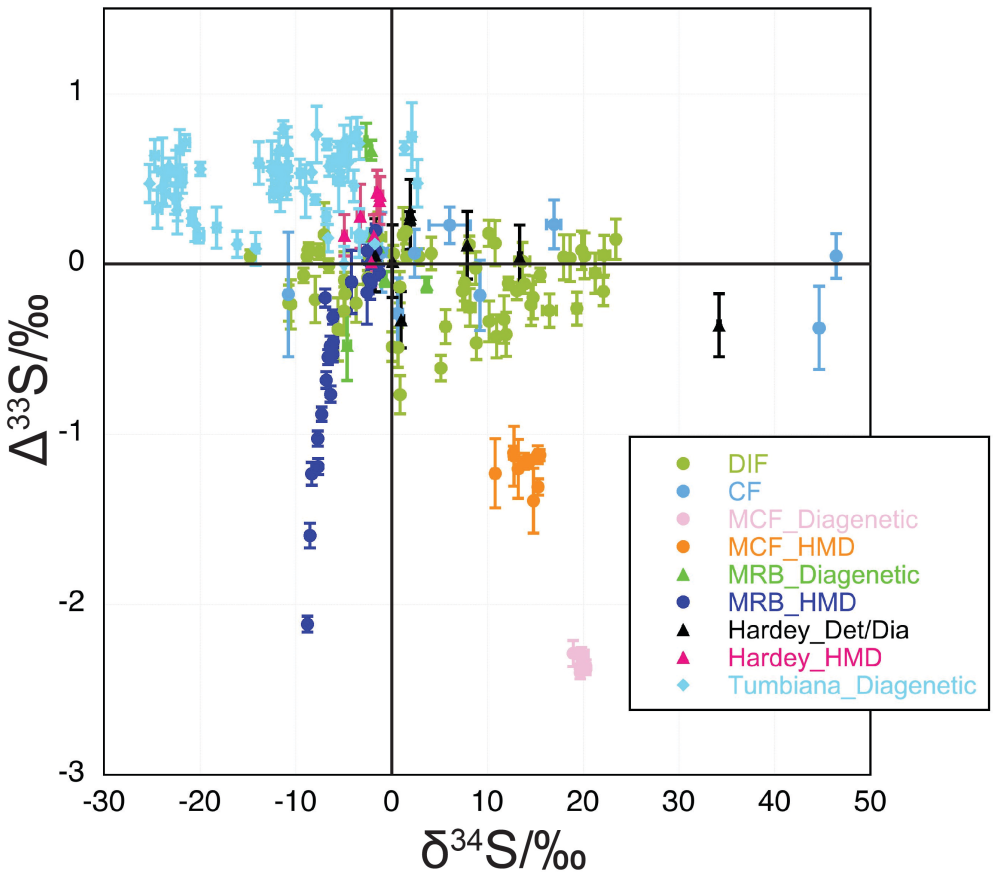

Fig. 2.6 $\delta^{34}S$-$\Delta^{33}S$ plot of the data for pyrite in metasedimentary rocks of ca. 3.2-2.72 Ga from the Pilbara Craton. The error bar is 2σ (2 standard errors). DIF: Dixon Island Formation; CF: Cleaverville Formation; MCF: Mosquito Creek Formation; MRB: Mt. Roe Basalt; HMD: Hydrothermally modified diagenetic; Det/Dia: Detrital or Diagenetic.

In the $\Delta^{33}S$-$\Delta^{36}S$ plot, only the data of the 3.2 Ga Dixon Island Formation with small magnitudes of $\Delta^{33}S$ and $\Delta^{36}S$, and that of the 2.76 Ga Hardey Formation are close to the ARA, the others (2.93 Ga Mosquito Creek Formation, 2.78 Ga Mt. Roe Basalt, and 2.72 Ga Tumbiana Formation) deviate from Archean Reference Array (ARA) to variable degrees (Fig. 2.7).

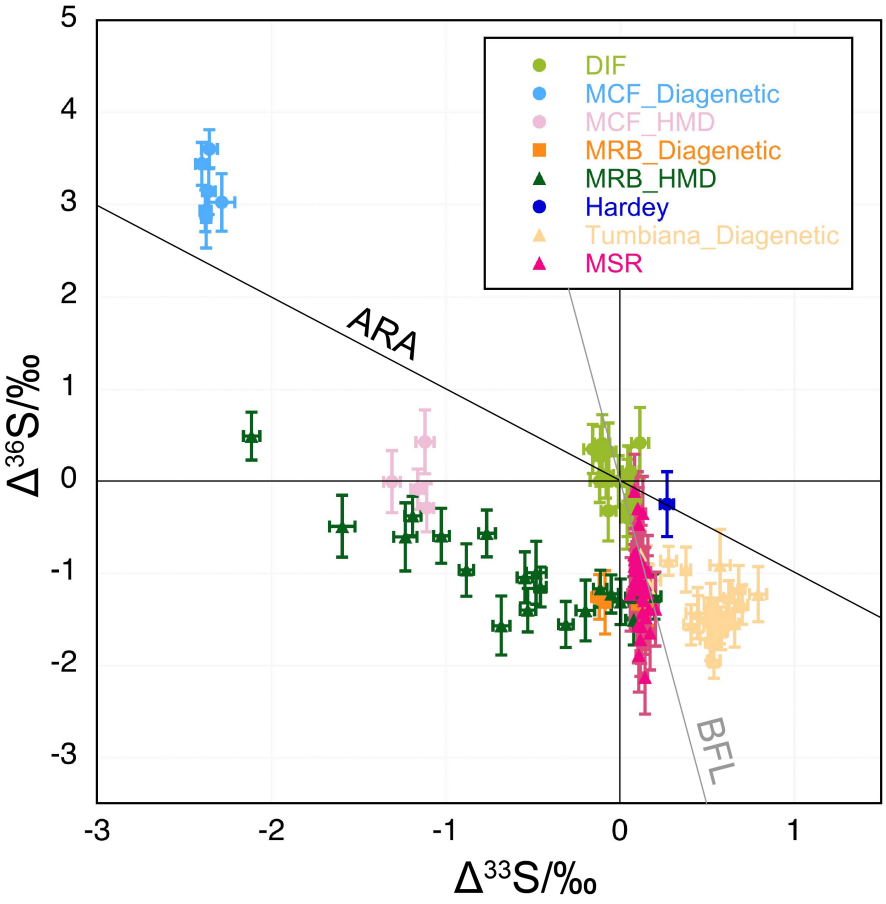

Fig. 2.7 $\Delta^{33}S$-$\Delta^{36}S$ plot of the quadruple sulphur isotopic composition data for pyrite in metasedimentary rocks of ca. 3.2-2.72 Ga from the Pilbara Craton, along with the data of the quadruple sulphur isotopic compositions of the products in the laboratory experiments of microbial sulphate reduction (Johnston et al., 2007), the Archean Reference Array (ARA, $\Delta^{36}S/\Delta^{33}S \approx -1$, Farquhar et al., 2001), and the Biological Fractionation Line (BFL, $\Delta^{36}S/\Delta^{33}S \approx -7$, Ono et al., 2006). The error bar is 2σ (2 standard errors). DIF: Dixon Island Formation; MCF: Mosquito Creek Formation; MRB: Mt. Roe Basalt; HMD: Hydrothermally modified diagenetic; MSR: Microbial sulphate reduction.

5. Discussion

5.1 Signatures of the ca. 3.2-2.72 Ga S-MIF in Pilbara Craton

The 3.2 Ga Dixon Island Formation and 3.0 Ga Cleaverville Formation have been demonstrated to be precipitates of seafloor hydrothermal environments (Kiyokawa et al.,

2014). As such, the sulphur is most likely to be a mixture of seawater sulphur and magmatic sulphur, which is also suggested by the $\delta^{34}S$-$\Delta^{33}S$ systematics (Fig. 2.8). In the $\delta^{34}S$-$\Delta^{33}S$ plot, one end member with $\Delta^{33}S$ of near 0 has a wide range of $\delta^{34}S$, while the other end member with $\Delta^{33}S$ of ~-0.8‰ has $\delta^{34}S$ of ~1‰ (Fig. 2.8). The former can be magmatic sulphur and the latter can be seawater sulphur. In this case, the S-MIF of seawater sulphur should have been diluted by magmatic sulphur to variable degrees. Although the exact ratio of the two sulphur components is unknown, the magnitude of $\Delta^{33}S$ of seawater sulphur should be larger than the measured minimum negative $\Delta^{33}S$ (-0.77‰).

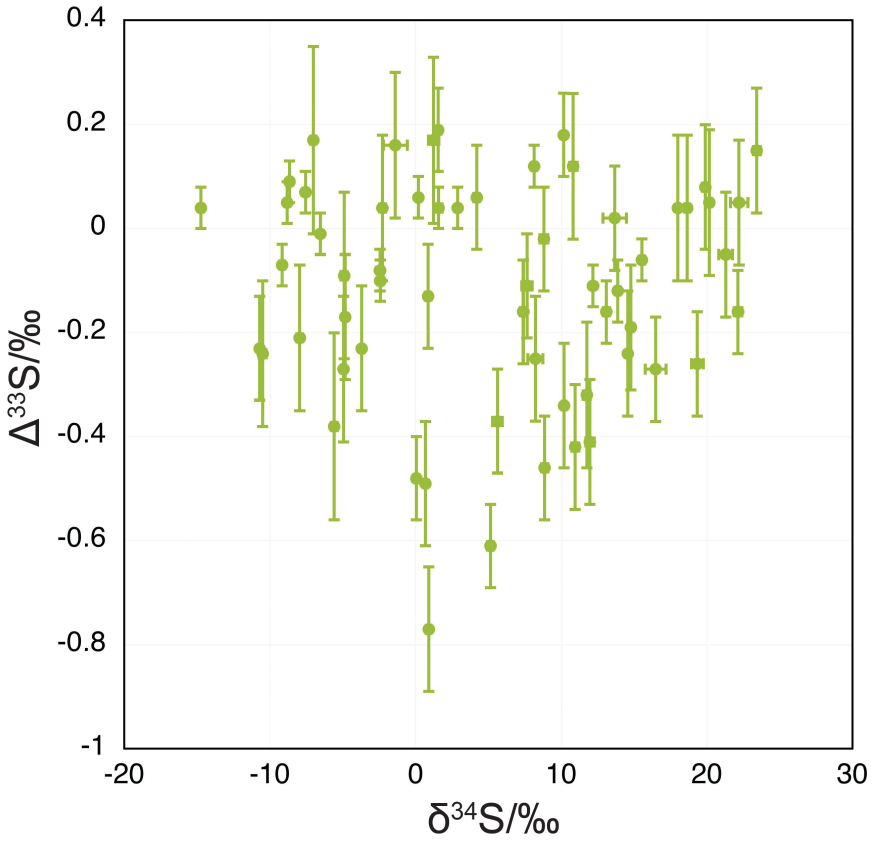

Fig. 2.8 $\delta^{34}S$-$\Delta^{33}S$ plot of the data for the hydrothermal (primary) pyrite in shale from the 3.2 Ga Dixon Island Formation.

Taking together the largest magnitude of $\Delta^{33}S$ (diagenetic pyrite) of the 2.93 Ga Mosquito Creek Formation (-2.40‰), the 2.78 Ga Mt. Roe Basalt (0.72‰), the 2.76 Ga Hardey Formation (-0.36‰), and the 2.72 Ga Tumbiana Formation (0.79‰), The $\Delta^{33}S$ of ca. 3.2-2.72

Ga recorded in the Pilbara Craton ranges from -2.40‰ to 0.79‰ (Fig. 2.9). It is noteworthy that the maximum magnitude of negative $\Delta^{33}S$ (-2.40‰) is larger than that of positive $\Delta^{33}S$ (0.79‰), which is in stark contrast to the other Archean periods when the maximum magnitude of positive $\Delta^{33}S$ is significantly larger than that of negative $\Delta^{33}S$ (Fig. 2.1).

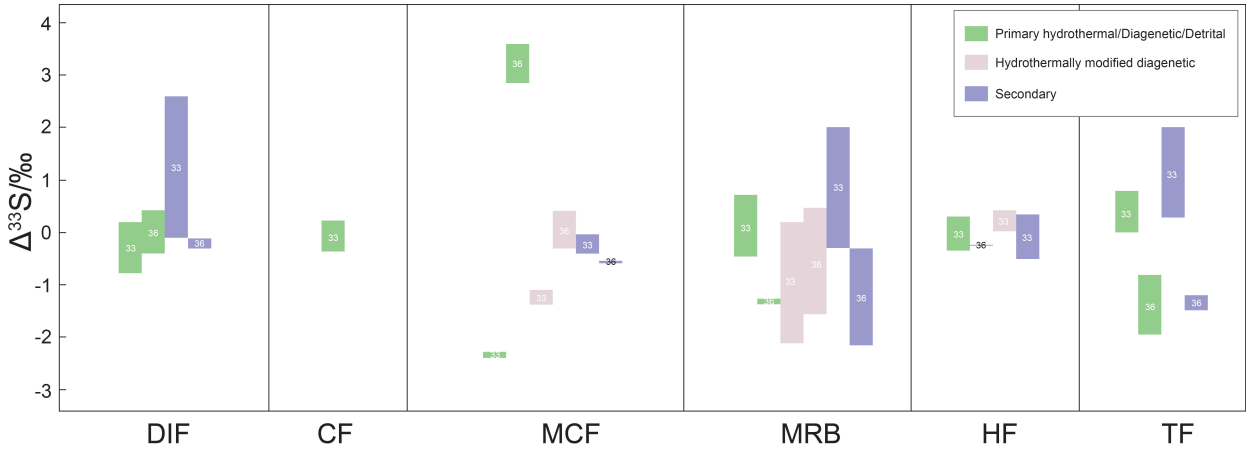

Fig. 2.9 Histogram summarizing the $\Delta^{33}S$ of the samples investigated in this study. DIF: Dixon Island Formation, CF: Cleaverville Formation, MCF: Mosquito Creek Formation, MRB: Mt. Roe Basalt, HF: Hardey Formation, TF: Tumbiana Formation.

Admittedly, the most negative $\Delta^{33}S$ obtained in this study is less than -4‰ reported in Guy et al. (2012). However, since the analytical method used was bulk rock, which could potentially involve sulphur of later stage. Therefore, we will only focus on the data obtained here.

Except for the data of the 3.2 Ga Dixon Island Formation, where the magnitudes of both $\Delta^{33}S$ and $\Delta^{36}S$ are very small, and that of the 2.76 Ga Hardey Formation are close to the ARA, nearly all the other data (2.93 Ga Mosquito Creek Formation, 2.78 Ga Mt. Roe Basalt, and 2.72 Ga Tumbiana Formation) deviate from this line (Fig. 2.7) to variable degrees, including both diagenetic pyrite and hydrothermally modified pyrite (Fig. 2.7).

5.2 Cause of the differences in S-MIF

The metasedimentary rocks of ca. 3.2-2.72 Ga in the Pilbara Craton that have been sampled are predominantly of shallow water sedimentary environments: continental shelf and delta for

the 2.93 Ga Mosquito Creek Formation (Eriksson et al., 1994 and references therein), lacustrine environment for the 2.78 Ga Mt. Roe Basalt, fluvial or fluvial-deltaic environment for the 2.76 Ga Hardey Formation (Thorne and Trendall, 2001; Hall, 2002), and lacustrine environment or shallow marine environment for the 2.72 Ga Tumbiana Formation (Thorne and Trendall, 2001; Sakurai et al., 2005; Bolhar and Van Kranendonk, 2007; Awramik and Buchheim, 2009). In contrast, the metasedimentary rocks of deep marine environments have not been sampled due to poor or no preservations. Although the 3.2 Ga Dixon Island Formation and the 3.0 Ga Cleaverville Formation are possibly of deep water environment, as discussed above, their S-MIF has been diluted by magmatic sulphur to variable degrees. Therefore, sampling bias is an important factor leading to the S-MIF differences.

Furthermore, the modeling results of Halevy (2013) show that positive $\Delta^{33}S$ is inclined to be preserved in the deep marine environment whereas a wide range of positive and negative $\Delta^{33}S$ is more likely to be preserved in shallow water environments. The measured $\Delta^{33}S$ range of ~3.2-2.72 Ga in the Pilbara Craton in this study is -2.40-0.79‰. Such a range characterized by larger maximum magnitude of negative $\Delta^{33}S$ is inconsistent with the results of almost all the previous experiments of producing S-MIF (Table 2.4), including photochemical reactions of gas phase sulphur-bearing species (e.g., SO_2 photolysis, SO_2 photoexcitation, CS_2 photopolymerization) and non-gas phase reactions (e.g., thermochemical sulphate reduction, heterogeneous reactions between organic materials and sulphur-bearing solutions under hydrothermal conditions). Although the products of SO_2 photolysis under radiation of a continuum from 220 nm to visible wavelengths in Farquhar et al. (2001) exhibit larger maximum magnitude of negative $\Delta^{33}S$ (-3.5‰) than that of positive $\Delta^{33}S$ (3.3‰), since the $\Delta^{33}S$ sign of the sulphate products is positive, opposite to that of Mesoarchean sulphate (-0.4‰, Hoering, 1989), thus this process is unlikely. Therefore, the maximum positive $\Delta^{33}S$ of this period is not preserved due to post-sedimentation destruction (e.g., subduction that was already in operation during the Mesoarchean in Pilbara; Smithies et al., 2007) or has not been measured because of the lack of available samples.

5.3 Explanation on the $\Delta^{36}S/\Delta^{33}S$ deviation

$\Delta^{36}S/\Delta^{33}S$ deviations of the diagenetic pyrite of the 2.93 Ga Mosquito Creek Formation, the 2.78 Ga Mt. Roe Basalt, and the 2.72 Ga Tumbiana Formation are probably induced by biological activities, whereas the others most likely result from post-diagenesis modifications by hydrothermal fluids. Detailed explanations are illustrated below.

5.3.1 Biological modification

For the data of the 2.72 Ga Tumbiana Formation, two processes can potentially result in the lower $\Delta^{36}S/\Delta^{33}S$ ratios: biological modification (Ono et al., 2006b; Johnston et al., 2007) and Rayleigh distillation (Johnston et al., 2007). Distillation in this context could relate to a closed basin and a finite sulphur reservoir. However, the $\delta^{34}S$ of the pyrite nodule first increases and then decreases from core, through mantle, to rim, suggesting an open rather than closed system, thus Rayleigh distillation is unlikely. Four data points are plotted within the microbial sulphate reduction area defined by the data of experiments on sulphate reducers (Johnston et al., 2007), and the others deviate from the ARA towards more negative $\Delta^{36}S$ in a trend similar to that of biological fractionation line (Ono et al., 2006b) and microbial sulphate reduction (Johnston et al., 2007; Fig. 2.7).

Although the positive $\Delta^{33}S$ is inconsistent with microbial sulphate reduction as previously proposed (e.g., Shen et al., 2009; Wacey et al., 2010), i.e., positive $\Delta^{33}S$ for sulphur disproportionation and negative $\Delta^{33}S$ for sulphate reduction because the products of SO_2 photolysis elemental sulphur and sulphate carry positive and negative $\Delta^{33}S$, respectively, such inconsistences can be reconciled if the pathways of pyrite formation are taken into account. According to previous experimental studies (Rickard, 2012 and references therein), Fe^{2+} is firstly combined with HS^- (magmatic, no S-MIF) or S^{2-} (product of sulphate reduction, negative $\Delta^{33}S$ or magmatic H_2S, no S-MIF) rapidly, forming an intermediate [FeS] with negative $\Delta^{33}S$ or no S-MIF ($Fe^{2+} + HS^- = [FeS] + H^+$ or $Fe^{2+} + S^{2-} = [FeS]$). Subsequently, [FeS] reacts with hydrogen sulphide ($[FeS] + H_2S = FeS_2 + H_2$, Rickard, 1997; Richard and

Luther, 1997) or polysulphide (S_n^{2-})([FeS] + S_n^{2-} = FeS_2 + S_{n-1}^{2-}, Rickard, 1975, n>=5, Luther, 1990), forming pyrite. Hydrogen sulphide can be product of sulphate reduction or magmatic in origin, and carries negative $\Delta^{33}S$ or no S-MIF, respectively, thus the former pathway produces $\Delta^{33}S$-negative or S-MDF pyrite. Polysulphide is derived from the combination of elemental sulphur produced in the atmosphere via SO_2 photolysis with S^{2-} generated from sulphate reduction (S_{n-1} + S^{2-} = S_n^{2-}). SO_2 photolysis-derived sulphate is easily diluted by magmatic SO_2-derived sulphate, which possesses no S-MIF, and all previous photochemical experiments show much larger magnitude of positive $\Delta^{33}S$ than negative $\Delta^{33}S$. Therefore, S_n^{2-} is most likely to be $\Delta^{33}S$-positive. It has been demonstrated that all the sulphur in pyrite synthesized via the polysulphide pathway is derived entirely from S_n^{2-} (Butler et al., 2004). Hence, the pyrite product of the latter pathway is $\Delta^{33}S$-positive. Additionally, at the temperatures (<100°C) of the sedimentary environment where diagenetic pyrites are formed, due to the nucleophilicity varying in the order of S_5^{2-} > S_4^{2-} > HS^- > HS_2^- > S_3^{2-} > H_2S (Luther, 1990), the polysulphide pathway is preferred over the H_2S pathway for the rapid formation of pyrite (Rickard, 2012 and references therein). Therefore, the sulphur of $\Delta^{33}S$-positive pyrite can also be derived from microbial sulphate reduction.

Furthermore, the extreme ^{34}S depletion of the Tumbiana pyrite supports a biological origin as well. Four main plausible processes are capable of inducing a significant $\delta^{34}S$ fractionation of -30 to -41‰ from initial sulphate to pyrite (the lowest $\delta^{34}S$ of Tumbiana pyrite is -25‰, $\delta^{34}S$ of Archean barite is 5-16‰, Ueno et al., 2008; Shen et al., 2009; Muller et al., 2016, Ono et al., 2003. The fractionation during pyrite formation from sulphide is less than 1‰, Price and Shieh, 1979): sulphur-involving metabolism (e.g., dissimilatory sulphate reduction, Shen et al., 2001, Sim et al., 2011; sulphur intermediate disproportionation, Habicht et al., 1998), thermochemical sulphate reduction (TSR, Machel, 2001), sulphate reduction by ferrous iron in minerals (Ohmoto and Goldhaber, 1997), and magmatic sulphur dioxide disproportionation (Cameron and Hattori, 1987). Experiments have shown that TSR mainly results in a $\Delta^{33}S$ shift without producing $\Delta^{36}S$ due to magnetic isotope effects (Oduro et al., 2011), which is in

contrast to the data obtained in this study that exhibit a wider range in $\Delta^{36}S$ compared with $\Delta^{33}S$. Experiments of sulphate reduction by ferrous iron-bearing minerals are conducted in hydrothermal conditions at temperatures higher than 200 °C (Ohmoto and Goldhaber, 1997 and references therein). Such conditions are inapplicable to the diagenetic nodular pyrites as diagenesis temperatures are lower than metamorphic temperatures of 100 to 300 °C (Smith et al., 1982; Lepot et al., 2008). According to the reaction equation of SO_2 disproportionation ($4SO_2 + 4H_2O = H_2S + 3SO_4^{2-} + 6H^+$), sulphate phases account for 75% the products, which, nevertheless, are not observed in the black shale sample. Thus, sulphur-associated metabolisms are the most likely cause of the significantly depleted $\delta^{34}S$.

The data of the diagenetic pyrites of the 2.93 Ga Mosquito Creek Formation with $\Delta^{33}S$ of around -2.2‰ deviate from the ARA towards higher positive $\Delta^{36}S$ in a similar trend to that of biological fractionation line (Ono et al., 2006b) and microbial sulphate reduction (Johnston et al., 2007; Fig. 2.7), indicating probable modifications by microbial sulphate reduction on the primary atmospheric-derived sulphur as well. The same goes for the diagenetic pyrites of the 2.78 Ga Mt. Roe Basalt (Fig. 2.7).

5.3.2 Hydrothermal modification

The BSE images and microphotographs of etched pyrite show that the other pyrites of the 2.93 Ga Mosquito Creek Formation have characteristic internal textures (Fig. 2.3), indicating recrystallization from two generations of pyrite. Thus their multiple sulphur isotopic compositions are of mixed sulphur rather than solely the initial sedimentary sulphur. Such mixing can be a fundamental cause of the deviations from the ARA. The sulphur of hydrothermal fluids can be magmatic-, metamorphic-, or multiple-sourced. Although magmatic sulphur with S-MDF made no contributions to the deviation, sulphur in metamorphic fluids is able to modify the $\Delta^{36}S/\Delta^{33}S$ as metamorphic fluids are derived from devolatilization of strata, and thus sulphur with $\Delta^{36}S/\Delta^{33}S$ of not -1 (e.g., sulphur of biological origin) can be involved.

The other pyrites of the 2.78 Ga Mt. Roe Basalt have been hydrothermally modified, as indicated by complicated internal textures revealed by BSE images and microphotographs of etched pyrite nodules and grains, e.g., irregular oscillatory zoning, sector zoning, porous texture, hydrothermal sulphides (Fig. 2.4A, B and C). Additionally, the linear correlation between $\delta^{34}S$ and $\Delta^{33}S$ (Fig. 2.6) suggests mixing between two end members, which can be the primary sedimentary sulphur and the sulphur in hydrothermal fluids. Therefore, the same reason can account for the $\Delta^{36}S/\Delta^{33}S$ deviations of the 2.78 Ga Mt. Roe Basalt as well.

6. Concluding remarks

The $\Delta^{33}S$ measured in the ca. 3.2-2.72 Ga samples from the Pilbara Craton ranges from -2.40‰ to 0.79‰. No experiment related to S-MIF production so far has yielded such a range characterized by larger magnitude of minimum negative $\Delta^{33}S$ than that of maximum positive $\Delta^{33}S$. Additionally, the available samples are mostly of shallow water environments. However, the products of SO_2 photolysis carrying positive $\Delta^{33}S$ are inclined to be preserved in deep marine environments. Thus, due to the lack of available samples, the maximum positive $\Delta^{33}S$ of this period either has not been measured or is not preserved.

Nearly all the data deviate from the ARA, with the exception of the smallest magnitudes of $\Delta^{33}S$ and $\Delta^{36}S$ of the 3.2 Ga Dixon Island Formation. Such deviations can be attributed to biological modifications for the diagenetic pyrite of the 2.72 Ga Tumbiana Formation, the 2.93 Ga Mosquito Creek Formation and the 2.78 Ga Mt. Roe Basalt samples, particularly for the Tumbiana Formation, the $\delta^{34}S$-$\Delta^{33}S$-$\Delta^{36}S$ systematics of which strongly indicates microbial sulphate reduction. Modification by hydrothermal fluids can account for the deviations for the hydrothermally modified pyrite.

Collectively, the S-MIF of ca. 3.2-2.72 Ga is not so diminished as previously considered. The $\Delta^{36}S/\Delta^{33}S$ deviations from the ARA probably arise from biological or hydrothermal modifications rather than different processes of producing S-MIF.

References

Awramik, S.M., and Buchheim, H.P., 2009. A giant, Late Archean lake system: The Meentheena Member (Tumbiana Formation; Fortescue Group), Western Australia. Precambrian Research 174 (3-4): 215-240.

Bagas, L., Bierlein, F.P., Bodorkos, S., Nelson, D.R., 2008. Tectonic setting, evolution and orogenic gold potential of the late Mesoarchaean Mosquito Creek Basin, North Pilbara Craton, Western Australia. Precambrian Research 160 (3-4): 227-244.

Bekker, A., Holland, H.D., Wang, P.L., Rumble III, D., Stein, H.J., Hannah, J.L., Coetzee, L.L., Beukes, N.J., 2004. Dating the rise of atmospheric oxygen. Nature 427: 117-120.

Blake, T.S., 1993. Late Archaean crustal extension, sedimentary basin formation, flood basalt volcanism and continental rifting: the Nullagine and Mount Jope Supersequences, Western Australia. Precambrian Research 60 (1-4): 185-241.

Blake, T.S., 2001. Cyclic continental mafic tuff and flood basalt volcanism in the Late Archaean Nullagine and Mount Jope Supersequences in the eastern Pilbara, Western Australia. Precambrian Research 107 (3-4): 139-177.

Bolhar, R., and Van Kranendonk, M.J., 2007. A non-marine depositional setting for the northern Fortescue Group, Pilbara Craton, inferred from trace element geochemistry of stromatolitic carbonates. Precambrian Research 155 (3-4): 229-250.

Butler, I.B., Böttcher, M.E., Rickard, D., Oldroyd, A., 2004. Sulfur isotope partitioning during experimental formation of pyrite via the polysulfide and hydrogen sulfide pathways: implications for the interpretation of sedimentary and hydrothermal pyrite isotope records. Earth and Planetary Science Letters 228 (3-4): 495-509.

Cameron, E.M., and Hattori, K., 1987. Archean gold mineralization and oxidized hydrothermal fluids. Economic Geology 82 (5): 1177-1191.

Colman, J.J., Xu, X., Thiemens, M.H., Trogler, W.C., 1996. Photopolymerization and Mass-Independent Sulfur Isotope Fractionations in Carbon Disulfide. Science 273 (5276): 774-776.

Crowe, D.E., and Vaughan, R.G., 1996. Characterization and use of isotopically homogeneous standards for in situ laser microprobe analysis of $^{34}S/^{32}S$ ratios. American Mineralogist 81 (1-2): 187-193.

Domagal-Goldman, S.D., Kasting, J.F., Johnston, D.T., Farquhar, J., 2008. Organic haze, glaciations and multiple sulfur isotopes in the Mid-Archean Era. Earth and Planetary Science Letters 269 (1-2): 29-40.

Endo, Y., Ueno, Y., Aoyama, S., Danielache, S.O., 2016. Sulfur isotope fractionation by broadband UV radiation to optically thin SO_2 under reducing atmosphere. Earth and Planetary Science Letters 453: 9-22.

Eriksson, K.A., Krapez, B., Fralick, P.W., 1994. Sedimentology of Archean greenstone belts: signatures of tectonic evolution. Earth-Science Reviews 37 (1-2): 1-88.

Farquhar, J., Peters, M., Johnston, D.T., Strauss, H., Masterson, A., Wiechert, U., Kaufman, A.J., 2007. Isotopic evidence for Mesoarchaean anoxia and changing atmospheric sulphur chemistry: Nature 449: 706-709.

Farquhar, J., Savarino, J., Airieau, S., Thiemens, M.H., 2001. Observation of wavelength-sensitive mass-independent sulfur isotope effects during SO_2 photolysis: Implications for the early atmosphere. Journal of Geophysical Research 106 (E12): 32829-32839.

Gregory, D.D., Large, R.R., Halpin, J.A., Steadman, J.A., Hickman, A.H., Ireland, T.R., Holden, P., 2015. The chemical conditions of the late Archean Hamersley basin inferred from whole rock and pyrite geochemistry with $\Delta^{33}S$ and $\delta^{34}S$ isotope analyses. Geochimica et Cosmochimica Acta 149: 223-250.

Guo, Q., Strauss, H., Kaufman, A.J., Schröder, S., Gutzmer, J., Wing, B., Baker, M.A., Bekker, A., Jin, Q., Kim, S.T., Farquhar, J., 2009. Reconstructing Earth's surface oxidation across the Archean-Proterozoic transition. Geology 37 (5): 399-402.

Guy, B.M., Ono, S., Gutzmer, J., Kaufman, A.J., Lin, Y., Fogel., M.L., Beukes, N.J., 2012. A multiple sulfur and organic carbon isotope record from non-conglomeratic sedimentary rocks of the Mesoarchean Witwatersrand Supergroup, South Africa. Precambrian Research 216-219: 208-231.

Habicht, K.S., Canfield, D.E., Rethmeier, J., 1998. Sulfur isotope fractionation during bacterial reduction and disproportionation of thiosulfate and sulfite. Geochimica et Cosmochimica Acta 62 (15): 2585-2595.

Halevy, I., 2013. Production, preservation, and biological processing of mass-independent sulfur isotope fractionation in the Archean surface environment. Proceedings of the National Academy of Sciences of the United States of America 110 (44): 17644-17649.

Hall, C.E., 2002. Sedimentology, Geochemistry and Palaeogeography of the lower Fortescue Group, Hamersley Province, Western Australia. Ph.D. thesis, University of Western Australia, Perth (unpublished).

Hickman, A.H., 2004. Two contrasting granite-greenstone terranes in the Pilbara Craton, Australia: evidence for vertical and horizontal tectonic regimes prior to 2900 Ma. Precambrian Research 131 (3-4): 153-172.

Hickman, A.H., 2012. Review of the Pilbara Craton and Fortescue Basin, Western Australia: Crustal evolution providing environments for early life. Island Arc 21: 1-31.

Hoering, T.C., 1989. The isotopic composition of bedded barites from the Archaean of southern India. Journal of the Geological Society of India 34: 461-466.

Ireland, T.R., Schram, N., Holden, P., Lanc, P., Ávila, J., Armstrong, R., Amelin, Y., Latimore, A., Corrigan, D., Clement, S., Foster, J.J., Compston, W., 2014. Charge-mode electrometer

measurements of S-isotopic compositions on SHRIMP-SI. International Journal of Mass Spectrometry 359: 26-37.

Izon, G., Zerkle, A.L., Zhelezinskaia, I., Farquhar, J., Newton, R.J., Poulton, S.W., Eigenbrode, J.L., Claire, M.W., 2015. Multiple oscillations in Neoarchaean atmospheric chemistry. Earth and Planetary Science Letters 431: 264-273.

Johnston, D.T., Farquhar, J., Canfield, D.E., 2007. Sulfur isotope insights into microbial sulfate reduction: When microbes meet models. Geochimica et Cosmochimica Acta 71 (16): 3929-3947.

Kamber, B.S., and Whitehouse, M.J., 2007. Micro-scale sulphur isotope evidence for sulphur cycling in the late Archean shallow ocean. Geobiology 5 (1): 5-17.

Kaufman, A.J., Johnston, D.T., Farquhar, J., Masterson, A.L., Lyons, T.W., Bates, S., Anbar, A.D., Arnold, G.L., Garvin, J., Buick, R., 2007. Late Archean Biospheric Oxygenation and Atmospheric Evolution. Science 317 (5846): 1900-1903.

Kiyokawa, S., Koge, S., Ito, T., Ikehara, M., 2014. An ocean-floor carbonaceous sedimentary sequence in the 3.2-Ga Dixon Island Formation, coastal Pilbara terrane, Western Australia. Precambrian Research 255 (1): 124-143.

Kopf, S., and Ono, S., 2012. Sulfur mass-independent fractionation in liquid phase chemistry: UV photolysis of phenacylphenylsulfone as a case study. Geochimica et Cosmochimica Acta 85: 160-169.

Kurzweil, F., Claire, M., Thomazo, C., Peters, M., Hannington, M., Strauss, H., 2013. Atmospheric sulfur rearrangement 2.7 billion years ago: Evidence for oxygenic photosynthesis. Earth and Planetary Science Letters 366: 17-26.

Lasaga, A.C., Otake, T., Watanabe, Y., Ohmoto, H., 2008. Anomalous fractionation of sulfur isotopes during heterogeneous reactions. Earth and Planetary Science Letters 268 (1-2): 225-238.

Lepot, K., Benzerara, K., Brown, G.E., Philippot, P., 2008. Microbially influenced formation of 2724-million-year-old stromatolites. Nature Geoscience 1: 118-121.

Luther, G.W., 1990. The frontier-molecular-orbital theory approach in geochemical processes. Stumm W. (Ed.), Aquatic Chemical Kinetics, Wiley, New York: 173-198.

Machel, H.G., 2001. Bacterial and thermochemical sulfate reduction in diagenetic setting - old and new insights. Sedimentary Geology 140 (1-2): 143-175.

Marin-Carbonne, J., Rollion-Bard, C., Bekker, A., Rouxel, O., Agangi, A., Cavalazzi, B., Wohlgemuth-Ueberwasser, C.C., Hofmann, A., McKeegan, K.D., 2014. Coupled Fe and S isotope variations in pyrite nodules from Archean shale. Earth and Planetary Science Letters 392: 67-79.

Masterson, A.L., Farquhar, J., Wing, B.A., 2011. Sulfur mass-independent fractionation patterns in the broadband UV photolysis of sulfur dioxide: Pressure and third body effects. Earth and Planetary Science Letters 306 (3-4): 253-260.

Muller, É., Philippot, P., Rollion-Bard, C., Cartigny, P., 2016. Multiple sulfur-isotope signatures in Archean sulfates and their implications for the chemistry and dynamics of the early atmosphere. Proceedings of the National Academy of Sciences 113 (27): 7432-7437.

Nelson, D.R., 2001. 168908: Crystal-lithic Tuff, Copper Hills. Compilation of Geochronology Data 1999, June 2007 Update, Geochronology Dataset 222. Geological Survey of Western Australia, Perth.

Oduro, H., Harms, B., Sintim, H.O., Kaufman, A.J., Cody, G., Farquhar, J., 2011. Evidence of magnetic isotope effects during thermochemical sulfate reduction. Proceedings of the National Academy of Sciences of the United States of America 108 (43): 17635-17638.

Ohmoto, H., and Goldhaber, M.B., 1997. Sulfur and carbon isotopes. In Barnes, H.L. (Ed.), Geochemistry of Hydrothermal Ore Deposits, Wiley, New York: 517-611.

Ohmoto, H., Watanabe, Y., Ikemi, H., Poulson, S.R., Taylor, B.E., 2006. Sulphur isotope evidence for an oxic Archaean atmosphere. Nature 442: 908-911.

Ono, S., Beukes, N.J., Rumble, D., Fogel, M.L., 2006a. Early evolution of atmospheric oxygen from multiple-sulfur and carbon isotope records of the 2.9 Ga Mozaan Group of the Pongola Supergroup, Southern Africa. South African Journal of Geology 109 (1-2): 97-108.

Ono, S., Eigenbrode, J.L., Pavlov, A.A., Kharecha, P., Rumble III, D., Kasting, J.F., Freeman, K.H., 2003. New insights into Archean sulfur cycle from mass-independent sulfur isotope records from the Hamersley Basin, Australia. Earth and Planetary Science Letters 213 (1-2): 15-30.

Ono, S., Kaufman, A.J., Farquhar, J., Sumner, D.Y., Beukes, N.J., 2009. Lithofacies control on multiple-sulfur isotope records and Neoarchean sulfur cycles. Precambrian Research 169 (1-4): 58-67.

Ono, S., Whitehill, A.R., Lyons, J.R., 2013. Contribution of isotopologue self-shielding to sulfur mass-independent fractionation during sulfur dioxide photolysis. Journal of Geophysical Research: Atmosphere 118 (5): 2444-2454.

Ono, S., Wing, B., Johnston, D., Farquhar, J., Rumble, D., 2006b. Mass-dependent fractionation of quadruple stable sulfur isotope system as a new tracer of sulfur biogeochemical cycles. Geochimica et Cosmochimica Acta 70 (9): 2238-2252.

Partridge, M.A., Golding, S.D., Baublys, K.A., Young, E., 2008. Pyrite paragenesis and multiple sulfur isotope distribution in late Archean and early Paleoproterozoic Hamersley Basin sediments. Earth and Planetary Science Letters 272 (1-2): 41-49.

Pavlov, A.A., and Kasting, J.F., 2002. Mass-Independent Fractionation of Sulfur Isotopes in Archean Sediments: Strong Evidence for an Anoxic Archean Atmosphere. Astrobiology 2 (1): 27-41.

Philippot, P., Van Zuilen, M., Lepot, K., Thomazo, C., Farquhar, J., Van Kranendonk, M.J., 2007. Early Archaean Microorganisms Preferred Elemental Sulfur, Not Sulfate. Science 317 (5844): 1534-1537.

Philippot, P., van Zuilen, M., Rollion-Bard, C., 2012. Variations in atmospheric sulphur chemistry on early Earth linked to volcanic activity. Nature Geoscience 5: 668-674.

Pike, G., and Cas, R.A.F., 2002. Stratigraphic Evolution of Archaean Volcanic Rock-Dominated Rift Basins from the Whim Creek Belt, West Pilbara Craton, Western Australia. In Altermann, W. and Corcoran, P. L. (eds.) Precambrian Sedimentary Environments: A Modern Approach to Ancient Depositional Systems, 464pp, International Association of Sedimentologists, Special Publication 33, Blackwell Science, Oxford.

Pike, G., Cas, R.A.F., Hickman, A.H., 2006. Archean volcanic and sedimentary rocks of the Whim Creek greenstone belt, Pilbara Craton, Western Australia. Western Australia Geological Survey, Report 101: 1-104.

Price, F.T., and Shieh, Y.N., 1979. Fractionation of sulfur isotopes during laboratory synthesis of pyrite at low temperatures. Chemical Geology 27 (3): 245-253.

Rasmussen, B., Fletcher, I.R., Muhling, J.R., 2007. In situ U-Pb dating and element mapping of three generations of monazite: Unravelling cryptic tectonothermal events in low-grade terranes. Geochimica et Cosmochimica Acta 71 (3): 670-690.

Rickard, D.T., 1975. Kinetics and mechanism of pyrite formation at low temperatures. American Journal of Science 275 (6): 636-652.

Rickard, D., 1997. Kinetics of pyrite formation by the H_2S oxidation of iron (II) monosulfide in aqueous solutions between 25 and 125 °C: The rate equation. Geochimica et Cosmochimica Acta 61 (1): 115-134.

Rickard, D., 2012. Sulfidic Sediments and Sedimentary Rocks. In Developments in Sedimentology, Amsterdam, Elsevier 65: 1-766.

Rickard, D., and Luther, G.W., 1997. Kinetics of pyrite formation by the H_2S oxidation of iron (II) monosulfide in aqueous solutions between 25 and 125 °C: The mechanism. Geochimica et Cosmochimica Acta 61 (1): 135-147.

Roerdink, D.L., Mason, P.R.D., Whitehouse, M.J., Reimer, T., 2013. High-resolution quadruple sulfur isotope analyses of 3.2 Ga pyrite from the Barberton Greenstone Belt in South Africa reveal distinct environment controls on sulfide isotopic arrays. Geochimica et Cosmochimica Acta 117: 203-215.

Sakurai, R., Ito, M., Ueno, Y., Kitajima, K., Maruyama, S., 2005. Facies architecture and sequence-stratigraphic features of the Tumbiana Formation in the Pilbara Craton, northwestern Australia: Implications for depositional environments of oxygenic stromatolites during the Late Archean. Precambrian Research 138 (3-4): 255-273.

Savarino, J., Romero, A., Cole-Dai, J., Bekki, S., Thiemens, M.H., 2003. UV induced mass-independent sulfur isotope fractionation in stratospheric volcanic sulfate. Geophysical Research Letters 30: 2131.

Shen, Y., Buick, R., Canfield, D.E., 2001. Isotopic evidence for microbial sulphate reduction in the early Archaean era. Nature 410: 77-81.

Shen, Y., Farquhar, J., Masterson, A., Kaufman, A.J., Buick, R., 2009. Evaluating the role of microbial sulfate reduction in the early Archean using quadruple isotope systematics. Earth and Planetary Science Letters 279 (3-4): 383-391.

Sim, M.S., Bosak, T., Ono, S., 2011. Large Sulfur Isotope Fractionation Does Not Require Disproportionation. Science 333 (6038): 74-77.

Smithies, R.H., Van Kranendonk, M.J., Champion, D.C., 2007. The Mesoarchean emergence of modern-style subduction. Gondwana Research 11 (1-2): 50-68.

Thomazo, C., Ader, M., Farquhar, J., Philippot, P., 2009. Methanotrophs regulated atmospheric sulfur isotope anomalies during the Mesoarchean (Tumbiana Formation, Western Australia). Earth and Planetary Science Letters 279 (1-2): 65-75.

Thomazo, C., Nisbet, E.G., Grassineau, N.V., Peters, M., Strauss, H., 2013. Multiple sulfur and carbon isotope composition of sediments from the Belingwe Greenstone Belt (Zimbabwe): A biogenic methane regulation on mass independent fractionation of sulfur during the Neoarchean? Geochimica et Cosmochimica Acta 121: 120-138.

Thorne, A.M., and Trendall, A.F., 2001. Geology of the Fortescue Group, Pilbara Craton, Western Australia. Geological Survey of Western Australia Bulletin 144: 1-249.

Van Kranendonk, M.J., Hickman, A.H., Smithies, R.H., Nelson, D.R., Pike, G., 2002. Geology and Tectonic Evolution of the Archean North Pilbara Terrain, Pilbara Craton, Western Australia. Economic Geology 97 (4): 695-732.

Van Kranendonk, M.J., Hickman, A.H., Smithies, R.H., Williams, I.R., Bagas, L., Farrell, T.R., 2006. Revised lithostratigraphy of Archean supracrustal and intrusive rocks in the northern Pilbara Craton, Western Australia. Geological Survey of Western Australia, Record 2006/15, 1-57.

Ueno, Y., Ono, S., Rumble, D., Maruyama, S., 2008. Quadruple sulfur isotope analysis of ca. 3.5 Ga Dresser Formation: New evidence for microbial sulfate reduction in the early Archean. Geochimica et Cosmochimica Acta 72 (23): 5675-5691.

Wacey, D., McLoughlin, N., Whitehouse, J., Kilburn, M.R., 2010. Two coexisting sulfur metabolisms in a ca. 3400 Ma sandstone. Geology 38 (12): 1115-1118.

Wacey, D., Noffke, N., Cliff, J., Barley, M.E., Farquhar, J., 2015. Micro-scale quadruple sulfur isotope analysis of pyrite from the ~3480 Ma Dresser Formation: New insights into sulfur cycling on the early Earth. Precambrian Research 258: 24-35.

Watanabe, Y., Farquhar, J., Ohmoto, H., 2009. Anomalous Fractionations of Sulfur Isotopes During Thermochemical Sulfate Reduction. Science 324 (5925): 370-373.

Whitehill, A.R., Jiang, B., Guo, H., Ono, S., 2015. SO_2 photolysis as a source for sulfur mass-independent isotope signatures in stratospheric aerosols. Atmospheric Chemistry and Physics 15: 1843-1864.

Whitehill, A.R., and Ono, S., 2012. Excitation band dependence of sulfur isotope mass-independent fractionation during photochemistry of sulfur dioxide using broadband light sources. Geochimica et Cosmochimica Acta 94: 238-253.

Whitehouse, M.J., 2013. Multiple Sulfur Isotope Determination by SIMS: Evaluation of Reference Sulfides for $\Delta^{33}S$ with Observations and a Case Study on the Determination of $\Delta^{36}S$. Geostandards and Geoanalytical Research 37 (1): 19-33.

Wille, M., Nebel, O., Van Kranendonk, M.J., Schoenberg, R., Kleinhanns, I.C., Ellwood, M.J., 2013. Mo-Cr isotope evidence for a reducing Archean atmosphere in 3.46-2.76 Ga black shales from the Pilbara, Western Australia. Chemical Geology 340: 68-76.

Williford, K.H., Ushikubo, T., Lepot, K., Kitajima, K., Hallmann, C., Spicuzza, M.J., Kozdon, R., Eigenbrode, J.L., Summons, R.E., Valley, J.W., 2016. Carbon and sulfur isotopic signatures of ancient life and environment at the microbial scale: Neoarchean shales and carbonates. Geobiology 14 (2): 105-128.

Williford, K.H., Van Kranendonk, M.J., Ushikubo, T., Kozdon, R., Valley, J.W., 2011. Constraining atmospheric oxygen and seawater sulfate concentrations during Paleoproterozoic glaciation: In

situ sulfur three-isotope microanalysis of pyrite from the Turee Cree Group, Western Australia. Geochimica et Cosmochimica Acta 75 (19): 5686-5705.

Yang, W., Holland, H.D., Rye, R., 2002. Evidence for low or no oxygen in the late Archean atmosphere from the ~2.76 Ga Mt. Roe#2 paleosol, Western Australia: Part 3. Geochimica et Cosmochimica Acta 66 (21): 3707-3718.

Zahnle, K., Claire, M., Catling, D., 2006. The loss of mass-independent fractionation in sulfur due to a Palaeoproterozoic collapse of atmospheric methane. Geobiology 4 (4): 271-283.

Zhelezinskaia, I., Kaufman, A.J., Farquhar, J., Cliff, J., 2014. Large sulfur isotope fractionations associated with Neoarchean microbial sulfate reduction. Science 346 (6210): 742-744.

Table 2.1 Drill core descriptions and associated drill hole names and locations.

Formation	Age	Drill hole name	Drill hole location	Depth of drill core/m	Description of drill core
Dixon Island Formation	ca. 3.2 Ga	DX	20°39′43.6″S 117°00′05.9″E	88.80-88.81	Black shale with a pyrite lamina.
				92.22-92.26	Black shale with irregular pyrite nodules.
				98.06-98.07	Black shale with veins and a big pyrite nodule, but the veins are not associated with the pyrite nodule.
				126.26-126.31	Alternating pyrite laminae and black shale laminae.
				132.26-132.28	Black shale with some short and thin irregular pyrite veinlets.
				134.14-134.15	Black shale with pyrite laminae.
				143.57-143.59	Black shale with a big pyrite nodule.
Cleaverville Formation	ca. 3.0 Ga	CL1	20°39′06.7″S 117°01′28.8″E	80.76-80.77 102.71-102.72	Black shale with a pyrite lamina.
				104.99-105.00	Black shale with a disseminated pyrite lamina.
Mosquito Creek Formation	ca. 2.93 Ga	ABDP5	21°41′53.7″S 120°37′14.5″E	38.35-38.36 40.74-40.75	Black shale. Pyrite occurs as nodules that have been truncated (only the one in 40.74-40.75m is complete) and fine disseminated grains within the matrix.
Mt. Roe Basalt	ca. 2.78 Ga	ABDP6	20°53′26.7″S 117°53′32.1″E	93.43-93.44	Black shale with a pyrite nodule.
				101.21-101.22 101.40-101.42	Black shale with pyrite nodules.
				115.80-115.81 128.97-128.99 129.64-129.66	Hydrothermally altered basalt.

Formation		Age	Drill hole name	Drill hole location	Depth of drill core/m	Description of drill core
Hardey Formation		ca. 2.76 Ga	ABDP3	21°24′22.2″S 120°14′29″E	261.63-261.64	Black shale with a big pyrite nodule.
					265.80-265.83	Black shale with pyrite nodules and a lamina.
					114.060-114.061	Dark grey shale with a pyrite nodule.
					115.680-115.682	
			FVG1	22°33'S 119°30'E	1843.86-1843.87	Greyish green ooidal siltstone to sandstone. It is composed of quartz, chlorite, plagioclase, and minor carbonate and iron oxide. Pyrite occurs as disseminated anhedral to euhedral grains within the ooids or matrix.
Tumbiana Formation	Meentheena Member	ca. 2.72 Ga	PDP1	21°18′15″S 120°24′40″E	43.15-43.16	Black Shale. Pyrite occurs as a nodule, surrounded by some disseminated grains.
					44.08-44.10	Pyritic black shale. Euhedral to subhedral pyrite grains of variable size are disseminated within the black shale. The majority are abundant in mineral inclusions.
					44.33-44.34	Black shale. Pyrite grains are disseminated and concentrated to a thin discrete lamina.
					81.00-81.01	Black shale. Pyrite occurs as disseminated nodules.

Table 2.2 Acquisition conditions of SHRIMP-SI.

Parameters	**Quadruple sulphur isotope (Big-spot analyses)**	**Triple sulphur isotope (Small-spot analyses)**
Spot size	ca. 27 μm × 20 μm	ca. 18 μm × 15 μm
Set(s)	4 (mainly) or 5	2 (mainly) or 4
Scans	40 or 50	20 or 40
Primary beam ion species	Cs^+	Cs^+
Source slit width	60 μm	60 μm
Collector slit width for $^{32}S^-$	300 μm	300 μm
Collector slit width for $^{33}S^-$	150 μm	150 μm
Collector slit width for $^{34}S^-$	200 μm	200 μm
Collector slit width for $^{36}S^-$	300 μm	300 μm
Mass resolution (at 10% peak height)	4000M/ΔM	4000M/ΔM
Primary beam energy	15 keV	15 keV
Total acceleration voltage for the extraction of secondary ions	10 kV	10 kV
Primary beam intensity (avg.)	ca. 6 nA	ca. 2 nA
Amplifier and V-F Converter range for $^{32}S^-$	Electrometer current mode, 10^{11} Ω, 0-50 V	Electrometer current mode, 10^{11} Ω, 0-50 V
Amplifier and V-F Converter range for $^{34}S^-$	Electrometer current mode, 10^{11} or 10^{12} Ω, 0-50 V	Electrometer current mode, 10^{11} or 10^{12} Ω, 0-50 V
Amplifier and V-F Converter range for $^{33}S^-$	Electrometer current mode, 10^{11} or 10^{12} Ω, 0-50 V	Electrometer current mode, 10^{11} or 10^{12} Ω, 0-50 V
Amplifier and V-F Converter range for $^{36}S^-$	Electrometer charge mode, 22 pF, 0-50 V	

Table 2.3 All quadruple and triple sulphur isotopic composition data of pyrite in ca. 3.2 to 2.72 Ga metasedimentary rocks from the Pilbara Craton, Western Australia.

Title	Formation	Age/ Ga	Drill core	Lithology	Pyrite genesis	$\delta^{33}S$/‰	1σ	$\delta^{34}S$/‰	1σ	$\delta^{36}S$/‰	1σ	$\Delta^{33}S$/ ‰	1σ	$\Delta^{36}S$/ ‰	1σ	Detector $^{32}S^-$ /CPS	Detector $^{33}S^-$ /CPS	Detector $^{34}S^-$ /CPS	Detector $^{36}S^-$ /CPS
1038-25_1	Dixon Island	3.2	DX_143.57-143.59m	Shale	Hydrothermal (primary)	-1.35	0.02	-2.42	0.08	-4.19	0.15	-0.10	0.02	0.40	0.16	1012925340	7905713	44239969	149298
1038-25_3	Dixon Island	3.2	DX_143.57-143.59m	Shale	Hydrothermal (primary)	-1.34	0.02	-2.45	0.06	-4.58	0.13	-0.08	0.02	0.07	0.13	1044301257	8150440	45608112	153780
1038-25_6.2	Dixon Island	3.2	DX_143.57-143.59m	Shale	Hydrothermal (primary)	1.53	0.03	2.88	0.06	5.49	0.11	0.04	0.02	0.01	0.11	1033248096	8088748	45378002	153675
1038-25_4.1	Dixon Island	3.2	DX_143.57-143.59m	Shale	Hydrothermal (primary)	4.29	0.03	8.13	0.08	15.91	0.17	0.12	0.02	0.41	0.19	997705255	7828957	44031290	149950
1038-25_4.2	Dixon Island	3.2	DX_143.57-143.59m	Shale	Hydrothermal (primary)	0.17	0.02	0.20	0.06	0.49	0.14	0.06	0.02	0.11	0.13	911118321	7119221	39883834	134660
1038-25_12.1	Dixon Island	3.2	DX_132.26-132.28m	Shale	Hydrothermal (primary)	6.15	0.02	12.19	0.05	23.56	0.15	-0.11	0.02	0.27	0.16	1009336753	7936274	44721942	152750
1038-25_14.1	Dixon Island	3.2	DX_132.26-132.28m	Shale	Hydrothermal (primary)	7.91	0.02	15.55	0.09	30.07	0.17	-0.06	0.02	0.32	0.15	994146167	7833046	44212049	151482
1038-25_14.1'	Dixon Island	3.2	DX_132.26-132.28m	Shale	Hydrothermal (primary)	7.01	0.03	13.88	0.08	26.54	0.12	-0.12	0.03	0.00	0.12	1012085300	7963228	44913538	153555
1038-25_15.1	Dixon Island	3.2	DX_132.26-132.28m	Shale	Hydrothermal (primary)	6.57	0.03	13.09	0.10	25.37	0.13	-0.16	0.03	0.35	0.13	1007946952	7927251	44697300	152852
1038-53_1.1	Dixon Island	3.2	DX_92.22-92.26m	Shale	Hydrothermal (primary)	-3.83	0.02	-7.57	0.07	-14.53	0.13	0.07	0.02	-0.20	0.13	978794384	7617675	42507515	142636
1038-53_1.10	Dixon Island	3.2	DX_92.22-92.26m	Shale	Hydrothermal (primary)	-4.79	0.02	-9.16	0.08	-17.65	0.15	-0.07	0.02	-0.32	0.16	902088327	7014615	39117420	130979
1038-53_1.15	Dixon Island	3.2	DX_92.22-92.26m	Shale	Hydrothermal (primary)	-4.37	0.02	-8.65	0.05	-16.58	0.15	0.09	0.02	-0.20	0.14	968668187	7533972	42012189	140521
1038-53_1.6	Dixon Island	3.2	DX_92.22-92.26m	Shale	Hydrothermal (primary)	-3.38	0.02	-6.54	0.06	-12.40	0.13	-0.01	0.02	0.00	0.14	972823779	7576539	42303192	141974
1038-53_1.9	Dixon Island	3.2	DX_92.22-92.26m	Shale	Hydrothermal (primary)	-7.57	0.02	-14.74	0.07	-28.11	0.14	0.04	0.02	-0.29	0.15	953989884	7396592	41131220	136903
1038-53_1.9'	Dixon Island	3.2	DX_92.22-92.26m	Shale	Hydrothermal (primary)	-4.50	0.02	-8.82	0.06	-16.64	0.20	0.05	0.02	0.05	0.17	953792924	7419892	41376170	138763
1038-53_1.15'	Dixon Island	3.2	DX_92.22-92.26m	Shale	Hydrothermal (primary)	0.86	0.02	1.58	0.13	2.61	0.17	0.04	0.02	-0.40	0.17	933277729	7297980	40916856	138325
1038-53_5.41	Dixon Island	3.2	DX_92.22-92.26m	Shale	Hydrothermal (primary)	0.81	0.09	1.24	0.18			0.17	0.08			440815004	3444430	19287632	
1038-53_5.32	Dixon Island	3.2	DX_92.22-92.26m	Shale	Hydrothermal (primary)	-1.14	0.07	-2.28	0.10			0.04	0.07			415531668	3242309	18128211	
1038-53_5.32'	Dixon Island	3.2	DX_92.22-92.26m	Shale	Hydrothermal (primary)	-0.55	0.07	-1.39	0.41			0.16	0.07			407616825	3184227	17825906	
1038-53_2.5	Dixon Island	3.2	DX_92.22-92.26m	Shale	Hydrothermal (primary)	-3.45	0.08	-7.03	0.08			0.17	0.09			399933130	3112914	17358172	
1038-24_1.1	Dixon Island	3.2	DX_126.26-126.31m	Shale	Hydrothermal (primary)	5.74	0.06	11.98	0.15			-0.41	0.06			404577412	3178460	17894219	
1038-24_1.2	Dixon Island	3.2	DX_126.26-126.31m	Shale	Hydrothermal (primary)	8.19	0.05	16.49	0.36			-0.27	0.05			406665000	3202862	18063988	
1038-24_2.1	Dixon Island	3.2	DX_126.26-126.31m	Shale	Hydrothermal (primary)	5.21	0.06	10.96	0.12			-0.42	0.06			411879774	3234725	18193259	
1038-24_4.1	Dixon Island	3.2	DX_126.26-126.31m	Shale	Hydrothermal (primary)	4.09	0.05	8.86	0.11			-0.46	0.05			386883156	3035694	17050729	

Title	Formation	Age/ Ga	Drill core	Lithology	Pyrite genesis	$\delta^{33}S$/‰	1σ	$\delta^{34}S$/‰	1σ	$\delta^{36}S$/‰	1σ	$\Delta^{33}S$/ ‰	1σ	$\Delta^{36}S$/ ‰	1σ	Detector $^{32}S^-$ /CPS	Detector $^{33}S^-$ /CPS	Detector $^{34}S^-$ /CPS	Detector $^{36}S^-$ /CPS
1038-24_4.3	Dixon Island	3.2	DX_126.26-126.31m	Shale	Hydrothermal (primary)	4.90	0.06	10.19	0.06			-0.34	0.06			412274317	3237986	18214055	
1038-24_4.2	Dixon Island	3.2	DX_126.26-126.31m	Shale	Hydrothermal (primary)	5.71	0.07	11.76	0.12			-0.32	0.07			411317916	3231394	18188484	
1038-24_5	Dixon Island	3.2	DX_126.26-126.31m	Shale	Hydrothermal (primary)	7.39	0.06	14.77	0.07			-0.19	0.06			393423726	3094240	17443974	
1038-52_1.4_1	Dixon Island	3.2	DX_126.26-126.31m	Shale	Hydrothermal (primary)	-0.13	0.06	0.68	0.06			-0.49	0.06			419260679	3275694	18350197	
1038-52_1.4_2	Dixon Island	3.2	DX_126.26-126.31m	Shale	Hydrothermal (primary)	-0.30	0.05	0.90	0.08			-0.77	0.06			402283022	3142055	17607882	
1038-52_1.5_1	Dixon Island	3.2	DX_126.26-126.31m	Shale	Hydrothermal (primary)	-0.45	0.04	0.06	0.04			-0.48	0.04			401337090	3134266	17548941	
1038-52_1.5_2	Dixon Island	3.2	DX_126.26-126.31m	Shale	Hydrothermal (primary)	2.53	0.05	5.63	0.17			-0.37	0.05			410638882	3217608	18059475	
1038-52_1.5_3	Dixon Island	3.2	DX_126.26-126.31m	Shale	Hydrothermal (primary)	2.04	0.04	5.14	0.10			-0.61	0.04			408580294	3199686	17956014	
1038-52_15.1	Dixon Island	3.2	DX_126.26-126.31m	Shale	Hydrothermal (primary)	11.18	0.03	22.14	0.13			-0.16	0.04			387511120	3061526	17318976	
1038-52_15.2	Dixon Island	3.2	DX_126.26-126.31m	Shale	Hydrothermal (primary)	7.24	0.06	14.57	0.05			-0.24	0.06			396698728	3121474	17593622	
1038-52_2.9.1	Dixon Island	3.2	DX_126.26-126.31m	Shale	Hydrothermal (primary)	0.31	0.05	0.85	0.08			-0.13	0.05			410836241	3212022	17977510	
1038-52_2.5	Dixon Island	3.2	DX_126.26-126.31m	Shale	Hydrothermal (primary)	9.65	0.04	19.34	0.20			-0.26	0.05			405079684	3197318	18054769	
1038-52_2.10	Dixon Island	3.2	DX_126.26-126.31m	Shale	Hydrothermal (primary)	-5.76	0.05	-10.71	0.06			-0.23	0.05			417722136	3247579	18077756	
1038-52_2.3.1	Dixon Island	3.2	DX_126.26-126.31m	Shale	Hydrothermal (primary)	-5.66	0.07	-10.51	0.12			-0.24	0.07			420171734	3265942	18183546	
1038-52_3.1	Dixon Island	3.2	DX_88.80-88.81m	Shale	Hydrothermal (primary)	10.38	0.05	20.16	0.09			0.05	0.07			391549785	3092824	17471688	
1038-52_3.9	Dixon Island	3.2	DX_88.80-88.81m	Shale	Hydrothermal (primary)	9.59	0.07	18.64	0.08			0.04	0.07			393953019	3111217	17556218	
1038-52_3.13_1	Dixon Island	3.2	DX_88.80-88.81m	Shale	Hydrothermal (primary)	9.26	0.07	17.99	0.05			0.04	0.07			413357960	3261593	18401089	
1038-52_3.13_2	Dixon Island	3.2	DX_88.80-88.81m	Shale	Hydrothermal (primary)	10.27	0.06	19.88	0.10			0.08	0.06			407167103	3215368	18161181	
1038-52_4.1_1	Dixon Island	3.2	DX_98.06-98.07m	Shale	Hydrothermal (primary)	5.41	0.04	10.17	0.06			0.18	0.04			389308893	3058668	17195380	
1035-52_4.3	Dixon Island	3.2	DX_98.06-98.07m	Shale	Hydrothermal (primary)	7.03	0.05	13.66	0.40			0.02	0.05			393516148	3097210	17444256	
1038-52_4.7	Dixon Island	3.2	DX_98.06-98.07m	Shale	Hydrothermal (primary)	10.86	0.07	21.29	0.24			-0.05	0.06			381225369	3013140	17033762	
1038-52_4.16_1	Dixon Island	3.2	DX_98.06-98.07m	Shale	Hydrothermal (primary)	5.69	0.06	10.83	0.13			0.12	0.07			392617698	3086813	17355873	
1038-52_4.16_2	Dixon Island	3.2	DX_98.06-98.07m	Shale	Hydrothermal (primary)	12.14	0.06	23.41	0.12			0.15	0.06			409675377	3240776	18335466	
1038-52_4.14	Dixon Island	3.2	DX_98.06-98.07m	Shale	Hydrothermal (primary)	11.43	0.06	22.22	0.29			0.05	0.06			391031660	3092410	17495695	
1038-54_1	Dixon Island	3.2	DX_132.26-132.28m	Shale	Hydrothermal (primary)	3.97	0.05	8.21	0.26			-0.25	0.06			393214838	3083122	17330654	

Title	Formation	Age/ Ga	Drill core	Lithology	Pyrite genesis	$\delta^{33}S$/‰	1σ	$\delta^{34}S$/‰	1σ	$\delta^{36}S$/‰	1σ	$\Delta^{33}S$/ ‰	1σ	$\Delta^{36}S$/ ‰	1σ	Detector $^{32}S^-$ /CPS	Detector $^{33}S^-$ /CPS	Detector $^{34}S^-$ /CPS	Detector $^{36}S^-$ /CPS
1038-54_5.1	Dixon Island	3.2	DX_132.26-132.28m	Shale	Hydrothermal (primary)	3.82	0.05	7.64	0.17			-0.11	0.05			431387270	3382686	19001837	
1038-54_5.2	Dixon Island	3.2	DX_132.26-132.28m	Shale	Hydrothermal (primary)	2.21	0.04	4.18	0.09			0.06	0.05			417372926	3267731	18322236	
1038-54_14	Dixon Island	3.2	DX_134.14-134.15m	Shale	Hydrothermal (primary)	-2.67	0.06	-4.83	0.06			-0.17	0.06			418115713	3257443	18187870	
1038-54_15.1	Dixon Island	3.2	DX_134.14-134.15m	Shale	Hydrothermal (primary)	-2.13	0.05	-3.69	0.05			-0.23	0.06			406115903	3167426	17689842	
1038-54_15.2	Dixon Island	3.2	DX_134.14-134.15m	Shale	Hydrothermal (primary)	-2.63	0.09	-4.91	0.11			-0.09	0.08			356397089	2778279	15504128	
1038-54_21	Dixon Island	3.2	DX_134.14-134.15m	Shale	Hydrothermal (primary)	-4.31	0.07	-7.96	0.09			-0.21	0.07			417647584	3250407	18109208	
1038-54_20	Dixon Island	3.2	DX_134.14-134.15m	Shale	Hydrothermal (primary)	-3.27	0.08	-5.59	0.10			-0.38	0.09			404424322	3151330	17585923	
1038-19	Dixon Island	3.2	DX_134.14-134.15m	Shale	Hydrothermal (primary)	-2.83	0.06	-4.96	0.07			-0.27	0.07			407628950	3177257	17739182	
1038-54_2	Dixon Island	3.2	DX_132.26-132.28m	Shale	Hydrothermal (primary)	3.64	0.05	7.39	0.09			-0.16	0.05			399624484	3134444	17600643	
1038-54_3	Dixon Island	3.2	DX_132.26-132.28m	Shale	Hydrothermal (primary)	4.50	0.06	8.80	0.14			-0.02	0.05			422888360	3320064	18656982	
1038-54_4	Dixon Island	3.2	DX_132.26-132.28m	Shale	Hydrothermal (primary)	0.99	0.04	1.55	0.09			0.19	0.04			379081306	2965079	16595019	
1038-53_1.4	Dixon Island	3.2	DX_92.22-92.26m	Shale	Secondary	2.34	0.01	4.51	0.02	8.48	0.14	0.03	0.02	-0.10	0.15	901776173	7062902	39646410	134535
1038-53_1.16	Dixon Island	3.2	DX_92.22-92.26m	Shale	Secondary	3.40	0.02	6.44	0.05	12.00	0.14	0.08	0.02	-0.28	0.13	954848259	7484353	42043667	142668
1038-24_10	Dixon Island	3.2	DX_126.26-126.31m	Shale	Secondary	4.89	0.05	9.61	0.04			-0.04	0.05			367684662	2887384	16221824	
1038-24_11.1	Dixon Island	3.2	DX_126.26-126.31m	Shale	Secondary	6.75	0.06	13.35	0.07			-0.11	0.06			402937423	3170315	17843210	
1038-24_16	Dixon Island	3.2	DX_126.26-126.31m	Shale	Secondary	6.04	0.05	11.58	0.10			0.09	0.06			402290563	3162302	17791001	
1038-52_2.8	Dixon Island	3.2	DX_126.26-126.31m	Shale	Secondary	5.20	0.10	5.09	0.09			2.58	0.08			386245213	3033957	16982644	
1038-53_3.2	Cleaverville	3	CL1_80.76-80.77m	Shale	Hydrothermal (primary)	22.38	0.13	44.65	0.13			-0.37	0.12			196340509	1568097	8967198	
1038-53_3.4	Cleaverville	3	CL1_80.76-80.77m	Shale	Hydrothermal (primary)	-5.74	0.18	-10.77	0.12			-0.18	0.18			192410110	1493446	8319529	
1038-53_3.2'	Cleaverville	3	CL1_80.76-80.77m	Shale	Hydrothermal (primary)	23.70	0.06	46.43	0.07			0.05	0.07			457107167	3652097	20901575	
1038-53_3.3	Cleaverville	3	CL1_80.76-80.77m	Shale	Hydrothermal (primary)	8.93	0.07	16.95	0.37			0.23	0.07			398668248	3139794	17723632	
1038-53_4.7	Cleaverville	3	CL1_104.99-105.00m	Shale	Hydrothermal (primary)	3.36	0.05	6.09	1.07			0.23	0.05			698379294	5477951	30761993	
1038-53_4.1	Cleaverville	3	CL1_104.99-105.00m	Shale	Hydrothermal (primary) or secondary?	0.04	0.10	0.64	0.25			-0.29	0.10			404564588	3160675	17710048	
1038-53_4.1'	Cleaverville	3	CL1_104.99-105.00m	Shale	Hydrothermal (primary) or secondary?	4.57	0.09	9.25	0.13			-0.18	0.10			400268609	3138936	17659871	
1038-53_4.11	Cleaverville	3	CL1_104.99-105.00m	Shale	Hydrothermal (primary) or secondary?	-0.46	0.13	-1.02	0.31			0.07	0.12			368194119	2876553	16087892	

Title	Formation	Age/ Ga	Drill core	Lithology	Pyrite genesis	$\delta^{33}S$/‰	1σ	$\delta^{34}S$/‰	1σ	$\delta^{36}S$/‰	1σ	$\Delta^{33}S$/ ‰	1σ	$\Delta^{36}S$/ ‰	1σ	Detector $^{32}S^-$ /CPS	Detector $^{33}S^-$ /CPS	Detector $^{34}S^-$ /CPS	Detector $^{36}S^-$ /CPS
1038-24_9	Cleaverville	3	CL1_102.71-102.72m	Shale	Hydrothermal (primary) or secondary?	1.32	0.07	2.44	0.34			0.06	0.07			384338063	3006885	16848238	
M-2_16	Mosquito Creek Formation	2.93	ABDP5_38.35-38.36m	Shale	Diagenetic	7.44	0.04	18.98	0.10	39.40	0.15	-2.29	0.04	3.02	0.16	1456031165	11556150	65248755	233416
M-2_2	Mosquito Creek Formation	2.93	ABDP5_38.35-38.36m	Shale	Diagenetic	7.72	0.02	19.70	0.10	40.62	0.17	-2.37	0.01	2.85	0.16	1269341635	10010591	56494772	209024
M-2_6	Mosquito Creek Formation	2.93	ABDP5_38.35-38.36m	Shale	Diagenetic	7.86	0.02	19.94	0.11	41.82	0.10	-2.36	0.02	3.61	0.10	1539215045	12131558	68767420	253765
M-2_7	Mosquito Creek Formation	2.93	ABDP5_38.35-38.36m	Shale	Diagenetic	7.72	0.02	19.74	0.12	41.27	0.11	-2.40	0.02	3.44	0.12	1560115424	12294317	69680126	256706
M-2_8	Mosquito Creek Formation	2.93	ABDP5_38.35-38.36m	Shale	Diagenetic	8.01	0.01	20.26	0.09	41.79	0.10	-2.38	0.02	2.93	0.11	1614792728	12732574	72184734	266257
M-2_9	Mosquito Creek Formation	2.93	ABDP5_38.35-38.36m	Shale	Diagenetic	8.03	0.02	20.28	0.12	42.02	0.09	-2.36	0.02	3.14	0.12	1520990406	11987544	67966689	250580
M-2_1'	Mosquito Creek Formation	2.93	ABDP5_38.35-38.36m	Shale	Diagenetic	7.87	0.02	19.83	0.34			-2.29	0.02			1138952789	8979636	50654685	
M-2_7	Mosquito Creek Formation	2.93	ABDP5_40.74-40.75m	Shale	Hydrothermally modified diagenetic	5.45	0.02	12.76	0.05	24.10	0.13	-1.11	0.02	-0.29	0.13	1001923567	7871370	44405771	151780
M-2_8	Mosquito Creek Formation	2.93	ABDP5_40.74-40.75m	Shale	Hydrothermally modified diagenetic	6.54	0.02	15.30	0.06	29.26	0.15	-1.31	0.02	-0.01	0.17	980019435	7705814	43534392	149057
M-2_14	Mosquito Creek Formation	2.93	ABDP5_40.74-40.75m	Shale	Hydrothermally modified diagenetic	6.23	0.02	14.39	0.04	27.44	0.10	-1.16	0.02	-0.09	0.11	1030119042	8099747	45732896	156489
M-2_9	Mosquito Creek Formation	2.93	ABDP5_40.74-40.75m	Shale	Hydrothermally modified diagenetic	6.72	0.03	15.28	0.15	29.66	0.19	-1.12	0.03	0.42	0.17	1040017389	8179952	46210632	158274
M-2_1.3	Mosquito Creek Formation	2.93	ABDP5_40.74-40.75m	Shale	Hydrothermally modified diagenetic	5.94	0.02	13.82	0.32			-1.16	0.02			1191560432	9380124	52710623	
M-2_1.2	Mosquito Creek Formation	2.93	ABDP5_40.74-40.75m	Shale	Hydrothermally modified diagenetic	6.83	0.02	15.50	0.18			-1.12	0.02			1073139324	8446098	47456900	
M-2.1	Mosquito Creek Formation	2.93	ABDP5_40.74-40.75m	Shale	Hydrothermally modified diagenetic	6.22	0.11	14.83	0.06			-1.39	0.09			251595149	1980310	11095462	
M-2.3	Mosquito Creek Formation	2.93	ABDP5_40.74-40.75m	Shale	Hydrothermally modified diagenetic	5.59	0.09	13.22	0.05			-1.20	0.09			253733399	1993254	11172812	
M-2.14	Mosquito Creek Formation	2.93	ABDP5_40.74-40.75m	Shale	Hydrothermally modified diagenetic	5.44	0.09	12.78	0.08			-1.13	0.09			251802459	1979217	11081578	
M-2.17	Mosquito Creek Formation	2.93	ABDP5_40.74-40.75m	Shale	Hydrothermally modified diagenetic	4.34	0.09	10.84	0.13			-1.23	0.10			235942530	1854010	10368295	

Title	Formation	Age/ Ga	Drill core	Lithology	Pyrite genesis	$\delta^{33}S$/‰	1σ	$\delta^{34}S$/‰	1σ	$\delta^{36}S$/‰	1σ	$\Delta^{33}S$/ ‰	1σ	$\Delta^{36}S$/ ‰	1σ	Detector $^{32}S^-$ /CPS	Detector $^{33}S^-$ /CPS	Detector $^{34}S^-$ /CPS	Detector $^{36}S^-$ /CPS
M-2_4	Mosquito Creek Formation	2.93	ABDP5_38.35-38.36m	Shale	Secondary	0.84	0.02	1.91	0.12	3.07	0.19	-0.14	0.02	-0.56	0.19	1141754565	8941412	49924687	180973
M-2_4'	Mosquito Creek Formation	2.93	ABDP5_38.35-38.36m	Shale	Secondary	0.67	0.02	1.63	0.27			-0.17	0.03			1083886994	8477167	47272214	
M-2_4"	Mosquito Creek Formation	2.93	ABDP5_38.35-38.36m	Shale	Secondary	1.12	0.02	2.26	0.21			-0.05	0.02			1117366867	8750451	48833796	
M-2.17"	Mosquito Creek Formation	2.93	ABDP5_40.74-40.75m	Shale	Secondary	0.03	0.13	0.61	0.08			-0.28	0.12			227337437	1775419	9883978	
M-2.17"''	Mosquito Creek Formation	2.93	ABDP5_40.74-40.75m	Shale	Secondary	0.05	0.11	0.88	0.06			-0.40	0.11			231053667	1805025	10046735	
1038-35_5	Mt. Roe Basalt	2.78	ABDP6_93.43-93.44m	Shale	Diagenetic	1.76	0.02	3.66	0.09	5.70	0.14	-0.12	0.02	-1.26	0.12	1301017567	10187003	57188431	193530
1038-35_8.1	Mt. Roe Basalt	2.78	ABDP6_93.43-93.44m	Shale	Diagenetic	-0.87	0.02	-2.02	0.13	-5.14	0.12	0.16	0.02	-1.31	0.13	1255129969	9798950	54758683	184309
1038-35_8.3	Mt. Roe Basalt	2.78	ABDP6_93.43-93.44m	Shale	Diagenetic	-0.60	0.02	-1.35	0.06	-3.90	0.11	0.10	0.02	-1.33	0.11	1297481279	10130500	56618936	190865
1038-35_11.1	Mt. Roe Basalt	2.78	ABDP6_261.63-261.64m	Shale	Diagenetic?	-0.42	0.03	-2.11	0.04			0.67	0.03			428640352	3348093	18698646	
1038-35_11.2	Mt. Roe Basalt	2.78	ABDP6_261.63-261.64m	Shale	Diagenetic?	-0.65	0.05	-2.66	0.05			0.72	0.05			414269660	3235940	18065103	
M-1_10	Mt. Roe Basalt	2.78	ABDP6_101.40-101.42m	Shale	Diagenetic	-2.86	0.09	-4.62	0.18			-0.48	0.10			852742801	6640217	37174663	
M-1_36.7	Mt. Roe Basalt	2.78	ABDP6_101.21-101.22m	Shale	Diagenetic?	-0.43	0.02	-0.67	0.05	-2.59	0.16	-0.09	0.02	-1.32	0.17	1138696679	8889889	49771236	167860
1038-35_1	Mt. Roe Basalt	2.78	ABDP6_93.43-93.44m	Shale	Hydrothermally modified diagenetic	-0.71	0.02	-1.28	0.05	-3.66	0.09	-0.05	0.02	-1.23	0.10	1352674204	10567678	59191813	199560
1038-35_1'	Mt. Roe Basalt	2.78	ABDP6_93.43-93.44m	Shale	Hydrothermally modified diagenetic	-1.21	0.02	-2.14	0.06	-5.23	0.11	-0.11	0.02	-1.17	0.10	1322030154	10318370	57769367	194902
1038-35_8.2	Mt. Roe Basalt	2.78	ABDP6_93.43-93.44m	Shale	Hydrothermally modified diagenetic	-1.11	0.02	-2.17	0.07	-5.43	0.12	0.00	0.02	-1.31	0.12	1323506136	10328589	57725135	194439
1038-35_8.4	Mt. Roe Basalt	2.78	ABDP6_93.43-93.44m	Shale	Hydrothermally modified diagenetic	-1.21	0.02	-2.49	0.13	-5.99	0.12	0.08	0.02	-1.26	0.11	1268298587	9898489	55291634	185967
1038-35_8.5	Mt. Roe Basalt	2.78	ABDP6_93.43-93.44m	Shale	Hydrothermally modified diagenetic	-0.75	0.03	-1.62	0.06	-4.58	0.13	0.08	0.02	-1.51	0.14	1264492669	9873383	55193180	186014
1038-35_2.1	Mt. Roe Basalt	2.78	ABDP6_93.43-93.44m	Shale	Hydrothermally modified diagenetic	-1.00	0.02	-2.12	0.11	-5.23	0.14	0.09	0.02	-1.21	0.14	1379359598	10766242	60167666	202580
1038-35_2.2	Mt. Roe Basalt	2.78	ABDP6_93.43-93.44m	Shale	Hydrothermally modified diagenetic	-0.65	0.02	-1.64	0.09	-4.37	0.12	0.20	0.02	-1.25	0.12	1338436528	10451592	58413729	196773

Title	Formation	Age/ Ga	Drill core	Lithology	Pyrite genesis	$\delta^{33}S$/‰	1σ	$\delta^{34}S$/‰	1σ	$\delta^{36}S$/‰	1σ	$\Delta^{33}S$/ ‰	1σ	$\Delta^{36}S$/ ‰	1σ	Detector $^{32}S^-$ /CPS	Detector $^{33}S^-$ /CPS	Detector $^{34}S^-$ /CPS	Detector $^{36}S^-$ /CPS
M-13_36.9	Mt. Roe Basalt	2.78	ABDP6_115.80-115.81m	Shale	Hydrothermally modified diagenetic	-3.75	0.03	-6.89	0.06	-14.46	0.18	-0.20	0.03	-1.41	0.17	859877183	6693021	37384931	125202
1038-46_9.1	Mt. Roe Basalt	2.78	ABDP6_265.80-265.83m	Shale	Hydrothermally modified diagenetic	-5.99	0.03	-8.52	0.05	-16.62	0.17	-1.59	0.04	-0.49	0.17	657424768	5108222	28557202	95709
1038-46_9.2	Mt. Roe Basalt	2.78	ABDP6_265.80-265.83m	Shale	Hydrothermally modified diagenetic	-5.52	0.03	-8.31	0.07	-16.34	0.20	-1.23	0.03	-0.61	0.18	660905216	5136077	28701096	96094
1038-46_10.1	Mt. Roe Basalt	2.78	ABDP6_265.80-265.83m	Shale	Hydrothermally modified diagenetic	-3.97	0.02	-6.64	0.07	-13.62	0.14	-0.55	0.02	-1.05	0.14	1094375084	8520485	47619901	159834
1038-46_11.1	Mt. Roe Basalt	2.78	ABDP6_265.80-265.83m	Shale	Hydrothermally modified diagenetic	-3.46	0.02	-6.11	0.05	-13.14	0.12	-0.31	0.02	-1.56	0.13	1101657962	8582973	47967511	161092
1038-46_15.1	Mt. Roe Basalt	2.78	ABDP6_265.80-265.83m	Shale	Hydrothermally modified diagenetic	-6.64	0.02	-8.77	0.03	-16.12	0.14	-2.11	0.02	0.49	0.13	1067640571	8290352	46362804	155436
1038-46_12.1	Mt. Roe Basalt	2.78	ABDP6_265.80-265.83m	Shale	Hydrothermally modified diagenetic	-5.15	0.02	-7.67	0.07	-14.90	0.09	-1.19	0.02	-0.38	0.11	1082637006	8417519	47046899	157693
1038-46_12.2	Mt. Roe Basalt	2.78	ABDP6_265.80-265.83m	Shale	Hydrothermally modified diagenetic	-4.64	0.02	-7.28	0.08	-14.75	0.15	-0.88	0.02	-0.97	0.14	1107157776	8613853	48133923	161620
1038-46_12.3	Mt. Roe Basalt	2.78	ABDP6_265.80-265.83m	Shale	Hydrothermally modified diagenetic	-4.99	0.02	-7.69	0.04	-15.15	0.14	-1.02	0.02	-0.59	0.15	1164136493	9054275	50605742	169607
1038-46_13.1	Mt. Roe Basalt	2.78	ABDP6_265.80-265.83m	Shale	Hydrothermally modified diagenetic	-3.67	0.02	-6.09	0.07	-12.93	0.12	-0.53	0.02	-1.40	0.12	1155081736	8992627	50263167	168763
1038-46_13.2	Mt. Roe Basalt	2.78	ABDP6_265.80-265.83m	Shale	Hydrothermally modified diagenetic	-4.06	0.02	-6.38	0.06	-12.66	0.13	-0.76	0.02	-0.57	0.13	1172854264	9130840	51037710	171371
1038-46_13.3	Mt. Roe Basalt	2.78	ABDP6_265.80-265.83m	Shale	Hydrothermally modified diagenetic	-3.57	0.02	-6.04	0.08	-12.60	0.10	-0.46	0.02	-1.15	0.11	1160658324	9039046	50521533	169638
1038-46_14.1	Mt. Roe Basalt	2.78	ABDP6_265.80-265.83m	Shale	Hydrothermally modified diagenetic	-4.20	0.02	-6.81	0.07	-14.48	0.17	-0.68	0.02	-1.57	0.16	965517213	7514001	41993818	140580
1038-46_15.2	Mt. Roe Basalt	2.78	ABDP6_265.80-265.83m	Shale	Hydrothermally modified diagenetic	-3.79	0.03	-6.42	0.05	-13.15	0.17	-0.48	0.03	-1.00	0.17	1013571805	7892502	44114036	148033
M-1_1	Mt. Roe Basalt	2.78	ABDP6_101.40-101.42m	Shale	Hydrothermally modified diagenetic	-1.31	0.04	-2.38	0.08			-0.09	0.04			802225460	6258505	35050337	
M-1_11	Mt. Roe Basalt	2.78	ABDP6_101.40-101.42m	Shale	Hydrothermally modified diagenetic	-2.25	0.10	-4.17	0.14			-0.10	0.09			867806421	6762184	37849284	
M-1_17	Mt. Roe Basalt	2.78	ABDP6_101.40-101.42m	Shale	Hydrothermally modified diagenetic	-1.47	0.08	-2.54	0.06			-0.17	0.09			867316649	6761200	37881560	
M-1_18	Mt. Roe Basalt	2.78	ABDP6_101.40-101.42m	Shale	Hydrothermally modified diagenetic	-1.23	0.06	-2.21	0.12			-0.09	0.06			797649084	6220800	34841642	

Title	Formation	Age/ Ga	Drill core	Lithology	Pyrite genesis	$\delta^{33}S$/‰	1σ	$\delta^{34}S$/‰	1σ	$\delta^{36}S$/‰	1σ	$\Delta^{33}S$/ ‰	1σ	$\Delta^{36}S$/ ‰	1σ	Detector $^{32}S^-$ /CPS	Detector $^{33}S^-$ /CPS	Detector $^{34}S^-$ /CPS	Detector $^{36}S^-$ /CPS
M-1_8	Mt. Roe Basalt	2.78	ABDP6_101.40-101.42m	Shale	Secondary?	-1.05	0.06	-2.01	0.11			-0.01	0.05			840689919	6558786	36741576	
M-1_7'	Mt. Roe Basalt	2.78	ABDP6_101.40-101.42m	Shale	Secondary	-0.76	0.07	-2.35	0.07			0.45	0.07			858331945	6698551	37501353	
M-1_3	Mt. Roe Basalt	2.78	ABDP6_101.40-101.42m	Shale	Secondary	-0.85	0.05	-2.44	0.10			0.41	0.05			898195536	7008245	39249427	
M-13_36.1	Mt. Roe Basalt	2.78	ABDP6_101.40-101.42m	Shale	Secondary	-2.77	0.02	-5.09	0.05	-10.17	0.17	-0.14	0.02	-0.51	0.15	888090466	6922000	38685631	130041
M-13_36.2	Mt. Roe Basalt	2.78	ABDP6_101.40-101.42m	Shale	Secondary	-2.91	0.02	-5.14	0.04	-10.46	0.16	-0.26	0.02	-0.72	0.16	893608238	6964621	38929809	130751
M-13_36.4	Mt. Roe Basalt	2.78	ABDP6_101.40-101.42m	Shale	Secondary	-2.91	0.03	-5.09	0.05	-9.96	0.14	-0.29	0.03	-0.32	0.14	842466333	6564442	36689104	123303
M-13_36.6	Mt. Roe Basalt	2.78	ABDP6_101.40-101.42m	Shale	Secondary	-2.90	0.03	-5.44	0.07	-10.77	0.15	-0.10	0.03	-0.46	0.14	866227471	6747834	37704644	126585
M-13_36.8	Mt. Roe Basalt	2.78	ABDP6_115.80-115.81m	Shale	Secondary?	-3.25	0.03	-7.65	0.05	-16.38	0.17	0.70	0.02	-1.89	0.17	823121478	6410938	35753767	119567
M-1_36.4	Mt. Roe Basalt	2.78	ABDP6_115.80-115.81m	Shale	Secondary	-3.40	0.02	-7.83	0.08	-16.97	0.13	0.64	0.02	-2.15	0.13	1117196196	8696057	48481571	162270
M-1_36.2	Mt. Roe Basalt	2.78	ABDP6_115.80-115.81m	Shale	Secondary	-2.75	0.02	-6.36	0.04	-14.02	0.09	0.53	0.02	-1.96	0.09	1215402694	9464106	52803298	176964
M-1_36.1	Mt. Roe Basalt	2.78	ABDP6_115.80-115.81m	Shale	Secondary	0.27	0.02	-1.81	0.10	-5.37	0.18	1.21	0.02	-1.94	0.16	1016328202	7938571	44347128	149137
1038-35_10.1	Mt. Roe Basalt	2.78	ABDP6_261.63-261.64m	Shale	Secondary	1.00	0.07	-1.59	0.05			1.82	0.08			383665142	3001894	16746639	
1038-35_15.1	Mt. Roe Basalt	2.78	ABDP6_261.63-261.64m	Shale	Secondary	0.85	0.05	-2.15	0.08			1.95	0.05			391612031	3062463	17091077	
1038-35_15.2	Mt. Roe Basalt	2.78	ABDP6_261.63-261.64m	Shale	Secondary	0.57	0.04	-2.77	0.12			1.99	0.04			381270872	2982033	16637343	
1038-35_14.1	Mt. Roe Basalt	2.78	ABDP6_261.63-261.64m	Shale	Secondary	-0.65	0.06	-2.78	0.08			0.78	0.05			421997371	3296640	18403637	
1038-35_14.2	Mt. Roe Basalt	2.78	ABDP6_261.63-261.64m	Shale	Secondary	-1.59	0.09	-4.08	0.06			0.51	0.08			401526764	3134299	17482971	
1038-46_2.1	Mt. Roe Basalt	2.78	ABDP6_129.64-129.66m	Hydrothermally altered basalt	Secondary	-1.17	0.02	-2.22	0.06	-4.90	0.13	-0.03	0.02	-0.69	0.14	1121673341	8756956	49028448	165186
1038-46_1.1	Mt. Roe Basalt	2.78	ABDP6_129.64-129.66m	Hydrothermally altered basalt	Secondary	-1.61	0.02	-3.10	0.08	-6.87	0.14	-0.01	0.02	-1.00	0.12	1053244793	8220288	46006056	155013

Title	Formation	Age/ Ga	Drill core	Lithology	Pyrite genesis	$\delta^{33}S$/‰	1σ	$\delta^{34}S$/‰	1σ	$\delta^{36}S$/‰	1σ	$\Delta^{33}S$/ ‰	1σ	$\Delta^{36}S$/ ‰	1σ	Detector $^{32}S^-$ /CPS	Detector $^{33}S^-$ /CPS	Detector $^{34}S^-$ /CPS	Detector $^{36}S^-$ /CPS
1038-46_1.2	Mt. Roe Basalt	2.78	ABDP6_129.64-129.66m	Hydrothermally altered basalt	Secondary	-1.26	0.02	-2.50	0.06	-5.65	0.13	0.03	0.02	-0.90	0.15	1076622672	8403200	47025645	158457
1038-46_6.1	Mt. Roe Basalt	2.78	ABDP6_128.97-128.99m	Hydrothermally altered basalt	Secondary	-1.22	0.03	-2.42	0.06	-5.23	0.16	0.03	0.03	-0.63	0.14	972135480	7591693	42494170	143250
1038-46_8.1	Mt. Roe Basalt	2.78	ABDP6_128.97-128.99m	Hydrothermally altered basalt	Secondary	-1.22	0.03	-2.46	0.05	-5.69	0.15	0.04	0.03	-1.03	0.14	960949496	7500068	41983439	141239
1038-46_8.2	Mt. Roe Basalt	2.78	ABDP6_128.97-128.99m	Hydrothermally altered basalt	Secondary	-0.33	0.02	-0.68	0.05	-2.02	0.15	0.02	0.02	-0.73	0.15	953105362	7448201	41713155	140771
1038-46_1.3	Mt. Roe Basalt	2.78	ABDP6_129.64-129.66m	Hydrothermally altered basalt	Secondary	-1.02	0.02	-2.01	0.05	-4.40	0.14	0.02	0.02	-0.58	0.14	1186757038	9263955	51857024	174787
1038-46_5.1	Mt. Roe Basalt	2.78	ABDP6_129.64-129.66m	Hydrothermally altered basalt	Secondary	-1.72	0.05	-3.49	0.04			0.08	0.05			399184582	3114429	17391981	
1038-46_5.2	Mt. Roe Basalt	2.78	ABDP6_129.64-129.66m	Hydrothermally altered basalt	Secondary	-1.63	0.07	-3.34	0.10			0.09	0.06			371055592	2896408	16175062	
1038-46_5.3	Mt. Roe Basalt	2.78	ABDP6_129.64-129.66m	Hydrothermally altered basalt	Secondary	-1.94	0.07	-3.91	0.11			0.07	0.07			363135378	2833203	15816577	
1038-46_4.1	Mt. Roe Basalt	2.78	ABDP6_129.64-129.66m	Hydrothermally altered basalt	Secondary	-2.02	0.07	-4.22	0.06			0.16	0.07			357362412	2787083	15565154	
1038-46_4.2	Mt. Roe Basalt	2.78	ABDP6_129.64-129.66m	Hydrothermally altered basalt	Secondary	-1.84	0.06	-3.78	0.07			0.11	0.06			360814929	2815294	15721054	
1038-46_4.3	Mt. Roe Basalt	2.78	ABDP6_129.64-129.66m	Hydrothermally altered basalt	Secondary	-2.20	0.04	-3.83	0.08			-0.22	0.05			366395850	2858783	15962339	
1038-46_4.4	Mt. Roe Basalt	2.78	ABDP6_129.64-129.66m	Hydrothermally altered basalt	Secondary	-2.23	0.07	-3.95	0.07			-0.19	0.07			377930250	2947985	16458411	
1038-46_3.1	Mt. Roe Basalt	2.78	ABDP6_129.64-129.66m	Hydrothermally altered basalt	Secondary	-1.39	0.08	-2.86	0.07			0.08	0.08			402305584	3138111	17539558	
1801M-14_2	Hardey Formation	2.76	FVG1_1843.86-1843.87m	Ooidal sandstone	Earlier stage. Detrital or diagenetic	-0.82	0.10	-1.70	0.11			0.05	0.11			231137052	1805250	10025845	
1801M-14_3	Hardey Formation	2.76	FVG1_1843.86-1843.87m	Ooidal sandstone	Earlier stage. Detrital or diagenetic	17.11	0.09	34.20	0.05			-0.36	0.09			228558017	1816565	10271224	
1801M-14_7	Hardey Formation	2.76	FVG1_1843.86-1843.87m	Ooidal sandstone	Earlier stage. Detrital or diagenetic	0.08	0.10	0.12	0.11			0.02	0.11			229266367	1792824	9964439	
1801M-14_11	Hardey Formation	2.76	FVG1_1843.86-1843.87m	Ooidal sandstone	Earlier stage. Detrital or diagenetic	4.18	0.11	7.91	0.08			0.11	0.10			213609330	1674772	9349092	
1801M-14_12	Hardey Formation	2.76	FVG1_1843.86-1843.87m	Ooidal sandstone	Earlier stage. Detrital or diagenetic	6.91	0.09	13.39	0.09			0.04	0.09			213021405	1677474	9380399	

Title	Formation	Age/ Ga	Drill core	Lithology	Pyrite genesis	$\delta^{33}S$/‰	1σ	$\delta^{34}S$/‰	1σ	$\delta^{36}S$/‰	1σ	$\Delta^{33}S$/ ‰	1σ	$\Delta^{36}S$/ ‰	1σ	Detector $^{32}S^-$ /CPS	Detector $^{33}S^-$ /CPS	Detector $^{34}S^-$ /CPS	Detector $^{36}S^-$ /CPS
1801M-14_9	Hardey Formation	2.76	FVG1_1843.86-1843.87m	Ooidal sandstone	Earlier stage. Detrital or diagenetic	1.32	0.09	1.99	0.04			0.29	0.10			220390763	1723017	9589849	
1801M-14_8	Hardey Formation	2.76	FVG1_1843.86-1843.87m	Ooidal sandstone	Earlier stage. Detrital or diagenetic	0.20	0.08	1.03	0.12			-0.33	0.08			233998748	1830485	10178598	
M-9_5	Hardey Formation	2.76	FVG1_1843.86-1843.87m	Ooidal sandstone	Earlier stage. Detrital or diagenetic	1.26	0.02	1.92	0.14	3.40	0.17	0.27	0.02	-0.25	0.18	1275621304	10057588	56014410	196349
1038-26_11	Hardey Formation	2.76	ABDP3_115.680-115.682m	Shale	Hydrothermally modified diagenetic	-1.39	0.09	-3.25	0.15			0.28	0.09			403671934	3149410	17594283	
1038-26_7	Hardey Formation	2.76	ABDP3_114.060-114.061m	Shale	Hydrothermally modified diagenetic	-0.27	0.07	-1.26	0.05			0.37	0.07			412884312	3221056	18012590	
1038-26_8	Hardey Formation	2.76	ABDP3_114.060-114.061m	Shale	Hydrothermally modified diagenetic	-0.35	0.07	-1.50	0.07			0.42	0.06			413456592	3225279	18040384	
1038-26_5	Hardey Formation	2.76	ABDP3_114.060-114.061m	Shale	Hydrothermally modified diagenetic	-1.06	0.07	-2.08	0.06			0.01	0.07			413804921	3226302	18042721	
1038-26_4	Hardey Formation	2.76	ABDP3_114.060-114.061m	Shale	Hydrothermally modified diagenetic	-0.77	0.05	-1.83	0.11			0.17	0.06			402351666	3138824	17549587	
1038-26_1	Hardey Formation	2.76	ABDP3_114.060-114.061m	Shale	Hydrothermally modified diagenetic	-0.20	0.05	-1.17	0.13			0.40	0.06			401233789	3130431	17505375	
1038-26_10	Hardey Formation	2.76	ABDP3_115.680-115.682m	Shale	Hydrothermally modified diagenetic	-2.36	0.06	-4.90	0.10			0.17	0.06			435669768	3393693	18952256	
1038-26_2	Hardey Formation	2.76	ABDP3_114.060-114.061m	Shale	Secondary	-1.10	0.09	-2.82	0.16			0.35	0.08			408580306	3188206	17815127	
1801M-14_4	Hardey Formation	2.76	FVG1_1843.86-1843.87m	Ooidal sandstone	Secondary	17.94	0.11	36.13	0.08			-0.51	0.10			224180787	1782108	10089149	
1801M-14_12'	Hardey Formation	2.76	FVG1_1843.86-1843.87m	Ooidal sandstone	Secondary	0.26	0.12	0.67	0.06			-0.08	0.13			205227510	1604147	8923310	
M-3_H3.1	Tumbiana Formation	2.72	PDP1_44.33-44.34m	Shale	Diagenetic	-5.88	0.09	-12.49	0.46			0.57	0.08			888979121	6899200	38431861	
M-3_1	Tumbiana Formation	2.72	PDP1_43.15-43.16m	Shale	Diagenetic	-11.31	0.04	-22.57	0.12			0.38	0.05			859509269	6637561	36796261	
M-3_2	Tumbiana Formation	2.72	PDP1_43.15-43.16m	Shale	Diagenetic	-11.17	0.06	-22.32	0.08			0.39	0.07			823740068	6362696	35275065	
M-3_3	Tumbiana Formation	2.72	PDP1_43.15-43.16m	Shale	Diagenetic	-8.20	0.04	-16.09	0.12			0.12	0.04			815280525	6312107	35115489	
M-3_4	Tumbiana Formation	2.72	PDP1_43.15-43.16m	Shale	Diagenetic	-11.84	0.09	-23.90	0.25			0.55	0.10			871353038	6723325	37233478	

Title	Formation	Age/ Ga	Drill core	Lithology	Pyrite genesis	$\delta^{33}S$/‰	1σ	$\delta^{34}S$/‰	1σ	$\delta^{36}S$/‰	1σ	$\Delta^{33}S$/ ‰	1σ	$\Delta^{36}S$/ ‰	1σ	Detector $^{32}S^-$ /CPS	Detector $^{33}S^-$ /CPS	Detector $^{34}S^-$ /CPS	Detector $^{36}S^-$ /CPS
M-3_5	Tumbiana Formation	2.72	PDP1_43.15-43.16m	Shale	Diagenetic	-12.61	0.05	-25.25	0.04			0.47	0.06			847838739	6536304	36180150	
M-3_6	Tumbiana Formation	2.72	PDP1_43.15-43.16m	Shale	Diagenetic	-12.33	0.06	-24.43	0.23			0.32	0.06			852427277	6571792	36391555	
M-3_7	Tumbiana Formation	2.72	PDP1_43.15-43.16m	Shale	Diagenetic	-10.36	0.05	-20.46	0.05			0.23	0.05			849040983	6561014	36414620	
M-3_8	Tumbiana Formation	2.72	PDP1_43.15-43.16m	Shale	Diagenetic	-9.21	0.07	-18.23	0.17			0.21	0.06			873035050	6754007	37548325	
M-3_9	Tumbiana Formation	2.72	PDP1_43.15-43.16m	Shale	Diagenetic	-12.15	0.05	-24.68	0.21			0.64	0.05			869133087	6704909	37119293	
M-3_10	Tumbiana Formation	2.72	PDP1_43.15-43.16m	Shale	Diagenetic	-11.27	0.07	-22.38	0.13			0.32	0.07			863907661	6670942	36989061	
M-3_11	Tumbiana Formation	2.72	PDP1_43.15-43.16m	Shale	Diagenetic	-11.10	0.06	-22.47	0.08			0.54	0.06			881354288	6807378	37728706	
M-3_12	Tumbiana Formation	2.72	PDP1_43.15-43.16m	Shale	Diagenetic	-4.97	0.04	-10.89	0.05			0.65	0.05			862762913	6702882	37359269	
M-3_13	Tumbiana Formation	2.72	PDP1_43.15-43.16m	Shale	Diagenetic	-5.66	0.04	-11.90	0.29			0.48	0.04			864147974	6709823	37386377	
M-3_14	Tumbiana Formation	2.72	PDP1_43.15-43.16m	Shale	Diagenetic	-5.58	0.05	-11.60	0.06			0.41	0.05			903059652	7010007	39079685	
M-3_15	Tumbiana Formation	2.72	PDP1_43.15-43.16m	Shale	Diagenetic	-6.57	0.06	-13.86	0.17			0.59	0.06			896762423	6960763	38744182	
M-3_16	Tumbiana Formation	2.72	PDP1_43.15-43.16m	Shale	Diagenetic	-1.44	0.07	-4.23	0.26			0.73	0.06			867289430	6760217	37812079	
M-3_17	Tumbiana Formation	2.72	PDP1_43.15-43.16m	Shale	Diagenetic	-4.19	0.08	-8.94	0.02			0.43	0.08			885719141	6888266	38436396	
M-3_18	Tumbiana Formation	2.72	PDP1_43.15-43.16m	Shale	Diagenetic	-1.09	0.06	-3.60	0.07			0.77	0.05			850127161	6630049	37091197	
M-3_19	Tumbiana Formation	2.72	PDP1_43.15-43.16m	Shale	Diagenetic	-11.96	0.05	-23.96	0.04			0.45	0.05			901027252	6951005	38505977	
M-3_20	Tumbiana Formation	2.72	PDP1_43.15-43.16m	Shale	Diagenetic	-2.55	0.05	-4.96	0.07			0.00	0.05			873041081	6799925	38043636	
M-3_21	Tumbiana Formation	2.72	PDP1_43.15-43.16m	Shale	Diagenetic	-1.84	0.05	-4.96	0.04			0.72	0.05			868879592	6773577	37865872	
M-3_22	Tumbiana Formation	2.72	PDP1_43.15-43.16m	Shale	Diagenetic	-4.39	0.04	-9.54	0.14			0.53	0.04			903265502	7022268	39173973	

Title	Formation	Age/ Ga	Drill core	Lithology	Pyrite genesis	$\delta^{33}S$/‰	1σ	$\delta^{34}S$/‰	1σ	$\delta^{36}S$/‰	1σ	$\Delta^{33}S$/ ‰	1σ	$\Delta^{36}S$/ ‰	1σ	Detector $^{32}S^-$ /CPS	Detector $^{33}S^-$ /CPS	Detector $^{34}S^-$ /CPS	Detector $^{36}S^-$ /CPS
M-3_23	Tumbiana Formation	2.72	PDP1_43.15-43.16m	Shale	Diagenetic	-4.97	0.07	-10.93	0.04			0.68	0.07			882181073	6854700	38209710	
M-3_24	Tumbiana Formation	2.72	PDP1_43.15-43.16m	Shale	Diagenetic	-5.39	0.05	-11.73	0.10			0.67	0.05			878271781	6823096	38011552	
M-3_25	Tumbiana Formation	2.72	PDP1_43.15-43.16m	Shale	Diagenetic	1.86	0.07	2.70	0.13			0.48	0.07			880881042	6892215	38693266	
M-3_26	Tumbiana Formation	2.72	PDP1_43.15-43.16m	Shale	Diagenetic	-2.27	0.05	-5.57	0.12			0.60	0.06			887259680	6914015	38636083	
M-3_27	Tumbiana Formation	2.72	PDP1_43.15-43.16m	Shale	Diagenetic	-1.54	0.06	-3.35	0.41			0.18	0.07			875868031	6827944	38226942	
M-3_28	Tumbiana Formation	2.72	PDP1_43.15-43.16m	Shale	Diagenetic	-3.27	0.08	-7.82	0.06			0.76	0.08			905019656	7045388	39328368	
M-3_29	Tumbiana Formation	2.72	PDP1_43.15-43.16m	Shale	Diagenetic	-1.01	0.04	-3.33	0.09			0.71	0.05			873288190	6813241	38120290	
M-3_30	Tumbiana Formation	2.72	PDP1_43.15-43.16m	Shale	Diagenetic	-2.35	0.09	-5.53	0.24			0.50	0.09			883103858	6878441	38466154	
M-3_31	Tumbiana Formation	2.72	PDP1_43.15-43.16m	Shale	Diagenetic	-5.68	0.05	-12.06	0.07			0.54	0.05			902884416	7010060	39061028	
M-3_32	Tumbiana Formation	2.72	PDP1_43.15-43.16m	Shale	Diagenetic	-10.78	0.06	-22.11	0.18			0.67	0.06			875556665	6767105	37502259	
M-3_33	Tumbiana Formation	2.72	PDP1_43.15-43.16m	Shale	Diagenetic	-7.23	0.05	-14.17	0.17			0.09	0.05			891858175	6913190	38487759	
M-3_34	Tumbiana Formation	2.72	PDP1_43.15-43.16m	Shale	Diagenetic	-2.13	0.05	-5.32	0.10			0.61	0.05			887701389	6914596	38659243	
M-3_35	Tumbiana Formation	2.72	PDP1_43.15-43.16m	Shale	Diagenetic	1.83	0.11	2.10	0.18			0.75	0.10			880169819	6885469	38629735	
M-3.1	Tumbiana Formation	2.72	PDP1_43.15-43.16m	Shale	Diagenetic	-2.26	0.02	-5.37	0.09	-11.66	0.10	0.51	0.02	-1.49	0.11	1558683013	12160375	67914768	243292
M-3.2	Tumbiana Formation	2.72	PDP1_43.15-43.16m	Shale	Diagenetic	-0.78	0.02	-1.74	0.35	-4.10	0.12	0.12	0.01	-0.80	0.13	1499532775	11716488	65556751	235917
M-3.4	Tumbiana Formation	2.72	PDP1_43.15-43.16m	Shale	Diagenetic	-11.59	0.03	-23.39	0.06	-45.69	0.11	0.52	0.03	-1.72	0.11	1584832705	12245425	67750198	238837
M-3.5	Tumbiana Formation	2.72	PDP1_43.15-43.16m	Shale	Diagenetic	-2.32	0.01	-5.68	0.12	-12.19	0.09	0.61	0.02	-1.43	0.09	1510105507	11780743	65758520	235761
M-3.6	Tumbiana Formation	2.72	PDP1_43.15-43.16m	Shale	Diagenetic	-9.76	0.02	-19.94	0.12	-39.04	0.12	0.56	0.02	-1.49	0.11	1521053289	11772919	65222465	230894

Title	Formation	Age/ Ga	Drill core	Lithology	Pyrite genesis	$\delta^{33}S$/‰	1σ	$\delta^{34}S$/‰	1σ	$\delta^{36}S$/‰	1σ	$\Delta^{33}S$/ ‰	1σ	$\Delta^{36}S$/ ‰	1σ	Detector $^{32}S^-$ /CPS	Detector $^{33}S^-$ /CPS	Detector $^{34}S^-$ /CPS	Detector $^{36}S^-$ /CPS
M-3.7	Tumbiana Formation	2.72	PDP1_43.15-43.16m	Shale	Diagenetic	-10.80	0.02	-21.89	0.23	-42.93	0.14	0.54	0.02	-1.76	0.13	1485029903	11491623	63668644	225216
M-3.8	Tumbiana Formation	2.72	PDP1_43.15-43.16m	Shale	Diagenetic	-3.76	0.03	-8.34	0.04	-17.37	0.10	0.54	0.03	-1.58	0.10	1497813449	11668906	65073769	232871
M-3.9	Tumbiana Formation	2.72	PDP1_43.15-43.16m	Shale	Diagenetic	-11.44	0.02	-23.20	0.04	-45.19	0.13	0.57	0.03	-1.57	0.10	1549228404	11974771	66270425	233841
M-3.10	Tumbiana Formation	2.72	PDP1_43.15-43.16m	Shale	Diagenetic	-2.76	0.02	-6.71	0.15	-14.06	0.13	0.70	0.02	-1.34	0.11	1539545653	12005461	66981388	240066
M-3.11	Tumbiana Formation	2.72	PDP1_43.15-43.16m	Shale	Diagenetic	-2.23	0.02	-5.37	0.03	-12.13	0.10	0.54	0.02	-1.95	0.10	1526029939	11907914	66493538	238409
M-3.12	Tumbiana Formation	2.72	PDP1_43.15-43.16m	Shale	Diagenetic	-5.24	0.02	-11.03	0.09	-22.29	0.10	0.45	0.02	-1.44	0.10	1565919441	12181790	67845984	242281
M-3.13	Tumbiana Formation	2.72	PDP1_43.15-43.16m	Shale	Diagenetic	-5.13	0.02	-10.98	0.08	-22.25	0.12	0.54	0.02	-1.49	0.11	1555486271	12097617	67367672	240361
M-3.14	Tumbiana Formation	2.72	PDP1_43.15-43.16m	Shale	Diagenetic	-1.46	0.01	-3.14	0.30	-7.08	0.11	0.16	0.01	-1.13	0.11	1553726858	12133571	67850468	244128
M-3.16	Tumbiana Formation	2.72	PDP1_43.15-43.16m	Shale	Diagenetic	-2.61	0.02	-6.18	0.08	-13.35	0.11	0.58	0.02	-1.63	0.10	1606413460	12525419	69905112	250498
M-3.17	Tumbiana Formation	2.72	PDP1_43.15-43.16m	Shale	Diagenetic	1.38	0.02	1.36	0.05	1.41	0.12	0.68	0.02	-1.17	0.13	1578350774	12360127	69230946	250216
M-3.18	Tumbiana Formation	2.72	PDP1_43.15-43.16m	Shale	Diagenetic	-5.30	0.02	-11.27	0.17	-22.65	0.11	0.52	0.02	-1.35	0.12	1604416193	12479992	69495898	248133
M-3.19	Tumbiana Formation	2.72	PDP1_43.15-43.16m	Shale	Diagenetic	-3.24	0.02	-6.82	0.15	-13.78	0.07	0.28	0.02	-0.87	0.08	1542672983	12023312	67097133	240369
M-3.20	Tumbiana Formation	2.72	PDP1_43.15-43.16m	Shale	Diagenetic	-1.92	0.01	-5.00	0.13	-11.02	0.12	0.66	0.01	-1.55	0.13	1600747281	12495560	69774492	250510
M-3.21	Tumbiana Formation	2.72	PDP1_43.15-43.16m	Shale	Diagenetic	-3.73	0.01	-7.96	0.14	-16.02	0.13	0.38	0.01	-0.96	0.12	1564602344	12188570	67982975	243467
M-3.22	Tumbiana Formation	2.72	PDP1_43.15-43.16m	Shale	Diagenetic	-5.92	0.02	-12.25	0.24	-24.71	0.11	0.41	0.02	-1.56	0.11	1589023776	12352206	68746451	245088
M-3.23	Tumbiana Formation	2.72	PDP1_43.15-43.16m	Shale	Diagenetic	-1.94	0.01	-4.98	0.07	-10.70	0.09	0.63	0.01	-1.27	0.09	1641033291	12806063	71516527	256747
M-3.24	Tumbiana Formation	2.72	PDP1_43.15-43.16m	Shale	Diagenetic	-10.24	0.02	-20.11	0.26	-39.03	0.10	0.17	0.02	-1.16	0.12	1637248585	12674557	70292679	249232
M-3_5	Tumbiana Formation	2.72	PDP1_43.15-43.16m	Shale	Diagenetic	-5.18	0.03	-10.90	0.06	-22.05	0.14	0.45	0.03	-1.44	0.14	1397683599	10963342	60772419	210852

Title	Formation	Age/ Ga	Drill core	Lithology	Pyrite genesis	$\delta^{33}S$/‰	1σ	$\delta^{34}S$/‰	1σ	$\delta^{36}S$/‰	1σ	$\Delta^{33}S$/ ‰	1σ	$\Delta^{36}S$/ ‰	1σ	Detector $^{32}S^-$ /CPS	Detector $^{33}S^-$ /CPS	Detector $^{34}S^-$ /CPS	Detector $^{36}S^-$ /CPS
M-3_6	Tumbiana Formation	2.72	PDP1_43.15-43.16m	Shale	Diagenetic	-3.27	0.04	-6.63	0.06	-13.64	0.19	0.15	0.04	-1.08	0.19	1344583429	10565099	58681306	204044
M-3_7	Tumbiana Formation	2.72	PDP1_43.15-43.16m	Shale	Diagenetic	-2.78	0.03	-6.51	0.08	-13.25	0.20	0.58	0.03	-0.91	0.19	1380132179	10853731	60273331	210087
M-3_9	Tumbiana Formation	2.72	PDP1_43.15-43.16m	Shale	Diagenetic	-5.04	0.02	-11.30	0.10	-22.59	0.16	0.79	0.02	-1.23	0.15	1469374325	11522464	63808846	221281
M-3_1	Tumbiana Formation	2.72	PDP1_43.15-43.16m	Shale	Diagenetic	-10.44	0.02	-21.54	0.23			0.71	0.02			995569104	7710750	42525936	
M-3_3	Tumbiana Formation	2.72	PDP1_43.15-43.16m	Shale	Diagenetic	-10.83	0.03	-21.84	0.14			0.48	0.03			1028736966	7962121	43907464	
M-3_4	Tumbiana Formation	2.72	PDP1_43.15-43.16m	Shale	Diagenetic	-11.80	0.04	-23.58	0.19			0.42	0.04			1019143320	7884282	43440299	
M-3_5	Tumbiana Formation	2.72	PDP1_43.15-43.16m	Shale	Diagenetic	-1.75	0.05	-4.56	0.06			0.60	0.06			987043924	7714672	42903585	
M-3_6	Tumbiana Formation	2.72	PDP1_43.15-43.16m	Shale	Diagenetic	-5.89	0.03	-12.47	0.07			0.55	0.03			918822880	7146604	39594622	
M-3_7	Tumbiana Formation	2.72	PDP1_43.15-43.16m	Shale	Diagenetic	-10.53	0.02	-20.86	0.15			0.27	0.02			990878554	7671311	42331299	
M-3_8	Tumbiana Formation	2.72	PDP1_43.15-43.16m	Shale	Diagenetic	-1.56	0.04	-3.93	0.10			0.46	0.05			982633627	7675596	42721406	
M-3_9	Tumbiana Formation	2.72	PDP1_43.15-43.16m	Shale	Diagenetic	-5.01	0.03	-10.82	0.13			0.58	0.03			1020537945	7946152	44056556	
M-3_H1.1	Tumbiana Formation	2.72	PDP1_44.33-44.34m	Shale	Mixture of the first and second generations	-2.51	0.08	-6.81	0.14			1.00	0.07			801011190	6238434	34835853	
M-3_H1.2	Tumbiana Formation	2.72	PDP1_44.33-44.34m	Shale	Mixture of the first and second generations	-7.08	0.07	-15.36	0.11			0.87	0.07			806106657	6252008	34745679	
M-3_H6	Tumbiana Formation	2.72	PDP1_81.00-81.01m	Shale	Secondary	-1.12	0.04	-3.01	0.37			0.43	0.05			768882722	5999786	33585392	
M-3_H5	Tumbiana Formation	2.72	PDP1_81.00-81.01m	Shale	Secondary	-2.02	0.09	-4.44	0.44			0.27	0.09			783075555	6099441	34102104	
M-3_H7	Tumbiana Formation	2.72	PDP1_44.08-44.10m	Shale	Secondary	1.11	0.07	-1.75	0.05			2.01	0.07			822495693	6430902	35957493	
M-3_H7'	Tumbiana Formation	2.72	PDP1_44.08-44.10m	Shale	Secondary	0.66	0.08	-2.52	0.13			1.96	0.08			772396602	6035920	33751692	
M-3_H10	Tumbiana Formation	2.72	PDP1_44.08-44.10m	Shale	Secondary	-0.38	0.08	-3.27	0.06			1.30	0.08			755487336	5895012	32973027	

Title	Formation	Age/ Ga	Drill core	Lithology	Pyrite genesis	$\delta^{33}S$/‰	1σ	$\delta^{34}S$/‰	1σ	$\delta^{36}S$/‰	1σ	$\Delta^{33}S$/ ‰	1σ	$\Delta^{36}S$/ ‰	1σ	Detector $^{32}S^-$ /CPS	Detector $^{33}S^-$ /CPS	Detector $^{34}S^-$ /CPS	Detector $^{36}S^-$ /CPS
M-3_H9	Tumbiana Formation	2.72	PDP1_44.08-44.10m	Shale	Secondary	0.58	0.06	-2.13	0.07			1.68	0.06			801250854	6261022	35008297	
M-3_H1.3	Tumbiana Formation	2.72	PDP1_44.33-44.34m	Shale	Secondary	0.40	0.03	-1.57	0.08			1.21	0.04			757962202	5920820	33139806	
M-3_H4	Tumbiana Formation	2.72	PDP1_44.33-44.34m	Shale	Secondary	-0.45	0.11	-3.08	0.08			1.14	0.11			855703815	6682583	37363891	
M-3_H2	Tumbiana Formation	2.72	PDP1_44.33-44.34m	Shale	Secondary	0.70	0.05	-0.95	0.22			1.19	0.07			793236037	6200016	34702961	
M-3.3	Tumbiana Formation	2.72	PDP1_43.15-43.16m	Shale	Secondary	-0.98	0.02	-3.55	0.08	-8.21	0.11	0.84	0.02	-1.48	0.13	1454092756	11358456	63466625	228042
M-3.15	Tumbiana Formation	2.72	PDP1_43.15-43.16m	Shale	Secondary	-0.75	0.01	-3.27	0.09	-7.40	0.11	0.93	0.02	-1.21	0.14	1612356783	12603712	70417268	253374
M-3_2	Tumbiana Formation	2.72	PDP1_43.15-43.16m	Shale	Secondary	-0.76	0.03	-3.28	0.07			0.93	0.03			977687150	7646726	42537414	
RUTTAN-1.1						0.74	0.03	1.44	0.05	2.92	0.14	0.00	0.03	0.19	0.13	951585525	7442807	41719395	141224
RUTTAN-1.2						0.71	0.03	1.36	0.06	2.44	0.16	0.01	0.03	-0.15	0.15	968498782	7573171	42465129	143711
Ruttan_1.3						0.67	0.02	1.13	0.07	2.04	0.17	0.09	0.02	-0.11	0.16	988527269	7730991	43322670	146566
Ruttan_1.4						0.59	0.02	1.14	0.04	2.21	0.14	0.01	0.02	0.05	0.14	961301413	7517041	42128145	142617
Ruttan_1.5						0.63	0.02	1.23	0.06	2.35	0.11	0.00	0.02	0.01	0.12	922914886	7215585	40444059	136714
Ruttan_1.6						0.71	0.02	1.42	0.04	2.64	0.15	-0.02	0.02	-0.06	0.15	954969739	7469560	41876006	141777
Ruttan_2.1						0.57	0.03	1.24	0.04	2.36	0.17	-0.07	0.03	0.00	0.16	851676864	6659078	37326315	126227
Ruttan_2.2						0.38	0.03	0.73	0.06	1.54	0.13	0.00	0.03	0.15	0.13	870782347	6806928	38141450	128936
Ruttan_2.3						0.63	0.03	1.10	0.05	1.78	0.16	0.07	0.02	-0.30	0.17	784074272	6130552	34360065	116223
Ruttan_2.4						0.54	0.03	1.21	0.03	2.52	0.15	-0.08	0.03	0.23	0.15	794959896	6216856	34844295	117915
BALMAT-1.1						7.75	0.03	15.11	0.05	28.98	0.10	0.00	0.03	0.07	0.11	905624053	7131111	40238899	137799
Balmat_1.2						7.85	0.03	15.38	0.03	29.43	0.16	-0.04	0.03	0.02	0.17	945205234	7445746	42024732	144025
Balmat_1.3						7.81	0.02	15.23	0.05	29.00	0.15	0.00	0.02	-0.14	0.17	900473732	7091070	40016161	137173
Balmat_2.1						7.90	0.02	15.47	0.04	29.71	0.14	-0.04	0.03	0.11	0.15	908874646	7161360	40413759	138408
Balmat_2.2						7.91	0.03	15.42	0.05	29.53	0.15	0.00	0.03	0.02	0.15	761143947	5995122	33837740	115822
Ruttan_1.1						0.70	0.02	1.26	0.05	2.43	0.13	0.06	0.02	0.03	0.14	938853747	7341167	41135893	139051

Title	Formation	Age/ Ga	Drill core	Lithology	Pyrite genesis	$\delta^{33}S$/‰	1σ	$\delta^{34}S$/‰	1σ	$\delta^{36}S$/‰	1σ	$\Delta^{33}S$/ ‰	1σ	$\Delta^{36}S$/ ‰	1σ	Detector $^{32}S^-$ /CPS	Detector $^{33}S^-$ /CPS	Detector $^{34}S^-$ /CPS	Detector $^{36}S^-$ /CPS
Ruttan_1.2						0.58	0.02	1.16	0.04	1.95	0.13	-0.01	0.02	-0.26	0.14	954130608	7457144	41800917	141303
Ruttan_1.3						0.73	0.02	1.50	0.04	3.04	0.14	-0.04	0.02	0.19	0.15	947974813	7411242	41546310	140599
Ruttan_1.4						0.63	0.02	1.26	0.04	2.70	0.21	-0.02	0.02	0.32	0.17	937834044	7331763	41081324	138881
Ruttan_1.5						0.34	0.02	0.80	0.03	1.08	0.13	-0.07	0.02	-0.44	0.14	959466381	7498277	42023307	141944
Ruttan_1.6						0.52	0.02	0.96	0.04	1.84	0.11	0.03	0.02	0.02	0.11	942398347	7364361	41265448	139367
Ruttan_2.1						0.76	0.02	1.56	0.04	3.02	0.13	-0.04	0.02	0.05	0.16	979273104	7656320	42913997	145217
Ruttan_2.2						0.55	0.02	1.10	0.05	2.42	0.13	-0.02	0.02	0.32	0.12	953655872	7454306	41767259	141256
Ruttan_2.3						0.70	0.02	1.35	0.03	2.80	0.14	0.01	0.02	0.24	0.14	978873706	7653899	42897625	145134
Ruttan_2.4						0.61	0.02	1.06	0.05	1.97	0.14	0.06	0.02	-0.05	0.14	959861521	7502463	42037374	142114
Ruttan_2.5						0.67	0.02	1.19	0.03	1.85	0.17	0.05	0.02	-0.42	0.16	989365122	7733741	43351886	146602
Balmat_1.1						7.64	0.02	14.74	0.06	28.50	0.13	0.07	0.02	0.31	0.14	915682058	7208380	40653766	139089
Balmat_1.2						7.72	0.02	15.07	0.04	29.05	0.18	-0.01	0.02	0.23	0.17	978772102	7707252	43485584	148876
Balmat_1.3						7.74	0.02	15.05	0.03	28.48	0.17	0.02	0.02	-0.31	0.16	980820660	7723240	43568476	149131
Balmat_2.1						7.92	0.02	15.50	0.04	29.90	0.13	-0.04	0.02	0.25	0.14	955417094	7524489	42466012	145362
Balmat_2.2						7.77	0.03	15.36	0.05	29.41	0.13	-0.12	0.03	0.02	0.13	907805011	7145386	40321822	138011
Ruttan_4.1						0.74	0.06	1.50	0.05			-0.03	0.07			345003306	2699287	15100933	
Ruttan_4.2						0.54	0.07	0.78	0.15			0.14	0.07			358937826	2806957	15694928	
Ruttan_4.3						0.60	0.07	1.31	0.05			-0.07	0.07			346208945	2707336	15148951	
Ruttan_4.4						0.55	0.07	1.29	0.08			-0.11	0.06			358865481	2808160	15711913	
Ruttan_4.5						0.41	0.07	0.88	0.14			-0.04	0.08			370566084	2898520	16218636	
Ruttan_4.7						0.77	0.08	1.18	0.09			0.17	0.08			349155181	2729545	15281356	
Ruttan_4.8						0.36	0.07	0.70	0.10			0.00	0.07			354504854	2770542	15510414	
Ruttan_4.9						0.60	0.08	1.05	0.11			0.06	0.08			362177347	2831946	15854298	
Ruttan_4.10						0.53	0.07	1.23	0.10			-0.10	0.07			346658706	2709999	15160890	
Ruttan_4.11						0.75	0.07	1.39	0.07			0.03	0.07			355845958	2782190	15570197	
Balmat_4.1						7.68	0.06	15.10	0.09			-0.06	0.07			394155942	3105440	17493561	
Balmat_4.2						7.26	0.06	14.50	0.12			-0.18	0.07			352901028	2780216	15660766	

Title	Formation	Age/ Ga	Drill core	Lithology	Pyrite genesis	$\delta^{33}S$/‰	1σ	$\delta^{34}S$/‰	1σ	$\delta^{36}S$/‰	1σ	$\Delta^{33}S$/ ‰	1σ	$\Delta^{36}S$/ ‰	1σ	Detector $^{32}S^-$ /CPS	Detector $^{33}S^-$ /CPS	Detector $^{34}S^-$ /CPS	Detector $^{36}S^-$ /CPS
Balmat_4.3						8.06	0.07	15.71	0.09			0.00	0.06			377144657	2970234	16747690	
Ruttan_1.1						0.67	0.07	1.42	0.07			-0.06	0.07			534806099	4179965	23417296	
Ruttan_1.2						0.51	0.09	1.44	0.09			-0.24	0.09			376721692	2944318	16493175	
Ruttan_1.3						0.91	0.07	1.20	0.06			0.30	0.08			419837911	3278577	18368821	
Ruttan_1.4						0.53	0.10	1.07	0.10			-0.02	0.10			426479471	3331063	18666110	
Ruttan_1.5						0.62	0.09	0.93	0.12			0.14	0.09			392379077	3066153	17174926	
Ruttan_1.6						0.67	0.08	1.15	0.14			0.08	0.08			376862865	2943313	16490615	
Ruttan_1.7						0.32	0.11	0.81	0.18			-0.09	0.11			359287272	2808020	15725576	
Ruttan_2.1						0.06	0.08	0.62	0.13			-0.26	0.08			343181819	2680732	15010562	
Ruttan_2.2						0.63	0.08	1.44	0.14			-0.12	0.07			383097093	2994282	16777812	
Ruttan_2.3						0.87	0.09	1.25	0.14			0.22	0.09			408559813	3191552	17887477	
Ruttan_2.4						0.95	0.08	1.51	0.12			0.17	0.08			410120362	3203365	17949699	
Ruttan_2.5						0.58	0.09	1.00	0.10			0.06	0.09			401405476	3137028	17567580	
Ruttan_2.6						0.73	0.09	1.76	0.09			-0.18	0.09			388901961	3039715	17030907	
Balmat_1.1						7.97	0.09	15.49	0.08			0.02	0.11			256075530	2016301	11367748	
Balmat_1.2						7.76	0.10	14.93	0.13			0.10	0.10			403839356	3175478	17915548	
Balmat_1.3						7.36	0.11	14.62	0.11			-0.14	0.11			354866725	2792284	15747009	
Balmat_2.1						7.47	0.11	14.77	0.16			-0.11	0.11			367632102	2892931	16312959	
Balmat_2.2						7.88	0.07	15.29	0.13			0.04	0.07			415976264	3273160	18461536	
Balmat_2.3						7.35	0.08	15.09	0.12			-0.39	0.09			414198663	3260376	18385323	
Ruttan_5.1						0.53	0.07	0.90	0.06			0.07	0.07			365191158	2854697	15977720	
Ruttan_5.2						0.48	0.06	0.78	0.06			0.08	0.06			357984217	2798885	15663026	
Ruttan_5.3						0.82	0.06	1.46	0.07			0.07	0.06			380879945	2980769	16682450	
Ruttan_5.4						0.37	0.07	0.67	0.10			0.03	0.06			373482079	2921641	16350819	
Ruttan_5.5						0.41	0.06	1.05	0.09			-0.14	0.07			369223255	2886927	16165515	
Ruttan_5.6						0.83	0.07	1.34	0.07			0.14	0.06			376179581	2941844	16475073	
Ruttan_5.7						0.50	0.07	0.92	0.07			0.03	0.06			372966315	2916056	16327526	

Title	Formation	Age/ Ga	Drill core	Lithology	Pyrite genesis	$\delta^{33}S$/‰	1σ	$\delta^{34}S$/‰	1σ	$\delta^{36}S$/‰	1σ	$\Delta^{33}S$/ ‰	1σ	$\Delta^{36}S$/ ‰	1σ	Detector $^{32}S^-$ /CPS	Detector $^{33}S^-$ /CPS	Detector $^{34}S^-$ /CPS	Detector $^{36}S^-$ /CPS
Ruttan_5.8						0.55	0.06	1.17	0.07			-0.05	0.07			369258569	2887063	16167696	
Ruttan_5.9						0.84	0.05	1.39	0.06			0.13	0.05			374319302	2926918	16389209	
Ruttan_5.10						0.42	0.04	0.65	0.06			0.08	0.04			353529253	2763544	15466313	
Ruttan_6.1						0.74	0.05	1.48	0.05			-0.02	0.05			370931154	2902176	16247446	
Ruttan_6.2						0.85	0.06	1.74	0.07			-0.04	0.06			381998435	2988797	16734405	
Ruttan_6.3						0.65	0.07	1.41	0.07			-0.08	0.07			383278965	2998575	16787781	
Ruttan_6.4						0.70	0.05	1.42	0.06			-0.03	0.05			379219966	2966559	16602757	
Ruttan_6.5						0.79	0.06	1.58	0.09			-0.03	0.06			388925498	3043659	17038698	
Ruttan_6.6						0.64	0.07	1.55	0.08			-0.15	0.07			394081306	3084096	17267010	
Ruttan_6.7						0.38	0.06	0.88	0.10			-0.08	0.06			385181854	3012992	16857986	
Balmat_5.1						8.05	0.05	15.48	0.06			0.10	0.05			383188168	3019426	17016688	
Balmat_5.2						8.04	0.07	15.54	0.09			0.06	0.07			383830003	3023708	17047807	
Balmat_5.3						7.75	0.07	14.91	0.11			0.10	0.06			372319405	2931329	16523019	
Balmat_5.4						7.87	0.06	15.10	0.09			0.12	0.06			368657617	2902812	16360874	
Balmat_5.5						7.99	0.05	15.50	0.04			0.04	0.06			366484706	2887628	16273842	
Balmat_6.1						7.32	0.06	14.59	0.08			-0.17	0.06			374761757	2952045	16630823	
Balmat_6.2						7.83	0.05	15.29	0.08			-0.01	0.05			398437935	3139455	17691896	
Ruttan_9.1						0.82	0.06	1.42	0.04			0.09	0.07			369192009	2886022	16158605	
Ruttan_9.2						0.42	0.05	0.86	0.07			-0.02	0.05			386310807	3021175	16901825	
Ruttan_9.1						0.47	0.06	1.12	0.10			-0.11	0.06			394357076	3084986	17267636	
Ruttan_9.2						0.33	0.07	0.70	0.10			-0.03	0.07			399138095	3121888	17473086	
Ruttan_9.4						0.87	0.04	1.57	0.06			0.06	0.05			387653074	3030519	16970934	
Ruttan_9.5						0.95	0.05	1.68	0.08			0.08	0.06			391419671	3061059	17138168	
Ruttan_9.6						0.56	0.05	1.14	0.07			-0.03	0.05			382589823	2990983	16735924	
Ruttan_9.7						0.76	0.06	1.70	0.09			-0.11	0.06			398167820	3114804	17440424	
Ruttan_9.8						0.83	0.06	1.48	0.07			0.06	0.06			386936653	3026992	16937775	
Ruttan_9.9						0.61	0.07	1.00	0.08			0.10	0.07			396448452	3101012	17352213	

Title	Formation	Age/ Ga	Drill core	Lithology	Pyrite genesis	$\delta^{33}S$/‰	1σ	$\delta^{34}S$/‰	1σ	$\delta^{36}S$/‰	1σ	$\Delta^{33}S$/ ‰	1σ	$\Delta^{36}S$/ ‰	1σ	Detector $^{32}S^-$ /CPS	Detector $^{33}S^-$ /CPS	Detector $^{34}S^-$ /CPS	Detector $^{36}S^-$ /CPS
Ruttan_9.10						1.06	0.04	2.17	0.06			-0.06	0.04			395946507	3098669	17349162	
Ruttan_9.11						0.86	0.06	1.70	0.06			-0.02	0.06			392644322	3072036	17196704	
Ruttan_9.12						0.53	0.08	1.12	0.07			-0.04	0.08			376164616	2942616	16466283	
Ruttan_9.13						0.38	0.07	0.91	0.08			-0.09	0.05			391041907	3058901	17115821	
Balmat_9.1						7.10	0.08	13.71	0.10			0.06	0.07			379628685	2988768	16825014	
Balmat_9.1						7.31	0.05	14.53	0.07			-0.15	0.05			385290326	3033399	17092673	
Balmat_9.2						7.77	0.05	15.08	0.32			0.03	0.05			625824846	4922711	27719868	
Balmat_9.3						7.41	0.05	14.36	0.06			0.04	0.06			380524836	2997076	16876052	
Balmat_9.4						7.15	0.06	14.06	0.07			-0.07	0.07			382113033	3009254	16948805	
Balmat_9.5						7.32	0.07	14.23	0.09			0.02	0.07			377790502	2975392	16754504	
Balmat_9.6						7.12	0.06	13.91	0.08			-0.02	0.06			382222201	3009934	16949691	
Ruttan_1						0.26	0.09	0.90	0.13			-0.20	0.10			231033020	1807821	10050980	
Ruttan_2						0.37	0.10	1.05	0.14			-0.18	0.11			232692626	1820531	10126717	
Ruttan_3						0.81	0.10	1.62	0.09			-0.03	0.11			232557144	1817019	10114059	
Ruttan_5						0.71	0.13	1.45	0.07			-0.03	0.12			215882201	1687060	9393785	
Ruttan_6						0.63	0.11	1.25	0.14			-0.01	0.10			223419333	1748270	9726134	
Ruttan_7						0.41	0.11	1.11	0.07			-0.17	0.12			212565511	1662919	9249452	
Ruttan_8						0.72	0.10	1.12	0.07			0.15	0.11			214838600	1679557	9346551	
Ruttan_9						0.98	0.11	1.67	0.07			0.12	0.11			208358044	1628780	9067194	
Balmat_1						7.94	0.08	15.77	0.07			-0.15	0.07			238209237	1876444	10514635	
Balmat_2						8.30	0.12	16.08	0.09			0.06	0.12			220503592	1737129	9740446	
Balmat_3						7.94	0.11	15.46	0.05			0.01	0.11			205197231	1616755	9055439	
Ruttan_1.1						0.29	0.02	0.64	0.13	1.59	0.10	-0.03	0.02	0.38	0.12	1527179217	11947747	66960356	242074
Ruttan_1.2						0.74	0.03	1.47	0.15	2.50	0.14	-0.02	0.02	-0.30	0.14	1431319120	11200036	62798188	226799
Ruttan_1.3						0.71	0.02	1.38	0.12	2.40	0.10	0.00	0.02	-0.23	0.12	1476077725	11552310	64754582	234091
Ruttan_1.4						0.72	0.02	1.31	0.10	2.64	0.14	0.05	0.03	0.15	0.13	1520201953	11899047	66697985	241103
Balmat_1.1						7.75	0.02	15.21	0.13	29.15	0.12	-0.05	0.02	0.06	0.12	1400513689	11034907	62276516	228024

Title	Formation	Age/ Ga	Drill core	Lithology	Pyrite genesis	$\delta^{33}S$/‰	1σ	$\delta^{34}S$/‰	1σ	$\delta^{36}S$/‰	1σ	$\Delta^{33}S$/ ‰	1σ	$\Delta^{36}S$/ ‰	1σ	Detector $^{32}S^-$ /CPS	Detector $^{33}S^-$ /CPS	Detector $^{34}S^-$ /CPS	Detector $^{36}S^-$ /CPS
Ruttan_1						0.40	0.03	0.85	0.11	1.68	0.26	-0.03	0.03	0.07	0.28	1131131266	8855905	49386632	179327
Ruttan_2						0.72	0.02	1.39	0.08	2.63	0.14	0.01	0.02	-0.02	0.15	1167839921	9144262	51030260	184884
Ruttan_3						0.65	0.02	1.18	0.08	2.41	0.18	0.04	0.02	0.16	0.19	1194670559	9354196	52193450	189317
Ruttan_4						0.69	0.02	1.38	0.07	2.41	0.16	-0.01	0.02	-0.20	0.15	1222486666	9575614	53430657	193705
Balmat_1						7.77	0.02	15.11	0.09	29.19	0.18	0.01	0.02	0.29	0.18	1156963706	9124805	51256330	188248
Ruttan_1.1						0.71	0.02	1.39	0.13			0.00	0.02			1081253197	8464266	47215996	
Ruttan_1.2						0.53	0.02	1.12	0.20			-0.05	0.02			1076564819	8418658	46920688	
Ruttan_1.3						0.67	0.02	1.25	0.11			0.03	0.02			1202833517	9415042	52508287	
Ruttan_1.4						0.34	0.02	0.64	0.28			0.01	0.02			1135854718	8886037	49533574	
Ruttan_1.5						0.85	0.01	1.61	0.21			0.02	0.01			1016634731	7957604	44384323	
Balmat_1.1						7.58	0.03	14.64	0.26			0.07	0.03			1026262105	8088569	45416502	
Balmat_1.2						7.63	0.03	14.90	0.17			-0.02	0.03			1166215079	9186660	51553667	
Ruttan_12.4						0.47	0.03	0.94	0.08	2.06	0.14	-0.01	0.03	0.27	0.15	1286053059	10131288	56570187	198493
Ruttan_12.5						0.41	0.03	0.80	0.09	1.15	0.15	0.00	0.03	-0.37	0.16	1285865330	10131563	56564871	198493
Ruttan_12.6						0.30	0.03	0.88	0.09	1.87	0.15	-0.15	0.04	0.20	0.16	1258390938	9916484	55382427	194234
Ruttan_12.7						0.14	0.03	0.56	0.12	1.06	0.12	-0.15	0.03	0.00	0.12	1242040285	9784057	54634179	191921
Ruttan_12.8						0.53	0.03	1.34	0.09	2.48	0.14	-0.16	0.03	-0.06	0.13	1302971461	10266465	57350933	201298
Ruttan_12.9						0.43	0.04	1.09	0.10	1.92	0.16	-0.13	0.04	-0.15	0.16	1273401889	10034936	56043372	196766
Ruttan_12.10						0.88	0.02	1.49	0.08	2.94	0.14	0.11	0.03	0.11	0.14	1371138264	10808920	60371397	212222
Ruttan_12.11						0.82	0.03	1.45	0.10	2.42	0.16	0.07	0.03	-0.33	0.15	1328691229	10476339	58509325	205361
Ruttan_2.1						0.75	0.03	1.12	0.08	2.16	0.14	0.17	0.03	0.04	0.15	1416147463	11160658	62315304	218789
Ruttan_2.2						0.99	0.03	1.63	0.07	3.13	0.10	0.15	0.02	0.03	0.13	1430028436	11270170	62945333	221254
Ruttan_2.3						1.13	0.02	1.85	0.08	3.63	0.12	0.18	0.03	0.10	0.12	1421610302	11210450	62609392	219860
Ruttan_2.4						0.53	0.03	1.21	0.09	2.09	0.17	-0.09	0.03	-0.22	0.17	1375644185	10841174	60561579	212581
Ruttan_2.5						0.81	0.03	1.52	0.05	2.78	0.13	0.03	0.03	-0.11	0.14	1394228979	10991143	61380490	215469
Ruttan_2.6						0.61	0.02	1.26	0.09	2.53	0.10	-0.04	0.03	0.13	0.12	1321807528	10413917	58170181	204240
Ruttan_2.7						0.71	0.03	1.17	0.11	2.15	0.10	0.11	0.03	-0.08	0.12	1351142144	10649918	59468406	208660

Title	Formation	Age/ Ga	Drill core	Lithology	Pyrite genesis	$\delta^{33}S$/‰	1σ	$\delta^{34}S$/‰	1σ	$\delta^{36}S$/‰	1σ	$\Delta^{33}S$/ ‰	1σ	$\Delta^{36}S$/ ‰	1σ	Detector $^{32}S^-$ /CPS	Detector $^{33}S^-$ /CPS	Detector $^{34}S^-$ /CPS	Detector $^{36}S^-$ /CPS
Ruttan_2.8						0.51	0.03	0.84	0.09	1.79	0.12	0.08	0.03	0.20	0.11	1399118048	11026520	61568863	216112
Ruttan_2.9						0.52	0.04	1.18	0.10	2.32	0.17	-0.09	0.04	0.07	0.17	1268347344	9994489	55820392	196042
Ruttan_2.10						0.57	0.03	1.26	0.09	2.55	0.15	-0.08	0.04	0.15	0.17	1278381165	10070727	56255352	197743
Balmat_12.1						7.38	0.03	14.54	0.11	27.71	0.11	-0.08	0.03	-0.08	0.13	1232054583	9775291	54940821	195288
Balmat_12.2						7.56	0.03	14.81	0.09	28.55	0.13	-0.03	0.03	0.22	0.13	1280028300	10161444	57125889	203266
Balmat_12.3						7.93	0.03	15.40	0.11	29.39	0.15	0.03	0.03	-0.08	0.15	1304856861	10360490	58256904	207114
Balmat_12.4						7.47	0.03	14.79	0.14	28.23	0.13	-0.12	0.03	-0.06	0.14	1231768322	9776356	54961819	195230
Balmat_2.1						8.27	0.03	15.99	0.08	30.66	0.10	0.07	0.03	0.07	0.13	1336093360	10609077	59673351	212569
Balmat_2.2						8.19	0.03	15.88	0.07	30.72	0.16	0.04	0.03	0.33	0.16	1369473004	10875791	61174966	217816
Balmat_2.3						8.16	0.03	15.81	0.08	30.31	0.13	0.05	0.03	0.06	0.13	1349948089	10719980	60285574	214245
Balmat_2.4						7.48	0.03	14.64	0.11	27.97	0.14	-0.04	0.04	-0.04	0.14	1310912838	10398869	58457118	207623
Ruttan_6.1						0.51	0.02	1.12	0.06	2.23	0.12	-0.07	0.02	0.09	0.14	1219747603	9538028	53484644	180897
Ruttan_6.2						0.59	0.03	1.20	0.07	2.27	0.11	-0.03	0.02	-0.01	0.11	1187089802	9285137	52054034	176351
Ruttan_6.3						0.83	0.02	1.49	0.05	2.71	0.11	0.06	0.02	-0.13	0.11	1221908773	9559925	53596958	181472
Ruttan_6.4						0.67	0.02	1.34	0.04	2.53	0.13	-0.02	0.02	-0.02	0.14	1213563021	9491582	53224181	180248
Ruttan_6.5						0.67	0.02	1.37	0.04	2.43	0.12	-0.04	0.02	-0.18	0.14	1232312945	9638822	54047489	183093
Ruttan_6.6						0.57	0.02	1.01	0.05	1.72	0.13	0.05	0.02	-0.21	0.12	1199443308	9378448	52575531	177541
Ruttan_7.1						0.58	0.02	1.10	0.08	2.22	0.13	0.02	0.02	0.13	0.14	1129381107	8833959	49523913	167697
Ruttan_7.2						0.47	0.03	1.06	0.05	1.91	0.11	-0.07	0.02	-0.10	0.10	1213435644	9490288	53219838	180167
Ruttan_7.3						0.54	0.02	0.91	0.06	1.92	0.13	0.07	0.02	0.19	0.14	1206628384	9438985	52905041	179245
Ruttan_7.4						0.75	0.02	1.40	0.06	2.88	0.14	0.03	0.02	0.22	0.15	1235635805	9664166	54192724	183303
Balmat_6.1						7.50	0.02	14.78	0.04	28.32	0.15	-0.08	0.02	0.06	0.15	1196567839	9425777	53189280	182037
Balmat_6.2						7.90	0.02	15.44	0.07	29.40	0.13	-0.02	0.02	-0.13	0.13	1185664461	9340840	52730615	180906
Balmat_7.1						7.11	0.02	13.73	0.07	26.01	0.10	0.07	0.02	-0.23	0.10	1178546149	9273272	52302283	178905
Balmat_7.2						7.41	0.02	14.14	0.06	27.01	0.11	0.15	0.02	-0.02	0.10	1187421136	9347693	52724349	180379
RUTTAN-1.1						0.88	0.02	1.65	0.04	3.17	0.16	0.03	0.02	0.03	0.16	1252422609	9793335	54829008	184939
RUTTAN-1.2						0.74	0.02	1.40	0.03	2.77	0.11	0.02	0.02	0.10	0.12	1270237087	9935202	55608558	187891

Title	Formation	Age/ Ga	Drill core	Lithology	Pyrite genesis	$\delta^{33}S$/‰	1σ	$\delta^{34}S$/‰	1σ	$\delta^{36}S$/‰	1σ	$\Delta^{33}S$/ ‰	1σ	$\Delta^{36}S$/ ‰	1σ	Detector $^{32}S^-$ /CPS	Detector $^{33}S^-$ /CPS	Detector $^{34}S^-$ /CPS	Detector $^{36}S^-$ /CPS
RUTTAN-1.3						0.19	0.03	0.43	0.18	0.57	0.11	-0.03	0.03	-0.24	0.11	1242429774	9708919	54334969	183489
RUTTAN-1.4						0.36	0.03	0.82	0.10	1.47	0.14	-0.06	0.03	-0.08	0.15	1181515936	9235462	51695143	174748
RUTTAN-1.5						0.61	0.03	1.14	0.07	2.26	0.14	0.02	0.03	0.10	0.15	1298099022	10148038	56805997	191964
RUTTAN-1.6						0.66	0.03	1.30	0.06	2.49	0.12	0.00	0.03	0.02	0.13	1242046393	9709456	54363790	183674
RUTTAN-1.7						0.78	0.02	1.33	0.05	2.32	0.17	0.10	0.02	-0.22	0.16	1196952050	9359651	52387952	177011
RUTTAN-1.8						0.75	0.03	1.56	0.04	3.13	0.15	-0.06	0.03	0.16	0.16	1193724746	9331677	52239392	176636
RUTTAN-1.9						0.59	0.03	1.16	0.03	2.34	0.14	-0.01	0.02	0.13	0.11	1153231617	9015560	50460585	170694
BALMAT-1.1						7.81	0.01	14.78	0.03	28.21	0.12	0.23	0.01	-0.05	0.13	1316343401	10365932	58388026	199912
BALMAT-1.2						8.00	0.02	15.14	0.04	29.05	0.15	0.23	0.02	0.09	0.14	1215784711	9576035	53942717	184742
RUTTAN-2.1						0.60	0.05	1.06	0.06			0.06	0.05			359353473	2810350	15724382	
RUTTAN-2.2						0.16	0.05	0.80	0.05			-0.25	0.05			355733373	2780568	15564481	
Ruttan_2.3						0.39	0.06	0.87	0.08			-0.06	0.06			374537142	2928518	16390806	
RUTTAN-2.4						0.12	0.07	0.39	0.10			-0.08	0.07			367429437	2872143	16077777	
Ruttan_2.4						0.71	0.06	1.49	0.05			-0.06	0.06			369496863	2888851	16176027	
Ruttan_2.5						0.71	0.06	1.54	0.07			-0.09	0.05			377783665	2955663	16545679	
Ruttan_3.1						0.75	0.05	1.62	0.08			-0.09	0.05			416468357	3259139	18248643	
Ruttan_3.2						0.73	0.06	0.99	0.07			0.22	0.07			404853103	3166475	17726199	
Ruttan_3.3						1.06	0.05	1.96	0.07			0.05	0.04			408241520	3193789	17885214	
Ruttan_3.4						0.53	0.06	0.74	0.06			0.15	0.06			400510379	3131544	17534297	
Ruttan_3.5						0.96	0.05	1.50	0.05			0.19	0.05			401535825	3140479	17585138	
Ruttan_3.6						0.88	0.05	1.75	0.03			-0.03	0.05			398288505	3114930	17445931	
Ruttan_3.7						0.56	0.07	1.02	0.07			0.04	0.07			401088322	3137808	17559567	
Ruttan_3.8						0.57	0.07	1.09	0.08			0.01	0.08			422233106	3301594	18485875	
Ruttan_3.9						0.55	0.06	1.18	0.10			-0.06	0.06			411641133	3219356	18027664	
BALMAT-2.1						7.53	0.05	14.71	0.07			-0.02	0.06			377580321	2974448	16753630	
Balmat_2.2						7.33	0.05	14.31	0.09			-0.01	0.05			385794410	3037666	17114641	
Balmat_3.1						7.89	0.07	15.07	0.06			0.16	0.07			379531744	2989349	16849360	

Title	Formation	Age/ Ga	Drill core	Lithology	Pyrite genesis	$\delta^{33}S$/‰	1σ	$\delta^{34}S$/‰	1σ	$\delta^{36}S$/‰	1σ	$\Delta^{33}S$/ ‰	1σ	$\Delta^{36}S$/ ‰	1σ	Detector $^{32}S^-$ /CPS	Detector $^{33}S^-$ /CPS	Detector $^{34}S^-$ /CPS	Detector $^{36}S^-$ /CPS
Balmat_3.2						8.16	0.07	15.73	0.03			0.08	0.06			373714897	2943195	16595551	
Balmat_3.3						8.18	0.05	15.45	0.05			0.26	0.05			374680025	2951846	16639121	
Ruttan_4.1						0.67	0.02	1.23	0.05	2.43	0.11	0.04	0.02	0.09	0.13	1101468936	8614663	48297154	163315
Ruttan_4.2						0.59	0.02	1.28	0.05	2.53	0.13	-0.07	0.02	0.10	0.13	1089431601	8518378	47767766	161468
Ruttan_4.3						0.77	0.02	1.44	0.05	2.56	0.10	0.02	0.02	-0.19	0.11	1166701098	9127170	51166878	173218
Ruttan_4.4						0.69	0.02	1.42	0.05	2.78	0.14	-0.05	0.02	0.08	0.14	1164917413	9110015	51085290	173016
Ruttan_5.1						0.48	0.02	0.99	0.07	2.17	0.10	-0.03	0.02	0.28	0.11	1111916047	8694045	48738031	164891
Ruttan_5.2						0.57	0.02	1.01	0.06	1.71	0.12	0.05	0.02	-0.21	0.12	1100579531	8606858	48236818	163096
Ruttan_5.3						0.69	0.02	1.19	0.07	2.31	0.12	0.08	0.02	0.04	0.12	1192722154	9331354	52312355	176973
Ruttan_5.4						0.50	0.02	1.02	0.09	1.76	0.15	-0.03	0.02	-0.19	0.15	1172452049	9168077	51401909	173878
Balmat_4.1						7.41	0.02	14.39	0.06	27.19	0.11	0.02	0.02	-0.33	0.12	1121097023	8824825	49787444	170418
Balmat_4.2						7.51	0.02	14.53	0.06	27.55	0.14	0.05	0.02	-0.25	0.14	1148492480	9043578	51016630	174533
Balmat_5.1						7.67	0.02	14.78	0.06	28.00	0.11	0.09	0.02	-0.26	0.13	1112203315	8758746	49413404	169110
Balmat_5.2						7.69	0.02	14.84	0.07	28.30	0.14	0.08	0.02	-0.07	0.16	1176253210	9264739	52277795	178835
Ruttan_3.1						0.37	0.03	0.87	0.07	1.69	0.16	-0.08	0.03	0.04	0.17	742477619	5807511	32554455	110133
Ruttan_3.2						0.51	0.03	0.91	0.05	1.62	0.18	0.04	0.03	-0.11	0.16	702753909	5494948	30810054	104218
Ruttan_3.3						0.36	0.03	0.66	0.10	1.57	0.19	0.02	0.03	0.32	0.20	649928160	5081774	28479425	96290
Ruttan_3.4						0.66	0.02	1.24	0.06	2.37	0.13	0.02	0.02	0.01	0.13	1147897853	8977773	50330909	170503
Ruttan_3.5						0.70	0.02	1.36	0.04	2.58	0.10	0.00	0.02	0.00	0.10	1156622245	9049262	50743471	171842
Ruttan_3.3						0.73	0.03	1.37	0.06	2.51	0.11	0.03	0.02	-0.08	0.12	1030658447	8063025	45212239	153034
Ruttan_3.4						0.69	0.02	1.52	0.06	2.96	0.13	-0.09	0.02	0.08	0.12	1031413215	8066925	45248026	153088
Ruttan_3.5						0.71	0.02	1.20	0.06	2.53	0.14	0.09	0.02	0.25	0.13	1067976589	8354988	46854134	158805
Ruttan_3.6						0.73	0.02	1.46	0.06	2.44	0.15	-0.02	0.02	-0.33	0.13	1099901791	8602506	48252471	163252
Ruttan_3.7						0.56	0.02	1.14	0.04	2.04	0.09	-0.03	0.02	-0.13	0.10	1139787330	8913327	49984910	168996
Ruttan_3.8						0.78	0.02	1.47	0.08	2.76	0.12	0.02	0.02	-0.04	0.13	1148208845	8981967	50371480	170670
Balmat_3.1						7.17	0.03	13.83	0.08	26.36	0.17	0.07	0.03	-0.07	0.17	668626612	5262852	29685304	101541
Balmat_3.2						7.45	0.02	14.44	0.08	27.34	0.13	0.04	0.03	-0.26	0.12	962298801	7578096	42754851	146418

Title	Formation	Age/ Ga	Drill core	Lithology	Pyrite genesis	$\delta^{33}S$/‰	1σ	$\delta^{34}S$/‰	1σ	$\delta^{36}S$/‰	1σ	$\Delta^{33}S$/ ‰	1σ	$\Delta^{36}S$/ ‰	1σ	Detector $^{32}S^-$ /CPS	Detector $^{33}S^-$ /CPS	Detector $^{34}S^-$ /CPS	Detector $^{36}S^-$ /CPS
Balmat_3.3						7.46	0.02	14.52	0.07	27.98	0.14	0.01	0.02	0.20	0.15	1074946183	8464162	47766557	163571
Ruttan_1.1						0.22	0.07	0.55	0.12			-0.06	0.07			815581428	6370225	35721959	
Ruttan_1.2						0.79	0.04	1.28	0.13			0.13	0.05			801050787	6259950	35124877	
Ruttan_1.3						0.45	0.06	1.19	0.11			-0.17	0.07			823027991	6432113	36084775	
Ruttan_1.4						0.87	0.09	1.48	0.07			0.10	0.11			838107186	6551364	36749009	
Ruttan_1.5						0.66	0.05	0.89	0.11			0.20	0.05			810986356	6338302	35542070	
Ruttan_1.5						0.97	0.08	1.85	0.09			0.02	0.08			842537987	6586371	36959707	
Ruttan_1.6						0.37	0.04	1.16	0.05			-0.22	0.05			781386933	6102790	34248531	
Balmat_1.1						7.39	0.04	14.77	0.04			-0.19	0.04			774270081	6091761	34398350	
Balmat_1.2						7.97	0.05	15.53	0.11			0.00	0.06			780654288	6144631	34715841	
Balmat_1.3						7.19	0.05	14.71	0.02			-0.36	0.06			768737481	6046715	34154334	
Ruttan_3.1						0.74	0.02	1.50	0.03	2.80	0.12	-0.03	0.02	-0.06	0.12	936956685	7324765	41047222	138734
Ruttan_3.2						0.71	0.03	1.38	0.06	2.59	0.17	0.00	0.03	-0.03	0.18	883684506	6905244	38685928	130648
Ruttan_3.3						0.86	0.02	1.60	0.07	2.91	0.13	0.03	0.02	-0.14	0.14	1028528750	8042025	45053644	152492
Ruttan_3.4						0.63	0.02	1.39	0.03	2.81	0.14	-0.09	0.02	0.17	0.14	1061777286	8299337	46504576	157293
Ruttan_4.1						0.64	0.02	1.29	0.04	2.64	0.13	-0.02	0.02	0.20	0.12	1022140132	7990485	44760594	151344
Ruttan_4.2						0.49	0.02	0.94	0.06	1.59	0.14	0.01	0.02	-0.19	0.13	1029091919	8041404	45055601	152101
Ruttan_4.3						0.55	0.02	1.01	0.04	2.17	0.14	0.04	0.02	0.26	0.16	1067928174	8344890	46743895	158319
Ruttan_4.4						0.51	0.02	1.10	0.05	1.89	0.14	-0.05	0.02	-0.19	0.16	1059036512	8275650	46365202	156655
Ruttan_4.5						0.43	0.02	0.66	0.07	1.44	0.15	0.09	0.02	0.19	0.16	1024160830	8002940	44825134	151417
Ruttan_4.6						0.61	0.02	1.14	0.06	1.96	0.16	0.02	0.02	-0.21	0.16	944657089	7382158	41358428	139699
Balmat_3.1						7.58	0.03	14.48	0.04	27.34	0.16	0.15	0.03	-0.36	0.16	894512519	7038297	39685212	135559
Balmat_3.2						7.36	0.02	14.44	0.05	27.46	0.13	-0.05	0.02	-0.14	0.13	1051134406	8269463	46629052	159356
Balmat_4.1						8.00	0.02	15.51	0.06	29.37	0.14	0.04	0.02	-0.31	0.14	1102054163	8676761	48942460	167538
Balmat_4.2						7.70	0.02	15.07	0.05	28.76	0.12	-0.03	0.03	-0.07	0.13	1055307685	8306662	46847941	160208
Ruttan_9.4						0.39	0.02	0.99	0.17	1.99	0.13	-0.12	0.02	0.11	0.16	1222347227	9631056	53650817	187944
Ruttan_9.5						0.03	0.01	0.28	0.19	0.32	0.17	-0.12	0.02	-0.21	0.16	1169118319	9207076	51270743	179300

Title	Formation	Age/ Ga	Drill core	Lithology	Pyrite genesis	$\delta^{33}S$/‰	1σ	$\delta^{34}S$/‰	1σ	$\delta^{36}S$/‰	1σ	$\Delta^{33}S$/ ‰	1σ	$\Delta^{36}S$/ ‰	1σ	Detector $^{32}S^-$ /CPS	Detector $^{33}S^-$ /CPS	Detector $^{34}S^-$ /CPS	Detector $^{36}S^-$ /CPS
Ruttan_9.6						0.50	0.01	1.22	0.14	2.04	0.15	-0.13	0.02	-0.28	0.16	1211407668	9544175	53171432	186861
Ruttan_9.7						-0.04	0.02	0.20	0.19	0.24	0.21	-0.14	0.03	-0.13	0.18	1160713477	9138690	50878260	177748
Ruttan_9.8						0.96	0.02	1.67	0.18	3.66	0.18	0.10	0.02	0.49	0.18	1251700378	9867713	54955708	192667
Ruttan_9.9						1.10	0.01	1.81	0.17	3.46	0.18	0.17	0.01	0.02	0.17	1247518796	9832873	54776583	191910
Ruttan_9.10						0.70	0.02	1.35	0.20	2.33	0.18	0.01	0.02	-0.23	0.17	1211426617	9547498	53179391	186361
Ruttan_9.11						0.91	0.01	1.57	0.13	3.12	0.15	0.10	0.01	0.13	0.15	1256999465	9906758	55196015	193820
Ruttan_9.12						1.02	0.01	1.72	0.14	3.38	0.16	0.14	0.02	0.10	0.15	1229961295	9697780	54014756	189398
Balmat_9.2						7.66	0.02	14.76	0.17	28.71	0.13	0.08	0.02	0.48	0.13	1296037852	10285553	57666957	204558
Balmat_9.3						7.71	0.01	14.79	0.16	28.78	0.18	0.12	0.02	0.49	0.18	1288132126	10223032	57309978	203339
Balmat_9.4						7.62	0.01	14.95	0.16	28.33	0.15	-0.05	0.02	-0.26	0.15	1227377185	9740500	54617788	193887
Ruttan_2						0.34	0.08	0.91	0.11			-0.13	0.09			201768677	1578649	8773879	
Ruttan_3						0.88	0.12	1.46	0.07			0.13	0.12			206060431	1611190	8965534	
Ruttan_4						0.74	0.10	1.15	0.09			0.15	0.10			214305759	1676593	9320505	
Ruttan_5						0.86	0.15	1.52	0.08			0.08	0.15			206572587	1615999	8988926	
Ruttan_6						0.94	0.12	1.50	0.06			0.16	0.12			206213232	1612234	8972594	
Balmat_1						7.50	0.12	14.66	0.08			-0.02	0.13			200257923	1576553	8828019	
Balmat_2						7.07	0.11	14.28	0.10			-0.26	0.12			206527402	1626740	9101180	
Balmat_3						7.46	0.09	14.44	0.09			0.05	0.10			200621693	1578303	8839840	
Ruttan_3.1						0.55	0.02	1.07	0.04	2.04	0.16	0.00	0.02	0.00	0.12	1357485417	10711409	59746432	209834
Ruttan_3.2						0.73	0.02	1.19	0.03	2.03	0.18	0.11	0.02	-0.23	0.20	1382538833	10909197	60856821	213964
Ruttan_3.3						0.56	0.02	0.95	0.03	1.88	0.14	0.07	0.02	0.07	0.15	1344226210	10605779	59147059	207471
Ruttan_3.4						0.56	0.02	1.01	0.03	2.25	0.12	0.04	0.02	0.33	0.12	1378309895	10873157	60638680	212777
Ruttan_3.5						0.55	0.02	1.42	0.02	2.39	0.15	-0.18	0.02	-0.31	0.16	1370300420	10809270	60305880	211808
Ruttan_3.6						0.53	0.03	1.10	0.05	1.82	0.17	-0.03	0.03	-0.26	0.15	1333662036	10522017	58692763	205937
Balmat_3.1						7.96	0.02	15.32	0.09	29.50	0.14	0.10	0.03	0.19	0.15	1383158851	10993379	61734320	219393
Balmat_3.2						7.58	0.02	14.69	0.04	28.20	0.15	0.04	0.02	0.10	0.15	1386679805	11018149	61862828	219607
Ruttan_1.1						0.45	0.07	0.97	0.05			-0.05	0.07			744176237	5812598	32619405	

Title	Formation	Age/ Ga	Drill core	Lithology	Pyrite genesis	$\delta^{33}S$/‰	1σ	$\delta^{34}S$/‰	1σ	$\delta^{36}S$/‰	1σ	$\Delta^{33}S$/ ‰	1σ	$\Delta^{36}S$/ ‰	1σ	Detector $^{32}S^-$ /CPS	Detector $^{33}S^-$ /CPS	Detector $^{34}S^-$ /CPS	Detector $^{36}S^-$ /CPS
Ruttan_1.2						0.56	0.06	1.15	0.05			-0.03	0.06			750386105	5861446	32899472	
Ruttan_1.4						0.53	0.04	0.98	0.08			0.02	0.04			764581161	5974191	33513887	
Ruttan_1.5						0.15	0.05	0.64	0.10			-0.17	0.05			777418561	6073906	34079451	
Ruttan_1.6						0.48	0.10	1.08	0.08			-0.07	0.10			800010244	6252468	35082036	
Ruttan_1.7						0.37	0.04	1.13	0.15			-0.21	0.05			761315004	5946348	33378688	
Ruttan_1.9						0.96	0.06	1.27	0.08			0.31	0.07			801084251	6261053	35133425	
Ruttan_1.10						0.64	0.06	1.13	0.05			0.06	0.07			792266905	6190943	34733332	
Ruttan_1.11						0.50	0.07	1.28	0.04			-0.16	0.08			819561397	6403627	35935728	
Ruttan_1.12						0.68	0.06	1.50	0.07			-0.10	0.06			809504053	6326596	35507115	
Ruttan_1.13						0.75	0.04	1.17	0.04			0.15	0.05			805496429	6295581	35319046	
Ruttan_1.14						0.54	0.07	1.00	0.04			0.03	0.07			822398892	6425849	36053816	
Ruttan_1.15						1.03	0.05	1.58	0.05			0.22	0.06			828294824	6474028	36318000	
Ruttan_1.16						0.69	0.05	1.15	0.08			0.10	0.06			820488977	6411674	35978442	
Ruttan_1.17						0.27	0.09	1.10	0.06			-0.29	0.09			830738258	6490977	36428484	
Ruttan_1.18						0.95	0.07	1.48	0.06			0.19	0.07			878157806	6866088	38512258	
Ruttan_1.19						0.82	0.05	1.30	0.11			0.15	0.05			827737110	6469892	36301206	
Ruttan_1.20						0.48	0.04	1.01	0.03			-0.04	0.04			805695815	6295872	35317060	
Balmat_1.1						8.14	0.07	15.58	0.09			0.14	0.07			729761615	5746385	32461244	
Balmat_1.2						7.48	0.05	14.75	0.09			-0.08	0.05			779891264	6137532	34656649	
Balmat_1.3						7.65	0.05	15.16	0.04			-0.13	0.06			814005774	6409025	36184965	
Balmat_1.4						7.85	0.03	15.06	0.06			0.13	0.04			794502057	6253343	35313843	
Balmat_1.5						7.86	0.05	15.36	0.06			-0.02	0.06			810286588	6377456	36024623	
Balmat_1.6						7.81	0.06	15.11	0.11			0.06	0.06			848056917	6675929	37704893	
Balmat_1.7						7.84	0.08	15.23	0.04			0.03	0.09			848662668	6680065	37727914	
Ruttan_1.1						0.61	0.02	1.16	0.07	2.22	0.11	0.01	0.02	0.01	0.11	1490803662	11665823	65387625	236259
Ruttan_1.2						0.69	0.02	1.48	0.05	2.78	0.09	-0.07	0.02	-0.04	0.09	1466584494	11476708	64341549	232709
Ruttan_1.3						0.60	0.02	1.29	0.09	2.24	0.14	-0.06	0.02	-0.21	0.13	1521185843	11907054	66744359	241506

Title	Formation	Age/ Ga	Drill core	Lithology	Pyrite genesis	$\delta^{33}S$/‰	1σ	$\delta^{34}S$/‰	1σ	$\delta^{36}S$/‰	1σ	$\Delta^{33}S$/ ‰	1σ	$\Delta^{36}S$/ ‰	1σ	Detector $^{32}S^-$ /CPS	Detector $^{33}S^-$ /CPS	Detector $^{34}S^-$ /CPS	Detector $^{36}S^-$ /CPS
Ruttan_1.4						0.64	0.01	1.34	0.09	2.42	0.15	-0.05	0.01	-0.12	0.13	1482150182	11598117	65021369	234873
Ruttan_1.5						0.48	0.02	0.79	0.13	1.67	0.13	0.07	0.02	0.17	0.11	1473394381	11525816	64575519	233324
Ruttan_1.6						0.74	0.02	1.40	0.07	2.86	0.11	0.02	0.02	0.19	0.11	1452233548	11364157	63698975	230400
Ruttan_1.7						0.60	0.01	1.11	0.10	2.22	0.10	0.03	0.01	0.10	0.11	1553655941	12158323	68141457	246455
Ruttan_1.8						0.51	0.02	0.94	0.11	1.76	0.11	0.03	0.02	-0.03	0.12	1494713184	11693833	65539118	236931
Ruttan_1.9						0.54	0.02	1.05	0.09	2.16	0.14	0.00	0.02	0.17	0.15	1546376605	12099134	67808122	245298
Ruttan_1.10						0.76	0.02	1.43	0.10	2.49	0.11	0.03	0.02	-0.23	0.10	1541750687	12067893	67643378	244643
Balmat_1.1						7.60	0.01	14.95	0.07	28.61	0.10	-0.08	0.02	0.01	0.12	1493027206	11765689	66401009	243129
Balmat_1.2						7.59	0.02	14.95	0.09	28.27	0.11	-0.08	0.02	-0.32	0.14	1590453282	12533832	70724295	259152
Balmat_1.3						7.35	0.02	14.27	0.10	27.35	0.11	0.02	0.02	0.06	0.11	1555220721	12253807	69104587	252881
Ruttan_1						0.81	0.02	1.43	0.06			0.08	0.02			947628095	7422967	41430089	
Ruttan_2						0.66	0.06	1.28	0.09			0.00	0.06			969993544	7597167	42402608	
Ruttan_3						0.51	0.03	1.06	0.09			-0.04	0.03			868401606	6799069	37939303	
Ruttan_4						0.83	0.04	1.52	0.04			0.05	0.03			875766840	6858859	38280037	
Ruttan_5						0.51	0.03	0.98	0.11			0.00	0.03			943798570	7389434	41228235	
Ruttan_6						0.38	0.03	0.93	0.07			-0.10	0.03			962440202	7536019	42049588	
Balmat-1						7.76	0.03	15.00	0.06			0.06	0.02			975257603	7692511	43215176	
Balmat-2						7.72	0.02	15.13	0.08			-0.05	0.02			970456792	7652280	42986415	

Table 2.4 Summarization of the maximum magnitudes of positive and negative $\Delta^{33}S$ of products from the previously proposed reactions producing S-MIF.

Reaction	Maximum positive $\Delta^{33}S$	Minimum negative $\Delta^{33}S$	Reference
SO_2 photolysis under UV radiation of 184.9 nm and 253.7 nm	500.6	-50.5	Farquhar et al., 2001
SO_2 photolysis under UV radiation of 193 nm	70.1	-23.3	Farquhar et al., 2001
SO_2 photolysis under UV radiation of 248 nm	2	-0.8	Farquhar et al., 2001
SO_2 photolysis under UV radiation of >220	3.3	-3.5	Farquhar et al., 2001
SO_2 photolysis under UV radiation of 200 nm	18.38	-0.14	Masterson et al., 2011
SO_2 photoexcitation under UV radiation of 250 nm	16.5	-3.91	Whitehill and Ono, 2012
SO_2 photolysis under UV radiation of 200 nm	21.6	-5.53	Whitehill and Ono, 2012
SO_2 photolysis under UV radiation of full spectrum (Xe)	22.1	-6.07	Whitehill and Ono, 2012
SO_2 photolysis under UV radiation of full spectrum (D)	24.3	-2.38	Whitehill and Ono, 2012
SO_2 photolysis under UV radiation of 190-400 nm	11.79	-0.02	Ono et al., 2013
SO_2 photolysis under UV radiation of 190-220 nm	9.13	No negative $\Delta^{33}S$	Whitehill et al., 2015
SO_2 photoexcitation under UV radiation of 250-350 nm	23.4	No negative $\Delta^{33}S$	Whitehill et al., 2015
SO_2 photolysis under UV radiation of 185-220 nm	10.54	-5.52	Endo et al., 2016
SO_2 photoexcitation under UV radiation of 245-320 nm	141.9	-48.56	Endo et al., 2016
CS_2 photopolymerization by UV radiation 280-370 nm	10	No negative $\Delta^{33}S$	Colman et al., 1996
Adsorption of SO_2 onto kerogen surface	13.6	No negative $\Delta^{33}S$	Lasaga et al., 2008
Sulfate reduction by amino acid under 150-200°C	2.1	No negative $\Delta^{33}S$	Watanabe et al., 2009
Photolysis of phenacylphenylsulfone	6.4	-2.1	Kopf and Ono, 2012

Chapter 3 Negative $\Delta^{33}S$ for ^{34}S-Depleted Pyrite in the 3.49 Ga Dresser Formation of Pilbara Craton, Western Australia

Abstract: The 3.49 Ga Dresser Formation has been widely considered to host the earliest sulphur-involving metabolism on the Earth based on sulphur isotopic evidence. However, bulk barite analyses and in-situ measurements gave opposite $\Delta^{33}S$ for the ^{34}S-depleted pyrite, which were interpreted as microbial sulphate reduction (negative $\Delta^{33}S$) and elemental sulphur disproportionation (positive $\Delta^{33}S$), respectively. This study first sorted out the pyrite generations by sodium hypochlorite etching and BSE imaging, and then measured the multiple sulphur isotopic compositions of each generation of pyrite using SHRIMP-SI. Two generations of pyrite were revealed: $\Delta^{33}S$-positive generation one and $\delta^{34}S$- and $\Delta^{33}S$-negative generation two. The ^{34}S-considerably depleted pyrite has negative $\Delta^{33}S$, suggesting sulphate reduction rather than elemental sulphur disproportionation. Nonetheless, the simple correspondance between the sign of $\Delta^{33}S$ and the type of sulphur-involving metabolism needs further confirmation. Although the significantly negative $\delta^{34}S$ is suggestive of microbial activities, the $\Delta^{33}S$-$\Delta^{36}S$ plot shows no apparent biological fractionations from the associated barite. Additionally, some other evidence do not support a biological origin as well. Therefore, it is still ambiguous whether sulphur-involving metabolisms were in operation 3.49 Ga ago on the Earth.

1. Introduction

The ca. 3.49 Ga Dresser Formation in the Pilbara Craton, Western Australia has been widely considered to preserve the earliest life on the Earth based on palaeontological and geochemical evidence, including possibly biogenic stromatolites (Buick et al., 1981; Groves et al., 1981), microbially induced sedimentary structures (i.e., the responses of microbial mats to physical sediment dynamics, Noffke et al., 2013), extremely negative $\delta^{13}C$ (<-56‰) of fluids extracted from methane-bearing fluid inclusions hosted in quartz of veins (Ueno et al., 2006), as well as large fractionation of $\delta^{34}S$ between barite and pyrite coupled with biological $\Delta^{36}S/\Delta^{33}S$ deviation from the Archean Reference Array (Shen et al., 2001; Philippot et al., 2007; Ueno et al., 2008; Shen et al., 2009).

Although sulphur isotope studies show probably biological $\delta^{34}S$-$\Delta^{33}S$-$\Delta^{36}S$ signatures in pyrite (considerably negative $\delta^{34}S$, and fractionation trends from the associated barite parallel

to the biological fractionation line in the $\Delta^{33}S$-$\Delta^{36}S$ plot), it is still controversial whether the associated biological activities are microbial sulphate reduction or elemental sulphur disproportionation based on negative (Shen et al., 2009) and positive (Philippot et al., 2007) $\Delta^{33}S$ of the pyrite in barite, respectively. Additionally, the pyrite is multiple-generation as a result of multiple stages of hydrothermal events forming the chert-barite unit of the Dresser Formation (Van Kranendonk et al., 2008). Thus, it is necessary to sort out the pyrite generations prior to sulphur isotope analysis. However, previous studies only divide the pyrite into two categories: macroscopic pyrite constituting pyrite laminae and microscopic pyrite within barite. Furthermore, experiments have shown that sulphate reduction by inorganic reductants such as ferrous iron-bearing minerals under hydrothermal conditions (e.g., 300 °C) is also able to induce large shifts (ca. 20‰) in $\delta^{34}S$ (Ohmoto and Goldhaber, 1997). Although $\Delta^{36}S/\Delta^{33}S$ points to possible biological activities, the associated analytical methods for quadruple sulphur isotopic compositions of pyrite are bulk barite (Ueno et al., 2008; Shen et al., 2009), which could contain multiple generations of pyrite and other sulphides such as sphalerite, thus the measured sulphur isotopic compositions could be of mixing sulphur components.

This study firstly established the generations of pyrite using sodium hypochlorite etching combined with SEM (Scanning Electron Microscope), and then measured the multiple (quadruple and triple) sulphur isotopic composition in situ with the upgraded SHRIMP-SI (Sensitive High Resolution Ion MicroProbe-Stable Isotope). In this way, we are able to uniquely identify the multiple sulphur isotopic composition of each generation of pyrite, and provide constraints on whether and which kind of sulphur-associated biological activities are involved in the formation of these pyrites.

2. Geological setting

The Dresser Formation crops out as a ring (up to 14 km in diameter) of the North Pole Dome in the East Pilbara Terrane of Pilbara Craton (Van Kranendonk et al., 2008). Stratigraphically, it is a subunit of the Warrawoona Group, Pilbara Supergroup, and consists of metabasalt interlayered with three chert horizons (Ueno et al., 2008). The lowermost chert hosts abundant barite, and is referred to as the chert-barite unit, which is the focus of most studies on the Dresser Formation. The bedded chert-barite unit is composed mainly of chert in variable colors, coarse barite in the form of bedding-concordant or discordant layers, carbonate,

conglomerate and sandstone comprising predominantly volcanic detritus, and interlayered stratiform and domical stromatolites. Below the bedded chert-barite unit are quantities of silica ± sulphides (pyrite and sphalerite) ± organic matter veins and barite veins of variable width intruding and transecting the underlying metabasalt, resulting in intense hydrothermal alterations around the veins (particularly chloritic alteration).

Initially, the chert-barite unit was interpreted to be deposited in a peritidal or sabkha environment based on sedimentary structures such as stromatolitic laminates, graded and cross-bedding, ripples, desiccation cracks, and abundant carbonates and sulphates (e.g., Lambert et al., 1978; Groves et al., 1981; Buick and Dunlop, 1990). The veins were considered to be formed during a post-depositional stage along the fractures of the dome (Hickman, 1973, 1983). Nevertheless, later detailed mapping combined with sedimentological and structural analyses revealed that the bedding-conformable chert and barite are contemporaneous with the veins (Nijman et al., 1998; Van Kranendonk and Pirajno, 2004), and X-ray computerized tomography investigation provided evidence demonstrating that the barite is hydrothermal in origin (Runnegar et al., 2001) rather than primarily proposed replacement of gypsum (Lambert et al., 1978; Groves et al., 1981; Buick and Dunlop, 1990).

The age of the Dresser Formation has been constrained to around 3.49 Ga based on a model lead age of 3490 Ma for galena from the North Pole barite deposit (Thorpe et al., 1992a), zircon U-Pb ages of 3471 ± 5 Ma for felsic volcanics and 3465 ± 3 Ma for felsic schist of the overlying Duffer Formation (Thorpe et al., 1992b. Additional age constraints are provided by zircon U-Pb ages of 3515 ± 3 Ma for rhyolite tuff (Buick et al., 1995) and 3498 ± 2 Ma for the rhyolite (Nelson, 2002) of the underlying Coonterunah Subgroup.

3. Samples and methods

3.1 Samples

All samples were obtained as drill cores from the Perth Core Library, Carlisle, Western Australia. One drill core interval is from the drill hole PDP2c (21°10'34.5"S, 119°25'51"E), and the other two intervals are from the drill hole PDP2b (21°10'34"S, 119°25'50.9"E). The samples are described in Table 3.1. Detailed drill hole descriptions can be found in Van Kranendonk et al. (2008).

Table 3.1 Descriptions of drill core samples investigated in this study.

Drill core samples	Descriptions	Pyrite generations
PDP2c_97.17-97.20m	Grey barite with irregular sulphide (mainly pyrite, minor sphalerite) laminae and silica veins. Barite (prismatic) is partly transected by silica veins of variable width. Pyrite occurs (1) as laminae or clusters, (2) within barite as small grains aligned in an array or as individual grains, and (3) between barite and silica veins as individual grains.	G1 and G2
PDP2b_90.94-90.97m	Grey barite with silica veins. Pyrite occurs as (1) disseminated grains in silica veins, (2) clusters or individual grains between barite and silica veinlets, and (3) tiny grains within barite.	G1 and G2
PDP2b_94.69-94.74m	Relatively pure grey barite with minor silica veins. Barite is prismatic. Only a small amount of pyrite grains occur, and the occurrences are mainly clusters or individual grains within barite or between barite and silica veinlets.	G2
PDP2b_102.26-102.27m	Quartz veins in basalt. Pyrite occurs within the quartz veins.	G2

3.2 Methods

3.2.1 Etching and SEM

Chips of barite with/without pyrite laminae/clusters were firstly cut from the drill cores and cast into the first batch of epoxy mounts. The mounts were polished and then immersed in sodium hypochlorite solution (8-12.5% NaOCl) for about two to five minutes, revealing the internal textures of pyrite. Subsequently, the mounts were observed in reflected light to identify potential generations of pyrite. Once identified, they were characterized and selected for sulphur isotope analysis. Special attention was paid to the size of small pyrite grains associated with barite to make sure that the selected grains were big enough for small-spot analysis (~15 μm × 10 μm) of SHRIMP-SI. The targeted pyrite grains were cut from the mounts, and were assembled to the second batch of mounts together with the reference materials (Ruttan pyrite and Balmat pyrite) for sulphur isotope measurement. These mounts

were immersed in the sodium hypochlorite solution again, and were photographed in the reflected light of a microscope after rinsing and drying. The immersed mounts were then polished with 1-μm diamond paste to remove the oxidized film on the surface, followed by photographing under the microscope.

The mounts were then cleaned, dried, and coated with 10 nanometers of gold or 15 nanometers of aluminium. After that, they were analyzed utilizing a JEOL JSM-6400 SEM, revealing the internal textures of pyrite by BSE (Back Scattered Electron) imaging and confirming that the minerals to be analyzed were compositionally pyrite by EDS (Energy Dispersive Spectroscopy). The analyses were conducted at the Research School of Earth Sciences, Australian National University, and the operating conditions were 15 kV (acceleration voltage), 1 nA (beam current), and 10 mm (working distance). After SEM analysis, the gold or aluminium film was removed firstly by potassium iodide solution (for gold) or decon90 detergent (for aluminium) and then by polishing with 1-μm diamond paste.

3.2.2 Measurement of multiple sulphur isotopes

Before sulphur isotope measurement, the mounts were again thoroughly cleaned in an ultrasonic bath using ethanol, RBS35 detergent, warm water, and deionized water. Subsequently, the mounts were dried and outgassed in a vacuum oven for around five days, and were then coated with 40 nanometers of gold or 45 nanometers of aluminium.

Detailed acquisition conditions are summarized in Table 3.2. A primary caesium beam was generated in a Kimbal Physics IGS5 ion gun with an internal acceleration energy of 5 keV. The ion beam was focused to a Kohler aperture that was used as the source for the immersion lens, which accelerated the beam through a further 10 keV to the sample potential. The incidence angle of the primary beam on the target was 45°, yielding elliptical spots on the sample surface. Due to the variable sizes of pyrite grains, both big-spot (~27 μm × 20 μm) and small-spot (~18 μm × 15 μm) analyses were conducted. The spot size was changed by adjusting the Kohler aperture.

Negative sulphur ions were accelerated to real ground with resultant 10 keV energy, and were then focused through an ion extraction system to the source slit. The width of the source slit was 60 μm. The secondary sulphur ions were focused through the mass analyzer to the collector. The four sulphur isotope ions were collected and measured in multiple collection

mode. The highest mass resolution (4000M/ΔM, 10% peak height) was used for resolving $^{33}S^-$ from $^{32}SH^-$, with a collector slit width of 150 μm. All four sulphur isotope ions were collected in Faraday cups; $^{32}S^-$, $^{33}S^-$ and $^{34}S^-$ ions were measured using current mode with 10^{11} or 10^{12} Ω resistors whereas $^{36}S^-$ was measured using charge mode with a 22 pF capacitor (Ireland et al., 2014).

Each run commenced with rastering the primary beam over an area slightly larger than the spot for five minutes, removing the gold/aluminium coat and allowing the sample surface to become conditioned with Cs^+ ions. During this period, an in-line valve between the source chamber and the electrostatic analyzer was closed and base-lines for the electrometers were collected. This was followed by steering the secondary ion beam to maximize the signal of sulphur ions and further stabilize the secondary ion beam.

Each run consisted of four or five sets for big-spot analyses, and only two sets for small-spot analyses. Each set comprised ten scans, and each scan comprised ten subcounts, with each subcount lasting for two seconds.

The primary reference material was Ruttan pyrite and the secondary reference material was Balmat pyrite. Each analytical session generally commenced with analyses of Ruttan pyrite and Balmat pyrite, followed by unknowns, and then Ruttan pyrite and Balmat pyrite, and so forth.

The raw sulphur isotope data were reduced using the POXI-MC software developed by the RSES of ANU. The measured $^{3x}S^-/^{32}S^-$ ratios are transformed to delta (δ) notation as permil deviations relative to the standard ratios of Vienna Canyon Diablo Troilite (V-CDT), $\delta^{3x}S_{V\text{-}CDT}$ (‰) = $[(^{3x}S/^{32}S)_{unknown}/(^{3x}S/^{32}S)_{V\text{-}CDT} - 1] \times 1000$, where $(^{3x}S/^{32}S)_{unknown}$ and $(^{3x}S/^{32}S)_{V\text{-}CDT}$ are the $^{3x}S/^{32}S$ ratios of the unknown and V-CDT, respectively. Since the unknowns were calibrated directly to the reference material Ruttan pyrite in this protocol, thus $\delta^{3x}S_{V\text{-}CDT}$ (‰) = $\delta^{3x}S_{V\text{-}CDT}(Ruttan) + [(^{3x}S/^{32}S)_{unknown}/(^{3x}S/^{32}S)_{Ruttan} - 1] \times 1000$, where $\delta^{3x}S_{V\text{-}CDT}(Ruttan)$ is the $\delta^{3x}S_{V\text{-}CDT}$ value of Ruttan pyrite ($\delta^{33}S_{V\text{-}CDT}(Ruttan)$, $\delta^{34}S_{V\text{-}CDT}(Ruttan)$, and $\delta^{36}S_{V\text{-}CDT}(Ruttan)$ are 0.62‰, 1.20‰, and 2.28‰, respectively, Crowe and Vaughan, 1996; Williford et al., 2011; Whitehouse, 2013; Ireland et al., 2014). $\Delta^{33}S$ and $\Delta^{36}S$ were calculated following $\delta^{33}S - 1000 \times [(1 + \delta^{34}S/1000)^{0.515} - 1]$ and $\delta^{36}S - 1000 \times [(1 + \delta^{34}S/1000)^{1.9} - 1]$, respectively.

Table 3.2 Detailed acquisition parameters of SHRIMP-SI.

Parameters	Quadruple sulphur isotopes (Big-spot analyses)	Triple sulphur isotopes (Small-spot analyses)
Spot size	ca. 27 μm × 20 μm	ca. 18 μm × 15 μm
Set(s)	4 or 5	2
Scans	40 or 50	20
Primary beam ion species	Cs^+	Cs^+
Total analysis time	ca. 21 min or 26 min	ca. 13 min
Source slit width	60 μm	60 μm
Collector slit width for $^{32}S^-$	300 μm	300 μm
Collector slit width for $^{33}S^-$	150 μm	150 μm
Collector slit width for $^{34}S^-$	200 μm	200 μm
Collector slit width for $^{36}S^-$	300 μm	300 μm
Mass resolution (at 10% peak height)	4000M/ΔM	4000M/ΔM
Primary beam energy	15 keV	15 keV
Total acceleration voltage for the extraction of secondary ions	10 kV	10 kV
Primary beam intensity	ca. 8 nA	ca. 2 nA
Amplifier and V-F Converter range for $^{32}S^-$	Electrometer current mode, 10^{11} Ω, 0-50 V	Electrometer current mode, 10^{11} Ω, 0-50 V
Amplifier and V-F Converter range for $^{34}S^-$	Electrometer current mode, 10^{11} or 10^{12} Ω, 0-50 V	Electrometer current mode, 10^{11} or 10^{12} Ω, 0-50 V
Amplifier and V-F Converter range for $^{33}S^-$	Electrometer current mode, 10^{11} or 10^{12} Ω, 0-50 V	Electrometer current mode, 10^{11} or 10^{12} Ω, 0-50 V
Amplifier and V-F Converter range for $^{36}S^-$	Electrometer charge mode, 22 pF, 0-50 V	

4. Results

The pyrite investigated in this study occurs as pyrite laminae, clusters, and individual grains. Sodium hypochlorite etching and BSE imaging show that some pyrite grains are homogeneous with no internal textures, while others display core-rim textures (Fig. 3.1).

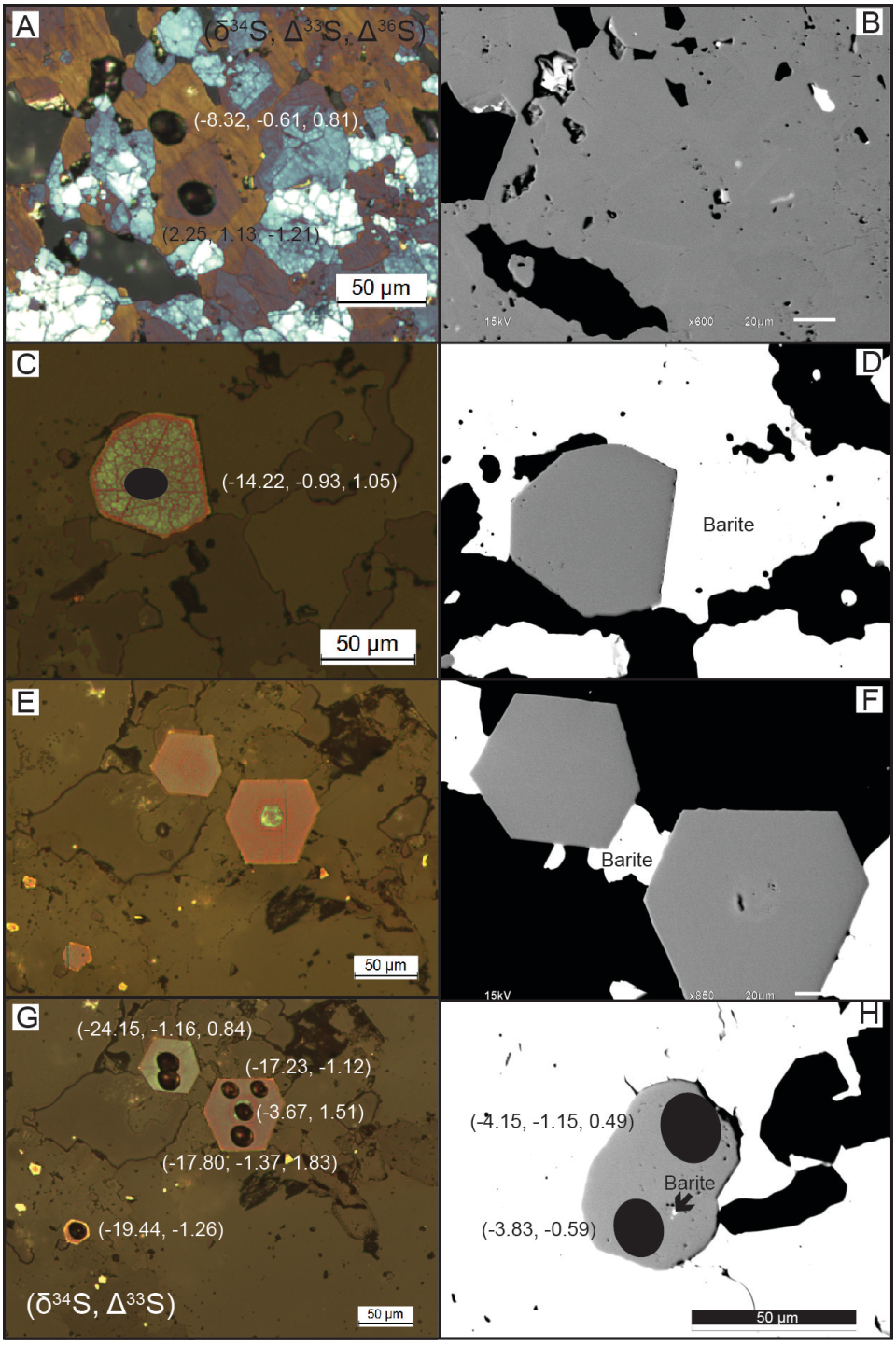

Figure 3.1. Microphotographs (reflected light) and BSE images of some pyrite grains measured in this study with no internal textures or core-rim textures. A: The microphotograph of etched pyrite and B: The BSE image of a core-rim textured pyrite grain in a pyrite lamina from PDP2c_97.17-97.20m, along with the quadruple sulphur isotopic compositions. C: The microphotograph of etched pyrite and D: The BSE image of a pyrite grain with no internal texture from PDP2b_94.69-94.74m, along with the quadruple sulphur isotopic composition. E and G: Microphotographs of three etched pyrite grains from PDP2b_90.94-90.97m, one of which shows core-rim texture whereas the other two display no

internal textures, along with the quadruple and triple sulphur isotopic compositions. F: The corresponding BSE image of E. H: The BSE image of a pyrite grain of generation two with barite inclusion from PDP2b_94.69-94.74m, along with the quadruple and triple sulphur isotopic compositions.

The sulphur isotope data are listed in Table 3.3. Internal precision is estimated in the value of one standard error of the Ruttan pyrite, and is on average 0.12‰ ($\delta^{34}S$), 0.03‰ ($\Delta^{33}S$), and 0.14‰ ($\Delta^{36}S$) for big-spot analyses, and 0.12‰ ($\delta^{34}S$) and 0.08‰ ($\Delta^{33}S$) for small-spot analyses. The reproducibility is assessed by the value of two standard deviations of Ruttan pyrite in each session, and is on average 0.60‰ ($\delta^{34}S$), 0.19‰ ($\Delta^{33}S$), and 0.35‰ ($\Delta^{36}S$) for big-spot analyses, and 0.54‰ ($\delta^{34}S$) and 0.25‰ ($\Delta^{33}S$) for small-spot analyses.

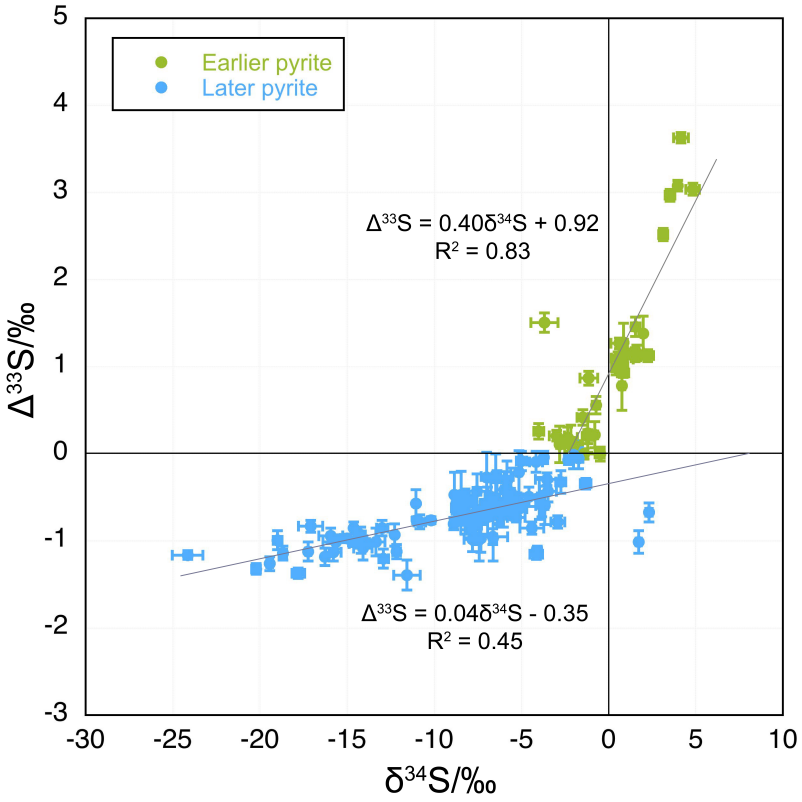

Figure 3.2. $\delta^{34}S$-$\Delta^{33}S$ plot of the data for earlier and later pyrite. The data include the results of both big-spot and small-spot analyses. Error bar is the value of two standard errors. Due to the mixing of rim with considerably negative $\delta^{34}S$, the datapoint of (-3.67‰, 1.51‰) was not included when yielding the line for $\Delta^{33}S$-positive datapoints.

$\delta^{34}S$ shows a relatively large range, varying from -24.15‰ to 4.83‰. By comparison, $\Delta^{33}S$ and $\Delta^{36}S$ are restricted to a narrow range, -1.37‰ to 3.63‰ and -2.94‰ to 1.83‰, respectively.

The majority of core-rim textured pyrite grains show $\Delta^{33}S$-positive (0 to 1.51‰) cores and $\Delta^{33}S$-negative (-1.37‰ to -0.08‰) rims. The $\Delta^{33}S$-positive cores have $\delta^{34}S$ of -3.67‰ to 2.25‰, and the $\Delta^{33}S$-negative rims have characteristic $\delta^{34}S$ of -18.68 to -3.47‰. Minor core-rim textured pyrite grains have core and rim with $\Delta^{33}S$ of the same sign, and only one grain has $\Delta^{33}S$-negative core and $\Delta^{33}S$-positive rim. The pyrite grains with no internal textures display two groups of multiple sulphur isotopic compositions. One group is characterized by negative $\delta^{34}S$ (-1.32‰ to -24.15‰), negative $\Delta^{33}S$ (-0.01‰ to -1.39‰) and positive $\Delta^{36}S$ (0.03‰ to 1.28‰). The other group exhibits positive $\Delta^{33}S$ (0.10‰ to 3.63‰) and negative $\Delta^{36}S$ (-2.94‰ to -0.18‰), with both positive and negative $\delta^{34}S$ (-4.01‰ to 4.83‰).

In the $\delta^{34}S$-$\Delta^{33}S$ plot, both $\Delta^{33}S$-positive and $\Delta^{33}S$-negative datapoints show good linear correlations between $\delta^{34}S$ and $\Delta^{33}S$ (Fig. 3.2). The former yields a line of $\Delta^{33}S = 0.40\delta^{34}S + 0.92$ ($R^2 = 0.83$), and the latter produces a line of $\Delta^{33}S = 0.04\delta^{34}S - 0.35$ ($R^2 = 0.45$). In the $\Delta^{33}S$-$\Delta^{36}S$ plot, most of the data are plotted close to the Archean Reference Array while distant from the Biological Fractionation Line (Fig. 3.3).

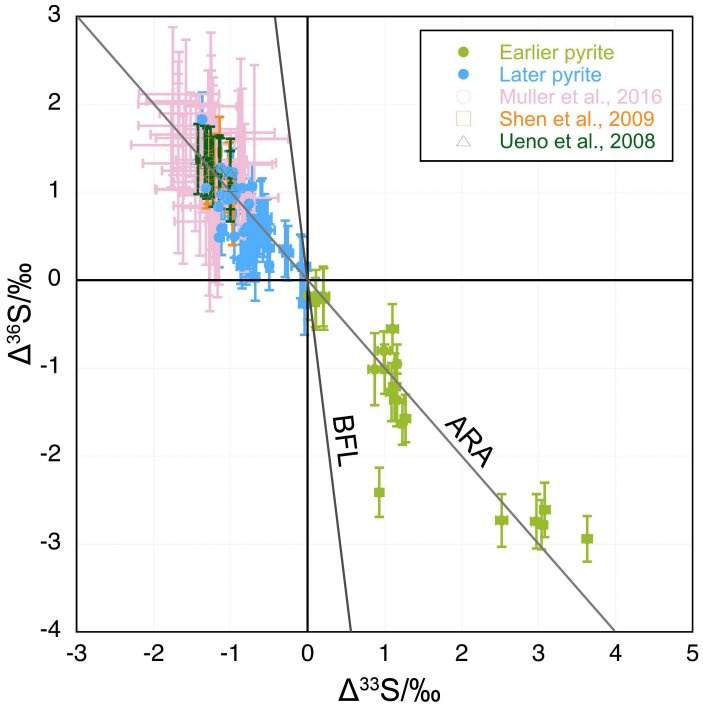

Figure 3.3. $\Delta^{33}S$-$\Delta^{36}S$ plot of the data for earlier and later pyrite. The $\Delta^{33}S$ and $\Delta^{36}S$ data of the Dresser barite from Ueno et al. (2008), Shen et al. (2009), and Muller et al. (2016) are also plotted. Error bar is the value of two standard errors. ARA is Archean Reference Array with a $\Delta^{36}S/\Delta^{33}S$ slope of around -1 (Farquhar et al., 2001), and BFL is Biological Fractionation Line with a $\Delta^{36}S/\Delta^{33}S$ slope of around -7 (Ono et al., 2006).

5. Discussion

5.1 The generations of pyrite

The majority of core-rim textured pyrite grains have $\Delta^{33}S$-positive cores and $\Delta^{33}S$-negative rims, indicating that $\Delta^{33}S$-positive pyrite is earlier than $\Delta^{33}S$-negative pyrite. Based on similar multiple sulphur isotopic composition, pyrite grains with no internal textures can also be categorized into two generations: earlier $\Delta^{33}S$-positive pyrite and later $\Delta^{33}S$-negative pyrite.

The linear correlations between $\delta^{34}S$ and $\Delta^{33}S$ of the two generations of pyrite (Fig. 3.2) suggest mixing between two sulphur end members respectively: a sulphur mass independent fractionation (S-MIF) end member and a sulphur mass dependent fractionation (S-MDF) end member. The S-MIF end member for generation one pyrite is $\delta^{34}S$- and $\Delta^{33}S$-positive, and that for generation two pyrite is $\delta^{34}S$- and $\Delta^{33}S$-negative (Fig. 3.2). Based on the spatially and temporally close-related volcanism during the formation of the chert-barite unit (Nijman et al., 1998; Van Kranendonk and Pirajno, 2004), the S-MDF end member of the two generations of pyrite can be magmatic sulphur. As indicated by the linear equation, the magmatic sulphur for generation one pyrite has $\Delta^{33}S$ of 0 and $\delta^{34}S$ of -2.3‰, and that for generation two pyrite has $\Delta^{33}S$ of 0 and $\delta^{34}S$ of 8.8‰.

$\Delta^{33}S$ and $\Delta^{36}S$ of both generations of pyrite are plotted close to the Archean Reference Array (Fig. 3.3). Since $\Delta^{33}S$-positive elemental sulphur and $\Delta^{33}S$-negative sulphate are the two main products of SO_2 photolysis in the atmosphere, the $\Delta^{33}S$-positive generation one pyrite and $\Delta^{33}S$-negative barite (Ueno et al., 2008; Shen et al., 2009; Muller et al., 2016) are probably simultaneously produced and sequestered products of SO_2 photolysis.

5.2 Sulphate reduction or elemental sulphur disproportionation?

Previous studies have proposed that positive $\Delta^{33}S$ corresponds to elemental sulphur disproportionation and negative $\Delta^{33}S$ to sulphate reduction, generally because elemental sulphur carries positive $\Delta^{33}S$ whereas sulphate carries negative $\Delta^{33}S$ (Philippot et al., 2007; Shen et al., 2009; Wacey et al., 2010). The significantly negative $\delta^{34}S$ of microscopic pyrite within barite has been attributed to microbial sulphate reduction based on negative $\Delta^{33}S$ measured from pyrite sulphur (chromium reducible sulphur) extracted from bulk barite (Ueno et al., 2008; Shen et al., 2009). In contrast, in-situ analyses of these tiny pyrite grains by SIMS

show positive $\Delta^{33}S$, which has led to a conclusion of elemental sulphur disproportionation rather than sulphate reduction (Philippot et al., 2007).

Here we did not analyze the microscopic pyrite grains aligning in an array within the barite due to the small sizes (less than 10 μm). Although some "grains" seem big enough for small-spot analyses, sodium hypochlorite solution etching and BSE imaging reveal that they are actually pyrite clusters composed of multiple grains, the sulphur isotopic compositions of which thus represent mixed sulphur components.

Two generations of pyrite have been revealed here. The $\Delta^{33}S$-positive generation one pyrite is mostly enriched in ^{34}S, which is unlikely to be biogenic since microbes prefer light sulphur (i.e., ^{32}S). Thus elemental sulphur disproportionation is less likely. The $\Delta^{33}S$-negative generation two pyrite is depleted in ^{34}S to variable degrees, and some pyrite grains associated with barite show considerably negative $\delta^{34}S$ (down to -24‰). Additionally, some generation two pyrite grains contain barite inclusions (Fig. 3.1), which can be relicts. Furthermore, barite and generation two pyrite have similar negative $\Delta^{33}S$. Therefore, the second generation of pyrite is most likely to be products of barite reduction.

On the other hand, due to the complicated formation processes of pyrite, it still needs further confirmation whether it is appropriate to simply use the $\Delta^{33}S$ sign of pyrite as an indicator of sulphate reduction and sulphur disproportionation.

According to previous experimental studies on the formation pathways of pyrite (Rickard, 2012 and references therein), Fe^{2+} is firstly combined with HS^- (magmatic, no S-MIF) or S^{2-} (sulphate reduction-derived sulphide, negative $\Delta^{33}S$ or magmatic H_2S, no S-MIF), forming an intermediate [FeS] with negative $\Delta^{33}S$ or no S-MIF ($Fe^{2+} + HS^- = [FeS] + H^+$ or $Fe^{2+} + S^{2-} = [FeS]$). Subsequently, [FeS] reacts with hydrogen sulphide ($[FeS] + H_2S = FeS_2 + H_2$, Rickard, 1997; Richard and Luther, 1997) or polysulphide ($[FeS] + S_n^{2-} = FeS_2 + S_{n-1}^{2-}$, Rickard, 1975, n>=5, Luther, 1990), forming pyrite.

For the hydrogen sulphide pathway, H_2S can be derived from sulphate reduction, sulphur disproportionation, or magmatic H_2S. When mixed with the $\Delta^{33}S$-negative or S-MDF [FeS], pyrite products can have negative, positive, or 0 $\Delta^{33}S$. Pyrite with negative $\Delta^{33}S$ can unambiguously indicate sulphate reduction with or without elemental sulphur disproportionation. However, when elemental sulphur disproportionation is involved, it is

ambiguous whether sulphate reduction or elemental sulphur disproportionation induces the large drifts towards negative $\delta^{34}S$. The same goes for pyrite with positive $\Delta^{33}S$.

For the polysulphide pathway, S_n^{2-} is derived from the combination of elemental sulphur with S^{2-} ($S_{n-1} + S^{2-} = S_n^{2-}$). The S^{2-} can be derived from sulphate reduction, sulphur disproportionation, or magmatic H_2S. SO_2 photolysis-derived sulphate is easily diluted by magmatic SO_2-derived sulphate, which possesses no S-MIF, and all previous photochemical experiments show much larger magnitudes of positive $\Delta^{33}S$ than negative $\Delta^{33}S$ (Ono et al., 2017 and references therein). Thus, S_n^{2-} is most likely to be $\Delta^{33}S$-positive, even if S^{2-} is sulphate reduction-derived. It has been demonstrated that all the sulphur in pyrite synthesized via the polysulphide pathway is derived entirely from S_n^{2-} (Butler et al., 2004). As such, the pyrite product of the polysulphide pathway is $\Delta^{33}S$-positive, even if in fact sulphate reduction is contributor.

5.3 Biological or abiological sulphate reduction?

Although the second generation of pyrite shows characteristic negative $\Delta^{33}S$ and considerably negative $\delta^{34}S$ indicative of possible microbial sulphate (barite) reduction, the $\Delta^{33}S$-$\Delta^{36}S$ plot exhibits no apparent biological fractionations from the associated barite despite variable degrees of deviations from the Archean Reference Array (Fig. 3.3), suggesting that abiological processes are still possible.

It is noteworthy that the highest temperature where the sulphate reducers (discovered so far) can live is 110 °C (Jørgensen et al., 1992), lower than the temperature of the hydrothermal fluids associated with the Dresser Formation (300 °C at depth to 120 °C near the paleosurface, Harris et al., 2009).

Additionally, although the considerable fractionations in $\delta^{34}S$ of pyrite have been extensively interpreted as resulting from sulphur-associated metabolisms, abiological processes can also produce such large fractionations, e.g., thermochemical sulphate reduction (TSR, Machel, 2001), sulphate reduction by ferrous iron in minerals (Ohmoto and Goldhaber, 1997), and magmatic sulphur dioxide disproportionation ($4SO_2 + 4H_2O = H_2S + 3SO_4^{2-} + 6H^+$, Cameron and Hattori, 1987). Since experiments have shown that TSR mainly yields $\Delta^{33}S$ shifts without inducing variations in $\Delta^{36}S$ due to magnetic isotope effects (Oduro et al., 2011), while generation two pyrite displays a similar range in $\Delta^{36}S$ to $\Delta^{33}S$, thus TSR is unlikely. Due to

the lack of an endmember with significantly depleted $\delta^{34}S$ and $\Delta^{33}S$ of 0, magmatic sulphur dioxide disproportionation can also be excluded. Nevertheless, experiments of sulphate reduction by ferrous iron-bearing minerals under hydrothermal conditions induced large fractionations (ca. 20‰) in $\delta^{34}S$ (Ohmoto and Goldhaber, 1997). The Dresser Formation has been subjected to multiple hydrothermal events that produced the chert-barite unit. Additionally, the study on the composition of associated fluid inclusions revealed a population rich in Fe (Foriel et al., 2004), which can potentially act as the reductant.

Therefore, sulphate reduction by inorganic materials under hydrothermal conditions is still a possibility of producing the considerably negative $\delta^{34}S$ observed in the second generation of pyrite in Dresser Formation.

6. Concluding remarks

A combination of sodium hypochlorite etching, BSE imaging, and multiple sulphur isotopes revealed two generations of pyrite in the chert-barite unit of the 3.49 Ga Dresser Formation: generation one pyrite has positive $\Delta^{33}S$, while generation two pyrite is characterized by negative $\Delta^{33}S$ and variably negative $\delta^{34}S$.

If negative $\Delta^{33}S$ corresponds to sulphate reduction and positive $\Delta^{33}S$ to elemental sulphur disproportionation as previous studies proposed, generation two pyrite with considerably depleted ^{34}S is $\Delta^{33}S$-negative, suggesting that sulphate reduction is more likely. However, the $\Delta^{33}S$-$\Delta^{36}S$ plot shows no apparent biological fractionations from the associated Dresser barite for the generation two pyrite. Additionally, some other evidence do not support sulphur-involving biological activities as well. For instance, the highest temperature available for sulphate reducers is much lower than the temperature of the hydrothermal fluids related to the chert-barite unit, and abiological process is also able to induce large shifts in $\delta^{34}S$. Thus it is still equivocal whether the Dresser Formation records the earliest sulphur-associated metabolism on the Earth. Future work such as laboratory experimental barite reduction should be conducted to further confirm whether abiological sulphate reduction can induce large fractionations in $\delta^{34}S$.

References

Buick, R., Dunlop, J.S.R., Groves, D.I., 1981. Stromatolite recognition in ancient rocks: an appraisal of irregularly laminated structures in an Early Archaean chert-barite unit from North Pole, Western Australia. Alcheringa (5): 161-181.

Buick, R., and Dunlop, J.S.R., 1990. Evaporitic sediments of Early Archaean age from the Warrawoona Group, North Pole, Western Australia. Sedimentology 37 (2): 247-277.

Buick, R., Thornett, J.R., McNaughton, N.J., Smith, J.B., Barley, M.E., Savage, M., 1995. Record of emergent continental crust ~3.5 billion years ago in the Pilbara craton of Australia. Nature 375: 574-577.

Butler, I.B., Böttcher, M.E., Rickard, D., Oldroyd, A., 2004. Sulfur isotope partitioning during experimental formation of pyrite via the polysulfide and hydrogen sulfide pathways: implications for the interpretation of sedimentary and hydrothermal pyrite isotope records. Earth and Planetary Science Letters 228 (3-4): 495-509.

Cameron, E.M., and Hattori, K., 1987. Archean gold mineralization and oxidized hydrothermal fluids. Economic Geology 82 (5): 1177-1191.

Crowe, D.E., and Vaughan, R.G., 1996. Characterization and use of isotopically homogeneous standards for in situ laser microprobe analysis of $^{34}S/^{32}S$ ratios. American Mineralogist 81 (1-2): 187-193.

Farquhar, J., Savarino, J., Airieau, S., Thiemens, M.H., 2001. Observation of wavelength-sensitive mass-independent sulfur isotope effects during SO_2 photolysis: Implications for the early atmosphere. Journal of Geophysical Research 106 (E12): 32829-32839.

Foriel, J., Philippot, P., Rey, P., Somogyi, A., Banks, D., Ménez, B., 2004. Biological control of Cl/Br and low sulfate concentration in a 3.5-Gyr-old seawater from North Pole, Western Australia. Earth and Planetary Science Letters 228 (3-4): 451-463.

Groves, D.I., Dunlop, J.S.R., Buick, R., 1981. An Early Habitat of Life. Scientific American 245 (4): 64-73.

Harris, A.C., White, N.C., McPhie, J., Bull, S.W., Line, M.A., Skrzeczynski, R., Mernagh, T.P., Tosdal, R.M., 2009. Early Archean Hot Springs above Epithermal Veins, North Pole, Western Australia: New Insights from Fluid Inclusion Microanalysis. Economic Geology 104 (6): 793-814.

Hickman, A.H., 1973. The North Pole barite deposits, Pilbara Goldfield. Annual Report of Geological Survey of Western Australia: 57-60.

Hickman, A.H., 1983. Geology of the Pilbara Block and its environs. Geological Survey of Western Australia Bulletin 127.

Ireland, T.R., Schram, N., Holden, P., Lanc, P., Ávila, J., Armstrong, R., Amelin, Y., Latimore, A., Corrigan, D., Clement, S., Foster, J.J., Compston, W., 2014. Charge-mode electrometer

measurements of S-isotopic compositions on SHRIMP-SI. International Journal of Mass Spectrometry 359: 26-37.

Jørgensen, B.B., Isaksen, M.F., Jannasch, H.W., 1992. Bacterial Sulfate Reduction Above 100°C in Deep-Sea Hydrothermal Vent Sediments. Science 258 (5089): 1756-1757.

Lambert, I.B., Donnelly, T.H., Dunlop, J.S.R., Groves, D.I., 1978. Stable isotopic compositions of early Archaean sulphate deposits of probable evaporitic and volcanogenic origins. Nature 276: 808-811.

Luther, G.W., 1990. The frontier-molecular-orbital theory approach in geochemical processes. *in* Stumm W. (Ed.), Aquatic Chemical Kinetics. Wiley, New York, p. 173-198.

Machel, H.G., 2001. Bacterial and thermochemical sulfate reduction in diagenetic setting - old and new insights. Sedimentary Geology 140 (1-2): 143-175.

Muller, É., Philippot, P., Rollion-Bard, C., Cartigny, P., 2016. Multiple sulfur-isotope signatures in Archean sulfates and their implications for the chemistry and dynamics of the early atmosphere. Proceedings of the National Academy of Sciences of the United States of America 113 (27): 7432-7437.

Nelson, D.R., 2002. Compilation of geochronology data, 2001. *in* Compilation of geochronology data, October 2004 update. Western Australia Geological Survey.

Nijman, W., de Bruijne, K.H., Valkering, M.E., 1998. Growth fault control of Early Archaean cherts, barite mounds and chert-barite veins, North Pole Dome, Eastern Pilbara, Western Australia. Precambrian Research 88 (1-4): 25-52.

Noffke, N., Christian, D., Wacey, D., Hazen, R.M., 2013. Microbially Induced Sedimentary Structures Recording an Ancient Ecosystem in the ca. 3.48 Billion-Year-Old Dresser Formation, Pilbara, Western Australia. Astrobiology 13 (12): 1103-1124.

Oduro, H., Harms, B., Sintim, H.O., Kaufman, A.J., Cody, G., Farquhar, J., 2011. Evidence of magnetic isotope effects during thermochemical sulfate reduction. Proceedings of the National Academy of Sciences of the United States of America 108 (43): 17635-17638.

Ohmoto, H., and Goldhaber, M.B., 1997. Sulfur and carbon isotopes. *in* Barnes, H.L. (Ed.), Geochemistry of Hydrothermal Ore Deposits. Wiley, New York, p. 517-611.

Ono, S., 2017. Photochemistry of Sulfur Dioxide and the Origin of Mass-Independent Isotope Fractionation in Earth's Atmosphere. Annual Review of Earth and Planetary Sciences: 45: 301-329.

Ono, S., Wing, B., Johnston, D., Farquhar, J., Rumble, D., 2006. Mass-dependent fractionation of quadruple stable sulfur isotope system as a new tracer of sulfur biogeochemical cycles. Geochimica et Cosmochimica Acta 70 (9): 2238-2252.

Philippot, P., Van Zuilen, M., Lepot, K., Thomazo, C., Farquhar, J., Van Kranendonk, M.J., 2007. Early Archaean Microorganisms Preferred Elemental Sulfur, Not Sulfate. Science 317 (5844): 1534-1537.

Rickard, D.T., 1975. Kinetics and mechanism of pyrite formation at low temperatures. American Journal of Science 275 (6): 636-652.

Rickard, D., 1997. Kinetics of pyrite formation by the H_2S oxidation of iron (II) monosulfide in aqueous solutions between 25 and 125 °C: The rate equation. Geochimica et Cosmochimica Acta 61 (1): 115-134.

Rickard, D., 2012. Sulfidic Sediments and Sedimentary Rocks. *in* Developments in Sedimentology. Elsevier 65: 1-766.

Rickard, D., and Luther, G.W., 1997. Kinetics of pyrite formation by the H_2S oxidation of iron (II) monosulfide in aqueous solutions between 25 and 125 °C: The mechanism. Geochimica et Cosmochimica Acta 61 (1): 135-147.

Runnegar, B., Dollase, W.A., Ketcham, R.A., Colbert, M., Carlson, W.D., 2001. Early Archean sulfates from Western Australia first formed as hydrothermal barites not gypsum evaporates. Geological Society of America Annual Meeting and Exposition Abstracts: A404.

Shen, Y., Buick, R., Canfield, D.E., 2001. Isotopic evidence for microbial sulphate reduction in the early Archaean era. Nature 410: 77-81.

Shen, Y., Farquhar, J., Masterson, A., Kaufman, A.J., Buick, R., 2009. Evaluating the role of microbial sulfate reduction in the early Archean using quadruple isotope systematics. Earth and Planetary Science Letters 279 (3-4): 383-391.

Thorpe, R.I., Hickman, A.H., Davis, D.W., Mortensen, J.K., Trendall, A.F., 1992a. Constraints to models for Archean lead evolution from precise zircon U-Pb geochronology for the Marble Bar region, Pilbara Craton, Western Australia. *in* Glover, J.E. and Ho, S.E. (Editors), The Archaean: Terrains, Processes and Metallogeny. Geology Department and University Extension, The University of Western Australia, Publication 22, p. 395-406.

Thorpe, R.I., Hickman, A.H., Davis, D.W., Mortensen, J.K., Trendall, A.F., 1992b. U-Pb zircon geochronology of Archaean felsic units in the Marble Bar region, Pilbara Craton, Western Australia. Precambrian Research 56 (3-4): 169-189.

Ueno, Y., Yamada, K., Yoshida, N., Maruyama, S., Isozaki, Y., 2006. Evidence from fluid inclusions for microbial methanogenesis in the early Archaean era. Nature 440: 516-519.

Ueno, Y., Ono, S., Rumble, D., Maruyama, S., 2008. Quadruple sulfur isotope analysis of ca. 3.5 Ga Dresser Formation: New evidence for microbial sulfate reduction in the early Archean. Geochimica et Cosmochimica Acta 72 (23): 5675-5691.

Van Kranendonk, M.J., and Pirajno, F., 2004. Geochemistry of metabasalts and hydrothermal alteration zones associated with c. 3.45 Ga chert and barite deposits: implications for the geological setting of the Warrawoona Group, Pilbara Craton, Australia. Geochemistry: Exploration, Environment, Analysis 4: 253-278.

Van Kranendonk, M.J., Philippot, P., Lepot, K., Bodorkos, S., Pirajno, F., 2008. Geological setting of Earth's oldest fossils in the ca. 3.5 Ga Dresser Formation, Pilbara Craton, Western Australia. Precambrian Research 167 (1-2): 93-124.

Wacey, D., McLoughlin, N., Whitehouse, M.J., Kilburn, M.R., 2010. Two coexisting sulfur metabolisms in a ca. 3400 Ma sandstone. Geology 38 (12): 1115-1118.

Whitehouse, M.J., 2013. Multiple Sulfur Isotope Determination by SIMS: Evaluation of Reference Sulfides for $\Delta^{33}S$ with Observations and a Case Study on the Determination of $\Delta^{36}S$. Geostandards and Geoanalytical Research 37 (1): 19-33.

Williford, K.H., Van Kranendonk, M.J., Ushikubo, T., Kozdon, R., Valley, J.W., 2011. Constraining atmospheric oxygen and seawater sulfate concentrations during Paleoproterozoic glaciation: In situ sulfur three-isotope microanalysis of pyrite from the Turee Cree Group, Western Australia. Geochimica et Cosmochimica Acta 75 (19): 5686-5705.

Table 3.3 All quadruple and triple sulphur isotopic composition data of pyrite from the ca. 3.49 Ga Dresser Formation.

Title	Sample	Location in the grain	Pyrite generation	$\delta^{33}S$/‰	1σ	$\delta^{34}S$/‰	1σ	$\delta^{36}S$/‰	1σ	$\Delta^{33}S$/‰	1σ	$\Delta^{36}S$/‰	1σ	CPS_$^{32}S^-$	CPS_$^{33}S^-$	CPS_$^{34}S^-$	CPS_$^{36}S^-$
M-12_36.5	PDP2c_97.17-97.20m	Core	1	1.65	0.02	0.82	0.11	-0.08	0.12	1.23	0.02	-1.63	0.12	1164300679	9114136	51021302	172139
1801M_11_14.1	PDP2c_97.17-97.20m	Rim_with slight mixing of core	2	-2.24	0.06	-4.16	0.19	-7.73	0.19	-0.09	0.06	0.16	0.18	935560813	7288276	40719690	136715
1801M_11_14.2	PDP2c_97.17-97.20m	Rim_with slight mixing of core	2	-2.11	0.04	-3.53	0.34	-6.34	0.17	-0.29	0.03	0.36	0.16	941092897	7332620	40979121	137823
D22_5	PDP2b_90.94-90.97m	Core_with slight mixing of rim	1	-0.38	0.07	-3.67	0.39			1.51	0.06			589722365	4603378	25701263	
D22_5'	PDP2b_90.94-90.97m	Rim	2	-10.03	0.06	-17.23	0.07			-1.12	0.06			603490689	4666737	25945441	
D22_5''	PDP2b_90.94-90.97m	Rim	2	-10.81	0.04	-18.68	0.11			-1.14	0.04			609727571	4711978	26179250	
D22_5.1	PDP2b_90.94-90.97m	Rim	2	-10.58	0.02	-17.80	0.18	-31.73	0.15	-1.37	0.03	1.83	0.15	1107796684	8565692	47598740	158559
D20_25.2	PDP2c_97.17-97.20m	Core	2	-1.96	0.03	-3.72	0.11	-7.32	0.18	-0.04	0.04	-0.27	0.17	997512774	7783305	43490713	146401
D20_25.1	PDP2c_97.17-97.20m	Rim	2	-4.73	0.05	-8.15	0.27	-14.86	0.17	-0.52	0.04	0.57	0.18	901208760	7010355	39124805	131338
D20_5.1_2	PDP2b_94.69-94.74m	Core_with slight mixing of rim	2	-3.23	0.03	-4.09	0.13	-7.18	0.14	-1.12	0.03	0.59	0.15	998688609	7780655	43525302	146490
D20_5.1_1	PDP2b_94.69-94.74m	Rim	2	-3.13	0.03	-4.41	0.35	-8.20	0.14	-0.85	0.03	0.16	0.12	977866878	7619155	42628485	143384
1801M_11_17.1	PDP2c_97.17-97.20m	Core	1	2.29	0.03	2.25	0.16	3.06	0.19	1.13	0.04	-1.21	0.19	910643027	7131426	39940152	134906
1801M_11_17.2	PDP2c_97.17-97.20m	Rim	2	-4.90	0.03	-8.32	0.17	-14.93	0.16	-0.61	0.04	0.81	0.16	814064300	6327414	35285902	118050
1801M-12_3'	PDP2c_97.17-97.20m	Core	1	0.28	0.04	-1.14	0.25	-3.18	0.16	0.87	0.04	-1.01	0.21	1125007453	8791698	49152824	165673
1801M-12_3	PDP2c_97.17-97.20m	Rim	2	-6.37	0.04	-10.83	0.17	-20.18	0.12	-0.78	0.04	0.31	0.14	1128644290	8763050	48818527	163109
1801M-12_6	PDP2c_97.17-97.20m	Core	1	1.58	0.03	0.61	0.24	-0.40	0.13	1.27	0.03	-1.57	0.13	1108451399	8676411	48510219	163418
1801M-12_6	PDP2c_97.17-97.20m	Rim	2	-2.22	0.06	-3.47	0.24			-0.43	0.06			637793917	4971825	27811512	
M-12_36.1	PDP2c_97.17-97.20m	Core	1	1.36	0.03	0.83	0.16	-0.83	0.17	0.93	0.02	-2.41	0.14	1185600096	9277152	51967148	175496
1801M-12_8	PDP2c_97.17-97.20m	Core	1	1.39	0.04	0.55	0.19	0.49	0.15	1.10	0.04	-0.55	0.14	1124917130	8798956	49215878	165864
1801M_11_9.1	PDP2c_97.17-97.20m	Core	1	1.51	0.03	0.80	0.30	0.25	0.16	1.09	0.03	-1.27	0.17	1017969462	7965142	44566989	150292
1801M_11_11	PDP2c_97.17-97.20m	Core	1	-0.24	0.04	-0.48	0.11	-1.07	0.13	0.00	0.04	-0.17	0.14	943155738	7367982	41234588	138771
1801M_11_16	PDP2c_97.17-97.20m	Core	1	1.99	0.05	1.61	0.19	1.70	0.12	1.16	0.04	-1.36	0.15	988646701	7742011	43301162	145996
D20_5.1_3	PDP2b_94.69-94.74m	Core	2	-3.46	0.03	-5.29	0.25	-9.42	0.19	-0.73	0.03	0.60	0.19	980170225	7637025	42698781	143497
D20_21.1	PDP2c_97.17-97.20m	Core	1	-1.32	0.03	-2.97	0.22	-5.85	0.15	0.21	0.03	-0.21	0.18	930627063	7266356	40627754	136879
D20_32.1	PDP2c_97.17-97.20m	Rim	2	-3.56	0.04	-6.40	0.46	-11.80	0.13	-0.26	0.03	0.31	0.15	997760716	7772895	43411347	145909

Title	Sample	Location in the grain	Pyrite generation	$\delta^{33}S$/‰	1σ	$\delta^{34}S$/‰	1σ	$\delta^{36}S$/‰	1σ	$\Delta^{33}S$/‰	1σ	$\Delta^{36}S$/‰	1σ	CPS_$^{32}S^-$	CPS_$^{33}S^-$	CPS_$^{34}S^-$	CPS_$^{36}S^-$
M-11_36.1	PDP2c_97.17-97.20m	No internal texture	2	-6.45	0.02	-11.01	0.06	-20.26	0.12	-0.76	0.02	0.55	0.12	1127087697	8754198	48826195	163498
M-11_36.2	PDP2c_97.17-97.20m	No internal texture	2	-4.53	0.02	-7.44	0.13	-13.38	0.12	-0.70	0.02	0.70	0.12	1149879638	8947338	49987199	167891
M-11_36.3	PDP2c_97.17-97.20m	No internal texture	2	-3.56	0.02	-5.53	0.04	-10.26	0.11	-0.71	0.02	0.22	0.12	1174187598	9143741	51137220	171947
M-11_36.3'	PDP2c_97.17-97.20m	No internal texture	2	-6.01	0.02	-10.18	0.07	-18.94	0.10	-0.76	0.02	0.31	0.09	1166779110	9062962	50570899	169302
M-11_26.3"	PDP2c_97.17-97.20m	No internal texture	2	-3.98	0.02	-6.76	0.13	-12.63	0.14	-0.50	0.02	0.17	0.14	1162790716	9049292	50561266	169788
M-11_36.4	PDP2c_97.17-97.20m	No internal texture	2	-4.05	0.01	-6.60	0.10	-11.95	0.14	-0.64	0.02	0.55	0.12	1201201810	9350084	52261451	175751
M-11_36.5	PDP2c_97.17-97.20m	No internal texture	2	-4.28	0.02	-6.90	0.08	-12.01	0.12	-0.72	0.02	1.07	0.13	1220003919	9495371	53063154	178339
M-11_36.5'	PDP2c_97.17-97.20m	No internal texture	2	-4.73	0.02	-7.81	0.07	-14.19	0.09	-0.70	0.02	0.59	0.09	1200849674	9341437	52195073	175192
M-12_36.5'	PDP2c_97.17-97.20m	No internal texture	2	-4.99	0.02	-8.47	0.09	-15.40	0.12	-0.62	0.02	0.63	0.12	1146339865	8914653	49777863	167079
M-12_36.4	PDP2c_97.17-97.20m	No internal texture	2	-4.46	0.02	-7.32	0.07	-13.83	0.13	-0.68	0.02	0.03	0.13	1145835667	8913690	49795790	167184
1801M_11_3	PDP2c_97.17-97.20m	No internal texture	2	-4.27	0.04	-7.13	0.12	-12.73	0.19	-0.59	0.04	0.78	0.19	1014317686	7889535	44029223	147497
1801M_11_5	PDP2c_97.17-97.20m	No internal texture	2	-4.90	0.04	-8.40	0.27	-15.17	0.14	-0.56	0.05	0.72	0.13	1003250032	7796480	43443699	145375
1801M_11_4	PDP2c_97.17-97.20m	No internal texture	2	-3.20	0.04	-5.09	0.19	-9.09	0.14	-0.57	0.04	0.57	0.15	1033587423	8052332	44988700	151136
1038_47_6.1	PDP2c_97.17-97.20m	No internal texture	2	-4.40	0.03	-7.18	0.14	-13.01	0.14	-0.69	0.03	0.59	0.16	988424787	7687506	42928374	143869
1038_47_7.2	PDP2c_97.17-97.20m	No internal texture	2	-5.38	0.04	-8.88	0.10	-16.54	0.16	-0.80	0.04	0.27	0.16	971787687	7552804	42113039	140945
1801M-12_1	PDP2c_97.17-97.20m	No internal texture	2	-5.13	0.03	-8.48	0.17	-15.19	0.13	-0.76	0.03	0.87	0.15	1110354205	8627554	48170455	161526
D20_18.2	PDP2c_97.17-97.20m	No internal texture	2	-4.66	0.04	-7.97	0.14	-14.40	0.11	-0.54	0.04	0.70	0.11	1023406421	7963190	44434229	149075
D20_14	PDP2c_97.17-97.20m	No internal texture	2	-4.02	0.03	-6.45	0.11	-11.87	0.15	-0.69	0.03	0.35	0.15	1007556042	7842975	43816485	147125
D20_32.2	PDP2c_97.17-97.20m	No internal texture	2	-5.14	0.03	-8.76	0.13	-15.91	0.12	-0.62	0.03	0.66	0.13	1006228208	7824228	43663042	146359
M-12_6	PDP2c_97.17-97.20m	No internal texture	2	-4.71	0.04	-7.60	0.07	-13.78	0.16	-0.79	0.04	0.60	0.19	1290906011	10117831	56308642	196416
M-12_7	PDP2c_97.17-97.20m	No internal texture	2	-4.50	0.02	-7.27	0.05	-13.52	0.13	-0.75	0.03	0.24	0.12	1340963727	10516015	58529010	204311
M-12_8	PDP2c_97.17-97.20m	No internal texture	2	-4.01	0.02	-6.47	0.13	-11.82	0.21	-0.67	0.03	0.45	0.18	1151552676	9033586	50297296	175377
M-12_11	PDP2c_97.17-97.20m	No internal texture	2	-4.76	0.02	-8.28	0.15	-15.31	0.15	-0.49	0.02	0.37	0.14	1374445761	10774103	59919599	208677
M-12_13	PDP2c_97.17-97.20m	No internal texture	2	-3.40	0.03	-5.46	0.15	-9.92	0.12	-0.58	0.03	0.44	0.12	1273789048	10006526	55758946	194877
1038-48_2_1	PDP2b_94.69-94.74m	No internal texture	2	-4.37	0.04	-6.64	0.43	-12.07	0.13	-0.95	0.05	0.50	0.12	1187655656	9233984	51551218	172878
1038-48_4	PDP2b_94.69-94.74m	No internal texture	2	-8.36	0.06	-14.09	0.26	-25.67	0.20	-1.08	0.07	0.93	0.21	1105538070	8563969	47573781	158000
1038-48_4'	PDP2b_94.69-94.74m	No internal texture	2	-9.67	0.04	-17.09	0.34	-31.68	0.14	-0.83	0.04	0.55	0.13	1119124494	8655280	48082135	159921
D25_2	PDP2b_94.69-94.74m	No internal texture	2	-8.28	0.05	-14.22	0.13	-25.80	0.14	-0.93	0.05	1.05	0.14	1247372484	9667730	53827381	179536

Title	Sample	Location in the grain	Pyrite generation	$\delta^{33}S$/‰	1σ	$\delta^{34}S$/‰	1σ	$\delta^{36}S$/‰	1σ	$\Delta^{33}S$/‰	1σ	$\Delta^{36}S$/‰	1σ	CPS_$^{32}S^-$	CPS_$^{33}S^-$	CPS_$^{34}S^-$	CPS_$^{36}S^-$
D25_3	PDP2b_94.69-94.74m	No internal texture	2	-8.41	0.04	-14.62	0.07	-26.55	0.13	-0.85	0.04	1.05	0.12	1269809379	9838344	54748533	182256
1038-48_2_2	PDP2b_94.69-94.74m	No internal texture	2	-9.29	0.05	-15.79	0.22	-28.51	0.15	-1.13	0.05	1.28	0.14	1193011696	9239265	51414329	171491
1038_47_2	PDP2b_94.69-94.74m	No internal texture	2	-2.29	0.03	-2.92	0.20	-5.13	0.14	-0.78	0.04	0.40	0.15	973309225	7585798	42441943	142852
D22_8.1	PDP2b_94.69-94.74m	No internal texture	2	-9.19	0.04	-15.94	0.34	-29.10	0.17	-0.94	0.04	0.97	0.17	1162660114	9003949	50041482	166594
D22_8.2	PDP2b_94.69-94.74m	No internal texture	2	-8.37	0.02	-14.19	0.15	-25.56	0.11	-1.03	0.03	1.24	0.11	1088863634	8439134	46969744	156583
D22_7.1	PDP2b_94.69-94.74m	No internal texture	2	-8.46	0.03	-14.38	0.25	-26.22	0.11	-1.03	0.03	0.92	0.12	1130291210	8759151	48769000	162803
D22_7.1'	PDP2b_94.69-94.74m	No internal texture	2	-8.71	0.02	-14.99	0.20	-27.05	0.12	-0.97	0.03	1.23	0.14	1184141204	9173324	51038005	170190
D22_5.3	PDP2b_90.94-90.97m	No internal texture	2	-11.79	0.03	-20.22	0.12	-37.02	0.10	-1.32	0.03	1.05	0.11	1113437351	8600501	47737891	158365
D22_5.2	PDP2b_90.94-90.97m	No internal texture	2	-13.67	0.02	-24.15	0.44	-44.55	0.11	-1.16	0.03	0.84	0.11	1101341979	8487881	47007796	155360
D20_1	PDP2b_94.69-94.74m	No internal texture	2	-7.41	0.04	-12.16	0.11	-22.00	0.14	-1.12	0.04	0.98	0.15	1039173223	8057444	44903916	149979
D20_6	PDP2b_94.69-94.74m	No internal texture	2	-4.95	0.04	-7.91	0.28	-14.73	0.12	-0.87	0.04	0.24	0.14	960780835	7473338	41723481	139900
D20_4.1	PDP2b_94.69-94.74m	No internal texture	2	-9.10	0.03	-15.65	0.37	-28.55	0.12	-1.01	0.04	0.98	0.12	981901829	7600619	42272977	140685
D20_4.2	PDP2b_94.69-94.74m	No internal texture	2	-3.29	0.03	-4.15	0.18	-7.38	0.15	-1.15	0.03	0.49	0.17	1011948257	7881438	44108578	148103
M-12_3	PDP2c_97.17-97.20m	No internal texture	1	1.66	0.02	0.97	0.18	0.89	0.10	1.16	0.02	-0.95	0.11	1355886715	10698624	59669716	209122
M-12_4	PDP2c_97.17-97.20m	No internal texture	1	1.41	0.03	0.80	0.15	0.52	0.14	1.00	0.03	-1.01	0.14	1344048321	10601850	59136388	207330
M-12_15	PDP2c_97.17-97.20m	No internal texture	1	1.21	0.03	0.44	0.13	0.03	0.12	0.99	0.04	-0.80	0.11	1444527609	11392342	63547017	222730
D22_1	PDP2b_90.94-90.97m	No internal texture	1	5.52	0.03	4.83	0.19	6.40	0.11	3.04	0.04	-2.78	0.14	1133161016	8902485	49831106	168249
D22_3	PDP2b_90.94-90.97m	No internal texture	1	5.76	0.03	4.15	0.22	4.96	0.15	3.63	0.03	-2.94	0.13	1159720957	9120000	50992581	172200
D22_9	PDP2b_90.94-90.97m	No internal texture	1	5.11	0.03	3.96	0.10	4.92	0.14	3.08	0.03	-2.61	0.15	1122904403	8820921	49333071	166863
D21_4	PDP2b_90.94-90.97m	No internal texture	1	4.78	0.04	3.52	0.14	3.95	0.17	2.97	0.03	-2.74	0.15	984955770	7733652	43248961	145741
D21_7	PDP2b_90.94-90.97m	No internal texture	1	4.13	0.03	3.14	0.13	3.25	0.14	2.52	0.03	-2.73	0.15	1011776970	7941764	44430639	149997
M-11_36.6	PDP2c_97.17-97.20m	No internal texture	1	-0.92	0.02	-1.98	0.07	-4.02	0.13	0.10	0.02	-0.25	0.14	1200288208	9373717	52471901	177016
1801M-12_5	PDP2c_97.17-97.20m	No internal texture	2	-1.26	0.02	-2.31	0.11	-4.23	0.15	-0.07	0.03	0.15	0.18	1110055831	8665381	48467017	163422
D20_18.1	PDP2c_97.17-97.20m	No internal texture	1	-0.97	0.02	-2.09	0.22	-4.18	0.17	0.11	0.02	-0.22	0.17	1002761679	7828138	43776211	147484
D20_29	PDP2c_97.17-97.20m	No internal texture	1	-0.42	0.04	-1.21	0.15	-2.48	0.13	0.20	0.04	-0.18	0.17	940041197	7346469	41097874	138708
D_33.24	PDP2c_97.17-97.20m	Core	1	2.40	0.09	1.98	0.05			1.38	0.10			215379197	1686770	9380829	
1801M_11_12	PDP2c_97.17-97.20m	Rim	1	-1.02	0.06	-2.35	0.28			0.19	0.06			560568298	4375126	24479133	
1801M_11_12'	PDP2c_97.17-97.20m	Rim	1	-0.35	0.04	-1.48	0.16			0.42	0.04			561483568	4385786	24536516	

Title	Sample	Location in the grain	Pyrite generation	$\delta^{33}S$/‰	1σ	$\delta^{34}S$/‰	1σ	$\delta^{36}S$/‰	1σ	$\Delta^{33}S$/‰	1σ	$\Delta^{36}S$/‰	1σ	CPS_$^{32}S^-$	CPS_$^{33}S^-$	CPS_$^{34}S^-$	CPS_$^{36}S^-$
1801M_11_15.2	PDP2c_97.17-97.20m	Core	1	1.92	0.04	1.52	0.12			1.14	0.04			595938083	4664960	26117403	
1801M_11_15.1	PDP2c_97.17-97.20m	Rim_with slight mixing of core	2	-2.66	0.05	-4.99	0.15			-0.08	0.06			573700320	4470306	24978373	
1801M_11_9.3	PDP2c_97.17-97.20m	Core	1	2.26	0.06	1.55	0.12			1.46	0.05			599195781	4690372	26257365	
1801M_11_9.4	PDP2c_97.17-97.20m	Rim_with slight mixing of core	1	0.19	0.05	-0.72	0.10			0.56	0.05			601257005	4698403	26297819	
1801M-12_2.2	PDP2c_97.17-97.20m	Core_slight mixing of adjacent pyrite grain	1	-0.73	0.03	-1.41	0.32			0.00	0.03			674320892	5265468	29457691	
1801M-12_2.1	PDP2c_97.17-97.20m	Rim	2	-3.81	0.07	-6.03	0.10			-0.70	0.07			586271252	4563571	25493610	
1038-47-1'	PDP2b_102.26-102.27m	Core_with slight mixing of later pyrite	2	-0.12	0.07	1.73	0.07			-1.01	0.06			378934462	2962293	16602187	
1038-47-1	PDP2b_102.26-102.27m	Rim	2	0.53	0.05	2.32	0.09			-0.67	0.06			379001603	2964881	16618922	
D_33.7	PDP2c_97.17-97.20m	Core	1	1.18	0.13	0.77	0.08			0.78	0.14			214367727	1679916	9328214	
D_33.8	PDP2c_97.17-97.20m	Rim	2	-3.31	0.12	-5.82	0.05			-0.31	0.12			187233142	1457778	8091142	
D_33.16	PDP2c_97.17-97.20m	Core	2	-2.87	0.14	-5.15	0.07			-0.21	0.13			212844644	1658371	9202984	
D_33.17	PDP2c_97.17-97.20m	Rim	1	-0.38	0.11	-1.21	0.05			0.24	0.11			219400666	1713705	9524504	
D_33.22	PDP2c_97.17-97.20m	Core	1	1.72	0.10	0.85	0.03			1.28	0.11			222333412	1739826	9672911	
D_33.23	PDP2c_97.17-97.20m	Rim	2	-2.48	0.11	-3.66	0.05			-0.59	0.11			216676665	1689838	9384389	
1801M_11_9.1	PDP2c_97.17-97.20m	Rim_with slight mixing of core	1	-0.97	0.08	-2.17	0.33			0.15	0.09			565870084	4415949	24715822	
1801M_11_9.2	PDP2c_97.17-97.20m	Rim_with slight mixing of core	1	-1.05	0.04	-2.08	0.22			0.03	0.04			584556670	4561955	25523632	
1801M-12_12.2	PDP2c_97.17-97.20m	Rim	2	-5.00	0.07	-7.80	0.25			-0.98	0.07			560960917	4362113	24348465	
D_33.19	PDP2c_97.17-97.20m	Rim	2	-3.87	0.08	-6.28	0.05			-0.63	0.08			213090118	1658826	9203664	
1038-47-16	PDP2c_97.17-97.20m	No internal texture	2	-2.84	0.04	-4.57	0.23			-0.49	0.05			399264099	3111779	17370375	
1038-48_3.1	PDP2c_97.17-97.20m	No internal texture	2	-3.92	0.07	-6.21	0.07			-0.72	0.06			357498734	2783165	15531816	
1038-48_3.2	PDP2c_97.17-97.20m	No internal texture	2	-1.73	0.07	-2.74	0.15			-0.32	0.07			366984018	2863957	16005542	
1038-48_3.3	PDP2c_97.17-97.20m	No internal texture	2	-4.24	0.08	-7.09	0.07			-0.58	0.08			343219533	2668921	14895915	
1038-48_5	PDP2c_97.17-97.20m	No internal texture	2	-3.35	0.06	-5.46	0.06			-0.54	0.05			353558424	2753633	15376320	
1038-48_6.1	PDP2c_97.17-97.20m	No internal texture	2	-4.89	0.05	-8.16	0.08			-0.68	0.06			353095146	2746586	15317332	
1038-48_6.2	PDP2c_97.17-97.20m	No internal texture	2	-4.75	0.07	-7.33	0.05			-0.97	0.08			357537638	2783203	15520983	
1038-48_7.2	PDP2c_97.17-97.20m	No internal texture	2	-4.96	0.06	-8.23	0.04			-0.71	0.05			416205075	3235655	18047426	
1038-48_8	PDP2c_97.17-97.20m	No internal texture	2	-6.27	0.08	-11.05	0.04			-0.57	0.08			375141574	2912018	16222165	
D_33.1	PDP2c_97.17-97.20m	No internal texture	2	-4.81	0.12	-7.43	0.10			-0.97	0.13			200090975	1557570	8633914	

Title	Sample	Location in the grain	Pyrite generation	$\delta^{33}S$/‰	1σ	$\delta^{34}S$/‰	1σ	$\delta^{36}S$/‰	1σ	$\Delta^{33}S$/‰	1σ	$\Delta^{36}S$/‰	1σ	CPS_$^{32}S^-$	CPS_$^{33}S^-$	CPS_$^{34}S^-$	CPS_$^{36}S^-$
D_33.2	PDP2c_97.17-97.20m	No internal texture	2	-4.33	0.11	-7.55	0.11			-0.43	0.10			220340451	1713676	9508657	
D_33.4	PDP2c_97.17-97.20m	No internal texture	2	-4.83	0.13	-8.45	0.04			-0.47	0.13			190754722	1482876	8223706	
D_33.5	PDP2c_97.17-97.20m	No internal texture	2	-2.56	0.12	-3.97	0.11			-0.51	0.12			209319287	1632522	9062309	
D_33.8	PDP2c_97.17-97.20m	No internal texture	2	-3.58	0.12	-6.48	0.06			-0.24	0.12			226445145	1762765	9781384	
1801M_11_19	PDP2c_97.17-97.20m	No internal texture	2	-4.00	0.10	-6.76	0.17			-0.51	0.10			595272840	4632902	25873198	
D_33.3	PDP2c_97.17-97.20m	No internal texture	2	-3.89	0.15	-7.00	0.05			-0.27	0.14			158903130	1236435	6859815	
D_33.5	PDP2c_97.17-97.20m	No internal texture	2	-3.85	0.14	-6.40	0.15			-0.55	0.13			194619216	1516774	8406732	
D_33.9	PDP2c_97.17-97.20m	No internal texture	2	-3.98	0.14	-6.76	0.07			-0.49	0.13			190631780	1483444	8232339	
D_33.10	PDP2c_97.17-97.20m	No internal texture	2	-4.91	0.14	-8.23	0.12			-0.66	0.13			206532755	1608514	8907243	
D_33.20	PDP2c_97.17-97.20m	No internal texture	2	-3.49	0.10	-5.97	0.09			-0.41	0.10			216726891	1687759	9362159	
D_33.28	PDP2c_97.17-97.20m	No internal texture	2	-5.03	0.13	-8.84	0.05			-0.47	0.13			201807834	1568095	8693024	
D_33.31	PDP2c_97.17-97.20m	No internal texture	2	-4.23	0.13	-6.94	0.06			-0.65	0.14			178796255	1390724	7719023	
D_33.33	PDP2c_97.17-97.20m	No internal texture	2	-4.38	0.11	-6.62	0.10			-0.96	0.13			188563987	1469879	8145149	
D_33.35	PDP2c_97.17-97.20m	No internal texture	2	-3.34	0.12	-5.61	0.10			-0.44	0.14			197833655	1540326	8551492	
1801M-12_4	PDP2c_97.17-97.20m	No internal texture	2	-1.02	0.04	-1.32	0.15			-0.34	0.03			605298088	4725924	26448338	
M-11_1'	PDP2c_97.17-97.20m	No internal texture	2	-4.74	0.11	-7.60	0.15			-0.82	0.11			414203082	3220580	17981020	
1038-48_1.1	PDP2b_94.69-94.74m	No internal texture	2	-7.28	0.07	-12.28	0.05			-0.93	0.06			374898804	2908037	16191740	
1038-48_1.2	PDP2b_94.69-94.74m	No internal texture	2	-9.59	0.05	-16.28	0.05			-1.18	0.05			374599224	2899125	16108590	
1038-48_2	PDP2b_94.69-94.74m	No internal texture	2	-7.36	0.08	-11.57	0.38			-1.39	0.08			343671324	2668190	14859579	
1038-48_3	PDP2b_94.69-94.74m	No internal texture	2	-7.91	0.07	-13.34	0.26			-1.01	0.08			577883779	4481021	24945086	
D22_6.2	PDP2b_94.69-94.74m	No internal texture	2	-7.86	0.06	-12.91	0.14			-1.20	0.06			568650453	4408522	24553496	
D22_7.1	PDP2b_94.69-94.74m	No internal texture	2	-7.56	0.04	-12.99	0.17			-0.85	0.05			566207840	4390155	24451278	
D22_8	PDP2b_94.69-94.74m	No internal texture	2	-8.36	0.07	-14.21	0.25			-1.02	0.06			584111697	4523865	25185690	
D22_5'''	PDP2b_90.94-90.97m	No internal texture	2	-11.32	0.04	-19.44	0.08			-1.26	0.04			581517801	4492276	24947809	
1038-47_3_3	PDP2b_94.69-94.74m	No internal texture	2	-3.27	0.04	-5.12	0.21			-0.63	0.05			586352529	4565451	25526579	
1038-47_2	PDP2b_94.69-94.74m	No internal texture	2	-3.59	0.05	-5.80	0.07			-0.60	0.05			616834031	4800628	26830960	
D20_2	PDP2b_94.69-94.74m	No internal texture	2	-10.82	0.05	-18.99	0.13			-0.99	0.05			567230173	4381567	24350191	
D20_4.2	PDP2b_94.69-94.74m	No internal texture	2	-2.57	0.05	-3.83	0.18			-0.59	0.07			595922044	4640736	25971948	

Title	Sample	Location in the grain	Pyrite generation	$\delta^{33}S$/‰	1σ	$\delta^{34}S$/‰	1σ	$\delta^{36}S$/‰	1σ	$\Delta^{33}S$/‰	1σ	$\Delta^{36}S$/‰	1σ	CPS_$^{32}S^-$	CPS_$^{33}S^-$	CPS_$^{34}S^-$	CPS_$^{36}S^-$
1038-47-19	PDP2c_97.17-97.20m	No internal texture	2	-0.93	0.06	-1.71	0.12			-0.05	0.06			388084445	3031884	16950716	
D_33.6	PDP2c_97.17-97.20m	No internal texture	2	-1.04	0.09	-2.01	0.08			-0.01	0.08			220603422	1722179	9573350	
1801M_11_2	PDP2c_97.17-97.20m	No internal texture	1	-1.80	0.04	-4.01	0.15			0.26	0.05			579754405	4519855	25258694	
D_33.10	PDP2c_97.17-97.20m	No internal texture	1	-1.34	0.11	-2.81	0.08			0.11	0.11			225240993	1759134	9767368	
1038-47_9.1	PDP2c_97.17-97.20m	No internal texture (slight addition of the adjacent pyrite grain)	1	-0.19	0.07	-0.79	0.08			0.22	0.08			693123018	5414666	30312022	
Ruttan_6.1				0.51	0.02	1.12	0.06	2.23	0.12	-0.07	0.02	0.09	0.14	1219747603	9538028	53484644	180897
Ruttan_6.2				0.59	0.03	1.20	0.07	2.27	0.11	-0.03	0.02	-0.01	0.11	1187089802	9285137	52054034	176351
Ruttan_6.3				0.83	0.02	1.49	0.05	2.71	0.11	0.06	0.02	-0.13	0.11	1221908773	9559925	53596958	181472
Ruttan_6.4				0.67	0.02	1.34	0.04	2.53	0.13	-0.02	0.02	-0.02	0.14	1213563021	9491582	53224181	180248
Ruttan_6.5				0.67	0.02	1.37	0.04	2.43	0.12	-0.04	0.02	-0.18	0.14	1232312945	9638822	54047489	183093
Ruttan_6.6				0.57	0.02	1.01	0.05	1.72	0.13	0.05	0.02	-0.21	0.12	1199443308	9378448	52575531	177541
Ruttan_7.1				0.58	0.02	1.10	0.08	2.22	0.13	0.02	0.02	0.13	0.14	1129381107	8833959	49523913	167697
Ruttan_7.2				0.47	0.03	1.06	0.05	1.91	0.11	-0.07	0.02	-0.10	0.10	1213435644	9490288	53219838	180167
Ruttan_7.3				0.54	0.02	0.91	0.06	1.92	0.13	0.07	0.02	0.19	0.14	1206628384	9438985	52905041	179245
Ruttan_7.4				0.75	0.02	1.40	0.06	2.88	0.14	0.03	0.02	0.22	0.15	1235635805	9664166	54192724	183303
Ruttan_4.1				0.67	0.02	1.23	0.05	2.37	0.11	0.04	0.02	0.03	0.12	1101468936	8614663	48297154	163299
Ruttan_4.2				0.59	0.02	1.28	0.05	2.64	0.13	-0.07	0.02	0.20	0.13	1089431601	8518378	47767766	161482
Ruttan_4.3				0.77	0.02	1.44	0.05	2.73	0.10	0.02	0.02	-0.01	0.11	1166701098	9127170	51166878	173245
Ruttan_4.4				0.69	0.02	1.42	0.05	2.87	0.14	-0.05	0.02	0.16	0.14	1164917413	9110015	51085290	173029
Ruttan_5.1				0.48	0.02	0.99	0.07	2.07	0.10	-0.03	0.02	0.18	0.11	1111916047	8694045	48738031	164874
Ruttan_5.2				0.57	0.02	1.01	0.06	1.84	0.12	0.05	0.02	-0.08	0.12	1100579531	8606858	48236818	163115
Ruttan_5.3				0.69	0.02	1.19	0.07	2.22	0.12	0.08	0.02	-0.05	0.11	1192722154	9331354	52312355	176954
Ruttan_5.4				0.50	0.02	1.02	0.09	1.51	0.15	-0.03	0.02	-0.44	0.15	1172452049	9168077	51401909	173833
Ruttan_1				0.51	0.03	0.71	0.10	1.17	0.09	0.14	0.04	-0.19	0.09	1249533185	9767050	54706672	184722
Ruttan_2				0.20	0.05	0.54	0.16	0.88	0.13	-0.07	0.05	-0.14	0.12	1163612163	9092721	50926441	171916
Ruttan_3				0.48	0.04	0.66	0.18	1.24	0.13	0.15	0.05	-0.01	0.15	1184523367	9261183	51869857	175171
Ruttan_4				0.41	0.04	0.73	0.13	1.39	0.11	0.04	0.04	0.01	0.12	1292921514	10109943	56646860	191367
Ruttan_5				0.62	0.04	1.29	0.21	2.41	0.15	-0.04	0.06	-0.04	0.13	1182717813	9249878	51833478	175239

Title	Sample	Location in the grain	Pyrite generation	$\delta^{33}S$/‰	1σ	$\delta^{34}S$/‰	1σ	$\delta^{36}S$/‰	1σ	$\Delta^{33}S$/‰	1σ	$\Delta^{36}S$/‰	1σ	CPS_$^{32}S^-$	CPS_$^{33}S^-$	CPS_$^{34}S^-$	CPS_$^{36}S^-$
Ruttan_6				0.61	0.04	1.31	0.13	2.53	0.15	-0.07	0.04	0.04	0.17	1272168025	9945848	55734964	188246
Ruttan_7				0.99	0.04	2.04	0.10	3.93	0.10	-0.06	0.05	0.05	0.11	1265404231	9902308	55501294	187786
Ruttan_8				1.12	0.03	1.91	0.11	3.65	0.11	0.14	0.03	0.02	0.12	1233936886	9651352	54070917	182820
Ruttan_9				0.45	0.04	1.01	0.14	1.77	0.11	-0.07	0.05	-0.15	0.12	1193215803	9329301	52280161	176677
Ruttan_10				0.82	0.03	1.61	0.11	3.28	0.16	-0.01	0.03	0.22	0.16	1180028716	9228990	51723369	175034
Ruttan_11				0.61	0.04	1.18	0.18	2.42	0.13	0.00	0.05	0.18	0.15	1173969474	9176185	51424386	173648
Ruttan_12				0.59	0.03	1.41	0.14	2.69	0.10	-0.13	0.03	0.02	0.12	1195190577	9345139	52386126	177058
Ruttan_1				0.52	0.05	0.91	0.22	2.05	0.15	0.05	0.06	0.33	0.17	938908992	7335542	41099571	138510
Ruttan_2				0.65	0.04	1.11	0.18	2.04	0.17	0.08	0.05	-0.07	0.19	982997361	7687235	43066436	145551
Ruttan_3				0.75	0.04	1.20	0.23	2.17	0.17	0.13	0.04	-0.11	0.17	958925222	7497480	41984848	141889
Ruttan_4				0.39	0.03	0.88	0.17	1.45	0.14	-0.07	0.04	-0.22	0.13	980115444	7659970	42891309	144823
Ruttan_5				0.80	0.03	1.52	0.14	2.97	0.13	0.01	0.03	0.08	0.12	969512319	7582199	42474867	143567
Ruttan_6				1.04	0.03	1.75	0.15	3.28	0.12	0.13	0.03	-0.06	0.15	968208891	7571988	42400829	143198
Ruttan_7				0.95	0.03	1.84	0.18	3.46	0.11	0.00	0.03	-0.04	0.11	967937113	7568855	42392015	143223
Ruttan_8				-0.15	0.04	0.39	0.27	0.83	0.16	-0.35	0.05	0.09	0.15	950674116	7425951	41602072	140325
Ruttan_1				0.03	0.05	0.03	0.31	0.08	0.13	0.01	0.04	0.02	0.15	1101703518	8611965	48224642	162911
Ruttan_2				0.52	0.03	1.12	0.19	1.76	0.15	-0.05	0.03	-0.36	0.15	1066755727	8342316	46728885	157993
Ruttan_3				0.46	0.03	1.31	0.13	2.65	0.11	-0.21	0.03	0.16	0.13	1081948815	8460166	47408966	160149
Ruttan_4				0.30	0.03	0.67	0.24	1.31	0.11	-0.04	0.03	0.03	0.12	1073431795	8393878	47026715	159144
Ruttan_5				0.63	0.03	1.07	0.13	1.85	0.14	0.08	0.03	-0.18	0.14	1126640521	8809344	49356738	166655
Ruttan_6				0.76	0.04	1.60	0.11	3.45	0.11	-0.07	0.04	0.41	0.12	1079445989	8442483	47311213	159782
Ruttan_7				0.71	0.03	1.31	0.12	2.60	0.16	0.04	0.04	0.10	0.18	1065762628	8332313	46698202	157930
Ruttan_8				0.80	0.02	1.43	0.13	2.63	0.15	0.06	0.02	-0.09	0.16	1075913689	8418421	47162711	159457
Ruttan_9				0.62	0.03	1.26	0.13	2.19	0.16	-0.03	0.03	-0.21	0.16	1129751869	8836966	49516868	167518
Ruttan_10				0.80	0.03	1.63	0.13	3.05	0.14	-0.04	0.03	-0.05	0.13	1095209941	8567438	48014220	162356
Ruttan_11				0.77	0.02	1.27	0.10	2.54	0.14	0.12	0.03	0.13	0.13	1097352471	8583944	48068705	162275
Ruttan_12				0.99	0.04	1.69	0.11	3.26	0.12	0.12	0.03	0.04	0.12	1143135813	8943547	50090599	169394
Ruttan_1				0.71	0.03	1.20	0.17	2.16	0.18	0.09	0.03	-0.13	0.20	953978738	7458879	41793851	141101

Title	Sample	Location in the grain	Pyrite generation	$\delta^{33}S$/‰	1σ	$\delta^{34}S$/‰	1σ	$\delta^{36}S$/‰	1σ	$\Delta^{33}S$/‰	1σ	$\Delta^{36}S$/‰	1σ	CPS_$^{32}S^-$	CPS_$^{33}S^-$	CPS_$^{34}S^-$	CPS_$^{36}S^-$
Ruttan_2				0.28	0.03	0.85	0.18	1.52	0.17	-0.15	0.03	-0.09	0.19	948961243	7416854	41560047	140628
Ruttan_3				0.73	0.02	1.32	0.22	2.71	0.14	0.04	0.02	0.19	0.16	931351482	7285029	40824268	138041
Ruttan_4				0.46	0.04	0.77	0.20	0.97	0.16	0.07	0.04	-0.50	0.16	929909244	7267545	40674810	137219
Ruttan_5				0.54	0.04	0.80	0.21	1.93	0.13	0.12	0.05	0.41	0.16	895872793	7002079	39210218	132477
Ruttan_6				0.83	0.04	1.42	0.12	2.91	0.16	0.11	0.04	0.22	0.18	935597207	7317942	40990329	138579
Ruttan_7				0.54	0.04	0.62	0.22	1.31	0.15	0.22	0.04	0.12	0.16	882260076	6902299	38647991	130680
Ruttan_8				0.66	0.03	1.21	0.14	2.26	0.14	0.04	0.04	-0.04	0.16	933739594	7301652	40916198	138314
Ruttan_9				0.44	0.03	1.36	0.12	2.54	0.14	-0.26	0.03	-0.04	0.15	906596361	7085322	39712950	134115
Ruttan_10				0.77	0.03	1.71	0.11	3.04	0.16	-0.11	0.03	-0.21	0.16	967553866	7567968	42414673	143242
Ruttan_11				0.67	0.03	1.37	0.13	2.85	0.13	-0.03	0.03	0.25	0.13	1001804616	7836068	43911877	148506
Ruttan_12				0.51	0.04	1.18	0.14	2.06	0.15	-0.10	0.04	-0.18	0.15	968410521	7574651	42448754	143479
Ruttan_13				0.89	0.03	1.79	0.16	3.40	0.13	-0.03	0.04	-0.01	0.15	1048649408	8200910	45964097	155356
Ruttan_12.4				0.47	0.03	0.94	0.08	2.06	0.14	-0.01	0.03	0.27	0.15	1286053623	10131288	56570187	198493
Ruttan_12.5				0.42	0.03	0.80	0.09	1.15	0.15	0.00	0.03	-0.37	0.16	1285863484	10131563	56564871	198493
Ruttan_12.6				0.30	0.03	0.88	0.09	1.87	0.15	-0.15	0.04	0.20	0.16	1258389514	9916484	55382427	194234
Ruttan_12.7				0.14	0.03	0.56	0.12	1.06	0.12	-0.15	0.03	0.00	0.12	1242040679	9784057	54634179	191921
Ruttan_12.8				0.53	0.03	1.34	0.09	2.48	0.14	-0.16	0.03	-0.06	0.13	1302969739	10266465	57350933	201298
Ruttan_12.9				0.44	0.04	1.09	0.10	1.92	0.16	-0.13	0.04	-0.15	0.16	1273401145	10034936	56043372	196766
Ruttan_12.10				0.88	0.02	1.49	0.08	2.94	0.14	0.11	0.03	0.11	0.14	1371141188	10808920	60371397	212222
Ruttan_12.11				0.82	0.03	1.45	0.10	2.42	0.16	0.07	0.03	-0.33	0.15	1328690797	10476339	58509325	205361
Ruttan_2.1				0.74	0.03	1.11	0.08	2.16	0.14	0.17	0.03	0.04	0.15	1416150187	11160658	62315304	218789
Ruttan_2.2				0.99	0.03	1.63	0.07	3.13	0.10	0.15	0.02	0.03	0.13	1430027887	11270170	62945333	221254
Ruttan_2.3				1.13	0.02	1.85	0.08	3.63	0.12	0.18	0.03	0.10	0.12	1421608892	11210450	62609392	219860
Ruttan_2.4				0.53	0.03	1.21	0.09	2.09	0.17	-0.09	0.03	-0.22	0.17	1375643933	10841174	60561579	212581
Ruttan_2.5				0.81	0.03	1.52	0.05	2.78	0.13	0.03	0.03	-0.11	0.14	1394228182	10991143	61380490	215469
Ruttan_2.6				0.61	0.02	1.26	0.09	2.53	0.10	-0.04	0.03	0.13	0.12	1321805799	10413917	58170181	204240
Ruttan_2.7				0.71	0.03	1.17	0.11	2.15	0.10	0.10	0.03	-0.08	0.12	1351142216	10649918	59468406	208660
Ruttan_2.8				0.51	0.03	0.84	0.09	1.79	0.12	0.08	0.03	0.20	0.11	1399117624	11026520	61568863	216112

Title	Sample	Location in the grain	Pyrite generation	$\delta^{33}S$/‰	1σ	$\delta^{34}S$/‰	1σ	$\delta^{36}S$/‰	1σ	$\Delta^{33}S$/‰	1σ	$\Delta^{36}S$/‰	1σ	CPS_$^{32}S^-$	CPS_$^{33}S^-$	CPS_$^{34}S^-$	CPS_$^{36}S^-$
Ruttan_2.9				0.52	0.04	1.18	0.10	2.32	0.17	-0.09	0.04	0.07	0.17	1268346041	9994489	55820392	196042
Ruttan_2.10				0.57	0.03	1.26	0.09	2.55	0.15	-0.08	0.04	0.15	0.17	1278381163	10070727	56255352	197743
Balmat_6.1				7.50	0.02	14.78	0.04	28.32	0.15	-0.08	0.02	0.06	0.15	1196567839	9425777	53189280	182037
Balmat_6.2				7.90	0.02	15.44	0.07	29.40	0.13	-0.02	0.02	-0.13	0.13	1185664461	9340840	52730615	180906
Balmat_7.1				7.11	0.02	13.73	0.07	26.01	0.10	0.07	0.02	-0.23	0.10	1178546149	9273272	52302283	178905
Balmat_7.2				7.41	0.02	14.14	0.06	27.01	0.11	0.15	0.02	-0.02	0.10	1187421136	9347693	52724349	180379
Balmat_4.1				7.41	0.02	14.39	0.06	27.24	0.11	0.02	0.02	-0.28	0.12	1121097023	8824825	49787444	170425
Balmat_4.2				7.51	0.02	14.53	0.06	27.71	0.14	0.05	0.02	-0.09	0.14	1148492480	9043578	51016630	174559
Balmat_5.1				7.67	0.02	14.78	0.06	28.13	0.11	0.09	0.02	-0.13	0.13	1112203315	8758746	49413404	169131
Balmat_5.2				7.69	0.02	14.84	0.07	28.41	0.14	0.08	0.02	0.03	0.16	1176253210	9264739	52277795	178850
Balmat_1				7.30	0.04	14.56	0.14	28.12	0.13	-0.17	0.05	0.26	0.15	1179938569	9281848	52347649	178850
Balmat_3				7.56	0.04	14.60	0.11	27.76	0.13	0.07	0.04	-0.16	0.14	1217626418	9580086	53997476	184458
Balmat_1				8.08	0.04	15.70	0.15	30.41	0.14	0.02	0.04	0.37	0.16	969772038	7642049	43109241	147595
Balmat_2				7.88	0.04	15.16	0.19	29.08	0.19	0.11	0.04	0.09	0.20	914172911	7198758	40557386	138724
Balmat_3				7.79	0.04	15.28	0.21	29.22	0.15	-0.06	0.04	-0.02	0.15	998393010	7864262	44355865	151495
Balmat_4				7.89	0.03	15.35	0.22	29.07	0.14	0.01	0.04	-0.31	0.15	950544722	7486732	42221183	144418
Balmat_1				7.49	0.04	14.72	0.14	28.58	0.12	-0.06	0.04	0.43	0.13	1109259654	8736943	49272548	168619
Balmat_2				7.15	0.04	14.46	0.25	27.69	0.21	-0.27	0.04	0.05	0.21	1052417800	8284652	46704402	159787
Balmat_3				7.72	0.04	14.71	0.22	28.56	0.14	0.17	0.04	0.43	0.14	1087913846	8569416	48291110	165090
Balmat_4				7.12	0.04	14.01	0.26	26.96	0.16	-0.07	0.04	0.18	0.16	1063302679	8370431	47189687	161397
Balmat_1				7.71	0.03	14.53	0.21	27.70	0.14	0.26	0.03	-0.10	0.15	995358983	7838899	44184989	151161
Balmat_2				7.91	0.03	15.03	0.24	28.38	0.14	0.20	0.04	-0.37	0.16	959252019	7556657	42616013	145843
Balmat_3				7.80	0.04	15.02	0.20	28.57	0.13	0.09	0.04	-0.16	0.15	1012505030	7973072	44952399	153638
Balmat_4				7.29	0.04	14.43	0.24	27.03	0.17	-0.11	0.04	-0.55	0.17	1163259995	9158735	51658481	176681
Balmat_12.1				7.38	0.03	14.54	0.11	27.71	0.11	-0.08	0.03	-0.08	0.13	1232054958	9775291	54940821	195288
Balmat_12.2				7.56	0.03	14.81	0.09	28.55	0.13	-0.04	0.03	0.22	0.13	1280028392	10161444	57125889	203266
Balmat_12.3				7.93	0.03	15.40	0.11	29.39	0.15	0.03	0.03	-0.08	0.15	1304857155	10360490	58256904	207114
Balmat_12.4				7.48	0.03	14.79	0.14	28.23	0.13	-0.12	0.03	-0.06	0.14	1231764800	9776356	54961819	195230

Title	Sample	Location in the grain	Pyrite generation	$\delta^{33}S$/‰	1σ	$\delta^{34}S$/‰	1σ	$\delta^{36}S$/‰	1σ	$\Delta^{33}S$/‰	1σ	$\Delta^{36}S$/‰	1σ	CPS_$^{32}S^-$	CPS_$^{33}S^-$	CPS_$^{34}S^-$	CPS_$^{36}S^-$
Balmat_2.1				8.27	0.03	15.99	0.08	30.66	0.10	0.07	0.03	0.07	0.13	1336092877	10609077	59673351	212569
Balmat_2.2				8.19	0.03	15.89	0.07	30.72	0.16	0.04	0.03	0.33	0.16	1369471068	10875791	61174966	217816
Balmat_2.3				8.16	0.03	15.81	0.08	30.31	0.13	0.05	0.03	0.06	0.13	1349947821	10719980	60285574	214245
Balmat_2.4				7.48	0.03	14.64	0.11	27.97	0.14	-0.04	0.04	-0.04	0.14	1310912278	10398869	58457118	207623
Ruttan_7.1				0.57	0.06	1.20	0.04			-0.05	0.05			376048318	2941510	16460806	
Ruttan_7.2				0.56	0.08	1.17	0.06			-0.04	0.07			399919964	3128434	17511154	
Ruttan_7.3				0.17	0.06	0.79	0.10			-0.24	0.08			390412194	3052222	17092003	
Ruttan_7.4				0.33	0.06	0.95	0.07			-0.16	0.07			384802940	3009406	16843367	
Ruttan_8.1				0.40	0.06	0.74	0.04			0.02	0.06			373037933	2916180	16328343	
Ruttan_8.2				0.89	0.06	1.71	0.04			0.01	0.07			384983673	3009639	16861579	
Ruttan_8.3				0.74	0.06	1.50	0.08			-0.03	0.07			390406807	3053076	17098672	
Ruttan_8.4				0.70	0.06	0.99	0.05			0.19	0.06			390150120	3050180	17075753	
Ruttan_8.5				0.76	0.03	1.37	0.07			0.05	0.04			396756898	3103768	17375961	
Ruttan_8.6				0.36	0.06	0.66	0.10			0.02	0.06			388250512	3035328	16991155	
Ruttan_8.7				0.47	0.07	0.95	0.06			-0.02	0.06			380524770	2974722	16656395	
Ruttan_8.8				0.98	0.07	1.73	0.03			0.09	0.06			392548113	3070751	17195619	
Ruttan_8.9				0.93	0.06	1.55	0.06			0.13	0.06			385305915	3013416	16874100	
Ruttan_8.10				0.55	0.06	1.10	0.04			-0.02	0.06			371157356	2901791	16244888	
Ruttan_8.11				0.85	0.05	1.60	0.04			0.03	0.05			382855357	2995862	16771055	
Ruttan_2				0.72	0.07	1.36	0.18			0.02	0.06			604683643	4727678	26496554	
Ruttan_3				0.32	0.05	1.05	0.12			-0.22	0.06			611610284	4781589	26791361	
Ruttan_4				0.49	0.06	1.44	0.16			-0.25	0.07			602355687	4709472	26394540	
Ruttan_6				0.57	0.05	1.06	0.17			0.03	0.06			592724890	4634151	25959757	
Ruttan_7				0.43	0.04	0.96	0.21			-0.07	0.04			586749722	4587046	25702615	
Ruttan_8				0.44	0.06	0.51	0.12			0.17	0.05			568105110	4439464	24850934	
Ruttan_9				0.75	0.09	1.56	0.12			-0.05	0.08			601501752	4704142	26347869	
Ruttan_10				1.14	0.05	1.79	0.10			0.22	0.05			610531613	4773897	26755314	
Ruttan_1				0.59	0.09	1.19	0.07			-0.03	0.10			231738626	1813212	10085404	

Title	Sample	Location in the grain	Pyrite generation	$\delta^{33}S$/‰	1σ	$\delta^{34}S$/‰	1σ	$\delta^{36}S$/‰	1σ	$\Delta^{33}S$/‰	1σ	$\Delta^{36}S$/‰	1σ	CPS_$^{32}S^-$	CPS_$^{33}S^-$	CPS_$^{34}S^-$	CPS_$^{36}S^-$
Ruttan_2				0.14	0.11	0.46	0.06			-0.10	0.10			230586745	1803327	10031765	
Ruttan_3				0.71	0.11	1.37	0.07			0.01	0.10			222966568	1744682	9709011	
Ruttan_3				0.76	0.15	1.29	0.09			0.10	0.13			216322240	1692712	9420821	
Ruttan_4				0.76	0.12	1.52	0.08			-0.02	0.12			213025238	1667742	9275756	
Ruttan_5				0.80	0.10	1.47	0.07			0.04	0.11			203620342	1592495	8866723	
Ruttan_6				0.39	0.10	0.90	0.12			-0.07	0.11			206369240	1615532	8985356	
Ruttan_7				0.80	0.12	1.40	0.05			0.08	0.13			208060785	1627610	9059713	
Ruttan_1				0.45	0.05	1.10	0.20			-0.12	0.06			532159904	4159909	23311573	
Ruttan_2				0.84	0.04	1.62	0.22			0.01	0.06			535493577	4189030	23479692	
Ruttan_3				1.39	0.07	2.21	0.22			0.26	0.07			571582748	4473154	25066453	
Ruttan_4				0.38	0.05	0.67	0.16			0.03	0.05			562358189	4394901	24626726	
Ruttan_5				0.34	0.05	1.02	0.17			-0.18	0.07			539136227	4215843	23618368	
Ruttan_6				0.56	0.04	0.95	0.10			0.07	0.05			549125124	4290503	24046887	
Ruttan_7				0.17	0.07	0.55	0.13			-0.11	0.08			547689964	4277928	23977413	
Ruttan_8				0.81	0.07	1.49	0.19			0.05	0.06			559180052	4370324	24501625	
Ruttan_1				0.15	0.12	0.74	0.10			-0.23	0.12			206962664	1618923	9005231	
Ruttan_2				0.48	0.11	1.36	0.10			-0.22	0.11			208136048	1628911	9061416	
Ruttan_3				0.97	0.10	1.35	0.05			0.28	0.10			211399123	1652650	9203755	
Ruttan_4				0.55	0.09	1.19	0.05			-0.07	0.08			211246038	1651777	9193915	
Ruttan_5				0.74	0.09	1.53	0.10			-0.05	0.09			210983783	1651656	9188870	
Ruttan_6				0.45	0.12	0.95	0.09			-0.04	0.12			212703896	1664301	9254733	
Ruttan_7				0.35	0.11	1.20	0.07			-0.27	0.12			202985483	1586724	8833411	
Ruttan_8				0.66	0.10	1.15	0.09			0.06	0.09			212611221	1663330	9252945	
Ruttan_9				1.01	0.13	1.42	0.11			0.28	0.14			203707257	1595435	8868459	
Ruttan_9				0.76	0.08	1.19	0.09			0.15	0.08			209156701	1635747	9103311	
Ruttan_10				0.68	0.13	1.12	0.10			0.11	0.12			212549824	1663835	9251449	
Ruttan_4				0.54	0.08	1.30	0.13			-0.13	0.07			583037913	4558702	25540714	
Ruttan_5				0.86	0.09	1.37	0.21			0.15	0.08			562618662	4400741	24654378	

Title	Sample	Location in the grain	Pyrite generation	$\delta^{33}S$/‰	1σ	$\delta^{34}S$/‰	1σ	$\delta^{36}S$/‰	1σ	$\Delta^{33}S$/‰	1σ	$\Delta^{36}S$/‰	1σ	CPS_$^{32}S^-$	CPS_$^{33}S^-$	CPS_$^{34}S^-$	CPS_$^{36}S^-$
Ruttan_6				0.50	0.04	0.94	0.17			0.02	0.05			563499199	4408235	24685002	
Ruttan_7				0.88	0.06	1.49	0.20			0.11	0.06			576040309	4504965	25245156	
Ruttan_8				0.77	0.06	1.77	0.11			-0.14	0.06			562377702	4397287	24643617	
Ruttan_9				0.59	0.07	1.11	0.31			0.02	0.06			571581709	4468083	25036242	
Ruttan_10				0.19	0.05	0.42	0.29			-0.02	0.06			594602637	4648741	26037862	
Ruttan_1				0.54	0.09	1.30	0.13			-0.13	0.08			591607408	4623500	25913822	
Ruttan_2				0.66	0.07	1.06	0.12			0.11	0.08			602301985	4704233	26370719	
Ruttan_3				0.66	0.07	1.24	0.17			0.03	0.08			565487004	4418117	24760811	
Ruttan_3.1				0.67	0.09	1.15	0.21			0.08	0.10			404409963	3157624	17698559	
Ruttan_3.2				0.83	0.09	1.40	0.13			0.11	0.09			402677049	3143548	17620624	
Ruttan_3.3				0.82	0.11	1.26	0.12			0.17	0.10			413950206	3232729	18119857	
Ruttan_3.4				0.96	0.07	1.66	0.10			0.11	0.09			411895254	3221639	18039098	
Ruttan_4.1				0.59	0.10	1.41	0.12			-0.13	0.10			416272290	3253469	18231107	
Ruttan_4.2				0.48	0.06	0.75	0.08			0.10	0.06			387091001	3024087	16934754	
Ruttan_4.3				0.29	0.11	0.98	0.13			-0.21	0.10			363896312	2843148	15920431	
Ruttan_4.4				0.30	0.07	0.98	0.08			-0.21	0.08			367021200	2867478	16059250	
Balmat_7.1				7.00	0.05	13.84	0.10			-0.10	0.06			390679771	3076651	17328688	
Balmat_7.2				7.36	0.06	14.38	0.05			-0.02	0.06			399352434	3145436	17715069	
Balmat_8.1				7.58	0.06	14.59	0.06			0.09	0.06			371686948	2925866	16487424	
Balmat_8.2				7.45	0.06	14.25	0.06			0.13	0.06			372064036	2929429	16504771	
Balmat_8.3				7.53	0.07	14.61	0.06			0.03	0.07			371696874	2925772	16493469	
Balmat_8.4				7.22	0.06	13.91	0.06			0.08	0.06			353923439	2784769	15686306	
Balmat_1				7.31	0.03	14.27	0.14			-0.01	0.03			576147706	4533096	25553194	
Balmat_2				7.36	0.06	14.62	0.13			-0.14	0.07			583369365	4592510	25895311	
Balmat_3				7.18	0.05	14.00	0.15			-0.01	0.06			576193484	4533798	25560410	
Balmat_1				8.05	0.11	14.78	0.06			0.46	0.11			209993525	1653873	9266900	
Balmat_2				7.83	0.12	14.91	0.08			0.18	0.12			185380636	1459946	8178630	
Balmat_1				7.66	0.05	14.13	0.18			0.40	0.05			562188859	4425148	24953150	

Title	Sample	Location in the grain	Pyrite generation	$\delta^{33}S/‰$	1σ	$\delta^{34}S/‰$	1σ	$\delta^{36}S/‰$	1σ	$\Delta^{33}S/‰$	1σ	$\Delta^{36}S/‰$	1σ	CPS_$^{32}S^-$	CPS_$^{33}S^-$	CPS_$^{34}S^-$	CPS_$^{36}S^-$
Balmat_2				8.17	0.06	15.36	0.14			0.29	0.06			570869905	4495896	25361907	
Balmat_3				7.48	0.04	14.28	0.24			0.15	0.04			554865733	4367907	24626640	
Balmat_4				8.44	0.04	15.81	0.14			0.33	0.05			573547690	4518091	25486419	
Balmat_1				7.48	0.09	14.58	0.07			-0.01	0.10			211660440	1666453	9336452	
Balmat_2				7.46	0.11	14.65	0.12			-0.06	0.11			205161677	1616936	9052691	
Balmat_3				7.30	0.09	14.51	0.07			-0.14	0.10			208046809	1638550	9176884	
Balmat_3				7.22	0.12	14.59	0.12			-0.27	0.13			208010878	1640034	9176561	
Balmat_2				8.15	0.05	15.95	0.13			-0.03	0.05			583924842	4599513	25952238	
Balmat_3				7.49	0.07	14.91	0.17			-0.16	0.07			577774997	4548295	25659694	
Balmat_1				7.94	0.09	15.17	0.11			0.15	0.08			606002242	4769242	26910369	
Balmat_3.1				7.80	0.08	15.40	0.14			-0.11	0.09			426031295	3353285	18914254	
Balmat_4.1				7.87	0.08	14.93	0.09			0.20	0.08			385506803	3034661	17105588	
Balmat_4.2				7.52	0.08	14.85	0.13			-0.10	0.08			372508958	2930815	16523243	

Chapter 4 The Sign of $\Delta^{33}S$ is Independent of Pyrite Morphology

Abstract: Previous bulk sulphide analyses have suggested a correlation between the morphology of pyrite in Archean metasedimentary rocks and the sign of associated $\Delta^{33}S$. However, it remains to be determined whether such a correlation exists and what the underlying mechanism is. This study measured the multiple sulphur isotopic compositions of pyrite nodules and disseminated pyrite grains from two typical Neoarchean shale samples with SHRIMP-SI, following detailed textural investigations by sodium hypochlorite etching and electron microscopy. The Roy Hill Shale sample shows two generations of pyrite in both nodules and disseminated grains reflected by textures. The first generation is $\Delta^{33}S$-weakly negative while the second generation is $\Delta^{33}S$-highly positive. Both generations of pyrite show linear relationships between $\delta^{34}S$ and $\Delta^{33}S$, although generation two displays wider ranges of $\delta^{34}S$ and $\Delta^{33}S$ compared with generation one. In the $\Delta^{33}S$-$\Delta^{36}S$ diagram, generation two plots along the Archean Reference Array (ARA, $\Delta^{36}S/\Delta^{33}S \approx -1$) whereas generation one deviates from the ARA in a trend similar to the Biological Fractionation Line ($\Delta^{36}S/\Delta^{33}S \approx -7$). The Nammuldi shale sample also exhibits two generations of pyrite, both of which are $\Delta^{33}S$- and $\delta^{34}S$-positive albeit of different magnitude. For these two shale samples, the sign of $\Delta^{33}S$ is not associated with the pyrite morphology. A plausible explanation for the morphology-specific $\Delta^{33}S$ reported in previous studies could be related to bulk analyses involving pyrite of different generations with opposite $\Delta^{33}S$. Furthermore, based on the distribution of the earlier nodular and disseminated pyrite in both samples, a model involving four stages is proposed for the formation process of pyrite nodules studied here: (1) formation of pyrite framboids composed of microcrystalline pyrite, (2) dissolution of framboidal pyrite and reprecipitation to generate larger single pyrite crystals, (3) aggregation of single pyrite crystals into nodules, and (4) injection of later hydrothermal fluids.

1. Introduction

Multiple sulphur isotopic composition of sulphides has become a key parameter in understanding the Archean rock records (e.g., Faruqhar et al., 2000; Ono et al., 2003; Kaufman et al., 2007; Shen et al., 2009; Guy et al., 2012). Sulphur is a relatively light element and so mass dependent fractionation effects are significant and widespread throughout the

Earth history. However, it is the so-called mass independent fractionation of sulphur (S-MIF) that is of most significance in the Archean. Sulphur is the lightest element with four stable isotopes. Two of the isotopes, expressed as $^{34}S/^{32}S$, are by convention used to quantify mass dependent fractionation effects. By definition, the S-MIF occurs because the minor isotopes, ^{33}S and ^{36}S (as $^{33}S/^{32}S$ and $^{36}S/^{32}S$), do not follow the mass dependent relationships predicted by $^{34}S/^{32}S$. Expressed in delta notation, mass dependent fractionation has the form $\delta^{33}S = 0.515\delta^{34}S$ and $\delta^{36}S = 1.90\delta^{34}S$. S-MIF is quantified by expressing the deviation of the measured $\delta^{33}S$ and $\delta^{36}S$ from the predicted value based on $\delta^{34}S$ and the mass fractionation law, i.e., $\Delta^{33}S = \delta^{33}S - 1000 \times [(1 + \delta^{34}S/1000)^{0.515} - 1]$ and $\Delta^{36}S = \delta^{36}S - 1000 \times [(1 + \delta^{34}S/1000)^{1.90} - 1]$ (Farquhar et al., 2013).

Paleoarchean and Neoarchean samples yield a line in the $\Delta^{33}S$-$\Delta^{36}S$ plot with a slope of around -1, which is termed the Archean Reference Array (ARA, Farquhar et al., 2001). This slope is broadly consistent with the fractionation associated with products of SO_2 photolysis under the ultraviolet radiation (e.g., Farquhar et al., 2001). The two main products of SO_2 photolysis are elemental sulphur and sulphate, which carry positive and negative $\Delta^{33}S$, respectively (Farquhar et al., 2001). After production in the atmosphere, both elemental sulphur and sulphate are transported to the ocean via rainfall, and are eventually sequestered mainly as sulphides (primarily pyrite) in sediments. This fractionation can only occur in an anoxic atmosphere and so the Great Oxidizing Event (Holland, 2002) in the earliest Proterozoic marks the end of large sulphur isotopic anomalies (Bekker et al., 2004) associated with atmospheric fractionation.

The ARA is distinct from the biological fractionation line, the $\Delta^{36}S/\Delta^{33}S$ slope of which is around -7 (Ono et al., 2006) or -9 (Johnston et al., 2007). This is the signature associated with microbial activities and represents the products of a series of mass dependent fractionation processes that follow slightly different mass dependent fractionation laws. As such it is sometimes referred to as a mass dependent fractionation line (Ono et al., 2006), but here we will use the term biological fractionation to distinguish it from the mass dependent fractionation derived solely from $\delta^{34}S$. The biological fractionation line is most evident in Phanerozoic rock records but the presence of this signature in Proterozoic and Archean rock records is considered as the indicator of microbial activities.

From the materials analysed so far, the magnitude of the maximum positive $\Delta^{33}S$ is much larger than that of the most negative $\Delta^{33}S$. This is taken as representing the potential of

elemental sulphur to preserve the isotopic signature whereas sulphate can be diluted in the atmosphere and seawater. In terms of the Archean rock records, the main repositories are sulphides and sulphates, with sulphides preserving both positive and negative $\Delta^{33}S$, while sulphates record only negative $\Delta^{33}S$.

Within Archean metasedimentary rocks (e.g., metablack/grey shale, metacarbonate rock, the prefix meta will be omitted hereafter), pyrite shows a variety of textures but occurs mostly in the form of disseminated grains, nodules, and layers/laminae. Previous studies (Partridge et al., 2008; Ono et al., 2009) have attempted to separate these three forms of pyrite and measure the multiple sulphur isotopic compositions using bulk sulphide analytical methods. Sulphur was extracted by physical combustion, chemical solutions (HCl and $CrCl_2$), or in-situ laser ablation (300-500 μm in diameter and 300 μm deep). The results of these work show that negative $\Delta^{33}S$ is concentrated in nodular and layered pyrite whereas positive $\Delta^{33}S$ is found primarily in disseminated grains. Such a correspondence between the sign of $\Delta^{33}S$ and pyrite morphology thus led the authors to come to the conclusion that $\Delta^{33}S$ is dependent on the morphology of pyrite (Partridge et al., 2008; Ono et al., 2009). However, the underlying mechanism giving rise to such dependence was not investigated. Furthermore, the bulk sulphide separations could well be compromised by involving mixed sulphur components, because even though pyrite of specific morphology was separated, these aliquots could still have multiple generations of pyrite that have not been identified.

Indeed, in recent years an increasing number of in-situ measurements coupled with detailed textural investigations have been conducted on pyrite nodules in Archean shales, and have revealed complicated mineral textures as well as diverse compositional distributions (Marine-Carbonne et al., 2014; Fischer et al., 2014; Li et al., 2017), which indicate an intricate growth history commonly with multiple generations of pyrite at the microscale. Etching of pyrite using sodium hypochlorite (NaOCl) solution combined with Back Scattered Electron (BSE) imaging has been demonstrated to be an effective and useful tool in revealing the internal textures of pyrite (Peterson and Mavrogenes, 2014; Tanner et al., 2016).

Here we studied pyrite in two typical Neoarchean shale samples from the Pilbara Craton, Western Australia. We first established the textural relationships for pyrite before in-situ multiple sulphur isotope analysis with the SHRIMP-SI (Sensitive High Resolution Ion MicroProbe-Stable Isotope). In previous studies, only nodular pyrite has been extensively measured in situ, because the associated disseminated pyrite grains within the black shale

matrix are too small to allow high precision analysis. In this study, pyrite of both morphologies was measured. Big-spot (~27 × 25 μm) analysis allowed sufficient ion beam intensity to measure all four sulphur isotopes (as $\delta^{34}S$, $\Delta^{33}S$ and $\Delta^{36}S$), whereas in small-spot (~18 × 15 μm) analysis only $\delta^{34}S$ and $\Delta^{33}S$ were determined to subpermil precision. Using these data, we attempted to confirm whether a correlation exists between the sign of $\Delta^{33}S$ and pyrite morphology, and explore related mechanisms for preservation of distinct sulphur isotope components.

2. Samples and geological background

Drill cores were examined at the Perth Core Library, Carlisle, Western Australia. Samples were obtained from two intervals (727.80-727.81m and 769.48-769.49m) of the drill hole FVG#1 (22°33'S, 119°30'E) located in the Fortescue Valley of the Pilbara Craton. Both drill cores are black carbonaceous shale, and pyrite occurs both as nodules and disseminated grains, which are typical occurrences of pyrite in shales of Archean age.

Stratigraphically, they belong to the Roy Hill Shale Member (769.48-769.49m) of the Jeerinah Formation, Fortescue Group, and the Nammuldi Member (727.80-727.81m) of the Marra Mamba Iron Formation, Hamersley Group, respectively. The Fortescue Group (2.78 Ga to 2.63 Ga, Trendall et al., 2004) and the Hamersley Group (2.63 Ga to 2.45 Ga, Trendall et al., 2004) are both subunits of the Mt. Bruce Supergroup. The Fortescue Group is a volcanic-sedimentary succession, and consists of the Bellary Formation, Mt. Roe Basalt, Hardey Formation, Kylena Formation, Tumbiana Formation, Maddina Formation, and Jeerinah Formation in ascending order. The Jeerinah Formation is composed of the Woodiana Sandstone Member (sandstone and siltstone), Warrie Member (carbonate and shale), and Roy Hill Shale (shale). The Jeerinah Formation was deposited during a transgression from the underlying subaerial basalt of Maddina Formation (Barley et al., 2005). The lowermost Woodiana Sandstone Member was deposited in a shallow marine environment, while the uppermost Roy Hill Shale was deposited in a deep marine environment. The Roy Hill Shale has been dated between 2629 ± 5 Ma and 2676 ± 11 Ma (Trendall et al., 2004; Rasmussen and Fletcher, 2010). The Hamersley Group is characterized by Banded Iron Formation, and consists of the Marra Mamba Iron Formation, Wittenoom Formation, Mt. Sylvia Formation, Mt. McRae Shale, Brockman Iron Formation, Weeli Wolli Formation, and Boolgeeda Iron Formation. The basal Marra Mamba Iron Formation is composed of the Nammuldi Member (shale), MacLeod Member (carbonate), and Mt. Newman Member (BIF). The age of the

Nammuldi Member, the base of the Marra Mamba Iron Formation, has been constrained between 2597 ± 5 Ma (Trendall et al., 1998) and 2629 ± 5 Ma (Trendall et al., 2004).

3. Methods

3.1 Etching and SEM analyses

Small black shale chips with pyrite were firstly cut from the drill cores, and were assembled and cast into the first batch of epoxy mounts. The mounts were then ground and polished to 1-μm diamond.

The mounts were etched in sodium hypochlorite solution (NaOCl, 8-12.5%) for about two minutes to reveal internal textures of pyrite, which were subsequently observed in the reflected light of a microscope. Pyrite nodules and disseminated pyrite grains appropriate for sulphur isotope analysis were selected and cut from the mounts, and were then assembled and cast into the second batch of mounts along with the pyrite reference materials for sulphur isotope measurements. The mounts were again polished and the etching step was repeated, followed by photographing of the etched mounts. The mounts were then lightly polished to remove the oxidized film on the surface, and then photographed.

Subsequently, the mounts were cleaned, dried, and then coated with 10 nanometers of gold for SEM (Scanning Electron Microscope) analysis. A JEOL JSM-6400 SEM at the Research School of Earth Sciences, Australian National University was used for BSE imaging and EDS (Energy Dispersive Spectroscopy) analysis. Operating conditions were 15 kV (acceleration voltage), 1 nA (beam current), and 11 mm (working distance). Semi-quantitative EDS analysis was used to verify that the target minerals was compositionally pyrite. BSE imaging was used to reveal any internal textures as a supplement of sodium hypochlorite etching. After SEM analysis, the gold film on the mounts was removed firstly by potassium iodide solution and then by polishing with 1-μm diamond paste.

3.2 Measuring multiple sulphur isotopes by SHRIMP-SI

Prior to sulphur isotope analysis, the mounts were thoroughly cleaned in an ultrasonic bath using ethanol, RBS35 detergent, warm water, and deionized water. The mounts were then dried and outgassed in a vacuum oven (0.098 MPa, 60 °C) for about five days. For SHRIMP-SI analysis, the mounts were coated with 40 nanometers of gold.

Detailed acquisition conditions for SHRIMP-SI analysis are summarized in Table 4.1. Briefly, a primary caesium ion beam was generated in a Kimbal Physics IGS5 ion gun with an internal acceleration energy of 5 keV. The ion beam was then focused to a Kohler aperture that was used as the source for the immersion lens that accelerated the beam through a further 10 keV to the sample potential. The incidence angle of the primary beam on the target was 45° resulting in elliptical spots on the target. Due to the variable sizes of the pyrite grains, both big-spot (~27 × 20 μm) and small-spot (~18 × 15 μm) analyses were conducted. Spot size was changed through placement of different Kohler apertures.

Negative sulphur secondary ions were accelerated to real ground with resultant 10 keV energy. Secondary ions were then focused through an ion extraction system (including steering) to the source slit. The width of the source slit was approximately 60 μm. Secondary ions were focused through the mass analyser to the collector. The four sulphur isotope ions were measured in multiple collection mode. The highest mass resolution (4000M/ΔM, 10% peak height) was used for the $^{33}S^-$ detector to exclude the $^{32}SH^-$ contribution; that resolution being obtained with a collector slit width of 150 μm. All four sulphur isotope ions were collected in Faraday cups; $^{32}S^-$, $^{33}S^-$, and $^{34}S^-$ were measured using current mode with 10^{11} or 10^{12} Ω resistors whereas $^{36}S^-$ was measured using charge mode with a 22 pF capacitor (Ireland et al., 2014). In one session, $^{36}S^-$ was measured in current mode with a 10^{12} Ω resistor.

Each run commenced with rastering the primary beam over an area slightly larger than the spot, removing the gold coat and conditioning the sample surface with caesium ions. During rastering, an in-line valve between the source chamber and the electrostatic analyzer was closed and base-lines for the electrometers were measured. This was followed by steering the secondary ion beam to maximize the sulphur ions signal and stabilize the secondary ion beam. As pyrite is conductive, no electron beam was needed for charge neutralization.

Each run consisted of four or five sets for big-spot analysis and two sets for small-spot analysis. Each set comprised ten scans, and each scan consisted of ten subcounts, with each subcount lasting for two seconds. The $^{36}S^-$ signal was high enough for high precision analysis in big-spot mode, but not in small-spot mode. Hence, the small-spot analyses were shorter because there was no requirement for high precision $^{36}S^-$ analysis.

The reference materials used in this work were Ruttan pyrite ($\delta^{34}S$ = 1.2 ‰, $\Delta^{33}S \approx 0$, and $\Delta^{36}S \approx 0$) and Balmat pyrite ($\delta^{34}S$ = 15.1 ‰, $\Delta^{33}S \approx 0$, and $\Delta^{36}S \approx 0$ ‰)(Crowe and Vaughan,

1996; Williford et al., 2011; Whitehouse, 2013; Ireland et al., 2014). Ruttan pyrite was the primary reference material because of its uniformity in $\delta^{34}S$. Balmat pyrite has been found to show more variability in $\delta^{34}S$, but offers the benefit of determining $\Delta^{33}S$ and $\Delta^{36}S$ at a significantly different $\delta^{34}S$. Each analytical session commenced with analyses of Ruttan pyrite and Balmat pyrite, followed by several unknowns, and then analyses of Ruttan pyrite and Balmat pyrite, and so forth. The raw data were reduced using the POXI-MC program developed at the RSES, ANU.

Table 4.1 Acquisition conditions of SHRIMP-SI.

Parameters	**Quadruple sulphur isotopes (Big-spot analyses)**	**Triple sulphur isotopes (Small-spot analyses)**
Spot size	~27 × 25 μm	~18 × 15 μm
Sets	4 or 5	2
Scans	40 or 50	20
Primary beam ion species	Cs^+	Cs^+
Primary beam intensity (avg.)	ca. 6 nA or 8 nA	ca. 2 nA
Primary beam energy	15 keV	15 keV
Total acceleration voltage for the extraction of secondary ions	10 kV	10 kV
Total analysis time	~22 min or ~25 min	~13 min
Source slit width	60 μm	60 μm
Collector slit width for $^{32}S^-$	300 μm	300 μm
Collector slit width for $^{33}S^-$	150 μm	150 μm
Collector slit width for $^{34}S^-$	200 μm	200 μm
Collector slit width for $^{36}S^-$	300 μm	300 μm
Amplifier and V-F Converter range for $^{32}S^-$	Electrometer current mode, 10^{11} Ω, 0-50 V	Electrometer current mode, 10^{11} Ω, 0-50 V
Amplifier and V-F Converter range for $^{34}S^-$	Electrometer current mode, 10^{11} Ω, 0-50 V	Electrometer current mode, 10^{11} Ω, 0-50 V
Amplifier and V-F Converter range for $^{33}S^-$	Electrometer current mode, 10^{11} or 10^{12} Ω, 0-50 V	Electrometer current mode, 10^{11} or 10^{12} Ω, 0-50 V
Amplifier and V-F Converter range for $^{36}S^-$	Electrometer charge mode, 22 pF, 0-50 V Electrometer current mode, 10^{12} Ω, 0-50 V	

Parameters	Quadruple sulphur isotopes (Big-spot analyses)	Triple sulphur isotopes (Small-spot analyses)
Mass Resolution (at 10% peak height)	4000M/ΔM	4000M/ΔM

The electrometer gains on the individual detectors were not precisely determined in this protocol. Rather, the unknowns were calibrated directly to the reference material such that the relative difference in isotopic composition between unknowns and reference material was determined. The measured ratios of the Ruttan pyrite were then fixed to the Vienna Canyon Diablo Troilite (V-CDT) reference frame.

All measured $^{3x}S^{-}/^{32}S^{-}$ ratios are expressed in delta (δ) notation as permil deviations relative to the V-CDT standard ratios. Since Ruttan pyrite was used as the primary reference material in this study, $\delta^{3x}S_{V\text{-}CDT}$ (‰) = $\delta^{3x}S_{V\text{-}CDT}$(Ruttan) + [$(^{3x}S/^{32}S)_{unknown}/(^{3x}S/^{32}S)_{Ruttan}$ - 1] × 1000, where $\delta^{3x}S_{V\text{-}CDT}$(Ruttan) is the $\delta^{3x}S_{V\text{-}CDT}$ value of Ruttan pyrite which are $\delta^{33}S_{V\text{-}CDT}$(Ruttan) = 0.62 ‰, $\delta^{34}S_{V\text{-}CDT}$(Ruttan) = 1.20 ‰, and $\delta^{36}S_{V\text{-}CDT}$(Ruttan) = 2.28 ‰ (Crowe and Vaughan, 1996; Williford et al., 2011; Whitehouse, 2013; Ireland et al., 2014). Deviations from the mass dependent fractionation laws are expressed as $\Delta^{33}S = \delta^{33}S - 1000 \times [(1 + \delta^{34}S/1000)^{0.515} - 1]$ and $\Delta^{36}S = \delta^{36}S - 1000 \times [(1 + \delta^{34}S/1000)^{1.90} - 1]$.

4. Results

4.1 Pyrite morphology

The Roy Hill Shale nodules are roughly ellipsoidal or lentoid in shape, with a semi-major axis ranging from 1.6 mm to 5.2 mm and a semi-minor axis from 1.1 mm to 2.8 mm. Etching and BSE images show rims varying from 6 to 30 μm in thickness on the pyrite nodules (Fig. 4.1). Disseminated pyrite grains within the shale matrix can be categorized into two groups: Group one pyrite grains that are 7 to 25 μm in size, euhedral to subhedral in form, and free of mineral inclusions, and Group two that are 27 × 40 μm to 31 × 71 μm, anhedral, and contain mineral inclusions (Fig. 4.1).

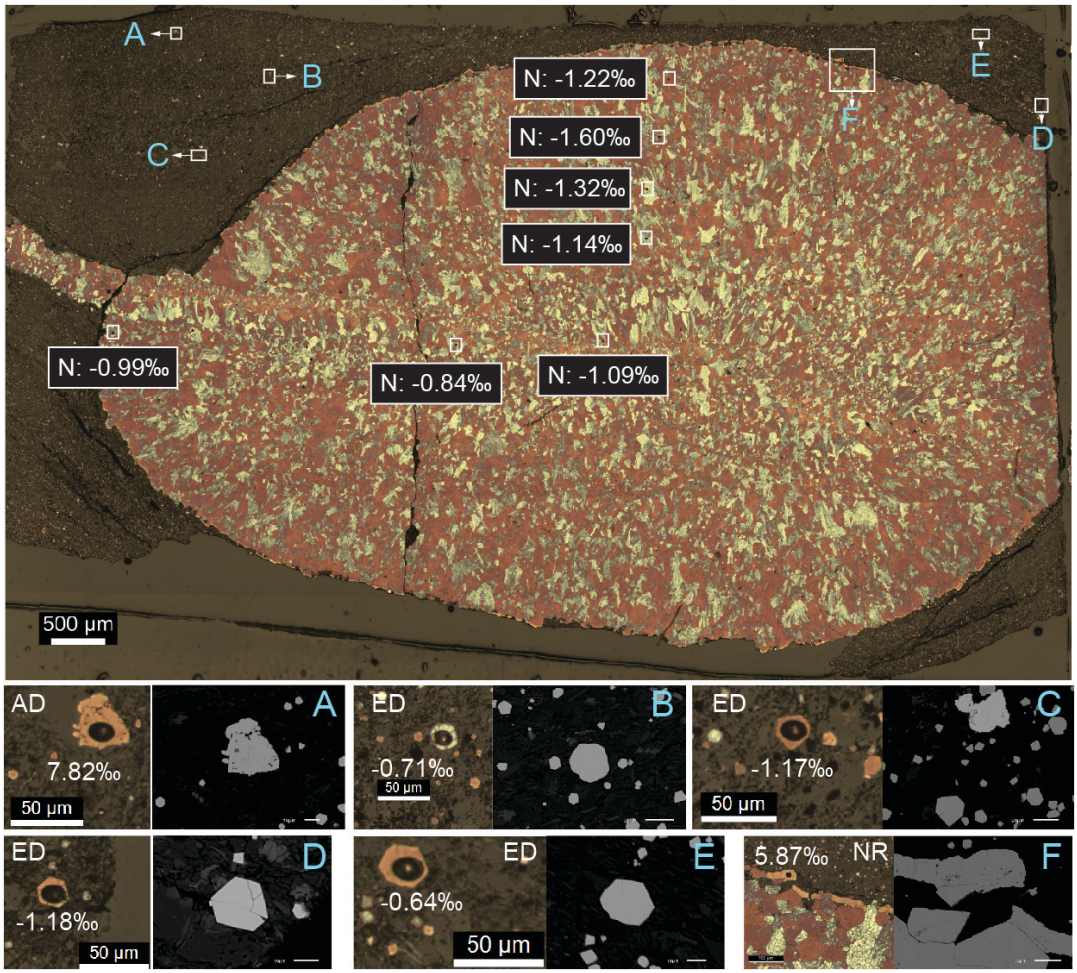

Fig. 4.1. Etching and BSE images of the Roy Hill Shale sample, including one of the pyrite nodules and some of the disseminated pyrite grains in the adjacent black shale matrix. The main body (core) of the nodule is composed of pyrite crystallites with a typical grain size of ~50-80 µm. The nodule is rimmed by a thin (the thickness is 30 µm at most) pyrite layer (F). Two types of disseminated pyrite are present, euhedral to subhedral grains with no mineral inclusions (B, C, D, and E), and anhedral grains with mineral inclusions (A). The $\Delta^{33}S$ of some spots are illustrated. AD = Anhedral disseminated, ED = Euhedral Disseminated, N = Nodule, NR = Nodule Rim.

The nodule in Nammuldi shale sample is also ellipsoidal, with a semi-major axis of 5.4 mm and a semi-minor axis of 3.5 mm (Fig. 4.2). The pyrite grains constituting the nodule are much smaller in size compared with those of the Roy Hill Shale nodules, with a typical grain size of ~10-15 µm (Fig. 4.2). Etching and BSE images display a thin rim (up to ~20 µm-thick) on the nodule, and replacement textures as well as a few euhedral coarse pyrite grains within the nodule (Fig. 4.2). The disseminated grains in the shale matrix are subhedral to anhedral, 7 to 29 µm in size, and exhibit core-rim textures in etching and BSE images.

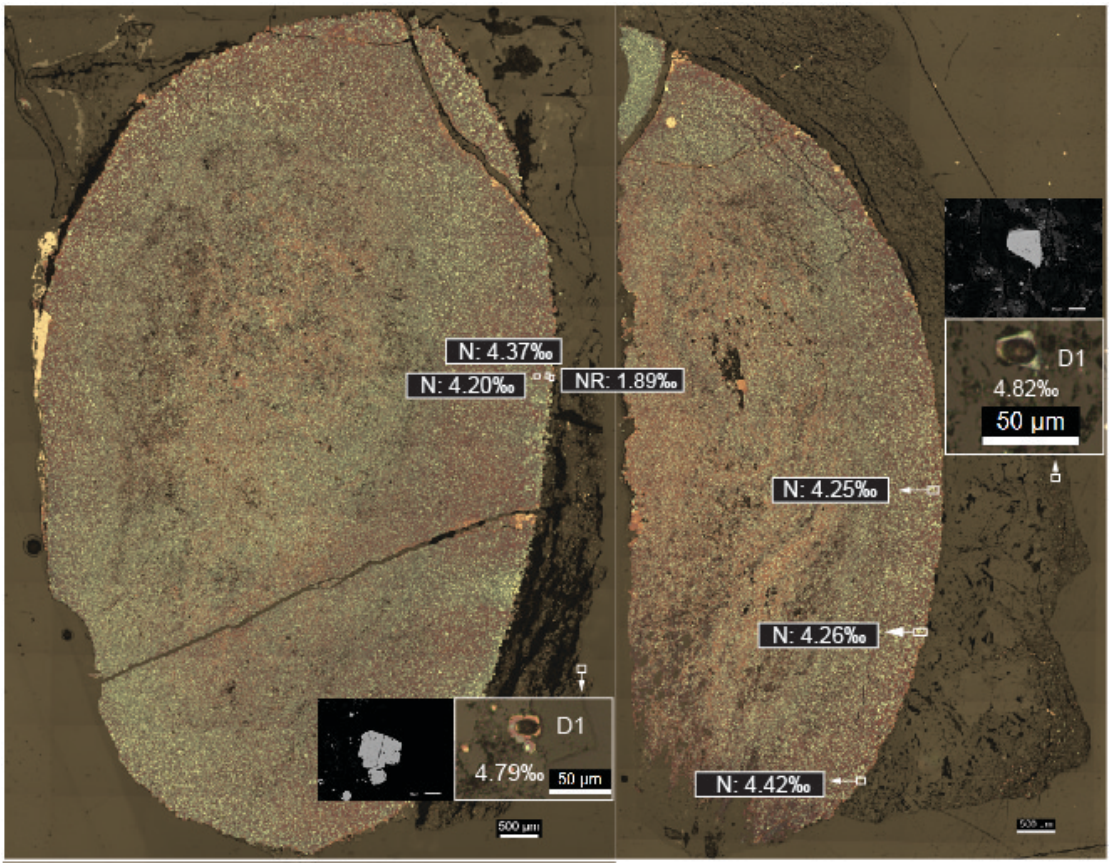

Fig. 4.2. Etching and BSE images of the Nammuldi shale sample, including pyrite nodules and disseminated pyrite grains in the black shale matrix, along with $\Delta^{33}S$ of some spots. Compared with the nodules of Roy Hill Shale sample, the constituent pyrite grains are much finer-grained with a typical grain size of ~10-15 µm. The disseminated grains in the matrix are also smaller, particularly the second generation that generally occurs as overgrowths on the first generation. N = Nodular pyrite, NR = Nodule rim, D1 = Disseminated_core.

4.2 Sulphur isotopes

All multiple sulphur isotopic compositions are listed in Table 4.2. The internal precision is expressed as one standard error of the primary reference material Ruttan pyrite in an analytical session, and is on average 0.10 ‰ ($\delta^{34}S$), 0.03 ‰ ($\Delta^{33}S$), and 0.21 ‰ ($\Delta^{36}S$) for big-spot analyses, and 0.11 ‰ ($\delta^{34}S$) and 0.12 ‰ ($\Delta^{33}S$) for small-spot analyses. The reproducibility is estimated as the value of two standard deviations of the mean measurements of Ruttan pyrite, and is on average 0.53 ‰ ($\delta^{34}S$), 0.18 ‰ ($\Delta^{33}S$), and 0.66 ‰ ($\Delta^{36}S$) for big-spot analyses, and 0.44 ‰ ($\delta^{34}S$) and 0.41 ‰ ($\Delta^{33}S$) for small-spot analyses.

For the Roy Hill Shale sample, twenty-three big-spot analyses were carried out comprising seventeen of nodular pyrite (three nodules of the same drill core sample, one nodule is in

mount M-14 and the other two nodules are in mount TDS-3), one pyrite of nodular rim, two disseminated euhedral to subhedral pyrite and three disseminated anhedral pyrite. In small-spot mode, eleven further analyses were conducted comprising seven disseminated euhedral to subhedral pyrite, two disseminated anhedral pyrite and two pyrite of nodular rim.

The analyses of nodular pyrite show a narrow range of $\delta^{34}S$, 0.5 to 3.0 ‰ for the nodule in mount M-14, and 3.7 to 4.8 ‰ for the two nodules in mount TDS-3. The $\Delta^{33}S$ ranges from -0.3 to a minimum of -1.6 ‰. Most data lie in a restricted range between -0.4 and -1.2 ‰. The $\Delta^{36}S$ of the nodule in mount M-14 ranges from -0.2 to 1.6 ‰, while that for the two nodules in mount TDS-3 is -1 to -0.8 ‰.

The quadruple sulphur isotopic composition of the nodular pyrite rim is distinct from that of the internal nodular pyrite, with a $\delta^{34}S$ of 6.5 ‰, $\Delta^{33}S$ of 5.4 ‰, and $\Delta^{36}S$ of -5.4 ‰. In small-spot mode, two additional analyses of nodular pyrite rim yield $\delta^{34}S$ of 3.5 to 6.2 ‰ and $\Delta^{33}S$ of 2.7 to 5.9 ‰.

The two big-spot analyses of disseminated euhedral to subhedral pyrite in the shale matrix yield a uniform $\delta^{34}S$ of 3.7 to 3.8 ‰, whereas the seven small-spot measurements show more variability and range from 0.5 to 6.1 ‰. The $\Delta^{33}S$ and $\Delta^{36}S$ values from big-spot analyses are quite restricted at -0.7 to -0.5 ‰ and -1.5 to -1.1 ‰, respectively, while the $\Delta^{33}S$ from small-spot analyses show an increased range from -1.2 to -0.6 ‰.

The $\delta^{34}S$ of disseminated anhedral pyrite in the shale matrix is variable, ranging from 3 to 10 ‰. The $\Delta^{33}S$ and $\Delta^{36}S$ are relatively high at 8 to 10 ‰ and -9 to -7 ‰, respectively.

For the Nammuldi shale sample, only small-spot analyses were conducted. Eight analyses of the nodular pyrite display high positive $\delta^{34}S$ (10.2 to 18.0 ‰) and are accompanied by high positive $\Delta^{33}S$ (4.0 to 5.8 ‰). Two measurements of euhedral coarse pyrite within the nodule have lower positive $\delta^{34}S$ (7.2 to 7.5 ‰) and $\Delta^{33}S$ (3.7 to 3.9 ‰). One analysis of the rimming pyrite on nodule appears to be distinct from the nodular pyrite with $\delta^{34}S$ of 4.9 ‰ and $\Delta^{33}S$ of 1.9 ‰. Three analyses of the cores of disseminated pyrite in the shale matrix exhibit similar $\delta^{34}S$ (8.5 to 12.1 ‰) and $\Delta^{33}S$ (4.8 to 5.8 ‰) to that of the nodular pyrite.

4.3 $\delta^{34}S$-$\Delta^{33}S$ systematics

4.3.1 Roy Hill Shale

$\delta^{34}S$ and $\Delta^{33}S$ of the nodular pyrite in Roy Hill Shale sample are similar to that of the disseminated euhedral to subhedral pyrite in the matrix. $\Delta^{33}S$ is relatively uniform, clustering between -2 and 0 ‰, while $\delta^{34}S$ shows moderate variability, ranging from 0 to 6 ‰ (Fig. 4.3). The $\delta^{34}S$-$\Delta^{33}S$ systematics of both types of pyrite also exhibits similar linear correlations (Fig. 4.3).

The pyrite of nodule rim and the disseminated anhedral pyrite show positive $\Delta^{33}S$ with larger magnitudes and elevated positive $\delta^{34}S$. Although the disseminated anhedral pyrite generally has larger $\delta^{34}S$ and $\Delta^{33}S$, it appears that the data for the two types of pyrite are distributed along one common line (Fig. 4.3).

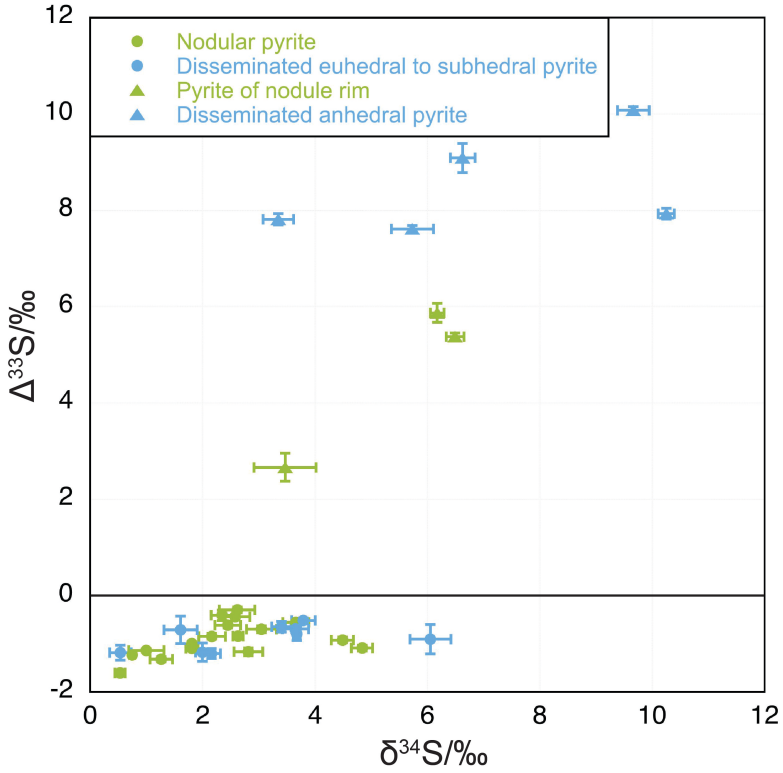

Fig. 4.3. $\delta^{34}S$-$\Delta^{33}S$ plot of the data for nodular pyrite, disseminated euhedral to subhedral pyrite, pyrite constituting nodule rim, and disseminated anhedral pyrite in the Roy Hill Shale sample. Error bar is the value of two standard errors.

4.3.2 Nammuldi

In the $\delta^{34}S$-$\Delta^{33}S$ plot, the nodular pyrite and the cores of disseminated pyrite in the matrix show two clusters (Fig. 4.4): Cluster one (only nodular pyrite) has higher positive $\delta^{34}S$ and slightly lower positive $\Delta^{33}S$ compared to Cluster two (nodular pyrite and cores of disseminated pyrite). Cluster two, euhedral coarse pyrite within nodule, and pyrite of nodule rim display evident linear correlations (Fig. 4.4).

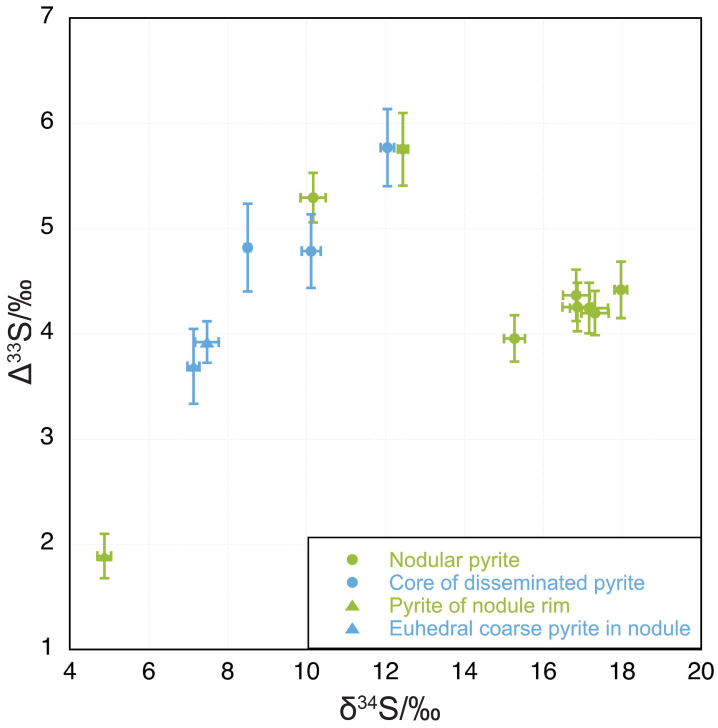

Fig. 4.4. $\delta^{34}S$-$\Delta^{33}S$ plot of the data for nodular pyrite, cores of disseminated pyrite, euhedral coarse pyrite within nodule, and pyrite of nodule rim in the Nammuldi shale sample. Error bar is the value of two standard errors.

4.4 $\Delta^{33}S$-$\Delta^{36}S$ systematics

In the $\Delta^{33}S$-$\Delta^{36}S$ plot for Roy Hill Shale sample, the majority of nodular pyrite and all of disseminated anhedral pyrite and pyrite of nodule rim are consistent with fractionation associated with the ARA with the characteristic $\Delta^{36}S/\Delta^{33}S$ slope of -1 (Fig. 4.5).

The disseminated euhedral to subhedral pyrite and the rest of nodular pyrite show negative $\Delta^{33}S$ accompanied by negative $\Delta^{36}S$. Such compositions deviate from the ARA in a trend roughly parallel to the biological fractionation line (Fig. 4.5).

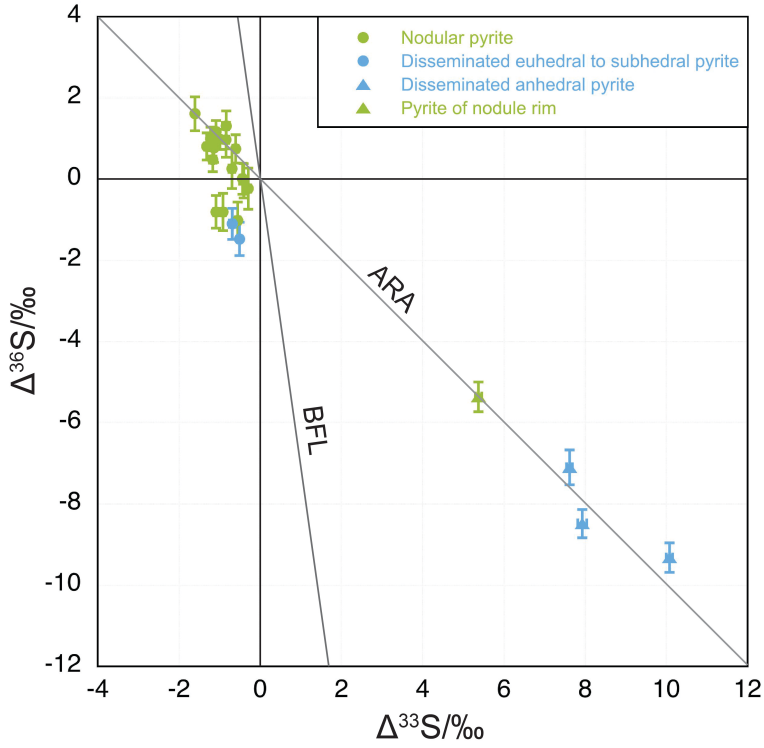

Fig. 4.5. $\Delta^{33}S$-$\Delta^{36}S$ plot of data for nodular pyrite, disseminated euhedral to subhedral pyrite, pyrite of nodule rim, and disseminated anhedral pyrite in the Roy Hill Shale sample. Error bar is the value of two standard errors. The slope of ARA (Archean Reference Array) is -1 (Farquhar et al., 2001), and that of BFL (biological fractionation line is -7, Ono et al., 2006).

5. Discussion

5.1 Pyrite generations

For the Roy Hill Shale sample, the nodular pyrite (main body of nodules) and the disseminated euhedral to subhedral pyrite in shale matrix have similar multiple sulphur isotopic compositions (magnitude and range of weakly negative $\Delta^{33}S$ and moderately positive $\delta^{34}S$, linear correlations of $\delta^{34}S$-$\Delta^{33}S$, and $\Delta^{33}S$-$\Delta^{36}S$ systematics, Fig. 4.3 and Fig. 4.5), indicating the same sulphur source for the formation of nodular pyrite and disseminated euhedral to subhedral pyrite. Similarly, the pyrite constituting nodule rim and the disseminated anhedral pyrite in shale matrix also possess similar $\delta^{34}S$-$\Delta^{33}S$-$\Delta^{36}S$ systematics, albeit of distinct signatures (highly positive $\delta^{34}S$ and $\Delta^{33}S$, Fig. 4.3 and Fig. 4.5), indicating the same sulphur source but totally different from that of nodular pyrite and disseminated euhedral to subhedral pyrite.

For the Nammuldi sample, the nodular pyrite and the cores of disseminated pyrite in the matrix have distinct multiple sulphur isotopic compositions from the pyrite of nodule rim, with the latter has much lower positive $\delta^{34}S$ and $\Delta^{33}S$ (Fig. 4.4). In the $\delta^{34}S$-$\Delta^{33}S$ plot, the data of euhedral coarse pyrite within nodule, the rim pyrite, and nodular pyrite and cores of disseminated pyrite are distributed roughly along a line (Fig. 4.4). Those of euhedral coarse pyrite are plotted in the middle, suggesting that they are probably formed via recrystallization of earlier nodular pyrite modified by later hydrothermal fluids.

Based on textural relationships and multiple sulphur isotopic compositions, two generations of pyrite are identified in both the Roy Hill Shale sample and the Nammuldi sample. For the Roy Hill Shale sample, the first generation of pyrite includes nodular pyrite and disseminated euhedral to subhedral pyrite, and is $\Delta^{33}S$-weakly negative. The second generation includes the pyrite constituting nodule rim and the disseminated anhedral pyrite, and is $\Delta^{33}S$-highly positive. For the Nammuldi sample, the nodular pyrite and the cores of disseminated pyrite are categorized to generation one, and the pyrite constituting nodule rim is categorized to generation two. The two generations of pyrite are both $\Delta^{33}S$-positive, but the magnitude of generation one is larger.

5.2 No dependence of $\Delta^{33}S$ on pyrite morphology

Nodular pyrite and disseminated pyrite can possess both negative and positive $\Delta^{33}S$ (Fig. 4.6). Therefore, the data obtained in this study are inconsistent with the previously proposed correlation between pyrite morphology and the sign of $\Delta^{33}S$, which suggested positive $\Delta^{33}S$ preserved in disseminated pyrite grains whereas negative $\Delta^{33}S$ recorded in nodular pyrite (Partridge et al., 2008; Ono et al., 2009). Apart from our study, Gregory et al. (2015) reported a pyrite nodule with positive $\Delta^{33}S$ of +0.68 ‰ to +2.42 ‰, similar to the small crystal clusters in the black shale matrix. All nodules studied in Li et al. (2017) show positive $\Delta^{33}S$ ranging from +0.5 ‰ to +2.6 ‰ rather than negative $\Delta^{33}S$. Collectively, the sign of $\Delta^{33}S$ is independent of pyrite morphology. Positive $\Delta^{33}S$ is not exclusively preserved in disseminated pyrite, and negative $\Delta^{33}S$ is not characteristic of nodular pyrite. It is the generation (i.e., source) of pyrite that determines the sign of $\Delta^{33}S$ rather than pyrite morphology (Fig. 4.6).

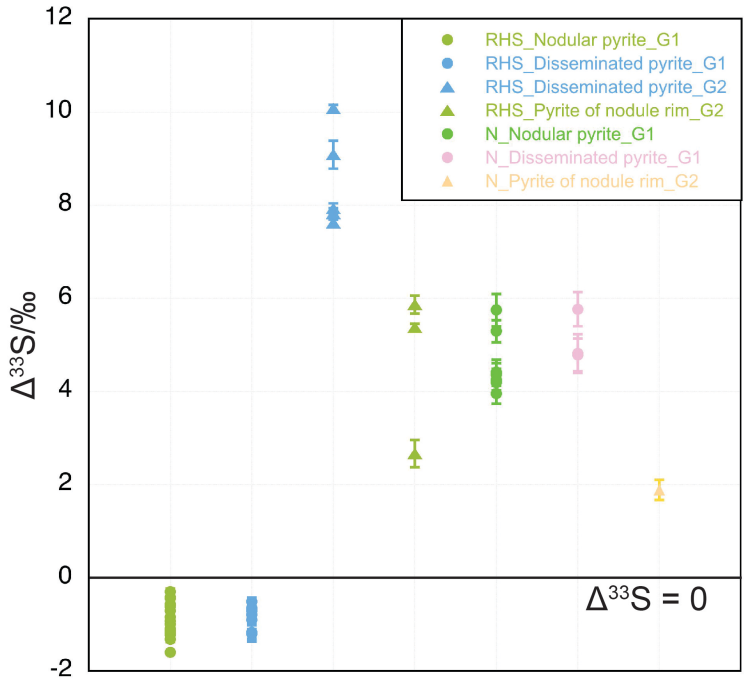

Fig. 4.6. Diagram illustrating the relationship between $\Delta^{33}S$ and pyrite morphology as well as generation. RHS = Roy Hill Shale, N = Nammuldi. Error bar is the value of two standard errors.

Based on the Roy Hill Shale sample, a plausible explanation for the pyrite morphology dependence of $\Delta^{33}S$ measured in previous studies is proposed as follows. When applying bulk sulphide extraction approaches (e.g., combustion, laser ablation, HCl and $CrCl_2$ solutions), nodules are most likely to show negative $\Delta^{33}S$ since the major portion is $\Delta^{33}S$-negative and the $\Delta^{33}S$-positive thin rim is negligible. In contrast, the magnitude of positive $\Delta^{33}S$ is dramatically larger than that of negative $\Delta^{33}S$, and the ratio of $\Delta^{33}S$-positive to $\Delta^{33}S$-negative grains of each bulk analysis is variable, thus the $\Delta^{33}S$ of disseminated grains can be variably positive, as previously reported (Partridge et al., 2008; Ono et al., 2009). Hence, the morphology dependence of $\Delta^{33}S$ concluded in previous studies could essentially stem from mixing of different generations of pyrite carrying $\Delta^{33}S$ of opposite sign.

5.3 Implications for the formation process of pyrite nodules

Marine-Carbonne et al. (2014) proposed a growth model of pyrite nodule based on the $\Delta^{33}S$-negative core (avg. -0.7 ‰) and $\Delta^{33}S$-positive rim (avg. +0.6 ‰) obtained by in-situ analysis using SIMS. In their model, the core pyrite is formed with iron from the dissolution of mackinawite (FeS), and sulphur derived from mixing of mackinawite sulphur and atmospheric-derived elemental sulphur. The rim pyrite of the nodule and the disseminated

pyrite grains in the matrix are formed by dissolution and aggregation of the disseminated small greigite (derived from solid reaction between the remaining mackinawite and elemental sulphur) during deep burial at a higher temperature and in the presence of late diagenetic or metasomatic fluids.

However, the same formation time and process for the rim and all disseminated pyrite grains in the matrix are inconsistent with the data obtained here. Based on the multiple sulphur isotopic compositions and textual relationships of nodular pyrite and disseminated pyrite, four main stages are proposed for the formation processes of the pyrite nodules studied here.

For the nodules in the Roy Hill Shale sample, pyrite framboids consisting of microcrystal pyrite are firstly formed via reactions

$Fe^{2+} + HS^- = [FeS] + H^+$ or $Fe^{2+} + S^{2-} = [FeS]$

$[FeS] + H_2S = FeS_2 + H_2$

(Rickard, 1997; Rickard and Luther, 1997), where HS^- and S^{2-} are magmatic sulphur with no S-MIF, [FeS] is an intermediate product (e.g., mackinawite), and H_2S is derived from biological (based on the deviation from ARA in a trend similar to the biological fractionation line, Fig. 4.5) reduction of atmospheric-derived sulphate carrying negative $\Delta^{33}S$. Subsequently, due to minimization of surface energy, framboids dissolve and reprecipitate, generating larger single crystals through processes such as Ostwald ripening, which are represented by the $\Delta^{33}S$-negative euhedral to subhedral disseminated pyrite grains in the shale matrix. The newly formed single crystals further aggregate to $\Delta^{33}S$-negative nodules. This nodule-forming process is significantly different from that of the experimentally synthesized nodules composed of radiating and acicular crystals, which rapidly grow individual acicular pyrite and then infill the spheroid (Rickard, 2012 and references therein). Additionally, it is noteworthy that these nodules are made up of separate pyrite grains of variable size and crystalline form rather than a single big grain typical of porphyroblast, which probably results from recrystallization and homogenization during metamorphism and deformation. After the nodules are formed, in some cases such as the Roy Hill Shale sample, the aggregated single pyrite crystals constituting the nodules are further subjected to Ostwald ripening, and are converted to larger grains, which are represented by the $\Delta^{33}S$-negative pyrite of the nodule main body. After diagenesis, a pulse of local (based on the high magnitudes of positive $\Delta^{33}S$)

hydrothermal fluid of probably metamorphic origin carrying $\Delta^{33}S$-positive sulphur (because magmatic origin carrying sulphur with no S-MIF) is injected, forming the $\Delta^{33}S$-positive rims and possibly some replacements in the nodules, as well as microcrystal clusters that are further crystallized to $\Delta^{33}S$-positive anhedral disseminated grains in the matrix. Such pyrites are formed via reactions

$$Fe^{2+} + HS^- = [FeS] + H^+ \text{ or } Fe^{2+} + S^{2-} = [FeS]$$

$$[FeS] + S_n^{2-} = FeS_2 + S_{n-1}^{2-} \text{ or } Fe^{2+} + S_n^{2-} = FeS_2 + S_{n-2}^{2-}$$

(n>=5, Rickard, 1975; Luther, 1990; Luther, 1991), where the polysulphide S_n^{2-} is derived from the combination of elemental sulphur and sulphide

$$S_{n-1} + S^{2-} = S_n^{2-}$$

and the elemental sulphur stems from photochemical reaction of sulphur-bearing gas species in the atmosphere and carries positive $\Delta^{33}S$. For the nodule in the Nammuldi sample, all the four stages are similar, except for the second reaction forming pyrite at the first stage, which is

$$[FeS] + S_n^{2-} = FeS_2 + S_{n-1}^{2-}$$

where the polysulphide carries positive $\Delta^{33}S$.

6. Concluding remarks

Integrated in-situ multiple sulphur isotopes and textural investigations into the pyrite nodules and associated disseminated pyrite grains in two typical Neoarchean shale samples from the Pilbara Craton, Western Australia show two generations of pyrite in both nodules and disseminated grains in the matrix. For the Roy Hill Shale sample, the first generation of pyrite (nodular pyrite and disseminated euhedral to subhedral pyrite in shale matrix) is characterized by a restricted range of negative $\Delta^{33}S$ and positive $\delta^{34}S$, and deviations from the ARA in a trend similar to the biological fractionation line in the $\Delta^{33}S$-$\Delta^{36}S$ plot. The second generation includes pyrite constituting the nodule rim and the disseminated anhedral grains in the matrix. They exhibit a distinct wide range of highly positive $\Delta^{33}S$ and $\delta^{34}S$, and are plotted close to the ARA. For the Nammuldi sample, both generations of pyrite (generation one: nodular

pyrite and cores of disseminated pyrite; generation two: pyrite of nodule rim) show positive $\Delta^{33}S$ and $\delta^{34}S$, except for the larger magnitudes of the first generation. Therefore, the sign of $\Delta^{33}S$ is independent of pyrite morphology (nodule or disseminated grains).

A model of pyrite nodule formation is proposed based on the data obtained in this study. Framboids composed of microcrystalline pyrite are firstly formed, which subsequently dissolve and reprecipitate as single pyrite crystals (the first generation of disseminated pyrite grains in the matrix). These newly formed single crystals further aggregate into the primary nodules, and are then enlarged in size via processes like Ostwald ripening, forming the recrystallized nodules (the first generation of nodular pyrite). After that, an injection of hydrothermal fluids (probably metamorphic in origin) precipitates the pyrite constituting the nodule rims and replacements in the nodules, as well as the second generation of disseminated pyrite in the shale matrix.

References

Barley, M.E., Bekker, A., Krapež, B., 2005. Late Archean to Early Paleoproterozoic global tectonics, environmental change and the rise of atmospheric oxygen. Earth and Planetary Science Letters 238: 156-171.

Bekker, A., Holland, H.D., Wang, P.L., Rumble III, D., Stein, H.J., Hannah, J.L., Coetzee, L.L., Beukes, N.J., 2004. Dating the rise of atmospheric oxygen. Nature 427: 117-120.

Crowe, D.E., Vaughan, R.G., 1996. Characterization and use of isotopically homogeneous standards for in situ laser microprobe analysis of $^{34}S/^{32}S$ ratios. American Mineralogist 81: 187-193.

Farquhar, J., Bao, H., Thiemens, M., 2000. Atmospheric Influence of Earth's Earliest Sulfur Cycle. Science 289: 756-758.

Farquhar, J., Cliff, J., Zerkle, A.L., Kamyshny, A., Poulton, S.W., Claire, M., Adams, D., Harms, B., 2013. Pathways for Neoarchean pyrite formation constrained by mass-independent sulfur isotopes. Proceedings of the National Academy of Sciences 110: 17638-17643.

Farquhar, J., Savarino, J., Airieau, S., Thiemens, M.H., 2001. Observation of wavelength-sensitive mass-independent sulfur isotope effects during SO_2 photolysis: Implications for the early atmosphere. Journal of Geophysical Research 106: 32829-32839.

Fischer, W.W., Fike, D.A., Johnson, J.E., Raub, T.D., Guan, Y., Kirschvink, J.L., Eiler, J.M., 2014. SQUID-SIMS is a useful approach to uncover primary signals in the Archean sulfur cycle. Proceedings of the National Academy of Sciences of the United States of America 111: 5468-5473.

Gregory, D.D., Large, R.R., Halpin, J.A., Steadman, J.A., Hickman, A.H., Ireland, T.R., Holden, P., 2015. The chemical conditions of the late Archean Hamersley basin inferred from whole rock and pyrite geochemistry with $\Delta^{33}S$ and $\delta^{34}S$ isotope analyses. Geochimica et Cosmochimica Acta 149: 223-250.

Guy, B.M., Ono, S., Gutzmer, J., Kaufman, A.J., Lin, Y., Fogel., M.L., Beukes, N.J., 2012. A multiple sulfur and organic carbon isotope record from non-conglomeratic sedimentary rocks of the Mesoarchean Witwatersrand Supergroup, South Africa. Precambrian Research 216-219: 208-231.

Holland, H.D., 2002. Volcanic gases, black smokers, and the great oxidation event. Geochimica et Cosmochimica Acta 66: 3811-3826.

Ireland, T.R., Schram, N., Holden, P., Lanc, P., Ávila, J., Armstrong, R., Amelin, Y., Latimore, A., Corrigan, D., Clement, S., Foster, J.J., Compston, W., 2014. Charge-mode electrometer measurements of S-isotopic compositions on SHRIMP-SI. International Journal of Mass Spectrometry 359: 26-37.

Johnston, D.T., Farquhar, J., Canfield, D.E., 2007. Sulfur isotope insights into microbial sulfate reduction: When microbes meet models. Geochimica et Cosmochimica Acta 71: 3929-3947.

Kaufman, A.J., Johnston, D.T., Farquhar, J., Masterson, A.L., Lyons, T.W., Bates, S., Anbar, A.D., Arnold, G.L., Garvin, J., Buick, R., 2007. Late Archean Biospheric Oxygenation and Atmospheric Evolution. Science 317: 1900-1903.

Li, J., Zhang, Z., Stern, R.A., Hannah, J.L., Stein, H.J., Yang, G., Li, L., 2017. Primary multiple sulfur isotopic compositions of pyrite in 2.7 Ga shales from the Joy Lake sequence (Superior Province) show felsic volcanic array-like signature. Geochimica et Cosmochimica Acta 202: 310-340.

Luther, G.W., 1990. The frontier-molecular-orbital theory approach in geochemical processes. Stumm, W. (Ed.), Aquatic Chemical Kinetics. Wiley-Interscience, p. 173-198.

Luther III, G.W., 1991. Pyrite synthesis via polysulfide compounds. Geochimica et Cosmochimica Acta 55: 2839-2849.

Marin-Carbonne, J., Rollion-Bard, C., Bekker, A., Rouxel, O., Agangi, A., Cavalazzi, B., Wohlgemuth-Ueberwasser, C.C., Hofmann, A., McKeegan, K.D., 2014. Coupled Fe and S isotope variations in pyrite nodules from Archean shale. Earth and Planetary Science Letters 392: 67-79.

Ono, S., Beukes, N.J., Rumble, D., 2009. Origin of two distinct multiple-sulfur isotope compositions of pyrite in the 2.5 Ga Klein Naute Formation, Griqualand West Basin, South Africa. Precambrian Research 169: 48-57.

Ono, S., Beukes, N.J., Rumble, D., Fogel, M.L., 2006. Early evolution of atmospheric oxygen from multiple-sulfur and carbon isotope records of the 2.9 Ga Mozaan Group of the Pongola Supergroup, Southern Africa. South African Journal of Geology 109: 97-108.

Ono, S., Eigenbrode, J.L., Pavlov, A.A., Kharecha, P., Rumble III, D., Kasting, J.F., Freeman, K.H., 2003. New insights into Archean sulfur cycle from mass-independent sulfur isotope records from the Hamersley Basin, Australia. Earth and Planetary Science Letters 213: 15-30.

Partridge, M.A., Golding, S.D., Baublys, K.A., Young, E., 2008. Pyrite paragenesis and multiple sulfur isotope distribution in late Archean and early Paleoproterozoic Hamersley Basin sediments. Earth and Planetary Science Letters 272: 41-49.

Peterson, E.C., Mavrogenes, J.A., 2014. Linking high-grade gold mineralization to earthquake-induced fault-valve processes in the Porgera gold deposit, Papua New Guinea. Geology 42: 383-386.

Rasmussen, B., Fletcher, I.R., 2010. Dating sedimentary rocks using in situ U-Pb geoochronology of syneruptive zircon in ash-fall tuffs <1 mm thick. Geology 38: 299-302.

Rickard, D.T., 1975. Kinetics and mechanism of pyrite formation at low temperatures. American Journal of Science 275: 636-652.

Rickard, D., 1997. Kinetics of pyrite formation by the H_2S oxidation of iron (II) monosulfide in aqueous solutions between 25 and 125 °C: The rate equation. Geochimica et Cosmochimica Acta 61: 115-134.

Rickard, D., 2012. Sulfidic Sediments and Sedimentary Rocks. Developments in Sedimentology, Amsterdam, Elsevier 65: 1-766.

Rickard, D., Luther III, G.W., 1997. Kinetics of pyrite formation by the H_2S oxidation of iron (II) monosulfide in aqueous solutions between 25 and 125 °C: The mechanism. Geochimica et Cosmochimica Acta 61: 135-147.

Shen, Y., Farquhar, J., Masterson, A., Kaufman, A.J., Buick, R., 2009. Evaluating the role of microbial sulfate reduction in the early Archean using quadruple isotope systematics. Earth and Planetary Science Letters 279: 383-391.

Tanner, D., Henley, R.W., Mavrogenes, J.A., Holden, P., 2016. Sulfur isotope and trace element systematics of zoned pyrite crystals from the El Indio Au-Cu-Ag deposit, Chile. Contributions to Mineralogy and Petrology 171:33: 1-17.

Trendall, A.F., Compston, W., Nelson, D.R., De Laeter, J.R., Bennett, V.C., 2004. SHRIMP zircon ages constraining the depositional chronology of the Hamersley Group, Western Australia. Australian Journal of Earth Sciences 51: 621-644.

Trendall, A.F., Nelson, D.R., De Laeter, J.R., Hassler, S.W., 1998. Precise zircon U-Pb ages from the Marra Mamba Iron Formation and Wittenoom Formation, Hamersley Group, Western Australia. Australian Journal of Earth Sciences 45: 137-142.

Whitehouse, M.J., 2013. Multiple Sulfur Isotope Determination by SIMS: Evaluation of Reference Sulfides for $\Delta^{33}S$ with Observations and a Case Study on the Determination of $\Delta^{36}S$. Geostandards and Geoanalytical Research 37: 19-33.

Williford, K.H., Van Kranendonk, M.J., Ushikubo, T., Kozdon, R., Valley, J.W., 2011. Constraining atmospheric oxygen and seawater sulfate concentrations during Paleoproterozoic glaciation: In situ sulfur three-isotope microanalysis of pyrite from the Turee Cree Group, Western Australia. Geochimica et Cosmochimica Acta 75: 5686-5705.

Table 4.2 Quadruple and triple sulphur isotopic composition data for pyrite of different morphology and generation in the shale samples of the Roy Hill Shale and Nammuldi members.

Title	Mount ID	Drill core ID	Strata	Pyrite morphology	Generation	$\delta^{33}S$/‰	1σ	$\delta^{34}S$/‰	1σ	$\delta^{36}S$/‰	1σ	$\Delta^{33}S$/‰	1σ	$\Delta^{36}S$/‰	1σ	CPS_$^{32}S^-$	CPS_$^{33}S^-$	CPS_$^{34}S^-$	CPS_$^{36}S^-$
Unknowns																			
M-14_1	M-14	FVG#1_769.48-769.49m	Roy Hill Shale	Nodular pyrite	1	-0.06	0.02	1.81	0.02	4.42	0.14	-0.99	0.02	0.98	0.12	1359609171	10722981	59881252	210487
M-14_3	M-14	FVG#1_769.48-769.49m	Roy Hill Shale	Nodular pyrite	1	0.51	0.02	2.63	0.04	6.32	0.19	-0.84	0.03	1.32	0.18	1332363697	10517549	58745914	206867
M-14_4	M-14	FVG#1_769.48-769.49m	Roy Hill Shale	Nodular pyrite	1	-0.16	0.03	1.81	0.05	4.61	0.15	-1.09	0.03	1.17	0.14	1267560933	9994286	55788810	196005
M-14_3	M-14	FVG#1_769.48-769.49m	Roy Hill Shale	Nodular pyrite	1	-0.62	0.02	1.00	0.16	2.67	0.16	-1.14	0.02	0.77	0.18	1325770616	10449757	58343678	205332
M-14_4	M-14	FVG#1_769.48-769.49m	Roy Hill Shale	Nodular pyrite	1	-0.67	0.02	1.26	0.10	3.21	0.18	-1.32	0.03	0.81	0.17	1284076886	10123069	56521008	198750
M-14_5	M-14	FVG#1_769.48-769.49m	Roy Hill Shale	Nodular pyrite	1	-1.33	0.02	0.53	0.04	2.62	0.21	-1.60	0.02	1.61	0.21	1296191507	10212199	57014055	200598
M-14_6	M-14	FVG#1_769.48-769.49m	Roy Hill Shale	Nodular pyrite	1	-0.84	0.02	0.75	0.02	2.42	0.18	-1.22	0.02	1.00	0.14	1297751660	10228989	57097558	200918
M-14-1_1	M-14	FVG#1_769.48-769.49m	Roy Hill Shale	Nodular pyrite	1	0.89	0.03	2.58	0.13	4.92	0.18	-0.44	0.03	0.02	0.19	891504312	6976894	38957604	132833
M-14-1_5	M-14	FVG#1_769.48-769.49m	Roy Hill Shale	Nodular pyrite	1	0.65	0.03	2.45	0.11	5.40	0.16	-0.61	0.03	0.75	0.17	809697281	6333972	35371446	120539
M-14-1_6	M-14	FVG#1_769.48-769.49m	Roy Hill Shale	Nodular pyrite	1	0.27	0.03	2.17	0.12	5.09	0.20	-0.84	0.03	0.97	0.22	840114709	6570278	36696908	125061
M-14-2_5'	M-14	FVG#1_769.48-769.49m	Roy Hill Shale	Nodular pyrite	1	1.05	0.03	2.62	0.16	4.75	0.26	-0.29	0.03	-0.23	0.25	820789819	6423283	35862520	122333
M-14-1_1'	M-14	FVG#1_769.48-769.49m	Roy Hill Shale	Nodular pyrite	1	0.80	0.05	2.34	0.10	4.42	0.22	-0.41	0.05	-0.03	0.21	808538800	6327062	35319631	120104
M-14-1_5	M-14	FVG#1_769.48-769.49m	Roy Hill Shale	Nodular pyrite	1	0.87	0.03	3.04	0.13	6.06	0.23	-0.70	0.04	0.26	0.24	824580000	6452520	36046145	123039
M-14-1_7	M-14	FVG#1_769.48-769.49m	Roy Hill Shale	Nodular pyrite	1	0.28	0.04	2.81	0.13	5.84	0.13	-1.17	0.04	0.49	0.15	861562305	6738802	37677256	128432
TDS-3_8'	TDS-3	FVG#1_769.48-769.49m	Roy Hill Shale	Nodular pyrite	1	1.33	0.02	3.66	0.12	5.94	0.24	-0.56	0.03	-1.02	0.23	806193889	6310680	35232913	120012
TDS-3_1	TDS-3	FVG#1_769.48-	Roy Hill	Nodular pyrite	1	1.39	0.04	4.49	0.10	7.74	0.22	-0.92	0.03	-0.81	0.23	818962243	6412303	35819673	121941

Title	Mount ID	Drill core ID	Strata	Pyrite morphology	Generation	$\delta^{33}S/‰$	1σ	$\delta^{34}S/‰$	1σ	$\delta^{36}S/‰$	1σ	$\Delta^{33}S/‰$	1σ	$\Delta^{36}S/‰$	1σ	CPS_$^{32}S^-$	CPS_$^{33}S^-$	CPS_$^{34}S^-$	CPS_$^{36}S^-$
		769.49m	Shale																
TDS-3_2	TDS-3	FVG#1_769.48-769.49m	Roy Hill Shale	Nodular pyrite	1	1.40	0.03	4.84	0.09	8.41	0.20	-1.09	0.03	-0.80	0.20	817975091	6405593	35796235	122105
TDS-3_10	TDS-3	FVG#1_769.48-769.49m	Roy Hill Shale	Disseminated euhedral to subhedral pyrite in shale matrix	1	1.19	0.03	3.65	0.12	5.85	0.20	-0.69	0.03	-1.10	0.19	869391934	6805908	37998525	129478
TDS-3_9	TDS-3	FVG#1_769.48-769.49m	Roy Hill Shale	Disseminated euhedral to subhedral pyrite in shale matrix	1	1.44	0.02	3.79	0.10	5.75	0.20	-0.51	0.02	-1.47	0.20	848795756	6645589	37106810	126471
M-14-8	M-14	FVG#1_769.48-769.49m	Roy Hill Shale	Disseminated euhedral to subhedral pyrite in shale matrix	1	2.21	0.15	6.05	0.18			-0.90	0.15			351717841	2757823	15445207	
M-14-5	M-14	FVG#1_769.48-769.49m	Roy Hill Shale	Disseminated euhedral to subhedral pyrite in shale matrix	1	0.12	0.15	1.61	0.15			-0.71	0.14			333196173	2606158	14577252	
M-14_14	M-14	FVG#1_769.48-769.49m	Roy Hill Shale	Disseminated euhedral to subhedral pyrite in shale matrix	1	-0.91	0.09	0.54	0.10			-1.18	0.08			860953105	6717383	37730654	
M-14_15	M-14	FVG#1_769.48-769.49m	Roy Hill Shale	Disseminated euhedral to subhedral pyrite in shale matrix	1	1.11	0.05	3.40	0.09			-0.64	0.05			829283218	6486698	36451042	
M-14_3	M-14	FVG#1_769.48-769.49m	Roy Hill Shale	Disseminated euhedral to subhedral pyrite in shale matrix	1	1.10	0.07	3.67	0.03			-0.79	0.07			820756015	6418010	36085588	
M-14_10	M-14	FVG#1_769.48-769.49m	Roy Hill Shale	Disseminated euhedral to subhedral pyrite in shale matrix	1	-0.09	0.05	2.16	0.08			-1.20	0.05			806154581	6298830	35390756	
M-14_5	M-14	FVG#1_769.48-769.49m	Roy Hill Shale	Disseminated euhedral to subhedral pyrite in shale matrix	1	-0.14	0.10	2.00	0.06			-1.17	0.10			849001453	6632353	37265610	
M-14-2	M-14	FVG#1_769.48-769.49m	Roy Hill Shale	Disseminated anhedral pyrite in shale matrix	2	12.50	0.16	6.63	0.11			9.09	0.15			328197977	2595755	14423171	
M-14_11	M-14	FVG#1_769.48-769.49m	Roy Hill Shale	Disseminated anhedral pyrite in shale matrix	2	9.54	0.05	3.34	0.14			7.82	0.06			828096097	6527729	36377783	
TDS-3_7	TDS-3	FVG#1_769.48-769.49m	Roy Hill Shale	Disseminated anhedral pyrite in shale matrix	2	13.20	0.06	10.25	0.07	11.09	0.18	7.93	0.06	-8.48	0.17	834011077	6605112	36677123	124709
TDS-3_4	TDS-3	FVG#1_769.48-769.49m	Roy Hill Shale	Disseminated anhedral pyrite in shale matrix	2	10.56	0.03	5.73	0.19	3.83	0.20	7.62	0.03	-7.09	0.21	716214262	5659253	31375022	106528
M-14-2_4	M-14	FVG#1_769.48-769.49m	Roy Hill Shale	Disseminated anhedral pyrite in shale matrix	2	15.04	0.04	9.66	0.14	9.12	0.19	10.08	0.04	-9.32	0.18	962491501	7639766	42355371	143887

Title	Mount ID	Drill core ID	Strata	Pyrite morphology	Generation	$\delta^{33}S$/‰	1σ	$\delta^{34}S$/‰	1σ	$\delta^{36}S$/‰	1σ	$\Delta^{33}S$/‰	1σ	$\Delta^{36}S$/‰	1σ	CPS_$^{32}S^-$	CPS_$^{33}S^-$	CPS_$^{34}S^-$	CPS_$^{36}S^-$
M-14-2_5	M-14	FVG#1_769.48-769.49m	Roy Hill Shale	Pyrite of the nodule rim	2	8.72	0.03	6.49	0.08	7.02	0.19	5.38	0.04	-5.36	0.18	1001876731	7901015	43950811	149454
M-14_13	M-14	FVG#1_769.48-769.49m	Roy Hill Shale	Pyrite of the nodule rim	2	9.05	0.10	6.17	0.06			5.87	0.10			821458406	6474914	36207346	
M-14-3	M-14	FVG#1_769.48-769.49m	Roy Hill Shale	Pyrite of the nodule rim	2	4.45	0.16	3.47	0.28			2.67	0.15			384429966	3022481	16856161	
TDS-4.1-13	TDS-4	FVG#1_727.80-727.81m	Nammuldi	Nodular pyrite	1	13.00	0.13	16.84	0.17			4.37	0.12			316129632	2501645	14043631	
TDS-4.1-14	TDS-4	FVG#1_727.80-727.81m	Nammuldi	Nodular pyrite	1	13.07	0.12	17.31	0.17			4.20	0.11			288955739	2289606	12846403	
TDS-4.1-18	TDS-4	FVG#1_727.80-727.81m	Nammuldi	Nodular pyrite	1	10.52	0.13	10.16	0.16			5.30	0.12			304841562	2407468	13456904	
TDS-4.2-8	TDS-4	FVG#1_727.80-727.81m	Nammuldi	Nodular pyrite	1	13.63	0.13	17.96	0.08			4.42	0.13			338953529	2685837	15080245	
TDS-4.2-9	TDS-4	FVG#1_727.80-727.81m	Nammuldi	Nodular pyrite	1	12.14	0.14	12.44	0.06			5.75	0.17			292493277	2313354	12939852	
TDS-4.2-10	TDS-4	FVG#1_727.80-727.81m	Nammuldi	Nodular pyrite	1	11.79	0.10	15.27	0.13			3.96	0.11			320789407	2534179	14224007	
TDS-4.2-11	TDS-4	FVG#1_727.80-727.81m	Nammuldi	Nodular pyrite	1	12.90	0.11	16.86	0.19			4.26	0.12			314785657	2491914	13985248	
TDS-4.2-13	TDS-4	FVG#1_727.80-727.81m	Nammuldi	Nodular pyrite	1	13.05	0.11	17.16	0.24			4.25	0.12			332082836	2627808	14759651	
TDS-4.1-2	TDS-4	FVG#1_727.80-727.81m	Nammuldi	Core of disseminated pyrite in shale matrix	1	9.98	0.16	10.11	0.12			4.79	0.18			286994467	2262610	12667800	
TDS-4.1-10	TDS-4	FVG#1_727.80-727.81m	Nammuldi	Core of disseminated pyrite in shale matrix	1	11.96	0.17	12.05	0.09			5.77	0.18			318775341	2521617	14099701	
TDS-4.2-4	TDS-4	FVG#1_727.80-727.81m	Nammuldi	Core of disseminated pyrite in shale matrix	1	9.19	0.19	8.50	0.03			4.82	0.21			297461983	2347530	13107496	
TDS-4.1-12	TDS-4	FVG#1_727.80-727.81m	Nammuldi	Pyrite of the nodule rim	2	4.40	0.10	4.87	0.09			1.89	0.11			279289135	2191524	12263681	
TDS-4.2-7	TDS-4	FVG#1_727.80-727.81m	Nammuldi	Euhedral coarse-grained pyrite within the nodule	2	7.36	0.20	7.13	0.08			3.69	0.18			287334741	2264022	12647679	
TDS-4.2-12	TDS-4	FVG#1_727.80-727.81m	Nammuldi	Euhedral coarse-grained pyrite within the nodule	2	7.77	0.10	7.47	0.15			3.92	0.10			289679366	2279832	12748515	

Reference materials

Title	Mount ID	Drill core ID	Strata	Pyrite morphology	Generation	$\delta^{33}S$/‰	1σ	$\delta^{34}S$/‰	1σ	$\delta^{36}S$/‰	1σ	$\Delta^{33}S$/‰	1σ	$\Delta^{36}S$/‰	1σ	CPS_$^{32}S^-$	CPS_$^{33}S^-$	CPS_$^{34}S^-$	CPS_$^{36}S^-$
Ruttan pyrite																			
Ruttan_14.1						0.15	0.02	0.57	0.04	1.29	0.15	-0.14	0.02	0.21	0.15	1290570962	10178334	56746874	199175
Ruttan_14.2						0.44	0.02	1.40	0.03	2.15	0.13	-0.28	0.02	-0.51	0.14	1339598591	10571553	58976750	207093
Ruttan_14.3						0.30	0.02	0.92	0.02	1.55	0.15	-0.17	0.02	-0.20	0.15	1321185068	10422171	58116832	203894
Ruttan_14.4						0.62	0.02	1.32	0.02	2.70	0.16	-0.06	0.02	0.19	0.15	1312799975	10360749	57779657	202939
Ruttan_14.5						0.05	0.01	-0.10	0.07	-0.50	0.14	0.10	0.02	-0.31	0.15	1246758395	9833088	54778889	192194
Ruttan_14.6						0.67	0.02	1.28	0.07	2.81	0.10	0.01	0.02	0.38	0.11	1283848687	10129180	56478396	198340
Ruttan_14.7						1.09	0.02	1.85	0.04	3.54	0.11	0.13	0.02	0.02	0.12	1282114626	10123741	56458195	198387
Ruttan_14.8						1.10	0.02	1.70	0.05	3.22	0.22	0.22	0.02	-0.02	0.20	1233121106	9737030	54284449	190944
Ruttan_14.9						1.15	0.02	1.87	0.08	3.77	0.17	0.18	0.02	0.22	0.15	1237116466	9768009	54469093	191469
Ruttan_1						0.31	0.03	0.75	0.17	1.02	0.21	-0.07	0.03	-0.39	0.20	840879622	6576262	36670621	124652
Ruttan_2						0.50	0.04	0.96	0.14	1.60	0.19	0.00	0.04	-0.22	0.19	835832320	6539108	36468754	123955
Ruttan_3						0.61	0.03	1.15	0.12	2.68	0.24	0.01	0.03	0.48	0.25	812361393	6356432	35451019	120750
Ruttan_4						0.70	0.03	1.30	0.15	2.17	0.26	0.03	0.03	-0.29	0.27	797180930	6236998	34789448	118533
Ruttan_5						0.67	0.04	1.29	0.14	2.70	0.20	0.00	0.04	0.25	0.21	778222021	6086957	33955708	115500
Ruttan_6						0.90	0.04	1.60	0.12	2.75	0.24	0.07	0.04	-0.29	0.24	772979790	6049708	33745469	114736
Ruttan_7						0.65	0.03	1.35	0.14	3.04	0.25	-0.05	0.03	0.46	0.25	779004114	6095025	33994426	115666
Ruttan_2						0.55	0.04	1.08	0.14	1.76	0.25	-0.01	0.04	-0.29	0.27	638620185	4995390	27842576	94749
Ruttan_3						0.67	0.03	1.30	0.11	2.64	0.27	0.00	0.04	0.17	0.28	643039806	5031671	28032283	95389
Ruttan_4						0.66	0.04	1.27	0.11	2.29	0.19	0.01	0.04	-0.12	0.18	641546430	5019111	27970427	95218
Ruttan_5						0.63	0.03	1.37	0.12	2.42	0.30	-0.07	0.03	-0.19	0.32	633997743	4959162	27644788	94335
Ruttan_8						0.67	0.04	1.24	0.15	2.55	0.23	0.03	0.05	0.20	0.24	617288944	4828806	26912186	91842
Ruttan_9						0.62	0.03	1.18	0.12	2.43	0.21	0.02	0.04	0.19	0.23	621674254	4864881	27110802	92387
Ruttan_10						0.67	0.04	1.08	0.13	2.23	0.25	0.11	0.04	0.17	0.27	614444908	4806335	26780894	91078
Ruttan_11						0.56	0.04	0.90	0.12	2.52	0.29	0.10	0.04	0.81	0.31	612001402	4787257	26670180	90702
Ruttan-1.1						1.12	0.18	1.80	0.09			0.20	0.17			332332879	2601007	14532730	
Ruttan-1.2						0.56	0.16	1.03	0.11			0.04	0.14			328935919	2573849	14376853	

Title	Mount ID	Drill core ID	Strata	Pyrite morphology	Generation	$\delta^{33}S$/‰	1σ	$\delta^{34}S$/‰	1σ	$\delta^{36}S$/‰	1σ	$\Delta^{33}S$/‰	1σ	$\Delta^{36}S$/‰	1σ	CPS_$^{32}S^-$	CPS_$^{33}S^-$	CPS_$^{34}S^-$	CPS_$^{36}S^-$
Ruttan-1.3						0.60	0.09	0.96	0.05			0.11	0.10			338395735	2647158	14787182	
Ruttan-1.4						0.94	0.13	1.62	0.09			0.11	0.12			354335558	2775260	15497451	
Ruttan-1.5						0.03	0.11	0.67	0.10			-0.32	0.12			332831841	2605415	14547960	
Ruttan-1.6						0.45	0.08	1.12	0.05			-0.13	0.09			333110447	2604929	14563935	
Ruttan_1.1						0.57	0.05	0.81	0.12			0.15	0.05			826730985	6462124	36247662	
Ruttan_1.2						0.82	0.06	1.43	0.05			0.09	0.07			844285410	6598085	37037621	
Ruttan_1.3						0.69	0.06	1.33	0.06			0.01	0.07			864262614	6754978	37915428	
Ruttan_1.4						0.62	0.05	1.32	0.09			-0.06	0.06			842498904	6587557	36960163	
Ruttan_1.5						0.39	0.06	1.11	0.03			-0.18	0.06			818987312	6400826	35914138	
Ruttan-1						0.78	0.16	0.99	0.13			0.27	0.16			287151174	2248412	12563856	
Ruttan-2						0.31	0.19	0.88	0.11			-0.14	0.22			282423308	2209427	12354161	
Ruttan-3						0.84	0.16	1.22	0.12			0.21	0.15			293523819	2297812	12843642	
Ruttan-4						0.82	0.17	1.04	0.11			0.29	0.18			293778298	2295290	12850749	
Ruttan-5						0.79	0.16	1.45	0.21			0.04	0.15			313585732	2452514	13723366	
Ruttan-6						0.29	0.16	1.46	0.24			-0.47	0.15			303296876	2370125	13268969	
Ruttan-7						0.49	0.14	1.35	0.19			-0.21	0.15			304521870	2380059	13323684	
Balmat pyrite																			
Balmat_14.1						7.31	0.02	14.59	0.02	28.35	0.17	-0.18	0.02	0.45	0.19	1309938717	10407476	58409775	207661
Balmat_14.2						6.58	0.03	13.77	0.05	25.71	0.23	-0.49	0.03	-0.60	0.22	1201248806	9538045	53542431	190056
Balmat_14.3						7.33	0.03	15.20	0.04	28.96	0.18	-0.47	0.03	-0.12	0.17	1187800355	9437737	53000402	188248
Balmat_14.4						7.54	0.02	15.29	0.03	29.34	0.15	-0.30	0.02	0.09	0.16	1126581211	8953456	50278271	178600
Balmat_1						7.50	0.03	14.67	0.13	28.01	0.20	-0.03	0.03	-0.05	0.22	798367027	6289598	35304493	121470
Balmat_2						7.52	0.03	14.69	0.15	28.39	0.18	-0.01	0.03	0.29	0.19	750213986	5908815	33169955	114359
Balmat_3						7.73	0.04	15.05	0.13	28.52	0.20	0.01	0.05	-0.27	0.21	756275973	5957818	33456009	114960
Balmat_1						7.82	0.04	14.98	0.17	29.56	0.30	0.13	0.05	0.91	0.29	594202336	4681948	26267911	90571
Balmat_2						7.92	0.04	15.09	0.15	29.29	0.26	0.17	0.04	0.42	0.26	592978431	4673758	26210790	90536
Balmat_3						7.87	0.03	14.87	0.14	29.40	0.25	0.24	0.03	0.97	0.23	569211868	4486162	25158505	86805

Title	Mount ID	Drill core ID	Strata	Pyrite morphology	Generation	$\delta^{33}S/‰$	1σ	$\delta^{34}S/‰$	1σ	$\delta^{36}S/‰$	1σ	$\Delta^{33}S/‰$	1σ	$\Delta^{36}S/‰$	1σ	CPS_$^{32}S^-$	CPS_$^{33}S^-$	CPS_$^{34}S^-$	CPS_$^{36}S^-$
Balmat-1.1						8.24	0.11	15.22	0.07			0.43	0.11			333863746	2632991	14796877	
Balmat-1.2						8.05	0.08	14.85	0.11			0.43	0.09			346236648	2730636	15352072	
Balmat_1.1						7.92	0.05	15.61	0.08			-0.09	0.05			803708221	6330146	35764157	
Balmat_1.2						7.18	0.09	14.99	0.08			-0.51	0.10			802203197	6311857	35675096	
Balmat-1						6.92	0.19	14.24	0.12			-0.39	0.18			269402676	2121050	11937706	
Balmat-2						7.24	0.18	14.46	0.21			-0.19	0.15			283278040	2228141	12552377	

Chapter 5 Quadruple Sulphur Isotopic Fractionation of Pyrite Desulphidation to Pyrrhotite

Abstract: The chemical and mineralogical conversion of pyrite-to-pyrrhotite has been studied in many aspects, but the associated quadruple sulphur isotopic fractionation has not been investigated previously. In this study, Ruttan pyrite and pyrite from a Neoarchean carbonaceous phyllite drill core were heated at 675 °C, and the released sulphur was fixed by metal iron. The products of both desulphidized pyrite and sulphidized metal iron are pyrrhotite. Compared with the starting pyrite, the $\delta^{34}S$ range of products expands, and the mean $\delta^{34}S$ increases or decreases by sub-permil to several permil, which can be attributed to matrix effect and mass dependent fractionation. The range of $\Delta^{33}S$ and $\Delta^{36}S$ of initial pyrite and both products are relatively constant, except that the $\Delta^{36}S$ range of products from carbonaceous phyllite pyrite is narrowed compared with that of initial pyrite, and can be induced by homogenization resulting from mixing of sulphur released from different pyrite grains. The fractionation in $\Delta^{33}S$ and $\Delta^{36}S$ between initial pyrite and products is slight (0.1 to 0.2‰), and can be ascribed to analytical uncertainty and kinetic mass dependent fractionation. Due to the small fractionation in $\Delta^{33}S$ and $\Delta^{36}S$ during the fixation of released sulphur by metal iron, the overall fractionation of $\Delta^{33}S$ and $\Delta^{36}S$ between the initial pyrite and liberated sulphur is slight. Considering the fact that $\delta^{34}S$ is sensitive to redox state, thus $\Delta^{33}S$ and $\Delta^{36}S$ can provide additional significant constraints for tracing sulphur sources.

1. Introduction

Metamorphic fluids derived from desulphidation of sulphides (mainly pyrite), dehydration of hydrous minerals, and decarbonation of carbonates have been widely proposed as the volatile sources of auriferous fluids for Archean gold deposits (e.g., Phillips and Powell, 2010; Tomkins, 2010). In this metamorphic model, sulphur in the fluids is liberated from pyrite via decomposition to pyrrhotite, largely through thermal desulphidation. One of the main lines of evidence supporting such a sulphur source is the multiple sulphur isotopic composition of ore-related pyrite in Archean gold deposits. Specifically, sulphur mass independent fractionation (S-MIF) with variable magnitudes of $\Delta^{33}S$ is widespread in gold mineralization-associated pyrite (e.g., Selvaraja et al., 2017; LaFlamme et al., 2018), which is most likely derived from the related Archean greenstone succession, because S-MIF is exclusively preserved in Archean metasedimentary rocks (e.g., Farquhar et al., 2000).

The pyrite-to-pyrrhotite transition has been examined via thermodynamics (Toulmin and Barton, 1964), kinetics (Lambert et al., 1998), sulphur isotopes (Kajiwara et al., 1981; Yamamoto, 1984; Ripley and Snyder, 2000), and trace elements (Pitcairn et al., 2010; Pitcairn et al., 2015; Finch and Tomkins, 2017). Previous sulphur isotope studies have investigated only two sulphur isotopes: ^{32}S and ^{34}S, and the results showed that the sulphur isotopic fractionation ($\delta^{34}S$) between the pyrrhotite products and initial pyrite is small (within ±0.5‰, Yamamoto, 1984; Ripley and Snyder, 2000), with the exception of Kajiwara et al. (1981), where the fractionation is up to +4.5‰.

Nevertheless, the quadruple sulphur isotopic fractionation of the pyrite-to-pyrrhotite conversion has not yet been investigated, although the quadruple sulphur isotopes have been increasingly used to trace the sulphur sources of Archean gold deposits ever since the report of the temporal distribution of S-MIF (Farquhar et al., 2000). This study released the sulphur from pyrite, and reacted this sulphur with metal iron to track the quadruple sulphur isotopic fractionation during the transition from pyrite to pyrrhotite.

2. Samples

Natural pyrite grains were selected from a carbonaceous phyllite drill core sample from a Neoarchean carbonate-facies Banded Iron Formation-hosted gold deposit of the Rio das Velhas Greenstone Belt, Quadrilátero Ferrífero. These pyrite grains occur within the carbonate-quartz veins of the carbonaceous phyllite.

The carbonaceous phyllite drill core was firstly crushed in a clean steel mortar. Subsequently, the fine fragments were placed under a binocular microscope, and the pyrite grains were selected. The attachments such as quartz and carbonaceous phyllite matrix on the pyrite grains were removed with tweezers under the binocular microscope, and the pyrite grains were then cleaned with ethanol.

3. Methods

3.1 Experiments

The pyrite grains (0.4997 g) from the carbonaceous phyllite were loaded into a silica glass tube with one end sealed that had been cleaned using aceton beforehand. A 30-mm-long silica rod of similar diameter (3 mm) to the tube was then placed over the pyrite grains, and metal

iron grains (0.6599 g) were placed on the top (Fig. 5.1). Subsequently, the unsealed end of the glass tube was connected to the hose of a pump, and was evacuated to vacuum. In order to seal the other end and keep the vacuum, the glass tube with the pumping hose on was then heated under the flame of a torch until soft and sealed.

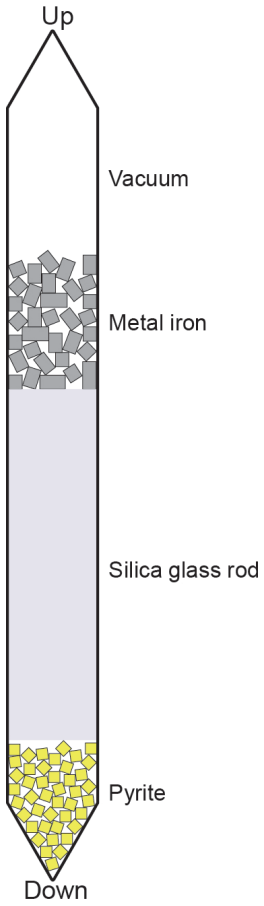

Fig. 5.1 A sketch diagram illustrating the internal apparatus of the silica glass tube.

An electric furnace was used to heat the pyrite grains. The temperature was increased to 675 °C gradually monitored by a thermocouple. The sealed glass tube was loaded into a steel vessel coupled to the furnace, which was subsequently sealed and put into the furnace. The pressure was set as 7 MPa just to avoid explosion. The pyrite grains were heated for five days, so that enough sulphur could be released to form new iron sulphide sufficiently thick for ion microprobe measurements.

Due to the potential heterogeneity of sulphur isotopic composition of the natural Archean pyrite grains, the relatively homogeneous Ruttan pyrite grains that are widely used as the

reference material for in situ measurement of sulphur isotopes by SIMS were also heated in the same way.

3.2 Measurements

3.2.1 Making mounts

The initial pyrite grains from different parts of the carbonaceous phyllite drill core were cast into mounts along with the reference materials Ruttan pyrite and Balmat pyrite. The products of desulphidized initial Neoarchean pyrite (DP1) and those from the reaction between metal iron and released sulphur (NP1) were cast into separate mounts. The initial Ruttan pyrite grains, desulphidized Ruttan pyrite (DP2) grains and sulphidized metal iron (NP2) were assembled into one mount.

3.2.2 SEM analysis

After polishing using diamond pastes (9 μm, 3 μm, 1 μm), thorough cleaning in a ultrasonic bath using ethanol, RBS35 detergent, warm water and deionized water, and drying in a vacuum oven (60 °C), the mounts were coated with 15 nanometers of aluminium for SEM (Scanning Electron Microscope) analysis, including BSE (backscattered electrons) imaging and EDS (Energy Dispersive X-Ray Spectroscopy) analysis. A JEOL JSM-6400 SEM was used, and the operation conditions were 15 kV (acceleration voltage), 1 nA (beam current), and 10 mm (working distance). Subsequent to SEM analysis, the aluminium film on the mounts was removed by decon90 detergent and polishing with 1-μm diamond paste.

3.2.3 SHRIMP-SI measurement

Prior to the measurement of quadruple sulphur isotopic composition by SHRIMP-SI (Sensitive High Resolution Ion Micro Probe-Stable Isotope) carried out at the Research School of Earth Sciences, Australian National University, the mounts were again thoroughly cleaned, degassed in the vacuum oven for at least four days, and then coated with 45 nanometers of aluminium.

Detailed acquisition conditions are summarized in Table 5.1. A primary caesium ion beam was generated in a Kimbal Physics IGS5 ion gun with an internal acceleration energy of 5 keV, and was then focused to a Kohler aperture. After the immersion lens, the beam was

accelerated through a further 10 keV to the sample potential. The incidence angle of the primary beam on the target was 45°, forming elliptical spots on the sample.

The secondary negative sulphur ions were accelerated to real ground with resultant 10 keV energy, and were then focused to the source slit (60 μm wide) through an ion extraction system. The secondary ions were focused through the mass analyser to the collector, and were measured in multiple collection mode. The highest mass resolution of 4000M/ΔM (10% peak height) was used for the $^{33}S^-$ detector to exclude the $^{32}SH^-$ contribution to the peak of $^{33}S^-$, with an associated collector slit width of 150 μm. All four sulphur isotope ions were collected in Faraday cups; The axial, auxiliary, low mass, and high mass Faraday cups collected $^{34}S^-$, $^{33}S^-$, $^{32}S^-$, and $^{36}S^-$, respectively. $^{32}S^-$, $^{33}S^-$, and $^{34}S^-$ were measured in current mode with 10^{11} or 10^{12} Ω resistors whereas $^{36}S^-$ was measured in charge mode with a 22 pF capacitor (Ireland et al., 2014).

Each analysis commenced with rastering the primary beam over an area slightly larger than the spot (~27 μm × 20 μm) for five minutes, removing the aluminium coat and allowing the sample surface to become conditioned with Cs^+ ions, while an in-line valve between the source chamber and electrostatic analyser was closed and baselines for the electrometers were collected. This was followed by horizontal and vertical steering of the emitted secondary sulphur ions in order to maximize and stabilize the secondary ion beam. No electron beam was used for charge neutralization because pyrite is conductive.

Each run comprised four sets, each set consisted of ten scans, and each scan was composed of ten subcounts, with each subcount lasting for two seconds.

Table 5.1. Acquisition conditions of SHRIMP-SI for quadruple sulphur isotopic composition measurement.

Parameters	
Spot size	~27 μm × 20 μm
Total sets	4
Total scans	40
Total analysis time	~21 min
Primary beam ion	Cs^+
Primary beam intensity	~5-8 nA

Primary beam energy	15 keV
Total acceleration voltage for the extraction of secondary ions	10 kV
Source slit width	60 μm
Collector slit width for $^{32}S^-$	300 μm
Collector slit width for $^{33}S^-$	150 μm
Collector slit width for $^{34}S^-$	200 μm
Collector slit width for $^{36}S^-$	400 μm
Amplifier and V-F Converter range for $^{32}S^-$	Electrometer current mode, 10^{11} Ω, 0-50 V
Amplifier and V-F Converter range for $^{34}S^-$	Electrometer current mode, 10^{11} Ω, 0-50 V
Amplifier and V-F Converter range for $^{33}S^-$	Electrometer current mode, 10^{12} Ω, 0-50 V
Amplifier and V-F Converter range for $^{36}S^-$	Electrometer charge-mode, 22 pF, 0-50 V
Mass Resolution (at 10% peak height)	4000 M/ΔM

For the measurement of initial Neoarchean pyrite, the reference materials were Ruttan pyrite (primary, $\delta^{34}S$ = 1.2‰, $\Delta^{33}S$ and $\Delta^{36}S \approx 0$) and Balmat pyrite (secondary, $\delta^{34}S$ = 15.1‰, $\Delta^{33}S$ and $\Delta^{36}S \approx 0$)(Crowe and Vaughan, 1996; Williford et al., 2011; Whitehouse, 2013; Ireland et al., 2014). Each measurement session started with two runs on Ruttan pyrite and one on Balmat pyrite, followed by around five runs on the unknowns as long as the conditions were stable, and then one or two runs on Ruttan pyrite and one on Balmat pyrite, and so forth. For the measurement of products (DP1 and NP1), the reference material was Anderson pyrrhotite ($\delta^{34}S$ = 1.4‰, $\Delta^{33}S$ and $\Delta^{36}S \approx 0$; Crowe et al., 1990; Crowe and Vaughan, 1996; Mojzsis et al., 2003). Each measurement commenced with two runs on Anderson pyrrhotite, and then three runs on the unknowns, followed by another two runs on Anderson pyrrhotite and three runs on the unknowns, and so forth.

The initial Ruttan pyrite grains (regarded as unknowns) and products of desulphidized Ruttan pyrite (DP2) and sulphidized metal iron (NP2) were measured in the same session with reference materials of both Ruttan pyrite and Anderson pyrrhotite. The session commenced with two runs on Ruttan pyrite (reference material) and two runs on Anderson pyrrhotite, followed by two to four runs on the products (DP2 and NP2) and one on initial Ruttan pyrite (regarded as unknown), and then two runs on Ruttan pyrite (reference material) and two runs on Anderson pyrrhotite, two to four runs on the products (DP2 and NP2) and one on initial Ruttan pyrite (regarded as unknown), and so forth.

The raw data were reduced using the POXI-MC software developed by the RSES of ANU. The measured $^{3x}S^-/^{32}S^-$ ratios are expressed in delta (δ) notation as permil deviations from the

Vienna Canyon Diablo Troilite (V-CDT) standard ratios, following the relationship of $\delta^{3x}S_{V\text{-}CDT}$ (‰) = $[(^{3x}S/^{32}S)_{unknown}/(^{3x}S/^{32}S)_{V\text{-}CDT} - 1] \times 1000$, where $(^{3x}S/^{32}S)_{unknown}$ and $(^{3x}S/^{32}S)_{V\text{-}CDT}$ are the $^{3x}S/^{32}S$ ratios of unknowns and V-CDT, respectively, and x is 3, 4 or 6.

For pyrite measurements, Ruttan pyrite was applied as the primary reference material, thus $\delta^{3x}S_{V\text{-}CDT}$ (‰) = $\delta^{3x}S_{V\text{-}CDT}$(Ruttan) + $[(^{3x}S/^{32}S)_{unknown}/(^{3x}S/^{32}S)_{Ruttan} - 1] \times 1000$, where $\delta^{3x}S_{V\text{-}CDT}$(Ruttan) is the $\delta^{3x}S_{V\text{-}CDT}$ value of Ruttan pyrite ($\delta^{33}S_{V\text{-}CDT}$(Ruttan), $\delta^{34}S_{V\text{-}CDT}$(Ruttan), and $\delta^{36}S_{V\text{-}CDT}$(Ruttan) are 0.618‰, 1.2‰, and 2.281‰, respectively, Crowe and Vaughan, 1996; Williford et al., 2011; Whitehouse, 2013; Ireland et al., 2014). For measurements of products, Anderson pyrrhotite was used as the reference material, thus $\delta^{3x}S_{V\text{-}CDT}$ (‰) = $\delta^{3x}S_{V\text{-}CDT}$(Anderson) + $[(^{3x}S/^{32}S)_{unknown}/(^{3x}S/^{32}S)_{Anderson} - 1] \times 1000$, where $\delta^{3x}S_{V\text{-}CDT}$(Anderson) is the $\delta^{3x}S_{V\text{-}CDT}$ value of Anderson pyrrhotite ($\delta^{33}S_{V\text{-}CDT}$(Anderson), $\delta^{34}S_{V\text{-}CDT}$(Anderson), and $\delta^{36}S_{V\text{-}CDT}$(Anderson) are 0.721‰, 1.4‰, and 2.662‰, respectively, Crowe et al., 1990; Crowe and Vaughan, 1996; Mojzsis et al., 2003). The magnitude of S-MIF is quantified as $\Delta^{33}S$ (= $\delta^{33}S - 1000 \times [(1 + \delta^{34}S/1000)^{0.515} - 1]$) and $\Delta^{36}S$ (= $\delta^{36}S - 1000 \times [(1 + \delta^{34}S/1000)^{1.9} - 1]$).

For the session with reference materials of both Ruttan pyrite and Anderson pyrrhotite, the sulphur isotopic compositions of initial Ruttan pyrite were normalized to Ruttan pyrite, and those of products were normalized to Anderson pyrrhotite. In addition, the Anderson pyrrhotite was normalized directly to Ruttan pyrite to assess the matrix effect between pyrite and pyrrhotite.

4. Results

4.1 Products

For the experiment with pyrite from carbonaceous phyllite, DP1 and NP1 display pink color in the reflected light of microscope and have similar chemical composition. DP1 is textually distinct from NP1. The former is spongy individual grains with abundant pores, while the latter sticks together, and displays typical metasomatic-relict texture (Fig. 5.2). The EDS results show that the atomic ratios of S to Fe range from 1.83 to 2 for pyrite (Ruttan pyrite, Balmat pyrite, and initial pyrite), 1.08 to 1.22 for Anderson pyrrhotite, 0.98 to 1.07 for DP1 and 0.92 to 1.03 for NP1 (Table 5.2).

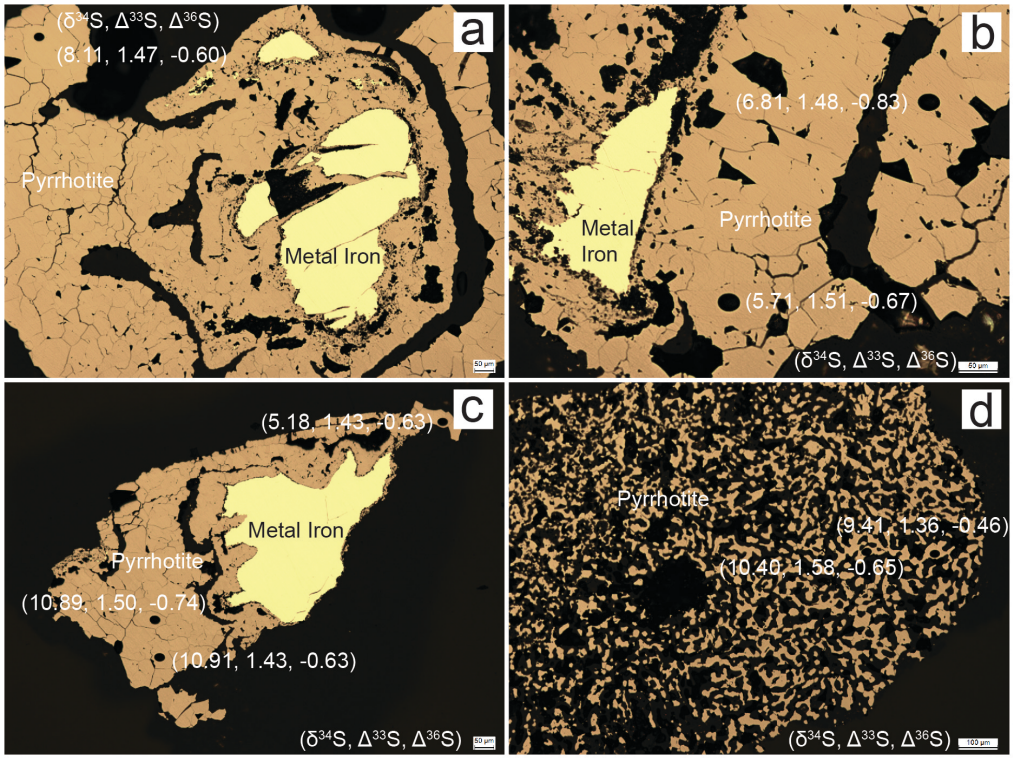

Fig. 5.2. Microphotographs of the pyrrhotite products in experiment with the Neoarchean pyrite from carbonaceous phyllite, along with the quadruple sulphur isotopic compositions. a, b and c are NP1 pyrrhotite (derived from sulphidation of metal iron) displaying metasomatic-relict texture. d is DP1 pyrrhotite (desulphidized pyrite) showing spongy texture.

For the experiment with Ruttan pyrite, the signatures of the two kinds of products (DP2 and NP2) are similar to those of DP1 and NP1. The S/Fe ratio of DP2 ranges from 1.04 to 1.19, and that of NP2 varies from 0.98 to 1.08 (Table 5.2).

4.2 Quadruple sulphur isotopic compositions

The sulphur isotope data of the experiment with pyrite from carbonaceous phyllite are listed in Table 5.3. The internal error is estimated in the value of two standard errors of the reference material, and the reproducibility is expressed in the value of two standard deviations of the reference material. For pyrite measurement, the internal error for Ruttan pyrite is 0.10‰ ($\delta^{34}S$), 0.03‰ ($\Delta^{33}S$), 0.23‰ ($\Delta^{36}S$) on average, and the reproducibility is 0.34‰ ($\delta^{34}S$), 0.11‰ ($\Delta^{33}S$), 0.33‰ ($\Delta^{36}S$) on average. For products measurement, the mean internal error for Anderson pyrrhotite is 0.38‰ ($\delta^{34}S$), 0.06‰ ($\Delta^{33}S$), 0.22‰ ($\Delta^{36}S$), and the mean reproducibility is 0.46‰ ($\delta^{34}S$), 0.10‰ ($\Delta^{33}S$), 0.26‰ ($\Delta^{36}S$).

For the initial pyrite in carbonaceous phyllite, $\Delta^{33}S$ is relatively constant, with a slight variation from 1.21‰ to 1.41‰, averaged at 1.34‰, whereas $\delta^{34}S$ ranges more from 6.75‰ to 9.50‰ (7.78‰ on average), and $\Delta^{36}S$ varies most from -1.33‰ to -0.19 (-0.61‰ on average). $\Delta^{33}S$ of both DP1 and NP1 remains relatively constant, but the average values are slightly larger (1.52‰ and 1.46‰, respectively). $\delta^{34}S$ varies considerably, particularly for NP1 (5.18‰ to 13.69‰), and the mean values are also higher (9.58‰ and 9.41‰ for DP1 and NP1, respectively). The range of $\Delta^{36}S$ narrows for both products, -0.71‰ to -0.27‰ for DP1 and -0.83‰ to -0.49‰ for NP1 (Fig. 5.3). Within the $\Delta^{33}S$-$\Delta^{36}S$ diagram, the data of DP1 and NP1 deviate slightly from those of initial pyrite in a trend towards the right (Fig. 5.4). Neither the data of initial pyrite nor products are on the Archean Reference Array, with the exception of two datapoints of initial pyrite (Fig. 5.4).

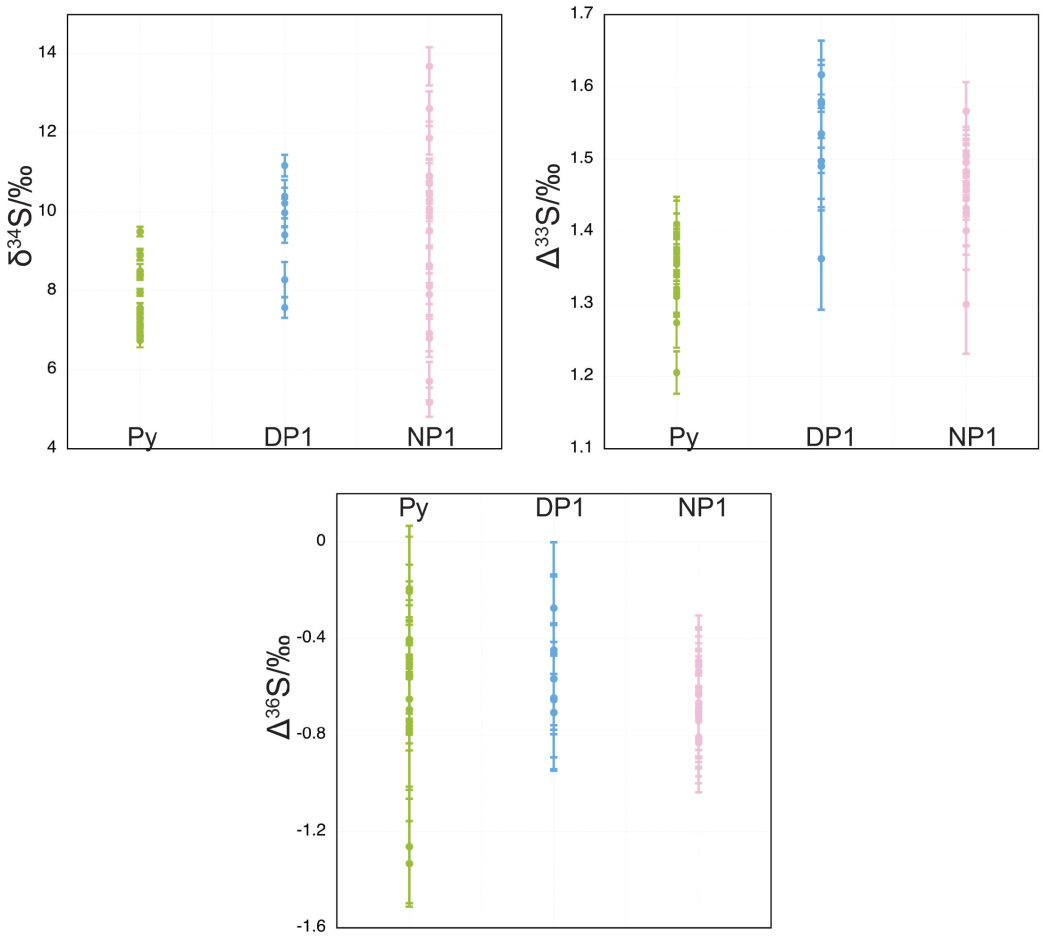

Fig. 5.3. Diagram of comparing $\delta^{34}S$, $\Delta^{33}S$, and $\Delta^{36}S$ of the initial pyrite and pyrrhotite products from the experiment with the Neoarchean pyrite. Error bar is two standard errors. Py: the initial pyrite; DP1: pyrrhotite derived from desulphidation of initial pyrite; NP1: pyrrhotite produced via reaction between metal iron and sulphur released from pyrite.

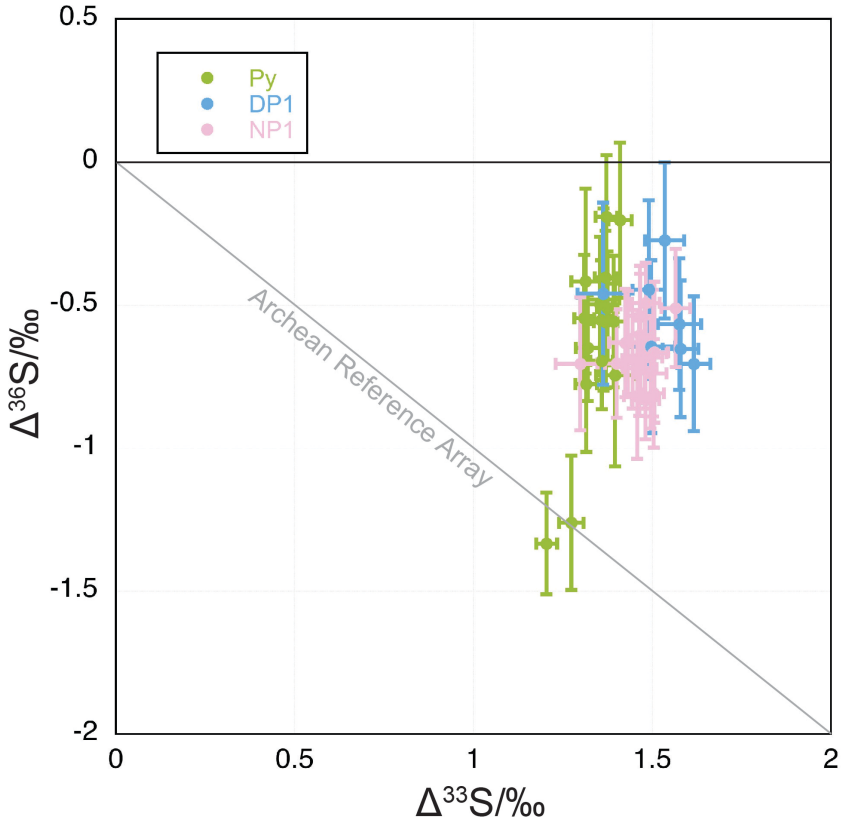

Fig. 5.4. $\Delta^{33}S$-$\Delta^{36}S$ plot diagram of the data of initial pyrite and pyrrhotite products from the experiment with the Neoarchean pyrite. Error bar is two standard errors. Py: the initial pyrite; DP1: pyrrhotite derived from desulphidation of initial pyrite; NP1: pyrrhotite produced via reaction between metal iron and sulphur released from pyrite.

The sulphur isotope data of the experiment with Ruttan pyrite are listed in Table 5.4. The sulphur isotopic compositions of initial Ruttan pyrite (regarded as unknowns) were obtained by normalizing to Ruttan pyrite (reference material), and those of products were calculated by normalizing to Anderson pyrrhotite. The internal error for Ruttan pyrite (reference material) is 0.21‰ ($\delta^{34}S$), 0.07‰ ($\Delta^{33}S$), 0.27‰ ($\Delta^{36}S$) on average, and that for Anderson pyrrhotite is 0.54‰ ($\delta^{34}S$), 0.08‰ ($\Delta^{33}S$), 0.21‰ ($\Delta^{36}S$) on average. The reproducibility for Ruttan pyrite (reference material) is 1.01‰ ($\delta^{34}S$), 0.37‰ ($\Delta^{33}S$), 0.21‰ ($\Delta^{36}S$) on average, and that for Anderson pyrrhotite is 0.67‰ ($\delta^{34}S$), 0.20‰ ($\Delta^{33}S$), 0.21‰ ($\Delta^{36}S$) on average.

The initial Ruttan pyrite has relatively concentrated $\Delta^{33}S$ (-0.17‰ to 0.06‰) and $\Delta^{36}S$ (-0.15‰ to 0.19‰), and slightly scattered $\delta^{34}S$ (1.06‰ to 1.94‰). The range of $\delta^{34}S$ for both DP2 and NP2 expands considerably, -0.99‰ to 2.75‰ for the former and -1.40‰ to 1.39‰ for the latter (Fig. 5.5). The $\Delta^{33}S$ of both products stays relatively constant (Fig. 5.5),

particularly DP2 (-0.18‰ to 0.15‰). The variation of $\Delta^{36}S$ increases slightly, -0.40‰ to 0.10‰ for DP2 and -0.24‰ to 0.27‰ for NP2 (Fig. 5.5).

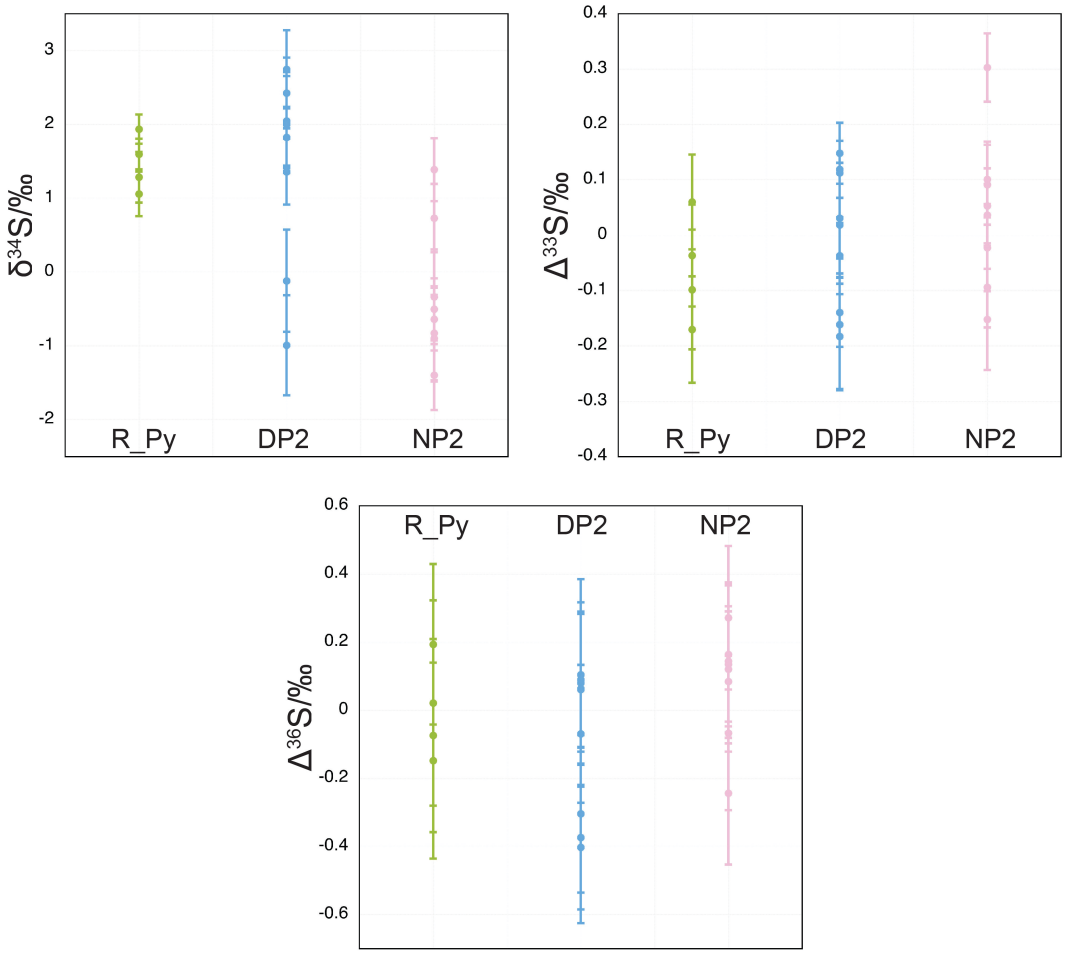

Fig. 5.5. Diagram of comparing $\delta^{34}S$, $\Delta^{33}S$, and $\Delta^{36}S$ of the initial Ruttan pyrite and pyrrhotite products. Error bar is two standard errors. R_Py: Ruttan pyrite, DP2: pyrrhotite derived from desulphidation of Ruttan pyrite, NP2: pyrrhotite derived from sulphidation of metal iron.

5. Discussion

5.1 Formation of products

The semi-quantitative S/Fe ratios and optical color in reflected light of both types of products (desulphidized pyrite and sulphidized metal iron) are similar to that of pyrrhotite, while distinct from pyrite, indicating that the products are both pyrrhotite rather than pyrite.

The spongy texture of DP1 and DP2 from initial pyrite suggests that pyrite is thermally desulphidized to pyrrhotite under vacuum condition, following the equation $xFeS_2 = Fe_xS +$

(2x-1)/nS_n, where FeS_2 is pyrite, Fe_xS is pyrrhotite 1, x is less than 1, S_n is liberated sulphur gas, and n is an integer between 1 and 8. The metasomatic-relict texture of NP1 and NP2 from metal iron indicates that the metal iron is sulphidized to pyrrhotite by the liberated sulphur gas under vacuum condition, following the equation $S_n + nxFe = nFe_xS$, where Fe is metal iron and Fe_xS is pyrrhotite 2.

5.2 Quadruple sulphur isotopic fractionation

Compared with the initial pyrite, the $\delta^{34}S$ range of products expands, and the mean $\delta^{34}S$ increases except for the products of sulphidized metal iron in experiment with Ruttan pyrite (Fig. 5.3 and Fig. 5.5), which can be attributed to three possible factors. The first one is matrix effect. Although the products and the reference material are both pyrrhotite (Fe_xS), the specific S/Fe ratio differs slightly. Such compositional differences can result in matrix effect in $\delta^{34}S$ as a comprehensive study has shown (Riciputi et al., 1998). Additionally, in the session of measuring the sulphur isotopes of desulphidized Ruttan pyrite and sulphidized metal iron, it shows that when Anderson pyrrhotite is normalized to Ruttan pyrite, the $\delta^{34}S$ decreases from 1.4‰ (true value) to -2.6‰ (Supplementary Table 3), and when Ruttan pyrite is normalized to Anderson pyrrhotite, the $\delta^{34}S$ increases from 1.2‰ (true value) to 5.3‰ (Table 5.4). As such, when an iron sulphide is normalized to another iron sulphide with higher S/Fe ratio, the $\delta^{34}S$ decreases. Since the S/Fe ratio of products is lower than that of Anderson pyrrhotite, thus the $\delta^{34}S$ is supposed to decrease, which is observed in pyrrhotite from sulphidized metal iron and some pyrrhotite grains from desulphidized pyrite in the experiment with Ruttan pyrite (Fig. 5.5). However, the other pyrrhotite products show increased $\delta^{34}S$ (Table 5.3 and Table 5.4), suggesting that other factors also contribute. Although the majority of studies on pyrite desulphidation show small mass dependent fractionation (within ±0.5‰, Yamamoto, 1984; Ripley and Snyder, 2000), Kajiwara et al. (1981) reported fractionations of up to 4.5‰, suggesting that mass dependent fractionation can also account for the increase in $\delta^{34}S$. Alternatively, some initial pyrite grains can have higher $\delta^{34}S$ than those measured, which increases the $\delta^{34}S$ of final products. Collectively, the wider range of $\delta^{34}S$ in products can be ascribed to variable degrees of matrix effect induced by different S/Fe ratios and variable extents of mass dependent fractionation. For the products of pyrite from carbonaceous phyllite, the increased $\delta^{34}S$ can also be induced by the higher $\delta^{34}S$ in some initial pyrite grains.

The $\Delta^{33}S$ of initial pyrite and products is relatively constant, both the range and mean value (Fig. 5.3 and Fig. 5.5). For the Ruttan pyrite experiment, the mean $\Delta^{33}S$ of initial Ruttan pyrite is -0.06‰, and that of desulphidized Ruttan pyrite (DP2) and sulphidized metal iron (NP2) is -0.01‰ and 0.04‰, respectively, resulting in a fractionation of 0.05‰ and 0.1‰. For the experiment of pyrite from carbonaceous phyllite, the mean $\Delta^{33}S$ of desulphidized pyrite (DP1, 1.52‰) and sulphidized metal iron (NP1, 1.46‰) is slightly (0.18‰ and 0.12‰) larger than that of initial pyrite (1.34‰). One possibility is newly produced S-MIF during desulphidation of pyrite and sulphidation of iron. Current proposed processes of producing S-MIF based on experiments include photochemical reactions of sulphur-bearing gases under the radiation of ultraviolet of variable wavelength (e.g., SO_2 photolysis, Farquhar et al., 2001; SO_2 photoexcitation, Whitehill and Ono, 2012; CS_2 photopolymerization, Colman et al., 1996) and non-gas phase reactions such as thermochemical sulphate reduction (Watanabe et al., 2009) and surface adsorption (Lasaga et al., 2008), none of which, however, is consistent with the pyrite-to-pyrrhotite transformation and iron-sulphur reaction in this study. Alternatively, such slight (sub-permil scale) S-MIF can be attributed to kinetic mass dependent fractionation (MDF) proposed by Young et al. (2002), because the exponent (β) relating the fractionation factors of two isotope ratios ($\alpha_{2/1} = \alpha_{3/1}^{\beta}$) for kinetic MDF ($\beta = \ln(M_1/M_2)/\ln(M_1/M_3)$, where M_1, M_2, M_3 are the reduced, molecular, or atomic masses) is different from that of equilibrium MDF ($\beta = (1/m_1 - 1/m_2)/(1/m_1 - 1/m_3)$, where m_1, m_2, m_3 are the atomic masses of the isotopes, and $m_1 < m_2 < m_3$), and such a difference in calculation can lead to small magnitude of S-MIF. As LaFlamme et al. (2018) has discussed this matter further, $\delta^{34}S$ of 14‰ in magnitude is required to obtain $\Delta^{33}S$ of 0.1‰ based on the equation $\Delta^{33}S = 1000(\delta^{34}S/1000 + 1)^{0.515} - 1000(\delta^{34}S/1000 + 1)^{\beta}$, where β can be 0.508 to 0.519 as summarized in LaFlamme et al. (2018). However, all the $\delta^{34}S$ measured here is less than this value, thus the kinetic MDF accounts for $\Delta^{33}S$ of less than 0.1‰. Another possibility is the analytical uncertainty. If considering both the internal error and reproducibility for the uncertainty ($[(\text{internal error})^2 + (\text{reproducibiligy})^2]^{1/2}$), the slight fractionation of 0.1‰ in the experiment with Ruttan pyrite is within analytical uncertainty (0.38‰ for pyrite measurement and 0.22‰ for pyrrhotite measurement). So is the fractionation of 0.18‰ in the experiment with pyrite from carbonaceous phyllite, where the total uncertainty is 0.23‰ (0.11‰ for pyrite measurement and 0.12‰ for pyrrhotite measurement).

The $\Delta^{36}S$ range of DP1 and NP1 narrows compared with that of initial pyrite, probably as a result of homogenization after the mixing of sulphur released from different pyrite grains. The

mean $\Delta^{36}S$ of NP1 (-0.67‰) is nearly the same as that of initial pyrite (-0.61‰), whereas that of DP1 is slightly smaller (-0.54‰). The $\Delta^{36}S$ range of initial Ruttan pyrite and products keeps constant, but the mean $\Delta^{36}S$ also fractionates from 0 of initial Ruttan pyrite to -0.08‰ and 0.08‰ of the products. The kinetic MDF-induced $\Delta^{36}S$ can be calculated following $\Delta^{36}S = 1000(\delta^{34}S/1000 + 1)^{1.9} - 1000(\delta^{34}S/1000 + 1)^{\beta}$, where the exponent β can be 1.89, 1.90, and 1.91 for $\Delta^{36}S$ (Hulston and Thode, 1965). $\Delta^{36}S$ of 0.08‰ (for Ruttan pyrite experiment) and 0.13‰ (for carbonaceous phyllite pyrite experiment) requires $\delta^{34}S$ of 8‰ and 13‰, respectively, which are higher than the $\delta^{34}S$ of Ruttan pyrite and carbonaceous phyllite pyrite. The analytical uncertainty of $\Delta^{36}S$ calculated following the method for that of $\Delta^{33}S$ is much larger than the fractionation. Therefore, the contributing factors can include kinetic MDF and analytical uncertainty.

5.3 Applications to tracing sulphur sources

As revealed above, $\Delta^{33}S$ and $\Delta^{36}S$ are relatively constant, with a fractionation of merely 0.1 to 0.2‰ between the initial pyrite and pyrrhotite products. The fractionation in $\Delta^{33}S$ and $\Delta^{36}S$ during the fixation of released sulphur ($S_n + nxFe = nFe_xS$) should also be slight, because this reaction is inconsistent with any proposed process of producing S-MIF as summarized in 5.2, and even if kinetic MDF occurs, the S-MIF produced should also be slight. Therefore, the $\Delta^{33}S$ and $\Delta^{36}S$ fractionation between initial pyrite and liberated sulphur during desulphidation ($xFeS_2 = Fe_xS + (2x-1)/nS_n$) is slight.

The liberated sulphur from pyrite is then involved in hydrothermal fluids, in the case of Archean gold deposits, metamorphic fluids, where sulphur can be in variable valences as a variety of sulphur-bearing species rather than only sulphides. Since $\delta^{34}S$ is sensitive to redox state, and variable degrees of fractionations will be produced between these sulphur-bearing species and the original sulphur (Rye and Ohmoto, 1974), as such the $\delta^{34}S$ of sulphides measured cannot represent that of the primary sulphur (bulk sulphur of the fluids). Unlike $\delta^{34}S$, $\Delta^{33}S$ and $\Delta^{36}S$ are not fractionated between the two reservoirs due to the exclusive processes of producing S-MIF (even if fractionated, the magnitude is extremely small). Therefore, $\Delta^{33}S$ and $\Delta^{36}S$ are more appropriate to represent the sulphur isotopic composition of bulk metamorphic fluids and the sulphides desulphidized to release sulphur, thus tracing the sulphur sources.

It is also noteworthy that although the $\Delta^{33}S$ and $\Delta^{36}S$ of liberated sulphur fractionate only slightly from the original source sulphides, in actual geological cases, due to the mixing of sulphur from other sources with different $\Delta^{33}S$ and $\Delta^{36}S$ (e.g., magmatic fluids or metamorphic fluids), as well as the interactions between fluids and surrounding rocks, they will potentially be changed significantly in the end. Hence, tracing sulphur sources using $\Delta^{33}S$ and $\Delta^{36}S$ should still be careful and take the specific geological settings into consideration.

6. Concluding remarks

Ruttan pyrite and the pyrite from a Neoarchean carbonaceous phyllite drill core were heated at 675 °C, and the released sulphur was sequestered by metal iron. The products of desulphidized pyrite and sulphidized metal iron are both pyrrhotite following the equations $xFeS_2 = Fe_xS + (2x-1)/nS_n$ and $S_n + nxFe = nFe_xS$ under vacuum conditions.

The $\delta^{34}S$ range of pyrrhotite products expands compared with that of initial pyrite. The mean $\delta^{34}S$ of the products in experiment with pyrite from carbonaceous phyllite increases while that of the products in experiment with Ruttan pyrite decreases. Such fractionations in $\delta^{34}S$ can be ascribed to matrix effect and mass dependent fractionation. The $\Delta^{33}S$ of initial pyrite and both products is relatively constant, particularly for the experiment with Ruttan pyrite. The fractionation in $\Delta^{33}S$ between initial pyrite and products is slight (0.05 to 0.18‰), which can be ascribed to analytical uncertainty and kinetic MDF. The $\Delta^{36}S$ range of products from carbonaceous phyllite pyrite is narrowed compared with that of initial pyrite, which can be attributed to homogenization as a result of mixing of sulphur released from different pyrite grains. The $\Delta^{36}S$ range of products from Ruttan pyrite stays constant. The mean $\Delta^{36}S$ of products from both experiments fractionates slightly (0.06 to 0.13‰), and can be also attributed to analytical uncertainty and kinetic mass dependent fractionation. Since the fractionation in $\Delta^{33}S$ and $\Delta^{36}S$ during the fixation of released sulphur by metal iron is also small, thus the $\Delta^{33}S$ and $\Delta^{36}S$ fractionation between the initial pyrite and liberated sulphur is slight. Due to the sensitivity of $\delta^{34}S$ on redox state, $\Delta^{33}S$ and $\Delta^{36}S$ can add significant constraints of sulphur sources.

References

Colman J. J., Xu X., Thiemens M. H., Trogler W. C., 1996. Photopolymerization and Mass-Independent Sulfur Isotope Fractionations in Carbon Disulfide. Science 273: 774-776.

Crowe D. E., Valley J. W., Baker K. L., 1990. Micro-analysis of sulfur-isotope ratios and zonation by laser microprobe. Geochimica et Cosmochimica Acta 54: 2075-2092.

Crowe D. E., and Vaughan R. G., 1996. Characterization and use of isotopically homogeneous standards for in situ laser microprobe analysis of $^{34}S/^{32}S$ ratios. American Mineralogist 81: 187-193.

Farquhar J., Bao H., Thiemens M., 2000. Atmospheric Influence of Earth's Earliest Sulfur Cycle. Science 289: 756-758.

Farquhar J., Savarino J., Airieau S., Thiemens M. H., 2001. Observation of wavelength-sensitive mass-independent sulfur isotope effects during SO_2 photolysis: Implications for the early atmosphere. Journal of Geophysical Research 106: 32829-32839.

Finch E. G., and Tomkins A. G., 2017. Pyrite-Pyrrhotite Stability in a Metamorphic Aureole: Implications for Orogenic Gold Genesis. Economic Geology 112: 661-674.

Hulston, J.R., and Thode, H.G., 1965. Variations in the S^{33}, S^{34}, and S^{36} Contents of Meteorites and Their Relation to Chemical and Nuclear Effects. Journal of Geophysical Research 70: 3475-3484.

Ireland, T.R., Schram, N., Holden, P., Lanc, P., Ávila, J., Armstrong, R., Amelin, Y., Latimore, A., Corrigan, D., Clement, S., Foster, J.J., Compston, W., 2014. Charge-mode electrometer measurements of S-isotopic compositions on SHRIMP-SI. International Journal of Mass Spectrometry 359: 26-37.

Kajiwara Y., Sasaki A., Matsubaya O., 1981. Kinetic sulfur isotope effects in the thermal decomposition of pyrite. Geochemical Journal 15: 193-197.

LaFlamme, C., Jamieson, J. W., Fiorentini, M. L., Thébaud, N., Caruso, S., Selvaraja, V., 2018. Investigating sulfur pathways through the lithosphere by tracing mass independent fractionation of sulfur to the Lady Bountiful orogenic gold deposit, Yilgarn Craton. Gondwana Research 58: 27-38.

LaFlamme C., Sugiono D., Thébaud N., Caruso S., Fiorentini M., Selvaraja V., Jeon H., Voute F., Martin L., 2018. Multiple sulfur isotopes monitor fluid evolution of an Archean orogenic gold deposit. Geochimica et Cosmochimica Acta 222: 436-446.

Lambert J. M., Simkovich G., Walker P. L., 1998. The kinetics and mechanism of the pyrite-to-pyrrhotite transformation. Metallurgical and Materials Transactions B 29: 385-396.

Lasaga A. C., Otake T., Watanabe Y., Ohmoto H., 2008. Anomalous fractionation of sulfur isotopes during heterogeneous reactions. Earth and Planetary Science Letters 268: 225-238.

Mojzsis S. J., Coath C. D., Greenwood J. P., McKeegan K. D., Harrison T. M., 2003. Mass-independent isotope effects in Archean (2.5 to 3.8 Ga) sedimentary sulfides determined by ion microprobe analysis. Geochimica et Cosmochimica Acta 67: 1635-1658.

Phillips G. N., and Powell R., 2010. Formation of gold deposits: a metamorphic devolatilization model. Journal of Metamorphic Geology 28: 689-718.

Pitcairn I. K., Olivo G. R., Teagle D. A. H., Craw D., 2010. Sulfide evolution during prograde metamorphism of the Otago and Alpine Schists, New Zealand. The Canadian Mineralogist 48: 1267-1295.

Pitcairn I. K., Skelton A. D. L., Wohlgemuth-Ueberwasser C. C., 2015. Mobility of gold during metamorphism of the Dalradian in Scotland. Lithos 233: 69-88.

Riciputi L. R., Paterson B. A., Ripperdan R. L., 1998. Measurement of light stable isotope ratios by SIMS: Matrix effects for oxygen, carbon, and sulfur isotopes in minerals. International Journal of Mass Spectrometry 178: 81-112.

Ripley E. M., and Snyder K., 2000. Experimental sulfur isotope studies of the pyrite to pyrrhotite conversion in a hydrogen atmosphere. Economic Geology 95: 1551-1554.

Rye R. O., and Ohmoto H., 1974. Sulfur and carbon isotopes and ore genesis: a review. Economic Geology 69: 826-842.

Selvaraja V., Caruso S., Fiorentini M. L., LaFlamme C. K., Bui T. H., 2017. Atmospheric sulfur in the orogenic gold deposits of the Archean Yilgarn Craton, Australia. Geology 45: 691-694.

Tomkins A. G., 2010. Windows of metamorphic sulfur liberation in the crust: Implications for gold deposit genesis. Geochimica et Cosmochimica Acta 74: 3246-3259.

Toulmin P., and Barton P. B., 1964. A thermodynamic study of pyrite and pyrrhotite. Geochimica et Cosmochimica Acta 28: 641-671.

Watanabe Y., Farquhar J., Ohmoto H., 2009. Anomalous Fractionations of Sulfur Isotopes During Thermochemical Sulfate Reduction. Science 324: 370-373.

Whitehouse M. J., 2013. Multiple Sulfur Isotope Determination by SIMS: Evaluation of Reference Sulfides for $\Delta^{33}S$ with Observations and a Case Study on the Determination of $\Delta^{36}S$. Geostandards and Geoanalytical Research 37: 19-33.

Whitehill A. R., and Ono S., 2012. Excitation band dependence of sulfur isotope mass-independent fractionation during photochemistry of sulfur dioxide using broadband light sources. Geochimica et Cosmochimica Acta 94: 238-253.

Williford K. H., Van Kranendonk M. J., Ushikubo T., Kozdon R., Valley J. W., 2011. Constraining atmospheric oxygen and seawater sulfate concentrations during Paleoproterozoic glaciation: In situ sulfur three-isotope microanalysis of pyrite from the Turee Cree Group, Western Australia. Geochimica et Cosmochimica Acta 75: 5686-5705.

Yamamoto M., 1984. Sulfur isotope effects in the thermal breakdown of pyrite. Earth and Planetary Science Letters 69: 335-340.

Young E. D., Galy A., Nagahara H., 2002. Kinetic and equilibrium mass-dependent isotope fractionation laws in nature and their geochemical and cosmochemical significance. Geochimica et Cosmochimica Acta 66: 1095-1104.

Table 5.2 EDS results for the chemical compositions of iron sulphides.

Title	Mineral	S	Fe	S/Fe
Reference materials				
Ruttan pyrite	Pyrite	66.27	33.73	1.96
Balmat pyrite	Pyrite	66.01	33.99	1.94
Anderson pyrrhotite	Pyrrhotite	52.41	47.59	1.1
Anderson pyrrhotite	Pyrrhotite	53	47	1.13
Anderson pyrrhotite	Pyrrhotite	54.98	45.02	1.22
Anderson pyrrhotite	Pyrrhotite	52.61	47.39	1.11
Anderson pyrrhotite	Pyrrhotite	51.89	48.11	1.08
Anderson pyrrhotite	Pyrrhotite	52.27	47.73	1.1
Anderson pyrrhotite	Pyrrhotite	52.2	47.8	1.09
Anderson pyrrhotite	Pyrrhotite	52	48	1.08
Experiment with pyrite from carbonaceous phyllite				
MAS-49B	Initial pyrite	66.68	33.32	2
3.1_pyrrhotite	Desulphidized initial pyrite (DP1)	50.55	49.45	1.02
3.3_pyrrhotite	Desulphidized initial pyrite (DP1)	50.76	49.24	1.03
3.6_pyrrhotite	Desulphidized initial pyrite (DP1)	49.66	50.34	0.99
3.8_pyrrhotite	Desulphidized initial pyrite (DP1)	49.53	50.47	0.98
3.9_pyrrhotite	Desulphidized initial pyrite (DP1)	50.05	49.95	1
3.10_pyrrhotite	Desulphidized initial pyrite (DP1)	50.64	49.36	1.03
3.11_pyrrhotite	Desulphidized initial pyrite (DP1)	50.33	49.67	1.01
3.12_pyrrhotite	Desulphidized initial pyrite (DP1)	50.85	49.15	1.03
p1_1	Desulphidized initial pyrite (DP1)	50.62	49.38	1.03
p1_2	Desulphidized initial pyrite (DP1)	50.36	49.64	1.01
p1_3	Desulphidized initial pyrite (DP1)	50.94	49.06	1.04
p1_4	Desulphidized initial pyrite (DP1)	50.5	49.5	1.02
p1_5	Desulphidized initial pyrite (DP1)	50.15	49.85	1.01
p1_6	Desulphidized initial pyrite (DP1)	50.91	49.09	1.04
p1_7	Desulphidized initial pyrite (DP1)	51.53	48.47	1.06
p1_8	Desulphidized initial pyrite (DP1)	51.72	48.28	1.07
p1_9	Desulphidized initial pyrite (DP1)	50.4	49.6	1.02
p1_10	Desulphidized initial pyrite (DP1)	50.55	49.45	1.02
p1_11	Desulphidized initial pyrite (DP1)	49.71	50.29	0.99
p1_12	Desulphidized initial pyrite (DP1)	50.42	49.58	1.02
p1_13	Desulphidized initial pyrite (DP1)	50.65	49.35	1.03
p1_14	Desulphidized initial pyrite (DP1)	50.27	49.73	1.01

Title	Mineral	S	Fe	S/Fe
2.1_pyrrhotite	Metal iron reacted with liberated sulphur gas (NP1)	49.29	50.71	0.97
2.3_pyrrhotite	Metal iron reacted with liberated sulphur gas (NP1)	49.02	50.98	0.96
2.5_pyrrhotite	Metal iron reacted with liberated sulphur gas (NP1)	49.53	50.47	0.98
2.6_pyrrhotite	Metal iron reacted with liberated sulphur gas (NP1)	49.51	50.49	0.98
2.8_pyrrhotite	Metal iron reacted with liberated sulphur gas (NP1)	49.71	50.29	0.99
2.9_pyrrhotite	Metal iron reacted with liberated sulphur gas (NP1)	49.33	50.67	0.97
2.10_pyrrhotite	Metal iron reacted with liberated sulphur gas (NP1)	48.92	51.08	0.96
AS_1	Metal iron reacted with liberated sulphur gas (NP1)	48.15	51.85	0.93
AS_2	Metal iron reacted with liberated sulphur gas (NP1)	49.82	50.18	0.99
AS_3	Metal iron reacted with liberated sulphur gas (NP1)	49.78	50.22	0.99
AS_4	Metal iron reacted with liberated sulphur gas (NP1)	48.69	51.31	0.95
AS_5	Metal iron reacted with liberated sulphur gas (NP1)	48.78	51.22	0.95
AS_6	Metal iron reacted with liberated sulphur gas (NP1)	49.23	50.77	0.97
AS_7	Metal iron reacted with liberated sulphur gas (NP1)	49.17	50.83	0.97
AS_8	Metal iron reacted with liberated sulphur gas (NP1)	49.47	50.53	0.98
AS_8'	Metal iron reacted with liberated sulphur gas (NP1)	49.27	50.73	0.97
AS_9	Metal iron reacted with liberated sulphur gas (NP1)	49.08	50.92	0.96
New_1.1	Metal iron reacted with liberated sulphur gas (NP1)	50.29	49.71	1.01
New_1.2	Metal iron reacted with liberated sulphur gas (NP1)	50.47	49.53	1.02
New_1.3	Metal iron reacted with liberated sulphur gas (NP1)	49.39	50.61	0.98
New_1.4	Metal iron reacted with liberated sulphur gas (NP1)	50.1	49.9	1
New_1.6	Metal iron reacted with liberated sulphur gas (NP1)	49.51	50.49	0.98
New_1.7	Metal iron reacted with liberated sulphur gas (NP1)	50.29	49.71	1.01
New_1.9	Metal iron reacted with liberated sulphur gas (NP1)	50.08	49.92	1
New_1.11	Metal iron reacted with liberated sulphur gas (NP1)	48.03	51.97	0.92
New_1.13	Metal iron reacted with liberated sulphur gas (NP1)	49.38	50.62	0.98
New_1.14	Metal iron reacted with liberated sulphur gas (NP1)	50.22	49.78	1.01
New_1.17	Metal iron reacted with liberated sulphur gas (NP1)	49.52	50.48	0.98
New_1.18	Metal iron reacted with liberated sulphur gas (NP1)	50.21	49.79	1.01
New_1.19	Metal iron reacted with liberated sulphur gas (NP1)	49.07	50.93	0.96
New_1.21	Metal iron reacted with liberated sulphur gas (NP1)	49.4	50.6	0.98
New_1.22	Metal iron reacted with liberated sulphur gas (NP1)	50.36	49.64	1.01
New_1.23	Metal iron reacted with liberated sulphur gas (NP1)	49.32	50.68	0.97
New_1.25	Metal iron reacted with liberated sulphur gas (NP1)	48.7	51.3	0.95
New_1.26	Metal iron reacted with liberated sulphur gas (NP1)	49.87	50.13	0.99
New_1.28	Metal iron reacted with liberated sulphur gas (NP1)	50.36	49.64	1.01
New_1.29	Metal iron reacted with liberated sulphur gas (NP1)	50.33	49.67	1.01
New_1.30	Metal iron reacted with liberated sulphur gas (NP1)	48.6	51.4	0.95

Title	Mineral	S	Fe	S/Fe
New_1.31	Metal iron reacted with liberated sulphur gas (NP1)	50.13	49.87	1.01
New_1.32	Metal iron reacted with liberated sulphur gas (NP1)	49.21	50.79	0.97
New_1.32'	Metal iron reacted with liberated sulphur gas (NP1)	49.83	50.17	0.99
New_1.33	Metal iron reacted with liberated sulphur gas (NP1)	50.37	49.63	1.01
p2_1	Metal iron reacted with liberated sulphur gas (NP1)	49.16	50.84	0.97
p2_2	Metal iron reacted with liberated sulphur gas (NP1)	50.23	49.77	1.01
p2_3	Metal iron reacted with liberated sulphur gas (NP1)	49.17	50.83	0.97
p2_4	Metal iron reacted with liberated sulphur gas (NP1)	49.45	50.55	0.98
p2_5	Metal iron reacted with liberated sulphur gas (NP1)	49.75	50.25	0.99
p2_6	Metal iron reacted with liberated sulphur gas (NP1)	49.41	50.59	0.98
p2_7	Metal iron reacted with liberated sulphur gas (NP1)	50.14	49.86	1.01
p2_8	Metal iron reacted with liberated sulphur gas (NP1)	49.39	50.61	0.98
p2_9	Metal iron reacted with liberated sulphur gas (NP1)	50.72	49.28	1.03
p2_10	Metal iron reacted with liberated sulphur gas (NP1)	49.21	50.79	0.97
p2_11	Metal iron reacted with liberated sulphur gas (NP1)	49.18	50.82	0.97
p2_12	Metal iron reacted with liberated sulphur gas (NP1)	49.27	50.73	0.97
p2_13	Metal iron reacted with liberated sulphur gas (NP1)	50.72	49.28	1.03
p2_14	Metal iron reacted with liberated sulphur gas (NP1)	49.45	50.55	0.98
Experiment with Ruttan pyrite				
Initial Ruttan pyrite	Pyrite	65.74	34.26	1.92
Initial Ruttan pyrite	Pyrite	64.63	35.37	1.83
1	Metal iron reacted with liberated sulphur gas (NP2)	51.88	48.12	1.08
2	Metal iron reacted with liberated sulphur gas (NP2)	51.06	48.94	1.04
3	Metal iron reacted with liberated sulphur gas (NP2)	50.5	49.5	1.02
5	Metal iron reacted with liberated sulphur gas (NP2)	49.59	50.41	0.98
6	Metal iron reacted with liberated sulphur gas (NP2)	50.18	49.82	1.01
7	Metal iron reacted with liberated sulphur gas (NP2)	50.38	49.62	1.02
9	Metal iron reacted with liberated sulphur gas (NP2)	50.49	49.51	1.02
11	Metal iron reacted with liberated sulphur gas (NP2)	51.17	48.83	1.05
12	Metal iron reacted with liberated sulphur gas (NP2)	49.98	50.02	1
13	Metal iron reacted with liberated sulphur gas (NP2)	50.95	49.05	1.04
17	Desulphidized Ruttan pyrite (DP2)	51.98	48.02	1.08
18	Desulphidized Ruttan pyrite (DP2)	51.24	48.76	1.05
19	Desulphidized Ruttan pyrite (DP2)	51.88	48.12	1.08
21	Desulphidized Ruttan pyrite (DP2)	52.12	47.88	1.09
22	Desulphidized Ruttan pyrite (DP2)	54.32	45.68	1.19

Title		Mineral	S	Fe	S/Fe
	25	Desulphidized Ruttan pyrite (DP2)	52.62	47.38	1.11
	26	Desulphidized Ruttan pyrite (DP2)	51.36	48.64	1.06
	28	Desulphidized Ruttan pyrite (DP2)	52.12	47.88	1.09
	29	Desulphidized Ruttan pyrite (DP2)	51.53	48.47	1.06
	30	Desulphidized Ruttan pyrite (DP2)	51.08	48.92	1.04

Table 5.3 Quadruple sulphur isotopic composition data of the initial pyrite and products for the experiment with the Neoarchean pyrite in carbonaceous phyllite.

Title	Iron sulphide	$\delta^{33}S$/‰	1σ/‰	$\delta^{34}S$/‰	1σ/‰	$\delta^{36}S$/‰	1σ/‰	$\Delta^{33}S$/‰	1σ/‰	$\Delta^{36}S$/‰	1σ/‰	CPS/$^{32}S^-$	CPS/$^{33}S^-$	CPS/$^{34}S^-$	CPS/$^{36}S^-$
Unknowns	(The session with titles MAS-49_n is not used here, because the δ33S, δ34S, δ36S, Δ33S, and Δ36S of the reference material Ruttan pyrite deviate from the true values to some degree, and the data of unknowns in this session are different from the other sessions to some extent as well, while the data of Ruttan pyrite in these sessions are very close to true values)														
MAS-49_7	Initial pyrite	5.47	0.03	7.39	0.07	13.33	0.14	1.67	0.03	-0.75	0.18	808539959	6358978	35599429	121280
MAS-49_6	Initial pyrite	5.83	0.04	8.05	0.10	14.40	0.19	1.69	0.03	-0.95	0.19	777688200	6117253	34264543	116767
MAS-49_5	Initial pyrite	5.76	0.04	8.20	0.08	14.99	0.20	1.54	0.04	-0.66	0.19	826070887	6496778	36401288	124200
MAS-49_4	Initial pyrite	4.76	0.02	5.78	0.07	9.81	0.14	1.79	0.02	-1.19	0.14	1093324738	8588662	48052217	163468
MAS-49_3'	Initial pyrite	6.49	0.03	9.34	0.09	17.38	0.17	1.69	0.03	-0.44	0.18	932475419	7339047	41138405	140228
MAS-49_2'	Initial pyrite	4.25	0.03	4.92	0.08	8.62	0.13	1.72	0.03	-0.74	0.14	1047937464	8229698	46019733	156372
QF-4-1_4	Initial pyrite	5.95	0.01	8.90	0.07	16.47	0.10	1.38	0.01	-0.51	0.10	1419280504	11222242	62713844	226633
QF-4-1_5	Initial pyrite	5.75	0.01	8.51	0.09	16.04	0.11	1.37	0.02	-0.19	0.11	1417555881	11207064	62615013	226192
QF-4-1_8	Initial pyrite	5.63	0.01	8.40	0.06	15.47	0.11	1.31	0.01	-0.55	0.11	1530051422	12093813	67569223	243848
QF-4-1_9	Initial pyrite	6.24	0.02	9.50	0.06	17.43	0.08	1.36	0.02	-0.69	0.08	1552337027	12276214	68625043	248118
QF-4-1_10	Initial pyrite	5.19	0.01	7.43	0.06	13.60	0.12	1.37	0.02	-0.56	0.12	1531875156	12102998	67593529	243999
QF-4-1_11	Initial pyrite	5.25	0.01	7.57	0.06	13.87	0.10	1.36	0.01	-0.55	0.10	1551925695	12262560	68486059	246900
QF-4-1_3_	Initial pyrite	5.98	0.02	8.93	0.07	16.47	0.11	1.39	0.02	-0.56	0.12	1431774513	11321420	63269690	228712
QF-4-2_1	Initial pyrite	4.79	0.02	6.75	0.09	12.22	0.09	1.32	0.02	-0.65	0.09	1390783439	10984608	61330315	221331
QF-4-2_4	Initial pyrite	5.02	0.02	7.14	0.08	13.11	0.11	1.36	0.02	-0.50	0.12	1348518274	10653111	59477400	214558
QF-4-2_5	Initial pyrite	5.13	0.01	7.31	0.08	13.54	0.08	1.37	0.01	-0.40	0.08	1395050737	11021424	61544760	221972
QF-4-2_8	Initial pyrite	5.08	0.02	7.53	0.08	13.03	0.09	1.21	0.01	-1.33	0.09	1334260953	10540506	58870355	212370
QF-4-2_9	Initial pyrite	4.99	0.01	7.15	0.06	12.86	0.13	1.32	0.02	-0.78	0.12	1465567135	11576608	64644304	233182
QF-4-2_10	Initial pyrite	4.91	0.02	7.07	0.06	12.22	0.12	1.27	0.02	-1.26	0.12	1202962866	9501195	53058699	191266
TE34_MAS-49B_11	Initial pyrite	5.50	0.02	7.96	0.04	14.97	0.14	1.41	0.02	-0.20	0.14	1588873501	12542292	69997808	238868
TE34_MAS-49_17	Initial pyrite	4.91	0.03	6.84	0.04	12.28	0.16	1.40	0.03	-0.75	0.16	1501335614	11846000	66080767	225133

Title	Iron sulphide	$\delta^{33}S$/‰	1σ/‰	$\delta^{34}S$/‰	1σ/‰	$\delta^{36}S$/‰	1σ/‰	$\Delta^{33}S$/‰	1σ/‰	$\Delta^{36}S$/‰	1σ/‰	CPS/$^{32}S^-$	CPS/$^{33}S^-$	CPS/$^{34}S^-$	CPS/$^{36}S^-$
TE34_MAS-49_12	Initial pyrite	5.70	0.02	8.43	0.04	15.60	0.15	1.36	0.02	-0.48	0.16	1463325749	11549893	64483747	220079
TE34_MAS-49_18	Initial pyrite	4.85	0.02	6.88	0.05	12.69	0.14	1.31	0.02	-0.42	0.16	1597874618	12607574	70336611	239764
Reference mateirals															
Ruttan_1	Ruttan Pyrite	1.28	0.04	1.98	0.06	3.68	0.16	0.26	0.04	-0.08	0.20	833326029	6523720	36497084	123668
Ruttan_2	Ruttan Pyrite	1.13	0.05	1.64	0.08	2.82	0.23	0.29	0.05	-0.29	0.24	794029359	6215079	34754482	117991
Ruttan_3	Ruttan Pyrite	0.75	0.03	0.91	0.10	1.29	0.17	0.28	0.03	-0.44	0.19	845374760	6614257	36986082	125285
Ruttan_4	Ruttan Pyrite	1.21	0.04	1.87	0.05	3.62	0.20	0.24	0.04	0.05	0.20	854971107	6693466	37442866	126910
Ruttan_5	Ruttan Pyrite	1.42	0.03	2.12	0.06	3.98	0.14	0.33	0.03	-0.04	0.17	832448767	6519875	36464752	123750
Ruttan_6	Ruttan Pyrite	1.37	0.04	2.02	0.07	3.35	0.24	0.33	0.04	-0.50	0.22	818541166	6406906	35848155	121569
Ruttan_7'	Ruttan Pyrite	1.46	0.03	2.10	0.06	3.50	0.15	0.38	0.03	-0.50	0.16	810115990	6344957	35481022	120266
RUTTAN_7.1	Ruttan Pyrite	0.79	0.01	1.39	0.06	2.81	0.09	0.07	0.01	0.18	0.09	1483291561	11668545	65054915	233388
RUTTAN_7.2	Ruttan Pyrite	0.68	0.01	1.40	0.06	2.58	0.09	-0.04	0.01	-0.07	0.09	1474719371	11599757	64674271	232202
RUTTAN_7.4	Ruttan Pyrite	0.67	0.01	1.37	0.08	2.64	0.09	-0.04	0.02	0.03	0.09	1501490037	11810507	65856234	236516
RUTTAN_7.5	Ruttan Pyrite	0.61	0.01	1.33	0.06	2.52	0.10	-0.07	0.01	-0.01	0.10	1500722048	11802882	65812000	236330
RUTTAN_7.6	Ruttan Pyrite	0.72	0.01	1.31	0.07	2.43	0.08	0.04	0.01	-0.06	0.08	1474185540	11594457	64645798	232112
RUTTAN_8.1	Ruttan Pyrite	0.44	0.01	0.91	0.07	1.69	0.12	-0.03	0.01	-0.03	0.12	1373636708	10801731	60210771	216136
RUTTAN_8.2	Ruttan Pyrite	0.44	0.01	0.81	0.05	1.46	0.08	0.02	0.01	-0.07	0.08	1392731428	10951164	61041201	219042
RUTTAN_8.3	Ruttan Pyrite	0.42	0.01	0.86	0.07	1.44	0.08	-0.02	0.02	-0.19	0.08	1360135762	10696666	59617262	213871
RUTTAN_3.12	Ruttan Pyrite	0.80	0.01	1.43	0.06	2.95	0.12	0.07	0.01	0.23	0.12	1629373975	12816001	71450381	256996

Title	Iron sulphide	$\delta^{33}S$/‰	1σ/‰	$\delta^{34}S$/‰	1σ/‰	$\delta^{36}S$/‰	1σ/‰	$\Delta^{33}S$/‰	1σ/‰	$\Delta^{36}S$/‰	1σ/‰	CPS/$^{32}S^-$	CPS/$^{33}S^-$	CPS/$^{34}S^-$	CPS/$^{36}S^-$
Ruttan_1	Ruttan Pyrite	0.49	0.02	1.00	0.05	2.01	0.12	-0.03	0.02	0.11	0.13	1579106719	12406192	69111675	234252
Ruttan_2	Ruttan Pyrite	0.56	0.02	1.18	0.04	2.48	0.13	-0.04	0.02	0.25	0.14	1547332128	12150032	67693381	229633
Ruttan_3	Ruttan Pyrite	0.62	0.03	1.19	0.04	2.06	0.13	0.01	0.03	-0.20	0.13	1593334558	12516332	69721050	236553
Ruttan_4	Ruttan Pyrite	0.72	0.01	1.26	0.03	2.28	0.13	0.07	0.01	-0.11	0.13	1598367109	12555503	69944766	237168
Ruttan_5	Ruttan Pyrite	0.71	0.02	1.31	0.04	2.67	0.13	0.03	0.02	0.18	0.13	1591082826	12498792	69640949	235976
Ruttan_6	Ruttan Pyrite	0.61	0.01	1.27	0.04	2.18	0.14	-0.04	0.01	-0.24	0.16	1587511326	12470454	69482855	235460
Balmat_1	Balmat Pyrite	8.25	0.04	15.64	0.05	29.43	0.18	0.22	0.04	-0.49	0.22	803087755	6333544	35653120	122532
Balmat_3'	Balmat Pyrite	8.52	0.03	15.97	0.06	30.01	0.18	0.32	0.03	-0.55	0.21	771144199	6082031	34243459	117550
BALMAT_5.3	Balmat Pyrite	7.74	0.01	15.12	0.06	28.91	0.09	-0.01	0.01	0.00	0.09	1517929460	12022913	67488692	245220
BALMAT_5.4	Balmat Pyrite	7.78	0.01	15.15	0.02	29.13	0.10	0.01	0.01	0.15	0.11	1799079144	14251262	79980035	290761
BALMAT_5.5	Balmat Pyrite	7.55	0.02	14.60	0.03	28.22	0.11	0.06	0.02	0.29	0.12	1512079876	11976887	67201456	244101
BALMAT_5.6	Balmat Pyrite	7.58	0.01	14.85	0.05	28.43	0.10	-0.04	0.01	0.03	0.10	1503559659	11908605	66835690	243017
BALMAT_3.8	Balmat Pyrite	7.51	0.02	14.56	0.07	28.17	0.10	0.04	0.02	0.33	0.10	1608406344	12738960	71466806	259855
Balmat_1	Balmat Pyrite	7.68	0.02	15.10	0.02	28.62	0.18	-0.07	0.02	-0.27	0.21	1580218998	12499663	70105427	241190
Balmat_2	Balmat Pyrite	7.69	0.02	14.96	0.06	28.17	0.15	0.01	0.02	-0.45	0.16	1580818176	12505858	70138206	240579
Balmat_3	Balmat Pyrite	7.65	0.02	15.06	0.05	28.51	0.16	-0.07	0.02	-0.30	0.16	1626521344	12867370	72174006	247629
Unknowns															
3.12	pyrrhotite from desulphidation of original pyrite (DP1)	6.83	0.03	10.23	0.19	18.95	0.12	1.58	0.03	-0.57	0.12	1283717395	10093923	56508989	192500
3.11	pyrrhotite from desulphidation of original pyrite (DP1)	7.27	0.02	11.17	0.14	21.06	0.14	1.54	0.03	-0.27	0.14	1289522523	10143315	56801362	193550
3.1	pyrrhotite from desulphidation of original pyrite (DP1)	6.20	0.03	9.41	0.10	17.50	0.15	1.36	0.04	-0.46	0.16	1126632606	8851709	49549718	168409
3.8	pyrrhotite from desulphidation of original pyrite	5.38	0.02	7.58	0.13	14.00	0.14	1.49	0.02	-0.45	0.16	1094318088	8588965	48026548	163021

Title	Iron sulphide	$\delta^{33}S$/‰	1σ/‰	$\delta^{34}S$/‰	1σ/‰	$\delta^{36}S$/‰	1σ/‰	$\Delta^{33}S$/‰	1σ/‰	$\Delta^{36}S$/‰	1σ/‰	CPS/$^{32}S^-$	CPS/$^{33}S^-$	CPS/$^{34}S^-$	CPS/$^{36}S^-$
	(DP1)														
3.6	pyrrhotite from desulphidation of original pyrite (DP1)	5.76	0.03	8.29	0.22	15.16	0.14	1.50	0.03	-0.65	0.15	1147371540	9009726	50400107	171323
3.3	pyrrhotite from desulphidation of original pyrite (DP1)	6.92	0.03	10.40	0.21	19.19	0.12	1.58	0.03	-0.65	0.12	1283614215	10091180	56492627	192529
3.1	pyrrhotite from desulphidation of original pyrite (DP1)	6.75	0.02	9.99	0.17	18.35	0.12	1.62	0.02	-0.71	0.12	1342311116	10550742	59061448	200965
New_1.1	pyrrhotite from reaction between released sulphur and metal iron (NP1)	6.63	0.01	10.09	0.16	18.57	0.08	1.45	0.01	-0.69	0.09	1837967135	14445886	80839881	275020
New_1.6	pyrrhotite from reaction between released sulphur and metal iron (NP1)	6.60	0.02	10.00	0.26	18.27	0.11	1.46	0.02	-0.82	0.11	1980064721	15566056	87088901	296609
New_1.4	pyrrhotite from reaction between released sulphur and metal iron (NP1)	7.94	0.02	12.62	0.22	23.57	0.09	1.47	0.02	-0.54	0.09	2007770783	15798632	88523550	301952
New_1.9	pyrrhotite from reaction between released sulphur and metal iron (NP1)	5.36	0.03	7.91	0.27	14.37	0.12	1.30	0.03	-0.71	0.12	1768843433	13884669	77633328	263852
New_1.13	pyrrhotite from reaction between released sulphur and metal iron (NP1)	6.76	0.02	10.31	0.23	18.95	0.08	1.46	0.02	-0.72	0.08	1982360478	15579292	87201586	296592
New_1.14	pyrrhotite from reaction between released sulphur and metal iron (NP1)	5.92	0.02	8.65	0.22	15.81	0.09	1.48	0.02	-0.68	0.09	1996764195	15681565	87690813	297957
New_1.21	pyrrhotite from reaction between released sulphur and metal iron (NP1)	6.99	0.02	10.72	0.25	19.97	0.07	1.48	0.02	-0.49	0.07	1917160849	15073620	84378176	287412
New_1.26	pyrrhotite from reaction between released sulphur and metal iron (NP1)	5.64	0.02	8.11	0.22	14.86	0.11	1.47	0.02	-0.60	0.11	1925692104	15120204	84533155	287163
New_1.31	pyrrhotite from reaction between released sulphur and metal iron (NP1)	7.03	0.02	10.91	0.22	20.20	0.09	1.43	0.02	-0.63	0.09	2012499271	15822291	88574178	301439
New_1.29	pyrrhotite from reaction between released sulphur and metal iron (NP1)	4.44	0.02	5.71	0.24	10.22	0.12	1.51	0.02	-0.67	0.12	2010533295	15765393	88044304	298297
New_1.33	pyrrhotite from reaction between released sulphur and metal iron (NP1)	4.09	0.02	5.18	0.19	9.23	0.09	1.43	0.03	-0.63	0.09	1900685470	14899279	83186099	281681
New_1.32	pyrrhotite from reaction between released sulphur and metal iron (NP1)	7.09	0.02	10.89	0.21	20.05	0.10	1.50	0.02	-0.74	0.10	1994652957	15683129	87797614	298845
New_1.30	pyrrhotite from reaction between released sulphur and metal iron (NP1)	4.98	0.02	6.81	0.25	12.14	0.06	1.48	0.02	-0.83	0.07	1966203547	15428095	86193959	292482

Title	Iron sulphide	$\delta^{33}S$/‰	1σ/‰	$\delta^{34}S$/‰	1σ/‰	$\delta^{36}S$/‰	1σ/‰	$\Delta^{33}S$/‰	1σ/‰	$\Delta^{36}S$/‰	1σ/‰	CPS/$^{32}S^-$	CPS/$^{33}S^-$	CPS/$^{34}S^-$	CPS/$^{36}S^-$
AS-1	pyrrhotite from reaction between released sulphur and metal iron (NP1)	8.53	0.01	13.69	0.24	25.36	0.09	1.50	0.01	-0.81	0.10	1919024106	15109345	84688438	289128
AS-2	pyrrhotite from reaction between released sulphur and metal iron (NP1)	5.13	0.02	6.93	0.23	12.69	0.09	1.57	0.02	-0.51	0.10	1868738332	14663590	81918387	278080
AS-9	pyrrhotite from reaction between released sulphur and metal iron (NP1)	6.29	0.02	9.52	0.19	17.46	0.09	1.40	0.03	-0.70	0.10	1830018272	14377116	80433334	273748
AS-8	pyrrhotite from reaction between released sulphur and metal iron (NP1)	7.60	0.02	11.87	0.21	22.01	0.11	1.50	0.02	-0.67	0.11	1952030972	15355026	85976386	293193
Reference material															
A1	Anderson Pyrrhotite	0.88	0.03	1.63	0.16	3.12	0.13	0.04	0.04	0.02	0.14	1171385933	9152741	51104987	172887
A2	Anderson Pyrrhotite	0.71	0.03	1.59	0.15	2.93	0.17	-0.11	0.04	-0.10	0.17	1200728714	9382851	52388414	177035
A3	Anderson Pyrrhotite	0.66	0.03	1.21	0.18	2.22	0.10	0.03	0.03	-0.09	0.11	1169522153	9134880	51006908	172415
A4	Anderson Pyrrhotite	0.53	0.03	1.21	0.14	2.37	0.10	-0.09	0.03	0.06	0.12	1109578679	8668155	48397840	163513
A5	Anderson Pyrrhotite	0.71	0.03	1.27	0.15	2.37	0.14	0.06	0.03	-0.04	0.13	1241350341	9698897	54130617	183095
A6	Anderson Pyrrhotite	0.97	0.02	1.64	0.13	3.49	0.11	0.12	0.03	0.37	0.13	1162623897	9085687	50722698	171323
A7	Anderson Pyrrhotite	0.75	0.04	1.48	0.18	2.70	0.13	-0.02	0.04	-0.11	0.12	1228505824	9599041	53584155	180870
A8	Anderson Pyrrhotite	0.75	0.02	1.31	0.15	2.17	0.13	0.07	0.03	-0.32	0.14	1221930273	9548309	53296799	180196
A9	Anderson Pyrrhotite	0.51	0.03	1.18	0.14	2.47	0.13	-0.10	0.03	0.23	0.14	1254000688	9793839	54676313	184719
A10	Anderson Pyrrhotite	0.75	0.04	1.47	0.14	2.79	0.10	-0.01	0.04	0.00	0.12	1238701300	9676020	54030781	182523
A-1	Anderson Pyrrhotite	0.84	0.03	1.63	0.15	2.76	0.13	0.00	0.03	-0.33	0.14	1854840443	14494365	80892163	273600
A-2	Anderson Pyrrhotite	0.89	0.03	1.72	0.16	3.32	0.10	0.01	0.03	0.05	0.11	1834669581	14336452	80014933	270486
A-3	Anderson Pyrrhotite	0.87	0.02	1.75	0.15	3.35	0.10	-0.03	0.03	0.01	0.10	1863916197	14564762	81297466	275402
A-4	Anderson Pyrrhotite	0.91	0.02	1.87	0.16	3.53	0.10	-0.06	0.03	-0.03	0.10	1866695606	14586504	81422994	275182
A-5	Anderson Pyrrhotite	0.87	0.02	1.70	0.16	3.21	0.11	-0.01	0.02	-0.02	0.11	1828332451	14286469	79735570	269606
A-6	Anderson Pyrrhotite	1.08	0.03	2.09	0.16	4.11	0.08	0.01	0.03	0.14	0.09	1867179168	14590469	81457590	275628
A-8	Anderson Pyrrhotite	0.64	0.02	1.26	0.22	2.39	0.11	0.00	0.02	0.00	0.10	1820233907	14222025	79354039	268441
A-9	Anderson Pyrrhotite	0.80	0.03	1.50	0.20	2.94	0.09	0.03	0.03	0.09	0.09	1826852854	14272550	79653476	269124

Title	Iron sulphide	$\delta^{33}S$/‰	1σ/‰	$\delta^{34}S$/‰	1σ/‰	$\delta^{36}S$/‰	1σ/‰	$\Delta^{33}S$/‰	1σ/‰	$\Delta^{36}S$/‰	1σ/‰	CPS/$^{32}S^-$	CPS/$^{33}S^-$	CPS/$^{34}S^-$	CPS/$^{36}S^-$
A-10	Anderson Pyrrhotite	0.60	0.02	1.13	0.23	2.10	0.10	0.01	0.03	-0.05	0.11	1770308850	13829051	77163041	260569
A-11	Anderson Pyrrhotite	0.43	0.03	0.77	0.24	1.50	0.11	0.03	0.03	0.03	0.12	1670978563	13051469	72817299	246552
A-12	Anderson Pyrrhotite	0.67	0.02	1.25	0.21	2.31	0.06	0.03	0.03	-0.07	0.06	1816179942	14186917	79163731	267352
A-13	Anderson Pyrrhotite	0.69	0.02	1.38	0.21	2.56	0.11	-0.02	0.02	-0.06	0.11	1823578498	14246355	79504418	268352
A-14	Anderson Pyrrhotite	0.55	0.02	1.08	0.23	2.04	0.09	-0.01	0.03	-0.01	0.09	1751339414	13678954	76324549	257764
A-15	Anderson Pyrrhotite	0.54	0.02	1.16	0.20	2.09	0.12	-0.06	0.02	-0.13	0.13	1798211804	14047902	78387115	264922
A-16	Anderson Pyrrhotite	0.70	0.03	1.45	0.22	2.93	0.11	-0.04	0.03	0.19	0.12	1793944958	14013112	78214628	263797
A-17	Anderson Pyrrhotite	0.77	0.03	1.42	0.20	2.77	0.09	0.04	0.03	0.08	0.11	1793474857	14008785	78180914	264065
A-18	Anderson Pyrrhotite	0.63	0.02	1.27	0.23	2.49	0.09	-0.02	0.02	0.08	0.10	1822968588	14241327	79472288	268518
A-19	Anderson Pyrrhotite	0.83	0.02	1.56	0.20	3.04	0.09	0.03	0.02	0.07	0.09	1807617709	14123393	78822744	266420
A-1	Anderson Pyrrhotite	0.44	0.02	0.76	0.31	1.29	0.09	0.05	0.03	-0.16	0.10	1707005292	13330180	74361643	251039
A-2	Anderson Pyrrhotite	0.74	0.02	1.52	0.22	2.89	0.09	-0.05	0.02	-0.01	0.10	1804279183	14092374	78631002	265483
A-3	Anderson Pyrrhotite	0.72	0.03	1.43	0.19	2.84	0.10	-0.01	0.03	0.13	0.12	1811187504	14149854	78955478	267129
A-4	Anderson Pyrrhotite	0.60	0.02	1.09	0.30	2.03	0.09	0.03	0.02	-0.06	0.10	1749920475	13666522	76224153	257386
A-5	Anderson Pyrrhotite	0.85	0.03	1.62	0.19	3.12	0.10	0.02	0.03	0.05	0.09	1744034387	13624073	76021177	256940
A-6	Anderson Pyrrhotite	0.88	0.02	1.70	0.20	3.37	0.09	0.01	0.02	0.14	0.10	1768522737	13816739	77102110	260926
A-7	Anderson Pyrrhotite	0.82	0.03	1.68	0.21	3.09	0.11	-0.05	0.03	-0.09	0.12	1775904603	13874160	77427984	261504

Table 5.4 Quadruple sulphur isotopic composition data of the initial Ruttan pyrite and products for the experiment with Ruttan pyrite.

Title	Iron sulphide	$\delta^{33}S$/‰	1σ/‰	$\delta^{34}S$/‰	1σ/‰	$\delta^{36}S$/‰	1σ/‰	$\Delta^{33}S$/‰	1σ/‰	$\Delta^{36}S$/‰	1σ/‰	CPS/$^{32}S^-$	CPS/$^{33}S^-$	CPS/$^{34}S^-$	CPS/$^{36}S^-$
Normalized to Anderson pyrrhotite (i.e., Anderson pyrrhotite as the reference material)															
	Unknowns														
1	Sulphidized metal iron (NP2)	-0.68	0.02	-1.40	0.24	-2.90	0.09	0.04	0.03	-0.24	0.10	1645647373	12828517	71632711	240317
2	Sulphidized metal iron (NP2)	-0.16	0.03	-0.50	0.21	-0.79	0.11	0.10	0.03	0.16	0.11	1585464919	12369170	69083589	232152
5	Sulphidized metal iron (NP2)	0.81	0.03	1.39	0.21	2.72	0.09	0.09	0.04	0.08	0.10	1486365663	11602680	64864412	218424
6	Sulphidized metal iron (NP2)	-0.35	0.03	-0.64	0.21	-0.94	0.10	-0.02	0.04	0.27	0.11	1456234555	11354694	63428281	212843
7	Sulphidized metal iron (NP2)	0.22	0.04	0.73	0.23	1.54	0.10	-0.15	0.05	0.14	0.11	1553180588	12115654	67727151	227570
9	Sulphidized metal iron (NP2)	-0.52	0.03	-0.83	0.32	-1.44	0.12	-0.09	0.04	0.13	0.12	1554944204	12124788	67726409	227522
12	Sulphidized metal iron (NP2)	-0.41	0.03	-0.90	0.29	-1.77	0.09	0.05	0.03	-0.07	0.11	1576290931	12289308	68635884	230445
13	Sulphidized metal iron (NP2)	0.13	0.03	-0.33	0.32	-0.51	0.09	0.30	0.03	0.12	0.09	1470662158	11473272	64087308	215497
17	Desulphidized Ruttan pyrite (DP2)	1.17	0.02	2.05	0.30	3.98	0.15	0.12	0.03	0.08	0.15	1488777576	11627104	65020308	218984
18	Desulphidized Ruttan pyrite (DP2)	1.27	0.04	2.43	0.24	4.21	0.09	0.02	0.05	-0.40	0.09	1487174646	11613923	64965347	218727
19	Desulphidized Ruttan pyrite (DP2)	1.18	0.02	2.00	0.33	3.87	0.12	0.15	0.03	0.06	0.11	1575132603	12301016	68797377	231781
21	Desulphidized Ruttan pyrite (DP2)	1.38	0.03	2.75	0.27	5.32	0.10	-0.04	0.03	0.09	0.10	1557437347	12163760	68064832	229331
22	Desulphidized Ruttan pyrite (DP2)	0.76	0.04	1.83	0.21	3.58	0.09	-0.18	0.05	0.10	0.11	1585366000	12371070	69213925	233083
25	Desulphidized Ruttan pyrite (DP2)	0.91	0.02	2.04	0.33	3.82	0.10	-0.14	0.03	-0.07	0.10	1468624381	11465527	64150032	216357
28	Desulphidized Ruttan pyrite (DP2)	0.81	0.03	1.36	0.22	2.65	0.14	0.11	0.05	0.06	0.11	1552780641	12124317	67804556	228225
29	Desulphidized Ruttan pyrite (DP2)	-0.03	0.04	-0.12	0.35	-0.60	0.13	0.03	0.05	-0.37	0.13	1539155336	12012726	67166139	226040
30	Desulphidized Ruttan pyrite (DP2)	-0.67	0.05	-0.99	0.34	-2.19	0.11	-0.16	0.06	-0.30	0.12	1532067890	11936779	66632635	223251
Ruttan_1	Pyrite	2.61	0.02	5.20	0.24	10.24	0.15	-0.06	0.02	0.34	0.15	1186952515	9284108	52015651	175607
Ruttan_3	Pyrite	1.91	0.03	4.29	0.09	8.73	0.10	-0.29	0.03	0.57	0.13	1177998687	9206155	51570521	174277
Ruttan_4	Pyrite	2.28	0.04	4.78	0.09	9.58	0.11	-0.19	0.04	0.47	0.12	1187260582	9283273	51999520	175766

Title	Iron sulphide	$\delta^{33}S$/‰	1σ/‰	$\delta^{34}S$/‰	1σ/‰	$\delta^{36}S$/‰	1σ/‰	$\Delta^{33}S$/‰	1σ/‰	$\Delta^{36}S$/‰	1σ/‰	CPS/$^{32}S^-$	CPS/$^{33}S^-$	CPS/$^{34}S^-$	CPS/$^{36}S^-$
Ruttan_5	Pyrite	2.54	0.03	5.34	0.11	10.46	0.14	-0.21	0.03	0.29	0.15	1275859237	9974340	55862577	188891
Ruttan_6	Pyrite	2.50	0.04	5.18	0.10	10.17	0.13	-0.16	0.04	0.31	0.15	1183323117	9249919	51838046	175265
Ruttan_7	Pyrite	2.37	0.04	5.16	0.08	10.02	0.13	-0.28	0.04	0.20	0.13	1315755340	10288019	57640521	194787
Ruttan_8	Pyrite	2.33	0.03	5.47	0.09	10.76	0.12	-0.49	0.03	0.34	0.12	1242467562	9715197	54466451	184090
Ruttan_9	Pyrite	2.90	0.04	6.12	0.07	11.98	0.12	-0.25	0.04	0.32	0.13	1266579528	9907795	55540306	187820
Ruttan_10	Pyrite	2.78	0.05	5.77	0.09	11.29	0.13	-0.19	0.04	0.29	0.13	1303076726	10188941	57120082	193159
Ruttan_11	Pyrite	2.14	0.04	5.45	0.08	10.60	0.12	-0.66	0.04	0.21	0.14	1309974798	10239115	57404399	193909
Ruttan_12	Pyrite	2.97	0.03	5.88	0.11	11.52	0.12	-0.05	0.03	0.32	0.12	1337326056	10464409	58647413	198328
Ruttan_13	Pyrite	1.97	0.04	4.95	0.10	9.78	0.12	-0.57	0.04	0.36	0.14	1316746375	10292815	57666763	195134
Ruttan_14	Pyrite	2.32	0.03	5.47	0.09	10.70	0.12	-0.49	0.03	0.28	0.13	1308469037	10230790	57337589	193999
Ruttan_15	Pyrite	2.35	0.04	5.08	0.15	9.85	0.13	-0.26	0.04	0.17	0.13	1326869165	10374354	58124354	196448
Reference material															
Anderson_1	Pyrrhotite	0.80	0.02	1.23	0.26	2.23	0.09	0.16	0.03	-0.12	0.09	1516437765	11838969	66172666	222805
Anderson_2	Pyrrhotite	0.79	0.03	1.45	0.26	2.60	0.11	0.05	0.03	-0.16	0.10	1522187570	11884661	66445362	223631
Anderson_3	Pyrrhotite	0.86	0.03	1.46	0.27	2.83	0.11	0.11	0.04	0.05	0.11	1605563914	12534246	70085628	235973
Anderson_4	Pyrrhotite	0.52	0.04	1.19	0.27	2.20	0.10	-0.09	0.04	-0.07	0.11	1592469559	12428687	69492575	233800
Anderson_5	Pyrrhotite	0.67	0.03	1.20	0.27	2.35	0.12	0.05	0.04	0.07	0.12	1577818569	12313210	68821682	231789
Anderson_6	Pyrrhotite	1.07	0.03	1.92	0.24	3.87	0.10	0.08	0.04	0.23	0.11	1635212047	12769521	71413552	240603
Anderson_7	Pyrrhotite	0.25	0.05	0.69	0.33	1.39	0.12	-0.11	0.05	0.08	0.12	1589454639	12403709	69332842	233364
Anderson_8	Pyrrhotite	0.42	0.04	1.01	0.29	2.00	0.10	-0.10	0.05	0.08	0.10	1645076681	12839624	71790633	241634
Anderson_9	Pyrrhotite	0.67	0.04	1.18	0.26	2.11	0.12	0.07	0.04	-0.13	0.12	1659739363	12955575	72421175	243639
Anderson_10	Pyrrhotite	1.15	0.03	2.24	0.24	4.28	0.08	-0.01	0.04	0.01	0.09	1649812696	12884165	72076698	242775
Anderson_11	Pyrrhotite	0.79	0.03	1.77	0.25	3.39	0.07	-0.13	0.05	0.02	0.09	1631766065	12737573	71252872	239946
Anderson_12	Pyrrhotite	0.66	0.04	1.45	0.28	2.69	0.09	-0.09	0.05	-0.06	0.09	1662646498	12978487	72588787	244466

Title	Iron sulphide	$\delta^{33}S$/‰	1σ/‰	$\delta^{34}S$/‰	1σ/‰	$\delta^{36}S$/‰	1σ/‰	$\Delta^{33}S$/‰	1σ/‰	$\Delta^{36}S$/‰	1σ/‰	CPS/$^{32}S^-$	CPS/$^{33}S^-$	CPS/$^{34}S^-$	CPS/$^{36}S^-$
Normalized to Ruttan pyrite (i.e., Ruttan pyrite as reference material)															
Unknowns															
MR_1	Initial Ruttan pyrite	0.65	0.05	1.60	0.10	3.23	0.10	-0.17	0.05	0.19	0.12	1194784061	9343478	52381651	177162
MR_2	Initial Ruttan pyrite	0.63	0.04	1.29	0.17	2.30	0.11	-0.04	0.05	-0.15	0.14	1238397116	9683656	54265991	183417
MR_3	Initial Ruttan pyrite	1.06	0.04	1.94	0.10	3.71	0.11	0.06	0.04	0.02	0.15	1270410985	9939161	55722535	188426
MR_4	Initial Ruttan pyrite	0.45	0.05	1.06	0.15	1.94	0.15	-0.10	0.05	-0.07	0.14	1249295429	9759795	54679948	184479
Anderson_1	Pyrrhotite	-0.97	0.02	-2.75	0.27	-5.65	0.09	0.45	0.03	-0.43	0.09	1516437765	11838969	66172666	222805
Anderson_2	Pyrrhotite	-0.97	0.03	-2.53	0.26	-5.27	0.11	0.33	0.03	-0.47	0.10	1522187570	11884661	66445362	223631
Anderson_3	Pyrrhotite	-0.90	0.03	-2.53	0.27	-5.05	0.11	0.40	0.04	-0.26	0.11	1605563914	12534246	70085628	235973
Anderson_4	Pyrrhotite	-1.24	0.04	-2.79	0.27	-5.68	0.10	0.20	0.04	-0.38	0.11	1592469559	12428687	69492575	233800
Anderson_5	Pyrrhotite	-1.09	0.03	-2.78	0.27	-5.52	0.12	0.34	0.04	-0.24	0.13	1577818569	12313210	68821682	231789
Anderson_6	Pyrrhotite	-0.69	0.03	-2.07	0.24	-4.01	0.10	0.37	0.04	-0.09	0.11	1635212047	12769521	71413552	240603
Anderson_7	Pyrrhotite	-1.51	0.05	-3.29	0.33	-6.48	0.12	0.18	0.05	-0.23	0.12	1589454639	12403709	69332842	233364
Anderson_8	Pyrrhotite	-1.35	0.04	-2.97	0.29	-5.87	0.10	0.19	0.05	-0.23	0.10	1645076681	12839624	71790633	241634
Anderson_9	Pyrrhotite	-1.09	0.04	-2.80	0.26	-5.76	0.12	0.35	0.04	-0.44	0.12	1659739363	12955575	72421175	243639
Anderson_10	Pyrrhotite	-0.62	0.03	-1.75	0.24	-3.61	0.08	0.28	0.04	-0.30	0.09	1649812696	12884165	72076698	242775
Anderson_11	Pyrrhotite	-0.98	0.03	-2.22	0.25	-4.49	0.07	0.16	0.05	-0.29	0.09	1631766065	12737573	71252872	239946
Anderson_12	Pyrrhotite	-1.11	0.04	-2.54	0.28	-5.19	0.09	0.20	0.05	-0.37	0.09	1662646498	12978487	72588787	244466
Reference material															
Ruttan_1	Ruttan pyrite	0.84	0.02	1.20	0.24	2.30	0.15	0.23	0.02	0.02	0.15	1186952515	9284108	52015651	175607
Ruttan_3	Ruttan pyrite	0.15	0.03	0.29	0.09	0.81	0.10	0.00	0.03	0.25	0.13	1177998687	9206155	51570521	174277
Ruttan_4	Ruttan pyrite	0.51	0.04	0.79	0.09	1.65	0.11	0.10	0.04	0.16	0.12	1187260582	9283273	51999520	175766

Title	Iron sulphide	$\delta^{33}S$/‰	1σ/‰	$\delta^{34}S$/‰	1σ/‰	$\delta^{36}S$/‰	1σ/‰	$\Delta^{33}S$/‰	1σ/‰	$\Delta^{36}S$/‰	1σ/‰	CPS/$^{32}S^-$	CPS/$^{33}S^-$	CPS/$^{34}S^-$	CPS/$^{36}S^-$
Ruttan_5	Ruttan pyrite	0.77	0.03	1.34	0.11	2.53	0.14	0.08	0.03	-0.02	0.15	1275859237	9974340	55862577	188891
Ruttan_6	Ruttan pyrite	0.74	0.04	1.18	0.10	2.24	0.13	0.13	0.04	0.00	0.15	1183323117	9249919	51838046	175265
Ruttan_7	Ruttan pyrite	0.60	0.04	1.16	0.08	2.08	0.13	0.01	0.04	-0.12	0.13	1315755340	10288019	57640521	194787
Ruttan_8	Ruttan pyrite	0.56	0.03	1.47	0.09	2.82	0.12	-0.20	0.03	0.02	0.12	1242467562	9715197	54466451	184090
Ruttan_9	Ruttan pyrite	1.13	0.04	2.11	0.07	4.03	0.12	0.04	0.04	0.01	0.13	1266579528	9907795	55540306	187820
Ruttan_10	Ruttan pyrite	1.01	0.05	1.77	0.09	3.34	0.13	0.10	0.04	-0.03	0.13	1303076726	10188941	57120082	193159
Ruttan_11	Ruttan pyrite	0.38	0.04	1.45	0.08	2.66	0.12	-0.37	0.04	-0.10	0.14	1309974798	10239115	57404399	193909
Ruttan_12	Ruttan pyrite	1.21	0.03	1.88	0.11	3.57	0.13	0.24	0.03	0.01	0.12	1337326056	10464409	58647413	198328
Ruttan_13	Ruttan pyrite	0.21	0.04	0.95	0.10	1.85	0.12	-0.28	0.04	0.05	0.14	1316746375	10292815	57666763	195134
Ruttan_14	Ruttan pyrite	0.55	0.03	1.47	0.09	2.76	0.12	-0.20	0.03	-0.04	0.13	1308469037	10230790	57337589	193999
Ruttan_15	Ruttan pyrite	0.59	0.04	1.08	0.15	1.92	0.13	0.03	0.04	-0.14	0.13	1326869165	10374354	58124354	196448

Chapter 6 Sulphur Origins of the Neoarchean Lamego Banded Iron Formation-Hosted Gold Deposit in the Rio das Velhas Greenstone Belt, Quadrilátero Ferrífero

Abstract: Internal texture, multiple sulphur isotopic composition, and abundance of gold, selenium, and molybdenum of the ore-related pyrite from a typical Neoarchean carbonate-facies BIF-hosted gold deposit in the Rio das Velhas Greenstone Belt, Quadrilátero Ferrífero were investigated to uncover the sulphur sources. Sodium hypochlorite etching and BSE imaging revealed pervasive zoning in pyrite. The zoning coupled with multiple sulphur isotopic composition and gold abundance of different zones revealed four generations of pyrite. Generation one has low to moderate gold abundance, and is subdivided into 1a and 1b. 1a shows negative $\delta^{34}S$ and moderate positive $\Delta^{33}S$, while 1b displays positive $\delta^{34}S$ and high positive $\Delta^{33}S$. The sulphur isotopic composition of generation two to four pyrite is similar to each other, and the majority has small positive $\delta^{34}S$ and $\Delta^{33}S$. Generation two is characterized by oscillatory zoning and the highest gold abundance, whereas generation three and four contain much less gold, particularly generation four. The extensive S-MIF in the four generations of pyrite suggests that the hydrothermal fluids can be metamorphic fluids, metamorphic fluids reacted with surrounding rocks, and magmatic fluids mixed with metamorphic fluids and/or interacted with wall rocks. The metamorphic fluids can be derived from devolatilization of the underlying Nova Lima Group of the Rio das Velhas Supergroup and the granite-gneiss basement. The hydrothermal fluids relevant to the four generations of pyrite can originate from the same source(s), and evolve from oxidized generation 1 to reduced generation 2 to 4. Alternatively, the hydrothermal fluids of generation 1 can be from different source(s) compared with that of generation 2 to 4. For both possibilities, reduction is the most likely trigger of gold precipitation.

1. Introduction

The Quadrilátero Ferrífero (QF) of the São Francisco Craton is one of the most important goldfields in the world (Goldfarb et al., 2001), and hosts abundant gold deposits of variable size within the Rio das Velhas Greenstone Belt (Lobato et al., 2001a). Despite many similarities to other Archean goldfields worldwide, QF gold deposits are characterized by BIF (Banded Iron Formation) as the predominant host rock and veins/veinlets coupled with

replacements (iron oxides/carbonates are sulphidizedd and replaced by iron sulphides) as the dominant mineralization styles (Lobato et al., 2001b). Previous studies have mainly focused on the geological characteristics of the deposits (e.g., Ribeiro-Rodrigues et al., 2007), fluid inclusions (e.g., Xavier et al., 2000), and mineralization age (Lobato et al., 2007), while rarely on sulphides, which are the most intimately associated with gold mineralization and are potentially powerful medium to place constraints on the source(s) and mineralization processes of these gold deposits. Consequently, understanding of the genesis remains inadequate compared with the other goldfields.

Zoning is ubiquitous in pyrite from gold ores regardless of their type and age, and can be readily revealed by chemical etching and SEM (Scanning Electron Microscope, e.g., Peterson and Mavrogenes, 2014). It is useful for indicating the mineralization history and allows placement of SHRIMP analyses within single domains of related type. Furthermore, multiple sulphur isotopes have been increasingly applied to tracing the sources of Archean gold deposits, and appear to be highly effective in distinguishing different provenances based on exclusive $\delta^{34}S$-$\Delta^{33}S$±$\Delta^{36}S$ systematics (e.g., Selvaraja et al., 2017).

This study investigated the zoning, mineral inclusions, high-resolution multiple sulphur isotopic composition and the concentration of Au, Se, and Mo of ore-related pyrite from a typical carbonate-facies BIF-hosted gold deposit in the Rio das Velhas Greenstone Belt using a combination of sodium hypochlorite (NaOCl) solution etching, SEM, SHRIMP-SI, and SHRIMP-II, in an attempt to reveal the sulphur sources.

2. Geological background

The Quadrilátero Ferrífero is located in the southern margin of the São Francisco Craton (Fig. 6.1a), and is composed of the granite-gneiss basement and the strata overlying, including the Archean Rio das Velhas Supergroup and the Proterozoic metasedimentary units of Minas Supergroup, Itacolomi Group, and Espinhaça Supergroup (Lobato et al., 2001a, and references therein, Fig. 6.1b). The basement was formed at ca. 3.28 Ga to 2.92 Ga (Machado and Carneiro, 1992), followed by magmatisms from 2.92 Ga to 2.85 Ga (Farina et al., 2016 and references therein). Volcanisms in the Rio das Velhas Supergroup took place between 2.75 and 2.79 Ga (Machaolo et al., 1992; Machado and Carneiro, 1992; Noce et al., 2005), accompanied by magmatisms of 2.80 Ga to 2.76 Ga (Farina et al., 2016 and references

therein). Subsequent potassic granitoid magmatisms were spatially and temporally extensive, spreading from 2760-2700 Ma to 2612-2613 Ma (Romano et al., 2013 and references therein).

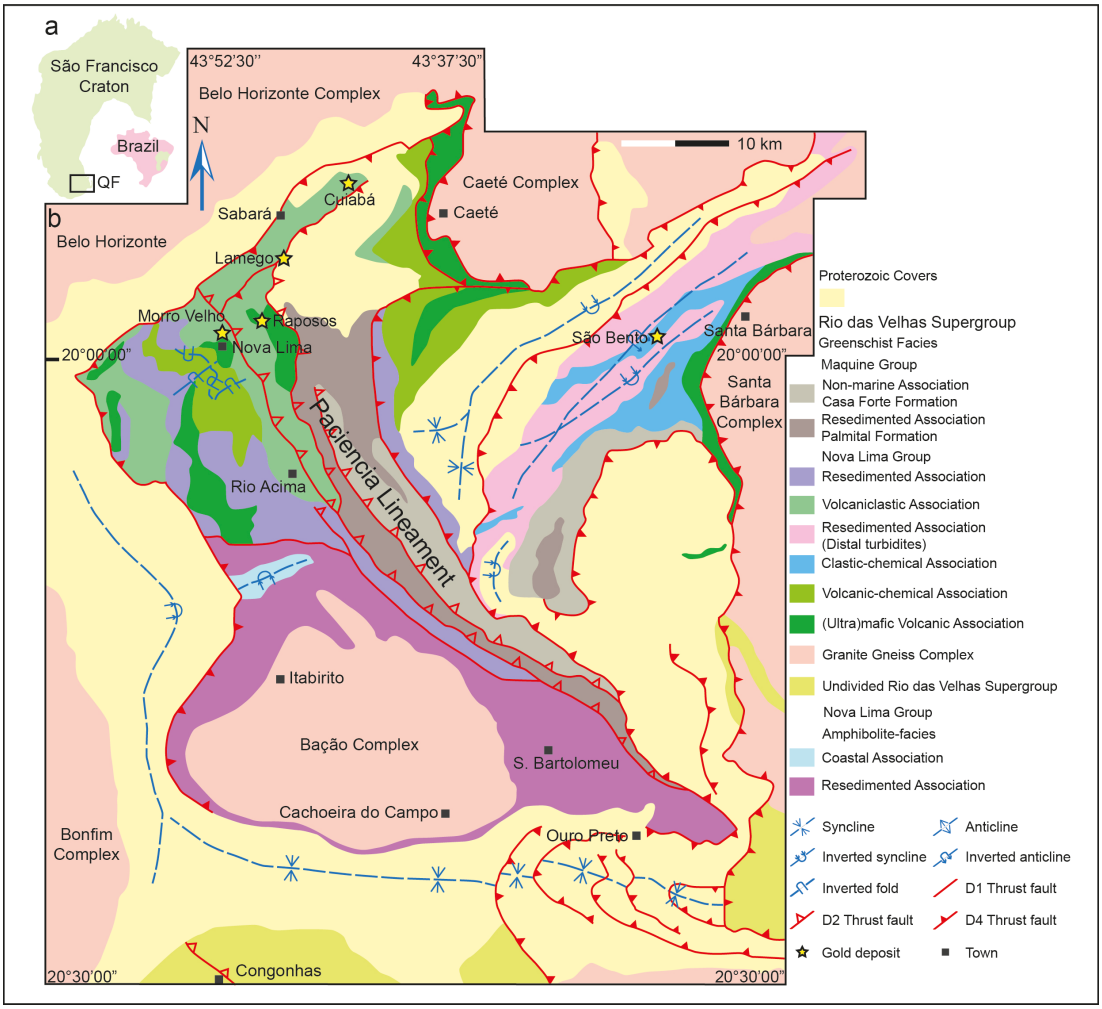

Fig. 6.1 a. Schematic map showing the approximate location of Quadrilátero Ferrífero in the southern margin of São Francisco Craton (modified from Alkmim and Marshak, 1998); b. Simplified geological map of the Rio das Velhas Greenstone Belt in the Quadrilátero Ferrífero area (modified from Baltazar and Zucchetti, 2007) and locations of important gold deposits (cited from Lobato et al., 2001a and de Souza Martins et al., 2016).

The Rio das Velhas Supergroup is a typical greenstone sequence consisting of the basal Nova Lima Group and the overlying Maquiné Group. Baltazar and Zucchetti (2007) classified the Rio das Velhas Supergroup into seven lithofacies associations, which are successively mafic-ultramafic volcanic, volcano-chemical-sedimentary, clastic-chemical-sedimentary, volcaniclastic, resedimented, coastal, and non-marine from base to top (Fig. 6.1b). The Maquiné Group is composed of the basal quartzite and quartz phyllite and upper sandstone and conglomerate. Abundant gold deposits occur within the Nova Lima Group, and are hosted

predominantly by carbonate- or oxide-facies BIF (e.g., Cuiabá, São Bento, Raposos, and Lamego, Lobato et al., 2001b), with a mineralization age of 2672 ± 14 Ma (Lobato et al., 2007).

The Rio das Velhas Greenstone Belt has been subjected to four main generations of deformation events (Baltazar and Zucchetti, 2007), among which the first and second generations are compressional deformations that occurred in Neoarchean. The ~2.7 Ga D2 structures are closely related to gold mineralization, represented by NW-striking thrust faults and associated overturned tight to isoclinal NW-trending and SW-verging folds (e.g., the Paciência lineament, Fig. 6.1b), as well as NE-trending ductile-brittle strike-slip shear zones.

Lamego is a typical carbonate-facies BIF-hosted gold deposit occurring along the Cuiabá-Lamego gold trend in the northern QF (de Souza Martins et al., 2016; Fig. 6.1b), and had 250,000 t gold measured reserves in 2014 (de Souza Martins et al., 2016). The Lamego sheath fold is the largest structure in the deposit area, covering the entire lithostratigraphic column (Fig. 6.2). In total, four orebodies have been identified in the deposit area: Cabeça de Pedra orebody at the hinge zone, Arco da Velha orebody on the normal limb, Queimada orebody on the overturned limb, and Carruagem orebody in the northeast of Lamego fold (Fig. 6.2). The lithostratigraphic succession from base to top is hydrothermally altered basalt (150-200 m), BIF (1-8 m, locally up to 15 m), smoky chert (4-5 m), carbonaceous phyllite (10-12 m), and micaceous phyllite (hundreds of meters)(Sales, 1998; de Souza Martins et al., 2016; Morales et al., 2016). No intrusions occur within the deposit area except for minor dolerite dykes and sills cropping out in the Cabeça de Pedra and Carruagem areas.

The majority of mineralization occurs within BIF and smoky chert. Sulphidation of siderite constituting the primary BIF converts the barren carbonate-facies BIF to mineralized sulphide-facies BIF, which is composed of predominantly pyrite, quartz, ankerite, subordinate arsenopyrite, and minor pyrrhotite. Banded ores consisting of alternating chlorite-rich bands and pyrite-rich bands are occasionally observed. The smoky chert is composed of quartz, calcite, ankerite, pyrite, and chlorite. Most of them occur above the BIF level, while the others crosscut BIF bands/laminae in the form of veins/veinlets, which are filled fractures that are effective paths for hydrothermal fluids to move laterally, penetrating and sulfidizing BIF. The majority of gold is invisibly contained in pyrite and arsenopyrite, a small amount occurs as

infillings of intra-grain fractures or inter-grain gaps, and the rest is present as native gold inclusions within recrystallized coarse pyrite grains.

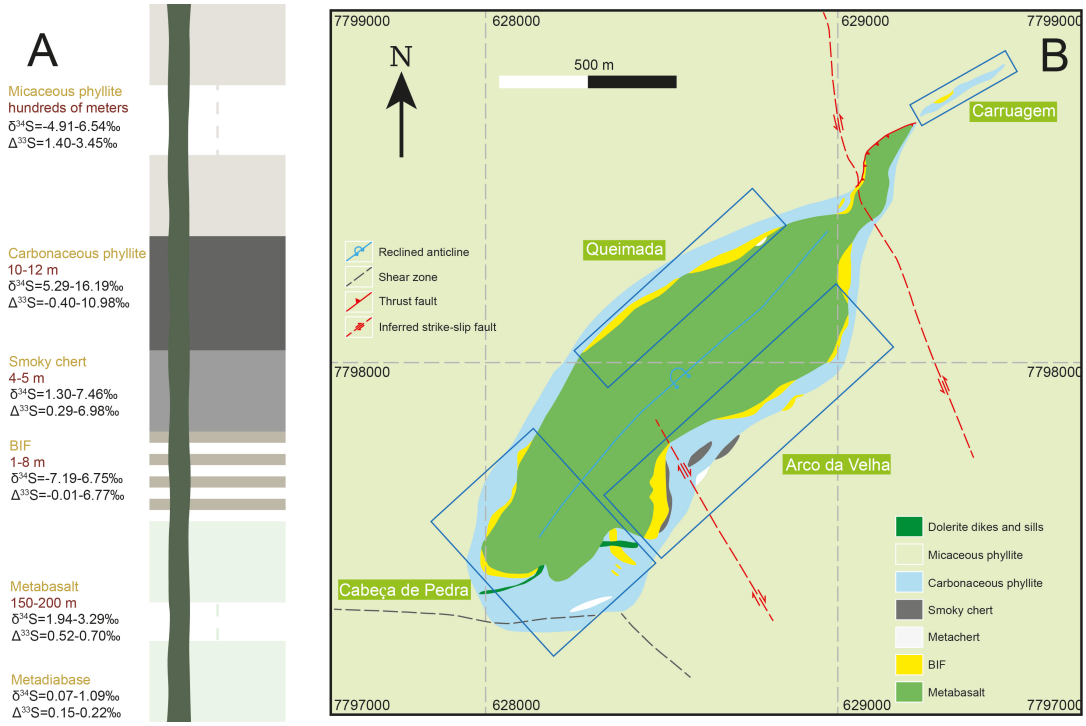

Fig. 6.2 A. Diagram illustrating the lithostratigraphic column of the Lamego gold deposit (modified from de Souza Martins et al., 2016), along with the multiple sulphur isotopic compositions. B. Geological map of the Lamego open pit mine (modified from Morales et al., 2016 and de Souza Martins et al., 2016).

3. Samples and methods

3.1 Samples

The samples analyzed herein cover the whole range of lithologies occurring at the Lamego gold deposit. The majority of ore samples are from the Cabeça de Pedra orebody, with several samples from the Arco da Velha and Queimada orebodies. Samples are described in Table 6.1.

Table 6.1 Sample descriptions.

Sample Code	Drill Core Sample	Description
Micaceous phyllite		
MAS-18	FPL-120_694.3m	Dark grey in color and variably foliated,
MAS-46	FPL-122_514.6m	characterized by euhedral to subhedral coarse

Sample Code	Drill Core Sample	Description
MAS-47	FPL-122_527.8m	pyrite porphyroblasts exhibiting well-developed pressure shadow. The pyrite porphyroblasts are inclusion-rich in core while inclusion-free in rim.
MAS-48	FPL-122_396.2m	
Carbonaceous phyllite		
FPL-179	FPL-179_395.0m	Banded in structure, composed of thick black carbonaceous phyllite bands and thin grey white quartz-ankerite-pyrite laminae. Pyrites in the white laminae are primarily microcrystal aggregates of variable size, and the large ones protrude into carbonaceous phyllite bands. By comparison, pyrites in carbonaceous phyllites are mostly recrystallized aggregates with abundant inclusions similar to the porphyroblastic pyrite in micaceous phyllite.
MAS-43	FPL-122_560.4m	Similar to FPL-179_395.0 m, but shows intense deformation. The primary bands and laminae have been truncated and deformed, resulting in discontinuous lenses.
MAS-49B	FPL-128_561.4m	Weak banded structure, the dark grey bands/laminae are not regular, neither in thickness nor boundary surfaces. Pyrites occur mainly as euhedral to subhedral medium to coarse grains within the gray bands/laminae, and contains abundant mineral inclusions.
Smoky chert-hosted ore		
MAS-37	FPL-122-654.4 m	Black grey chert involving some short white quartz veinlets, in which pyrite occurs as fine to medium euhedral to subhedral grains within the white quartz veinlet.
MAS-57	FLU-173	Black grey chert, composed of quartz, calcite, ankerite, chlorite, and pyrite. Pyrites occur as (1) disseminated small euhedral to subhedral grains, (2) microcrystal aggregates, (3) chlorite-pyrite veinlets, and (4) coarse grains.

Sample Code	Drill Core Sample	Description
Banded chlorite-rich ore		
MAS-62	FLU-157_13.60 m	Banded in structure, consisting of alternating chlorite- and pyrite-rich bands.
MAS-68	FLU-168	
BIF-hosted ore		
LQ	Not drillcore sample	Clear bands, 2 mm to 3 mm thick. Characterized by abundant arsenopyrite, and native gold within pyrite grains (mostly coarse).
MAS-8	FPL-122_598.0 m	Typical banded sulfide-facies BIF, composed of alternating quartz-carbonate bands/laminae and sulfide bands/laminae. The bands of 599 m and 623.6 m are relatively thick, typically between 8 mm and 10 mm. 598 m and 634.6 m display ambiguous bands. Within the light bands of 634.6 m, fine euhedral to subhedral pyrite grains are aligned as laminae. Coarse pyrite grains in 599 m are abundant in inclusions such as quartz, ankerite, apatite, calcite and siderite, and are intergrown with coarse pyrrhotite grains. Native gold in 599 m occurs within medium anhedral inclusion-free pyrite and coarse inclusion-rich pyrite grains, while that of 598 m fills fractures or seals gaps between two pyrite grains.
MAS-33	FPL-122_634.6 m	
MAS-44	FPL-122_599.0 m	
MAS-50	FPL-122_623.6 m	
FLV-167	FLV-167_225 m	Pyrite-aligned laminae rather than clear bands. Sulfide laminae are abundant in fine euhedral arsenopyrite. Native gold seals the gaps between two pyrite grains.
MAS-25	FPL-120_639.2 m	Carbonate-facies BIF consisting of altenating white and dark grey laminae crosscut by quartz-ankerite-pyrite veinlets. Native gold is present as inclusions in coarse subhedral and medium anhedral pyrite grains.
MAS-26	FPL-120_656.2 m	
Basalt		

Sample Code	Drill Core Sample	Description
MAS-40	FOA-11-92.4m	Greenish beige in color, fine-grained, and foliated. Euhedral to subhedral fine- to coarse- pyrite grains occur as porphyroblasts, which are abundant in mineral inclusions.
Dolerite dyke		
MAS-31	FPL-122_113.7m	Greyish green in color, massive, fine- to medium-grained, composed predominantly of amphibole and plagioclase. Pyrite occurs as euhedral to subhedral grains containing abundant mineral inclusions.

3.2 Making mounts and etching

Small offcuts containing pyrite were firstly cut from the drill cores, assembled and cast into the first batch of mounts. These mounts were subsequently ground, polished and then immersed in sodium hypochlorite (NaOCl) solution to reveal internal textures of pyrite. The duration of etching was variable, one to two minutes or five to six minutes, depending on the NaOCl concentration (as NaOCl dissociates with time) and the nature of the pyrite itself. The etched mounts were then observed in reflected light microscopy to find the appropriate pyrite grains for further analysis. Specific regions were marked and then cut out along with the lithological matrix. These smaller offcuts were then assembled and cast into the second batch of mounts together with polished grains of pyrite reference materials for multiple sulphur isotope analysis. These mounts were repolished and then etched again with subsequent photography. They were then polished to remove the oxidized film on the surface, thoroughly cleaned in the ultrasonic bath, dried in the vacuum oven (0.1 MPa, 60 °C), and coated with 15 nanometers of aluminium for SEM characterization including BSE imaging and EDS analysis.

3.3 SEM and laser Raman analyses

A JEOL JSM-6400 SEM was utilized to (1) assure the sulphides to be analyzed are pyrite, (2) confirm the internal textures particularly zoning revealed by etching, and (3) identify mineral inclusions in pyrite. The analyses were conducted at the Research School of Earth Sciences, Australian National University. Operating conditions were 15 kV (acceleration voltage), 1 nA (beam current), and 11 mm (working distance).

To further confirm identification, laser Raman analyses were also performed on carbonaceous material inclusions using a Microdil 28 spectrometer coupled to a Spectra Physics 2020 5W argon laser.

3.4 SHRIMP-SI sulphur-isotope measurements

Following SEM analysis, the aluminium on the mounts was removed by decon90 detergent and 1-μm polishing. The mounts were thoroughly cleaned, dried and degassed in the vacuum oven (0.1 MPa, 60 °C) for at least five days, and then were coated with 45 to 55 nanometers of aluminium and loaded onto the outer rack of SHRIMP-SI. Due to the variable sizes of different growth zones, both big-spot (~27 × 20 μm) and small-spot (~18 × 15 μm) analyses were conducted. Big-spot analyses were applied to relatively homogeneous pyrite grains such as the porphyroblastic pyrite in micaceous phyllite and big homogeneous regions of zoned pyrite grains to measure the quadruple sulphur isotopic compositions, while small-spot analyses were applied to all growth zones to obtain the triple sulphur isotopic compositions and observe the sulphur isotopic variation from zone to zone. Detailed acquisition parameters are summarized in Table 6.2.

Table 6.2 Acquisition parameters of SHRIMP-SI for multiple sulphur isotope analyses.

Parameters	**Quadruple sulphur isotopes (Big-spot analyses)**	**Triple sulphur isotopes (Small-spot analyses)**
Spot size	~27 μm × 20 μm	~18 μm × 15 μm
Total sets	4	2 or 4
Total scans	40	20 or 40
Total analysis time	~21 min	~14 min or ~21min
Primary ion beam	Cs^+	Cs^+
Primary beam intensity	~8 nA	~3 nA
Primary beam energy	15 keV	15 keV
Total acceleration voltage for the extraction of secondary ions	10 kV	10 kV
Source slit width	60 μm	60 μm
Collector slit width for $^{32}S^-$	300 μm	300 μm
Collector slit width for $^{33}S^-$	150 μm	150 μm
Collector slit width for $^{34}S^-$	200 μm	200 μm
Collector slit width for $^{36}S^-$	400 μm	400 μm

Parameters	Quadruple sulphur isotopes (Big-spot analyses)	Triple sulphur isotopes (Small-spot analyses)
Amplifier and V-F Converter range for $^{32}S^-$	Electrometer current mode, 10^{11} Ω, 50 V	Electrometer current mode, 10^{11} Ω, 50 V
Amplifier and V-F Converter range for $^{34}S^-$	Electrometer current mode, 10^{11} or 10^{12} Ω, 50 V	Electrometer current mode, 10^{11} or 10^{12} Ω, 50 V
Amplifier and V-F Converter range for $^{33}S^-$	Electrometer current mode, 10^{11} or 10^{12} Ω, 50 V	Electrometer current mode, 10^{11} or 10^{12} Ω, 50 V
Amplifier and V-F Converter range for $^{36}S^-$	Electrometer charge-mode, 22 pF, 50 V	
Mass Resolution (at 10% peak height)	4000 M/ΔM	4000 M/ΔM

The primary ions for sputtering were Cs^+. Each analysis commenced with rastering the primary ion beam over an area slightly larger than the spot for two or five minutes, and in doing so removing the aluminium coat and allowing the sample surface to become conditioned with Cs^+ ions. During this time, the in-line valve between the source chamber and electrostatic analyzer was closed and base-lines for the electrometers were collected. This was followed by steering and centering of the secondary ion beam in order to further stabilize the S^- signal. Each run comprised four sets for big-spot analyses and two or four sets for small-spot analyses. Each set consisted of ten scans, and each scan was composed of ten subcounts. The four sulphur ions were collected simultaneously in multiple collectors. The ions of $^{32}S^-$, $^{33}S^-$, $^{34}S^-$, and $^{36}S^-$ were collected by the axial, auxiliary, low mass, and high mass Faraday cups, respectively. The iFlex electrometers for axial, auxiliary, and low mass Faraday cups operated in current mode, and $^{32}S^-$, $^{33}S^-$ and $^{34}S^-$ were measured using resistors, while the cVar electrometer of the high mass Faraday cup operated in charge mode, and $^{36}S^-$ was measured on a capacitor. The collector slit widths for detectors were 300 μm for $^{32}S^-$, 150 μm for $^{33}S^-$, 200 μm for $^{34}S^-$, and 300 μm for $^{36}S^-$. The resulting mass resolution for $^{33}S^-$ was higher than 4000M/ΔM at 10% peak height and clearly resolved $^{33}S^-$ and $^{32}SH^-$.

The reference materials used in this study were Ruttan pyrite (primary, $\delta^{34}S$ = 1.20‰, $\Delta^{33}S$ and $\Delta^{36}S \approx 0$) and Balmat pyrite (secondary, $\delta^{34}S$ = 15.1‰, $\Delta^{33}S$ and $\Delta^{36}S \approx 0$)(Crowe and Vaughan, 1996; Williford et al., 2011; Whitehouse, 2013; Ireland et al., 2014). Each analytical session started with several runs on Ruttan pyrite and Balmat pyrite, followed by several runs on the unknowns as long as the conditions were stable, and then one or two runs on Ruttan pyrite and one on Balmat pyrite, and so forth.

Sulphur isotope data were reduced using the POXI-MC software developed by the Research School of Earth Sciences, Australian National University.

The measured $^{3x}S^{-}/^{32}S^{-}$ ratios are expressed in delta (δ) notation as permil deviations from the Vienna Canyon Diablo Troilite (V-CDT) standard ratios, following the relationship $\delta^{3x}S_{V\text{-}CDT}$ (‰) = $[(^{3x}S/^{32}S)_{unknown}/(^{3x}S/^{32}S)_{V\text{-}CDT} - 1] \times 1000$, where $(^{3x}S/^{32}S)_{unknown}$ and $(^{3x}S/^{32}S)_{V\text{-}CDT}$ are the $^{3x}S/^{32}S$ ratios of unknowns and V-CDT, respectively, and x is 3, 4 or 6. Since Ruttan pyrite was applied as the primary reference material, thus $\delta^{3x}S_{V\text{-}CDT}$ (‰) = $\delta^{3x}S_{V\text{-}CDT}$(Ruttan) + $[(^{3x}S/^{32}S)_{unknown}/(^{3x}S/^{32}S)_{Ruttan} - 1] \times 1000$, where $\delta^{3x}S_{V\text{-}CDT}$(Ruttan) is the $\delta^{3x}S_{V\text{-}CDT}$ value of Ruttan pyrite ($\delta^{33}S_{V\text{-}CDT}$(Ruttan), $\delta^{34}S_{V\text{-}CDT}$(Ruttan), and $\delta^{36}S_{V\text{-}CDT}$(Ruttan) are 0.62‰, 1.20‰, and 2.28‰, respectively, Crowe and Vaughan, 1996; Williford et al., 2011; Whitehouse, 2013; Ireland et al., 2014). The magnitude of S-MIF is quantified as $\Delta^{33}S$ (= $\delta^{33}S - 1000 \times [(1 + \delta^{34}S/1000)^{0.515} - 1]$) and $\Delta^{36}S$ (= $\delta^{36}S - 1000 \times [(1 + \delta^{34}S/1000)^{1.9} - 1]$).

3.5 SHRIMP-II trace element abundance measurements

The gold concentration of pyrite was semi-quantitatively determined on SHRIMP-II. Positive Cs^{+} primary beam was used to generate a negative secondary ion beam and hence maximize the yield of secondary gold ions ($^{197}Au^{-}$). The general principle was to compare the relative values of the ratio CPS($^{197}Au^{-}$)/CPS(M^{-}), where CPS is short for counts per second, and M^{-} is an ion with relatively constant count rate comprising the matrix element(s) of pyrite (FeS_2). Similar to sulphur isotope analyses, both big-spot (~27 × 20 μm) and small-spot (~18 × 15 μm) analyses were carried out due to the variable sizes of pyrite grains and growth zones. Detailed run and set parameters are summarized in Table 6.3. Each run commenced with rastering an area slightly larger than the spot for seven minutes (three minutes for the second session) and subsequent burning for another three minutes (1 minute for the second session), in order to remove the aluminium coat, avoid any gold contamination, and condition the sample surface with Cs^{+} ions. The next step was tuning the secondary ion beam through steering the quadrupole triplet, thereby stabilizing the transmission of secondary ions. Each analytical run consisted of one set (four scans through the run table). The secondary $^{197}Au^{-}$ ions were collected by an ETP^{TM} discrete-dynode electron multiplier (DDEM) at the rear of the multi-collector chamber owing to the low signal of gold ions and the high sensitivity and low noise of electron multiplier. The peak of $^{197}Au^{-}$ was set using a pure gold sample. The peak position of $^{197}Au^{-}$ was centered using that of $^{133}Cs^{32}S_2^{-}$, the peak and count rate of which were relatively stable, and was the closest peak to the mass position of $^{197}Au^{-}$.

Table 6.3 Run and set parameters of SHRIMP-II for semi-quantitative measurement of gold abundance in pyrite.

Parameters	Big-spot analyses	Small-spot analyses
Spot size	~27 μm × 20 μm	~18 μm × 15 μm
Set	1	1
Scans	4	4
Total analysis time	~14 min	~14 min (first session) or ~8 min (second session)
Primary beam ion species	Cs^+	Cs^+
Primary beam energy	15 keV	15 keV
Total acceleration voltage for the extraction of secondary ions	10 kV	10 kV
Source slit width	~60 μm	~60 μm
Collector slit width	~100 μm	~100 μm

The concentrations of Se and Mo were also semi-quantitatively determined by SHRIMP-II with the same principle. The primary ions were Cs^+, while only small-spot (~18 × 15 μm) analyses were performed. Detailed run and set parameters are summarized in Table 6.4. The spots were firstly rastered for two minutes and then burned for one minute. Subsequently, the first quadrupole triplet was adjusted to steer and maximize the secondary beam intensity. The negative ions were cycled to establish a hysteresis loop in the magnet, entered through electrostatic deflection in the quadrupole lens of the mass analyzer, and were then collected by an electron multiplier. $^{98}Mo^{32}S^-$ ion instead of $^{98}Mo^-$ ion was used because of much higher yield. The peaks of $^{80}Se^-$ and $^{98}Mo^{32}S^-$ were set using clausthalite and molybdenite, respectively. The $^{54}Fe^{32}S^-$ ion was used as the normalizing ion.

Table 6.4 Run and set parameters of SHRIMP-II for semi-quantitative measurement of Se and Mo content in pyrite.

Parameters	Small-spot analyses
Spot size	~18 μm × 15 μm
Sets	1
Scans	4
Total analysis time	~9 min
Primary beam ion species	Cs^+

Primary beam energy	15 keV
Total acceleration voltage for the extraction of secondary ions	10 kV
Source slit width	~60 μm
Collector slit width	~100 μm

4. Results

4.1 Results of etching, SEM and laser Raman spectroscopy

Sodium hypochlorite etching revealed pronounced zoning in ore-related pyrite (Fig. 6.3 and Fig. 6.4). The majority of the pyrite in BIF-hosted ores displays either two-stage or three-stage stepped zoning profiles (type A and B, respectively, Fig. 6.3 and Table 6.5), and occasionally four-stage zonation (type C, Fig. 6.3 and Table 6.5). Pyrite laminae associated with smoky chert veinlets crosscutting BIF show oscillatory zonation (type D and E, Fig. 6.4 and Table 6.5), which were also revealed in some of the first growth zones of B-zoned grains and the second growth zones of C-zoned grains. Pyrite in smoky chert-hosted ores exhibits mainly oscillatory zoning (type G, Fig. 6.4 and Table 6.5), and merely a few grains display three-stage stepped zoning (type F, Fig. 6.3 and Table 6.5).

EDS analyses show that the inclusions within the first growth zones of C-zoned pyrite are siderite and less dolomite, while those of the other growth zones are mostly carbonaceous material; laser Raman spectroscopic signatures suggest that these are poorly crystallized graphite (Fig. 6.5).

4.2 Multiple sulphur isotopic compositions

Sulphur isotope data are listed in Table 6.6. The internal error is expressed in the value of two standard errors of the Ruttan pyrite, and is on average 0.13‰ (big-spot) and 0.19‰ (small-spot) for $\delta^{34}S$, 0.03‰ (big-spot) and 0.12‰ (small-spot) for $\Delta^{33}S$, and 0.29‰ (big-spot) for $\Delta^{36}S$. The reproducibility is expressed in the value of two standard deviations of the Ruttan pyrite of each session, and is on average 0.31‰, 0.09‰, and 0.39‰ for $\delta^{34}S$, $\Delta^{33}S$, and $\Delta^{36}S$, respectively for big-spot analyses, and 0.60‰ and 0.23‰ for $\delta^{34}S$ and $\Delta^{33}S$, respectively for small-spot analyses.

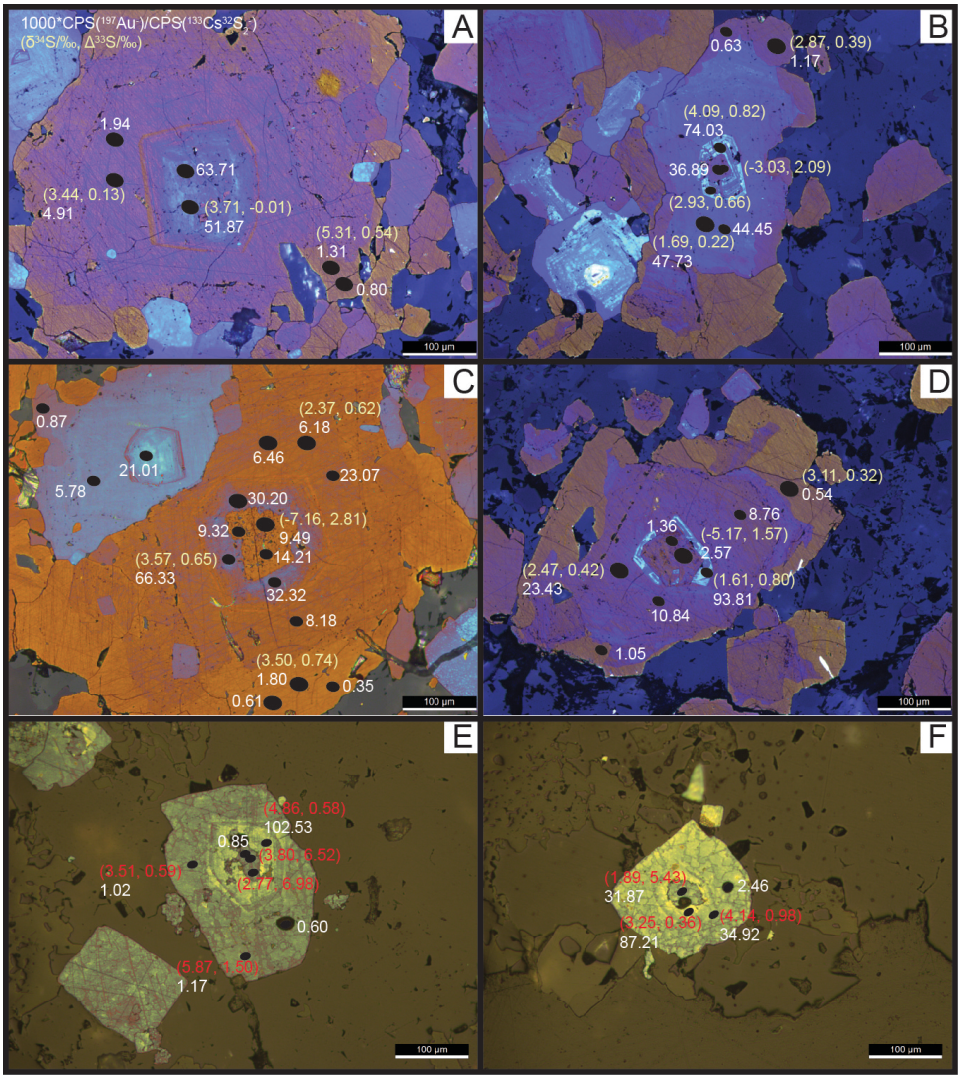

Fig. 6.3 Microphotographs of sodium hypochlorite etched pyrite grains in BIF- and smoky chert-hosted ores showing stepped zoning, along with the associated multiple sulphur isotopic composition and gold abundance. A. Triple-zoned (generation two to four, type B) pyrite in BIF-hosted ore FPL-122_598.0m. B and D. Quadruple-zoned (generation one to four, type C) pyrite grains in arsenopyrite-rich BIF-hosted ore FLV-167_225m. C. Quadruple-zoned (generation one to four, type C) and triple-zoned (generation two to four, type B) pyrite grains in BIF-hosted ore FPL-122_598.0m. E and F. Triple-zoned (generation one to three, type F) pyrite grains in smoky chert-hosted ore FLU-173.

The pyrite in ores shows three distinct groups of multiple sulphur isotopic compositions (Fig. 6.6). The first group (zone 1 of C-zoned pyrite) is characterized by negative $\delta^{34}S$ (-7.19 to -1.97‰), moderate positive $\Delta^{33}S$ (1.37 to 3.02‰) and negative $\Delta^{36}S$ (-3.32 to -2.71‰). The second group (zone 1 of D- and F-zoned pyrite as well as the disseminated pyrite in chert) displays small to moderate positive $\delta^{34}S$ (1.89 to 7.46‰), high positive $\Delta^{33}S$ (4.29 to 6.98‰) and negative $\Delta^{36}S$ (-5.31 to -3.35‰). The third group (all zones of A-, B-, E-, G- zoned pyrite,

zone 2 to 4 of C-zoned pyrite, zone 2 and 3 of F-zoned pyrite, and zone 2 of D-zoned pyrite) exhibits small positive $\delta^{34}S$ (0.73 to 5.87‰), low magnitude of $\Delta^{33}S$ (-0.01 to 1.95‰) and $\Delta^{36}S$ (-1.93 to 1.16‰).

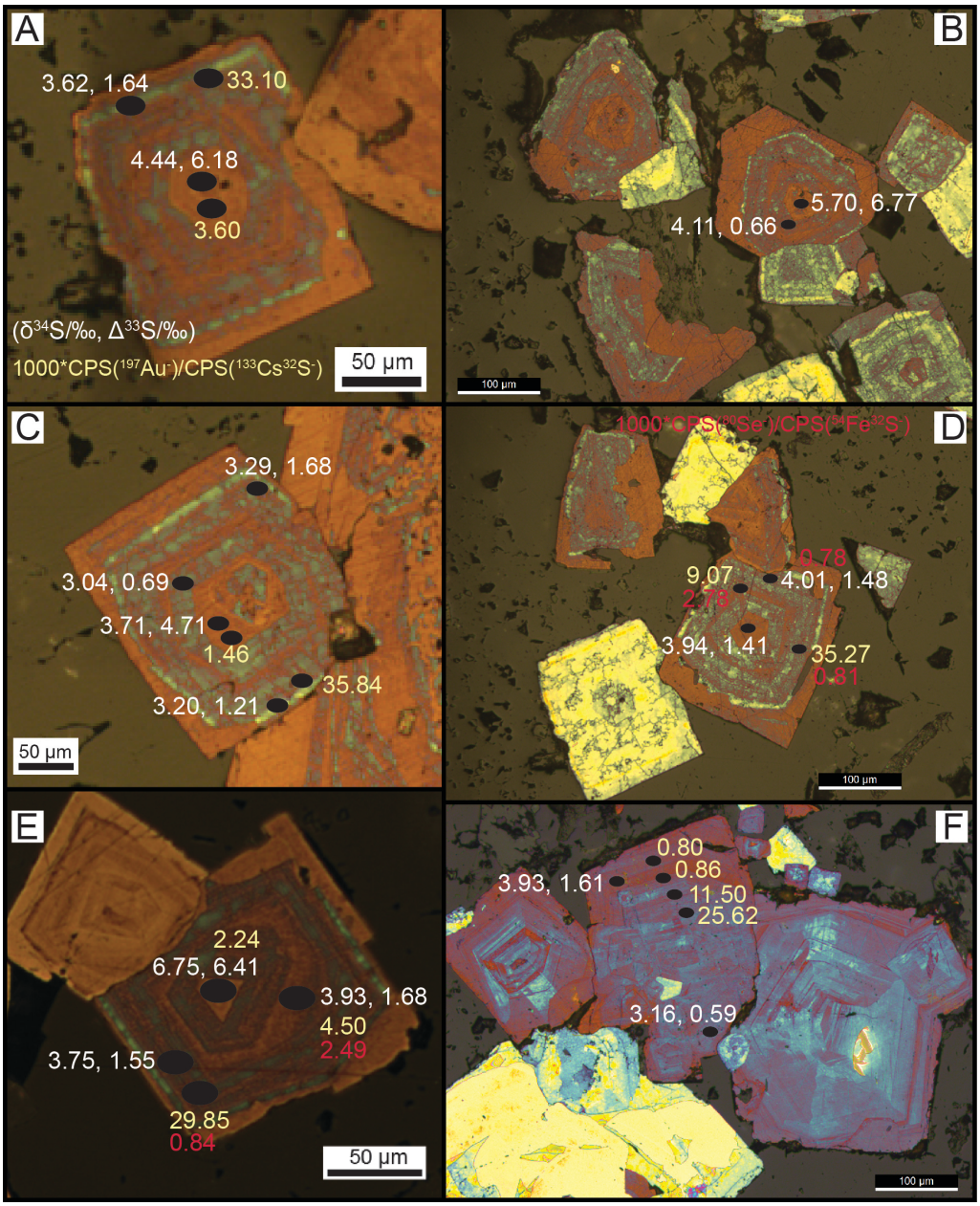

Fig. 6.4 Microphotographs of sodium hypochlorite etched pyrite grains in BIF- and smoky chert-hosted ores displaying oscillatory zoning, along with the associated multiple sulphur isotopic composition, gold (and selenium) abundance. A, B, C and E. Oscillatory-zoned (generation one and two, type D) pyrite grains constituting the BIF pyrite laminae (FPL-120_639.2m) closely associated with smoky chert veinlet crosscutting BIF. D. Oscillatory-zoned (generation two, type E) pyrite grain constituting the BIF pyrite laminae (FPL-120_639.2m) closely associated with smoky chert veinlet

crosscutting BIF. F. Oscillatory-zoned (generation two, type G) pyrite grains in smoky chert-hosted ore FLU-173.

The pyrite in different wall rocks displays distinct multiple sulphur isotopic compositions (Fig. 6.7). The microcrystal pyrite aggregates and the recrystallized grains in the vein of carbonaceous phyllite are characterized by a wide range of $\delta^{34}S$ (5.29 to 16.19‰), $\Delta^{33}S$ (-0.40 to 10.98‰) and $\Delta^{36}S$ (-9.98 to -1.18‰), and the data exhibit good linear relationships of $\delta^{34}S$-$\Delta^{33}S$ and $\Delta^{33}S$-$\Delta^{36}S$ close to the Archean Reference Array (ARA). In comparison, the medium- to coarse-grained pyrite in the veins of carbonaceous phyllite shows relatively constant $\Delta^{33}S$ (1.20 to 1.40‰, 1.34‰ on average) and a very restricted range of $\delta^{34}S$ (6.75 to 9.50‰) and $\Delta^{36}S$ (-1.34 to -0.19‰). The porphyroblastic pyrite in micaceous phyllite exhibits a narrow range of $\Delta^{33}S$ (1.40 to 3.45‰) and $\Delta^{36}S$ (-4.86 to -0.92‰), but a wider range of $\delta^{34}S$ (-4.91 to 6.54‰). The pyrite in hydrothermally altered basalt is characterized by a relatively limited range of $\delta^{34}S$ (1.94 to 3.29‰), $\Delta^{33}S$ (0.52 to 0.70‰) and $\Delta^{36}S$ (-0.55 to -0.18‰), similar to those of the third group sulphur isotopic compositions of the ore-related pyrite. The pyrite in dolerite dyke displays $\delta^{34}S$, $\Delta^{33}S$ and $\Delta^{36}S$ of near 0.

4.3 Gold, Se and Mo abundance

The semi-quantitative concentration of Au is listed in Table 6.7 and that of Se and Mo is listed in Table 6.8.

The results show that the first growth zones of B-zoned pyrite and the second growth zones of C- and F-zoned pyrite have much higher gold abundance than the other regions of the same grains. For D-, E-, and G-zoned pyrite, the laminae with blue etching color have significantly higher gold abundance than the alternating orange laminae.

F-zoned pyrite and the majority of B-zoned pyrite have higher Se abundance in the first growth zones than the other regions of the same grains. For E-zoned pyrite and the oscillatory regions of D-zoned pyrite, the laminae with orange etching color have higher Se abundance compared with the blue-colored laminae. The Mo abundance shows no regular or systematic variations.

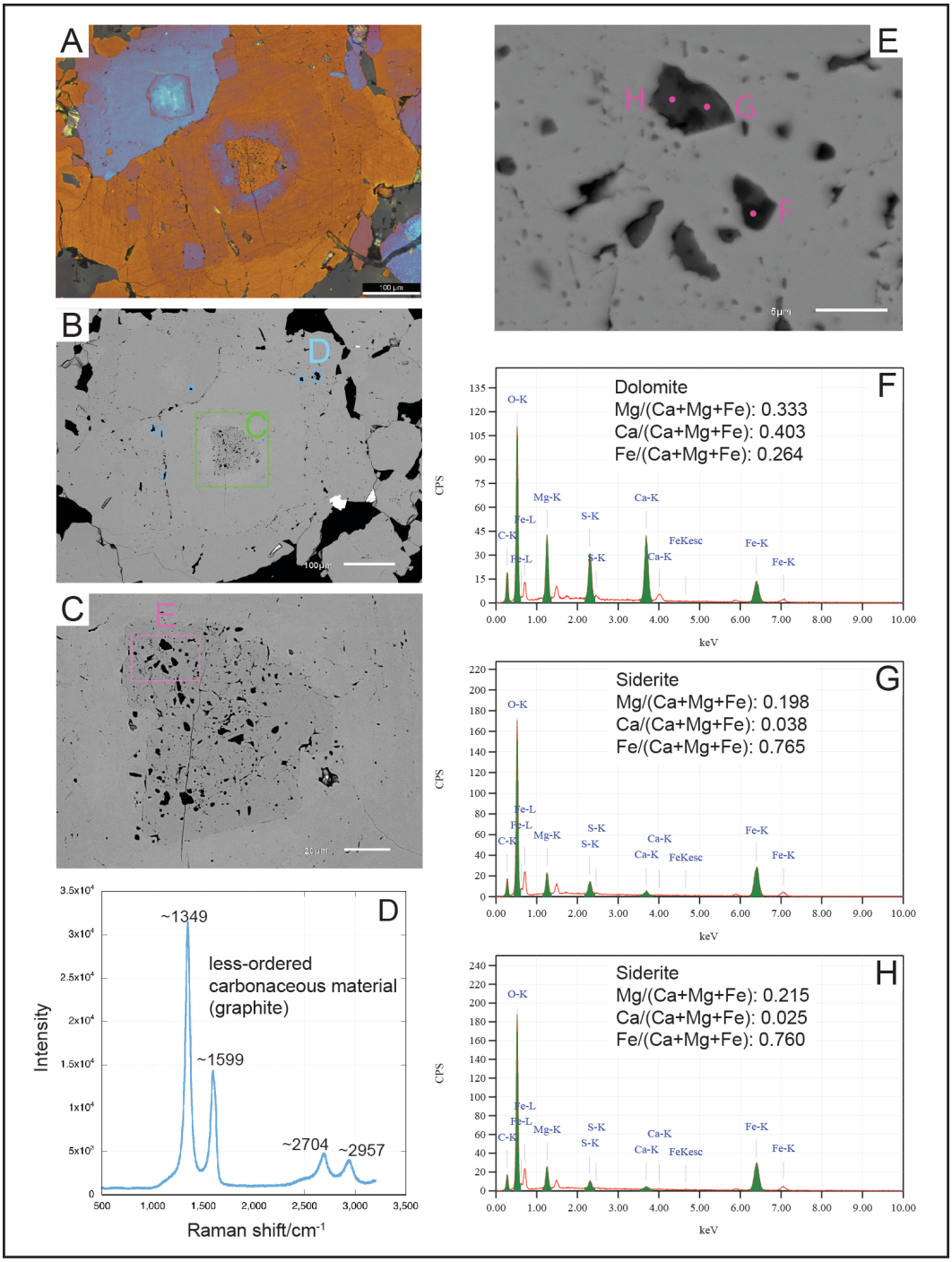

Fig. 6.5 Spectrograms of EDS and Raman for identification of inclusions in generation one and three pyrite in a typical pyrite grain from the BIF-hosted ore FPL-122_598.0m. A. A microphotograph of the sodium hypochlorite etched pyrite grain. B, C and E. BSE images of the pyrite grain. D. Raman spectrogram of the carbonaceous materials in generation three pyrite. F, G and H. EDS spectrograms of the siderite and dolomite inclusions in generation one pyrite. The other inclusions in C that are not displayed in detail have similar texture and chemical compositions. Note that due to the small size of these inclusions, the EDS results unavoidably involve composition of the host pyrite (FeS_2). The

calculation of Mg/(Ca + Mg + Fe), Ca/(Ca + Mg + Fe), and Fe/(Ca + Mg + Fe) have subtracted the pyrite iron based on the ratio of Fe atom to S atom in the chemical formula of pyrite.

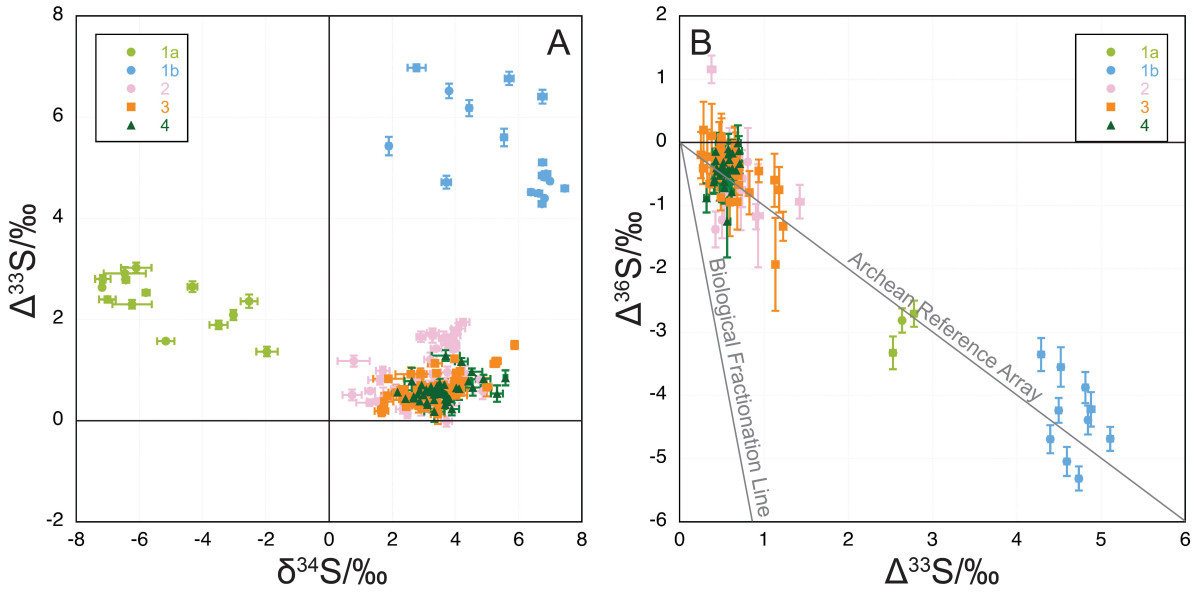

Fig. 6.6 A. $\delta^{34}S$-$\Delta^{33}S$ and B. $\Delta^{33}S$-$\Delta^{36}S$ diagrams of the data for ore-related pyrite. The value of error bar is two standard errors.

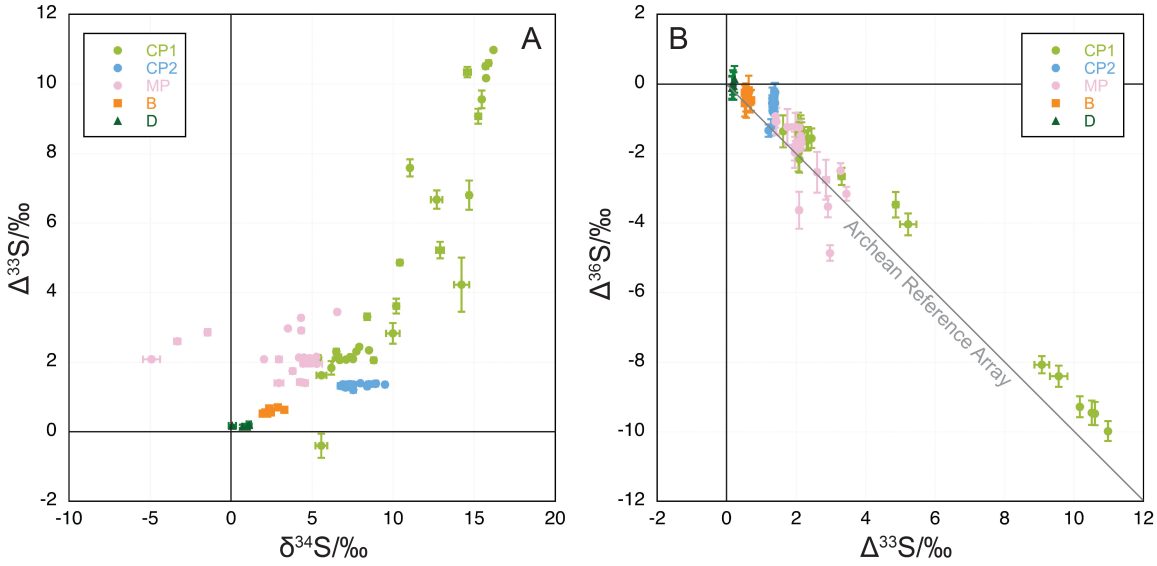

Fig. 6.7 A. $\delta^{34}S$-$\Delta^{33}S$ and B. $\Delta^{33}S$-$\Delta^{36}S$ diagrams of the data for pyrite in wall rocks. CP1: Microcrystal pyrite aggregates and the recrystallized grains in the vein of carbonaceous phyllite. CP2: Medium- to coarse-grained pyrite in the veins of carbonaceous phyllite. MP: Porphyroblastic pyrite in micaceous phyllite. B: Pyrite in hydrothermally altered basalt. D: Dolerite dyke. The value of error bar is two standard errors.

5. Discussion

5.1 Pyrite generations

The structures of variable scale crosscutting BIF are the main channel for hydrothermal fluids to enter BIF, migrating laterally and sulphidizing the iron-bearing minerals (siderite). Therefore, the vein-cutting relationships are unreliable indicators for sorting the chronological order of pyrite. Here, a combination of pyrite internal texture, multiple sulphur isotopic composition, and Au and Se abundance is applied as the basis of clarifying the pyrite generations. Four generations in total have been identified.

Generation one is subdivided into two types: 1a and 1b. Generation 1a occurs in BIF-hosted ores, and is characterized by carbonate inclusions (siderite and dolomite), negative $\delta^{34}S$ and moderate positive $\Delta^{33}S$, low to moderate Au abundance and high Se abundance (Table 6.5 and Fig. 6.8). Generation 1b occurs in both BIF- and chert-hosted ores as the first growth zones of D-zoned pyrite in BIF, and disseminated euhedral to subhedral grains and the first growth zones of F-zoned pyrite in chert. Generation 1b pyrite possesses positive $\delta^{34}S$, high positive $\Delta^{33}S$, low gold abundance and high Se abundance (Table 6.5 and Fig. 6.8). Generation 1b is most likely to be modified products of generation 1a via interactions with the carbonaceous phyllite. Because the pyrite in carbonaceous phyllite have the highest $\Delta^{33}S$ (11‰) and $\delta^{34}S$ (16‰)(Fig. 6.7), and the BIF-chert layer is spatially close to carbonaceous phyllite.

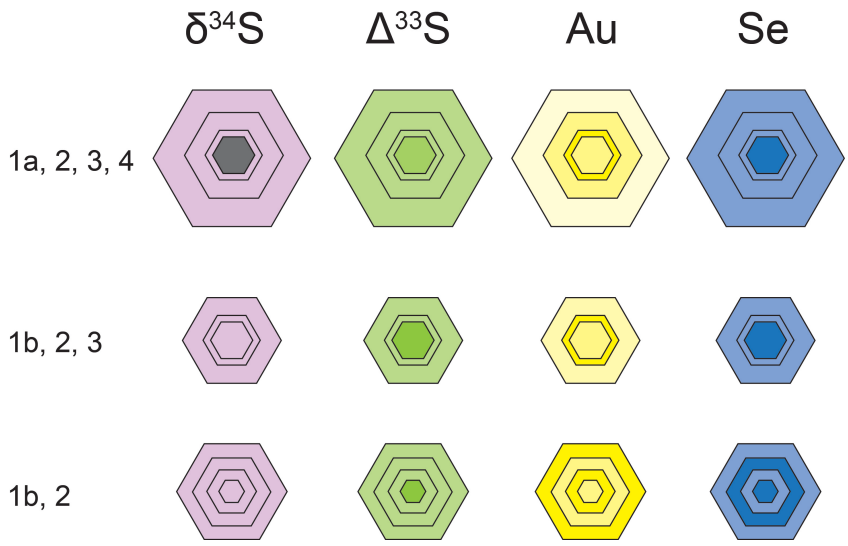

Fig. 6.8 Sketch of the zonings of $\delta^{34}S$, $\Delta^{33}S$, Au content, and Se content for pyrite grains with growth zones. The gradation of the colours stands for magnitudes/degrees: The darker, the larger. The exception is the $\delta^{34}S$ of the first zone of 1a-2-3-4 pyrite that represents negative $\delta^{34}S$, while the purple zones stand for positive $\delta^{34}S$.

Generation two occurs in every type of zoning (except for A), and shows a characteristic combination of signatures, including euhedral crystal forms, blue etching color, oscillatory zoning, graphite inclusion, small positive $\delta^{34}S$ and $\Delta^{33}S$ (only three have weakly negative $\Delta^{33}S$), high gold abundance and low Se abundance (Table 6.5 and Fig. 6.8). Generation three and four are represented by the last two growth zones of B- and C-zoned pyrite, and they are similar in respects of inclusion (dominantly graphite), multiple sulphur isotopic compositions (small positive $\delta^{34}S$ and $\Delta^{33}S$) and Se abundance, except that the third generation contains more gold than the fourth generation (Table 6.5 and Fig. 6.8).

5.2 Sources of sulphur

Conventionally, $\delta^{34}S$ alone has been used to trace the sulphur sources of ore deposits. Nevertheless, $\delta^{34}S$ is sensitive to the redox state of hydrothermal fluids. According to mass balance, when multiple sulphur-bearing species exist, particularly if sulphides are not the dominant species, those in high sulphur valence (e.g., sulphate) have higher $\delta^{34}S$ while those in low sulphur valence (e.g., sulphide) possess lower $\delta^{34}S$ compared with the $\delta^{34}S$ of bulk hydrothermal fluids (Ohmoto and Rye, 1979). Therefore, in such cases, $\delta^{34}S$ of sulphides may be unsuitable to represent that of bulk hydrothermal fluids and hence may be inappropriate to characterize the sulphur sources. Unlike $\delta^{34}S$, howerver, $\Delta^{33}S$ is not fractionated between the two reservoirs, and stays constant despite variable amounts of other sulphur-bearing species. Thus, $\Delta^{33}S$ can add more significant constraints on the bulk sulphur isotopic composition of hydrothermal fluids and trace the sulphur source(s).

The pyrite of generation 1 (1a and 1b) has moderate to high positive $\Delta^{33}S$ (1.4 to 7.0‰), and generation 1a has characteristic negative $\delta^{34}S$ (-7.2 to -2.0‰). The pyrite of generation 2 to 4 mostly has low to moderate positive $\delta^{34}S$ (0.7 to 5.9‰) and $\Delta^{33}S$ (0 to 2.0‰). Such sulphur isotopic composition signatures can be interpreted in two main ways. The associated hydrothermal fluids of the four generations of pyrite can be derived from the same source(s), and evolved from generation 1 through to 4. Alternatively, the hydrothermal fluids of the first

generation of pyrite (1a and 1b) can be from different origin(s) compared with that of the later three generations of pyrite.

Since S-MIF is mostly preserved in sulphur-bearing species of Archean metasedimentary rocks (e.g., Farquhar et al., 2000), thus the pervasive S-MIF in the four generations of pyrite can only be derived from metasedimentary rocks of the Rio das Velhas supergroup. The pyrite with $\Delta^{33}S$ of less than 0.2‰ (the boundary between S-MDF and S-MIF defined in Farquhar and Wing, 2003) can be a signature of the original hydrothermal fluids or mixing products of positive and negative $\Delta^{33}S$ via interaction between the original hydrothermal fluids and metasedimentary rocks. As such, the mineralization hydrothermal fluids can be metamorphic fluids alone, metamorphic fluids reacted with surrounding rocks (wall rocks of pathways upwards and deposition location), and magmatic fluids mixed with metamorphic fluids and/or reacted with surrounding rocks.

The metamorphic fluids can be formed by devolatilization of hydrous minerals (H_2O), carbonates (CO_2), and sulphides (H_2S) in the metasedimentary and metavolcanic rocks constituting the Nova Lima Group of the Rio das Velhas Supergroup and the granite-gneiss basement. Although spatially, no granitoids occur within the Lamego deposit area except for minor late dolerite dykes and sills crosscutting or parallel to the primary bedding, magmatic fluids is still a possibility. The three major regional magmatisms are concentrated in 2920-2850 Ma, 2800-2760 Ma, and 2760-2680 Ma (Farina et al., 2016). The youngest magmatism (2680 Ma) is close to the mineralization age (2672 ± 14 Ma, Lobato et al., 2007) when taking the uncertainty into consideration.

The hydrothermal fluids associated with the pyrite of generation 1 to 4 can be considered in an evolving perspective. The first generation of pyrite is characterized by negative $\delta^{34}S$, higher Se contents, and carbonate (siderite and ankerite) inclusions, when compared with generation 2 to 4 (positive $\delta^{34}S$, lower Se contents, and carbonaceous material inclusions). The negative $\delta^{34}S$ probably results from oxidized sulphur-bearing species in the hydrothermal fluids such as sulphate, which possesses higher $\delta^{34}S$ according to the principle of mass balance. According to previous fluid inclusion study on the Lamego gold deposit, an estimated temperature of the mineralization hydrothermal fluids is 300 to 375 °C (Morales et al., 2016). The second diagram in Huston et al. (1995) shows that at 300 °C, the Se content in pyrite increases with oxidation state, thus the higher Se contents in generation 1 pyrite suggest more oxidized conditions. Therefore, the hydrothermal fluids evolve in a direction of

reduction. The declined magnitudes of S-MIF can be explained as decreasing degrees of interaction between hydrothermal fluids and surrounding metasedimentary rocks.

Although the evolving model can well explain the different chemical and mineralogical signatures of the four generations of pyrite, it still cannot be excluded that the pyrite of generation 1a and 1b is from different sources based on particularly the distinct higher positive $\Delta^{33}S$. Such characteristic $\Delta^{33}S$ can indicate that the devolatilized rocks host larger magnitudes of S-MIF.

The multiple sulphur isotopic compositions of ore-related pyrite of the Lamego gold deposit are in good accordance with previous studies on the Archean gold deposits worldwide, including those from the Yilgarn Craton of Western Australia, the Barberton Greenstone Belt of South Africa, and the Quadrilátero Ferrífero of Brazil (Bühn et al., 2012; Steadman et al., 2015; Agangi et al., 2016; Gregory et al., 2016; Selvaraja et al., 2017; Godefroy-Rodríguez et al., 2018; Kresse et al., 2018; Fig. 6.9). They all show variable degrees of S-MIF in ore-related sulphides, with $\Delta^{33}S$ ranging from -1.18‰ to 2.18‰ (Fig. 6.9), in contrast to the results of Xue et al. (2013), the $\Delta^{33}S$ in which is near zero. Such consistent sulphur isotope signatures indicate that S-MIF is widespread in ore-related sulphides of Archean gold deposits. The sulphur can be derived from multiple sources (e.g., metamorphic fluids, magmatic fluids, wall rocks), and one of the essential contributors is the metasedimentary rocks in associated Archean strata.

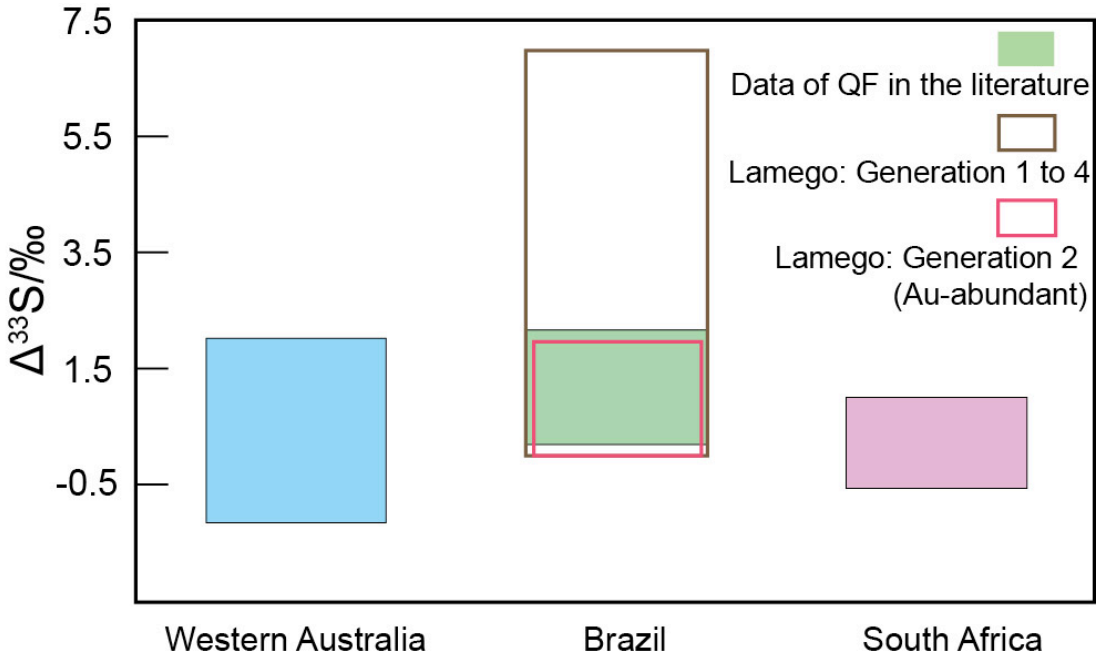

Fig. 6.9 A summary of the $\Delta^{33}S$ range of ore-related sulphides in Archean gold deposits from Western Australia, South Africa, and Brazil. Data compiled are from Bühn et al., 2012; Steadman et al., 2015; Agangi et al., 2016; Gregory et al., 2016; Selvaraja et al., 2017; Godefroy-Rodríguez et al., 2018; Kresse et al., 2018.

5.3 Gold precipitation mechanism

The mechanisms of gold precipitation mainly include boiling/phase separation caused by pressure drop, desulphidation, and change of redox state. If the hydrothermal fluids relevant to the four generations of pyrite are from the same source(s), and evolve from generation 1 to 4, then as discussed above, the hydrothermal fluids of generation 2 to 4 are reduced from that of generation 1. As the pyrite of generation 2 has the highest gold abundance, thus reduction can be the trigger of gold precipitation.

If the hydrothermal fluids of generation 1 are different from that of generation 2 to 4 in origin, then some insights can still be gained by viewing the unique signatures of generation 2 pyrite.

The second generation of pyrite with the most gold has the characteristic oscillatory zoning composed of alternating gold-rich and gold-poor laminae. One possibility is that each lamina of the oscillatory zoning represents one pulse of fluid flow. The repeating laminae represent the cyclicity of the deposition of gold-rich and gold-poor pyrite laminae, which result from fault valve (Peterson and Mavrogenes, 2014). The gold precipitation of gold-rich pyrite laminae is triggered by flash vaporization arising from rapid pressure decrease when faults are formed (Peterson and Mavrogenes, 2014). Since pressure drop can lead to the release of H_2S, resulting in oxidation of the hydrothermal fluids. However, this is inconsistent with the Se content. The gold-poor laminae have higher Se abundance than the gold-rich laminae (Table 6.8, Fig. 6.4 and Fig. 6.8), indicating that the hydrothermal fluids of the former are oxidized compared with that of the latter. Therefore, pressure decrease is less likely to be the trigger of gold precipitation. The Lamego gold deposit is hosted by carbonate-facies (mainly siderite) BIF, and the ore-related pyrite is mostly generated by sulphidation of siderite (desulphidation of hydrothermal fluids). Although desulphidation occurs throughout the four generations, the second generation of pyrite precipitates the most gold, suggesting desulphidation is not the predominant factor as well. Collectively, it seems that change of redox state, i.e., reduction, based on the characteristic Se content in gold-poor and gold-rich pyrite, induces the deposition of gold in the Lamego god deposit.

6. Concluding remarks

The internal texture of pyrite revealed by sodium hypochlorite etching and BSE imaging, coupled with high-resolution multiple sulphur isotopic composition (measured by SHRIMP-SI) and abundance of gold, selenium, and molybdenum (determined by SHRIMP-II) in different zones of pyrite grains has revealed four generations of pyrite in BIF- and chert-hosted ores. Generation one is subdivided into 1a and 1b, which show distinct multiple sulphur isotopic compositions (negative $\delta^{34}S$ and moderate positive $\Delta^{33}S$ for 1a and high positive $\Delta^{33}S$ for 1b) and higher Se contents. Generation two is characterized by oscillatory zoning, the highest gold contents, and low to moderate positive $\delta^{34}S$ and $\Delta^{33}S$. Generation three and four have similar multiple sulphur isotopic compositions to generation two, but contain much less gold, particularly generation four.

S-MIF is widespread in the four generations of pyrite. The associated hydrothermal fluids can be metamorphic fluids alone, metamorphic fluids interacted with surrounding rocks, or magmatic fluids mixed with metamorphic fluids and/or interacted with wall rocks. Such metamorphic fluids are derived from devolatilization of the underlying Nova Lima Group of the Rio das Velhas Supergroup and the granite-gneiss basement. The hydrothermal fluids for the four generations of pyrite can be from the same source(s), and evolve (reduction) from generation 1 to 2, 3 and 4. Alternatively, the first generation is different from the later three generations in origin(s) based on the distinct signatures, particularly $\delta^{34}S$ and $\Delta^{33}S$. Compiled data from previous studies and that obtained here show that S-MIF is pervasive in Archean gold deposits, and the sulphur can be multiple-sourced, and one essential contributor should be the metasedimentary rocks in the related strata.

If the four generations of pyrite are from the same source(s), then redox state change (reduction) is the trigger of gold precipitation. If the hydrothermal fluids of generation 1 are different from that of generation 2 to 4, then based on the Se contents in gold-poor and gold-rich laminae of the oscillatory-zoned pyrite of generation 2 with the most abundant gold, reduction is also the critical factor of inducing gold deposition.

References

Agangi, A., Hofmann, A., Eickmann, B., Marin-Carbonne, J., Reddy, S.M., 2016. An atmospheric source of S in Mesoarchaean structurally-controlled gold mineralisation of the Barberton Greenstone Belt. Precambrian Research 285: 10-20.

Alkmima, F.F., Marshakb, S., 1998. Transamazonian Orogeny in the Southern São Francisco Craton Region, Minas Gerais, Brazil: evidence for Paleoproterozoic collision and collapse in the Quadrilátero Ferrífero. Precambrian Research 90: 29-58.

Baltazar, O.F., and Zucchetti, M., 2007. Lithofacies associations and structural evolution of the Archean Rio das Velhas greenstone belt, Quadrilátero Ferrífero, Brazil: A review of the setting of gold deposits. Ore Geology Reviews 32: 471-499.

Bühn, B., Santos, R.V., Dardenne, M.A., de Oliveira, C.G., 2012. Mass-dependent and mass-independent sulfur isotope fractionation ($\delta^{34}S$ and $\delta^{33}S$) from Brazilian Archean and Proterozoic sulfide deposits by laser ablation multi-collector ICP-MS. Chemical Geology 312-313: 163-176.

Crowe, D.E., and Vaughan, R.G., 1996. Characterization and use of isotopically homogeneous standards for in situ laser microprobe analysis of $^{34}S/^{32}S$ ratios. American Mineralogist 81: 187-193.

Farina, F., Albert, C., Martínez Dopico, C., Aguilar Gil, C., Moreira, H., Hippertt, J.P., Cutts, K., Alkmim, F.F., Lana, C., 2016. The Archean-Paleoproterozoic evolution of the Quadrilátero Ferrífero (Brasil): Current models and open questions. Journal of South American Earth Sciences 68: 4-21.

Farquhar, J., Bao, H., Thiemens, M., 2000. Atmospheric Influence of Earth's Earliest Sulfur Cycle. Science 289: 756-758.

Farquhar, J., and Wing, B.A., 2003. Multiple sulfur isotopes and the evolution of the atmosphere. Earth and Planetary Science Letters 213: 1-13.

Gregory, D.D., Large, R.R., Bath, A.B., Steadman, J.A., Wu, S., Danyushevsky, L., Bull, S.W., Holden, P., Ireland, T.R., 2016. Trace Element Content of Pyrite from the Kapai Slate, St. Ives Gold District, Western Australia. Economic Geology 111: 1297-1320.

Godefroy-Rodríguez, M., Hageman, S., LaFlamme, C., Fiorentini, M., 2018. The multiple sulfur isotope architecture of the Golden Mile and Mount Charlotte deposits, Western Australia. Mineralium Deposita, doi: 10.1007/s00126-018-0828-y.

Goldfarb, R.J., Groves, D.I., Gardoll, S., 2001. Orogenic gold and geologic time: a global synthesis. Ore Geology Reviews 18: 1-75.

Huston, D.L., Sie, S.H., Suter, G.F., 1995. Selenium and its importance to the study of ore genesis: the theoretical basis and its application to volcanic-hosted massive sulfide deposits using pixeprobe analysis. Nuclear Instruments and Methods in Physics Research B 104: 476-480.

Kresse, C., Lobato, L.M., Hagemann, S.G., e Silva, R.C.F., 2018. Sulfur isotope and metal variations in sulfides in the BIF-hosted orogenic Cuiabá gold deposit, Brazil: Implications for the hydrothermal fluid evolution. Ore Geology Reviews 98: 1-27.

Lobato, L.M., Ribeiro-Rodrigues, L.C., Zucchetti, M., Noce, C.M., Baltazar, O.F., Silva, L.C., Pinto, C.P., 2001a. Brazil's premier gold province. Part I: The tectonic, magmatic, and structural setting of the Archean Rio das Velhas greenstone belt, Quadrilátero Ferrífero. Mineralium Deposita 36: 228-248.

Lobato, L.M., Ribeiro-Rodrigues, L.C., Vieira, F.W.R., 2001b. Brazil's premier gold province. Part II: geology and genesis of gold deposits in the Archean Rio das Velhas greenstone belt, Quadrilátero Ferrífero. Mineralium Deposita 36: 249-277.

Lobato, L.M., Santos, J.O.S., McNaughton, N.J., Fletcher, I.R., Noce, C.M., 2007. U-Pb SHRIMP monazite ages of the giant Morro Velho and Cuiabá gold deposits, Rio das Velhas greenstone belt, Quadrilátero Ferrífero, Minas Gerais, Brazil. Ore Geology Reviews 32: 674-680.

Machado, N., and Carneiro, M., 1992. U-Pb evidence of late Archean tectono-thermal activity in the southern São Francisco shield, Brazil. Canadian Journal of Earth Sciences 29: 2341-2346.

Machado, N., Noce, C.M., Ladeira, E.A., Oliveira, O.B., 1992. U-Pb geochronology of Archean magmatism and Proterozoic metamorphism in the Quadrilátero Ferrífero, southern São Francisco Craton, Brazil. Geological Society of America Bulletin 104: 1221-1227.

de Souza Martins, B., Lobato, L.M., Rosière, C.A., Hagemann, S.G., Santos, J.O.S., dos Santos Peixoto Villanova, F.L., e Silva, R.C.F., de Ávila Lemos, L.H., 2016. The Archean BIF-hosted Lamego gold deposit, Rio das Velhas greenstone belt, Quadrilátero Ferrífero: Evidence for

Cambrian structural modification of an Archean orogenic gold deposit. Ore Geology Reviews 72: 963-988.

Morales, M.J., e Silva, R.C.F., Lobato, L.M., Gomes, S.D., Gomes, C.C.C.O., Banks, D.A., 2016. Metal source and fluid-rock interaction in the Archean BIF-hosted Lamego gold mineralization: Microthermometric and LA-ICP-MS analyses of fluid inclusions in quartz veins, Rio das Velhas greenstone belt, Brazil. Ore Geology Reviews 72: 510-531.

Noce, C.M., Zuccheti, M., Baltazar, O.F., Armstrong, R., Dantas, E., Renger, F.E., Lobato, L.M., 2005. Age of felsic volcanism and the role of ancient continental crust in the evolution of the Neoarchean Rio das Velhas Greenstone belt (Quadrilátero Ferrífero, Brazil): U-Pb zircon dating of volcaniclastic graywackes. Precambrian Research 141: 67-82.

Ohmoto, H., and Rye, R.O., 1979. Isotopes of sulfur and carbon, in Barnes, H.L., ed., Geochemistry of Hydrothermal Ore Deposits: New York, Wiley, p. 509-567.

Peterson, E.C., and Mavrogenes, J.A., 2014. Linking high-grade gold mineralization to earthquake-induced fault-valve processes in the Porgera gold deposit, Papua New Guinea. Geology 42: 383-386.

Ribeiro-Rodrigues, L.C., Oliveira, C.G., Friedrich, G., 2007. The Archean BIF-hosted Cuiabá Gold deposit, Quadrilátero Ferrífero, Minas Gerais, Brazil. Ore Geology Reviews 32: 543-570.

Romano, R., Lana, C., Alkmim, F.F., Stevens, G., Armstrong, R., 2013. Stabilization of the southern portion of the São Francisco craton, SE Brazil, through a long-lived period of potassic magmatism. Precambrian Research 224: 143-159.

Sales, M.A.S., 1998. The Geological Setting of the Lamego Banded Iron-Formation-Hosted Gold Deposit, Quadrilátero Ferrífero District, Minas Gerais – Brazil [Master's Thesis]: Kingston, Ontario, Canada, Queen's University, 182 p.

Selvaraja, V., Caruso, S., Fiorentini, M.L., LaFlamme, C.K., Bui, T.H., 2017. Atmospheric sulfur in the orogenic gold deposits of the Archean Yilgarn Craton, Australia. Geology 45: 691-694.

Steadman, J.A., Large, R.R., Meffre, S., Olin, P.H., Danyushevsky, L.V., Gregory, D.D., Belousov, I., Lounejeva, E., Ireland, T.R., Holden, P., 2015. Synsedimentary to Early Diagenetic Gold in Black Shale-Hosted Pyrite Nodules at the Golden Mile Deposit, Kalgoorlie, Western Australia. Economic Geology 110: 1157-1191.

Whitehouse, M.J., 2013. Multiple Sulfur Isotope Determination by SIMS: Evaluation of Reference Sulfides for $\Delta^{33}S$ with Observations and a Case Study on the Determination of $\Delta^{36}S$. Geostandards and Geoanalytical Research 37: 19-33.

Williford, K.H., Van Kranendonk, M.J., Ushikubo, T., Kozdon, R., Valley, J.W., 2011. Constraining atmospheric oxygen and seawater sulfate concentrations during Paleoproterozoic glaciation: In situ sulfur three-isotope microanalysis of pyrite from the Turee Cree Group, Western Australia. Geochimica et Cosmochimica Acta 75: 5686-5705.

Xavier, R.P., Toledo, C.L.B., Taylor, B., Schrank, A., 2000. Fluid evolution and gold deposition at the Cuiabá mine, SE Brazil: Fluid inclusions and stable isotope geochemistry of carbonates. *Revista* Brasileira de Geociências 30: 337-341.

Xue, Y., Campbell, I., Ireland, T.R., Holden, P., Armstrong, R., 2013. No mass-independent sulfur isotope fractionation in auriferous fluids supports a magmatic origin for Archean gold deposits. Geology 41: 791-794.

Table 6.5 Zoning types of pyrite in BIF- and smoky chert-hosted ores and associated multiple sulfur isotopic composition and gold abundance.

Zoning type	Pyrite in BIF-hosted ore			
	Zoning signatures	Pyrite generation(s)	$\delta^{34}S$-$\Delta^{33}S$ signatures	Abundance of Au and Se
A	Double-zoned.	3, 4	Both 3 and 4 have positive $\delta^{34}S$ and small magnitude of positive $\Delta^{33}S$.	
B	Triple-zoned. At the end of the first zones usually shows oscillatory zoning.	2, 3, 4	All of 2, 3, and 4 have positive $\delta^{34}S$ and small magnitude of positive $\Delta^{33}S$.	2 has the highest gold abundance, followed by 3, and 4 has the lowest gold abundance.
C	Quadruple-zoned. The first zones usually contain siderite and dolomite inclusions. The second zones are mostly oscillatory zoning.	1a, 2, 3, 4	1a has negative $\delta^{34}S$ and moderate magnitude of positive $\Delta^{33}S$, 2, 3, and 4 have positive $\delta^{34}S$ and small magnitude of positive $\Delta^{33}S$.	2 has the highest gold abundance, followed by 3 and 1a, and 4 has the lowest gold abundance. 1a has higher selenium abundance than 2, 3 and 4.
D	Double-zoned. The second zoning is oscillatory.	1b, 2	1b has positive $\delta^{34}S$ and high magnitude of positive $\Delta^{33}S$, 2 has positive $\delta^{34}S$ and small magnitude of positive $\Delta^{33}S$.	The laminae with blue etching color of 2 have higher gold abundance than those with orange etching color and 1b. The selenium content of 1b is similar to that of the orange laminae of

E	Oscillatory.	2	Both types of laminae have positive $\delta^{34}S$ and small magnitude of positive $\Delta^{33}S$.	2, but higher than that of the blue laminae of 2. The laminae with blue etching color have higher gold abundance and lower selenium content than those with orange etching color.
Zoning type	**Pyrite in smoky chert-hosted ore**			
	Zoning signatures	Pyrite generation(s)	$\delta^{34}S$-$\Delta^{33}S$ signatures	Abundance of Au and Se
F	Triple-zoned. The second zones are oscillatory zoning.	1b, 2, 3	1b, 2 and 3 have positive $\delta^{34}S$. 1b has high magnitude of positive $\Delta^{33}S$, 2 and 3 have small magnitude of positive $\Delta^{33}S$.	2 has the highest gold abundance, followed by 1b and 3. 1b has higher selenium content than 2 and 3.
G	Oscillatory.	2	Both types of laminae have positive $\delta^{34}S$ and small magnitude of positive $\Delta^{33}S$.	The laminae with blue etching color have higher gold abundance than those with orange etching color.

Table 6.6 Quadruple and triple sulphur isotopic compositions of pyrite in ores and wall rocks.

Title	Sample Code	Drill Core	Lithology and pyrite occurrence	Zoning type	Zone	Pyrite generation	$\delta^{33}S$/‰	1σ/‰	$\delta^{34}S$/‰	1σ/‰	$\delta^{36}S$/‰	1σ/‰	$\Delta^{33}S$/‰	1σ/‰	$\Delta^{36}S$/‰	1σ/‰	CPS/$^{32}S^-$	CPS/$^{33}S^-$	CPS/$^{34}S^-$	CPS/$^{36}S^-$
QF-4-3_3	MAS-33	FPL-122_634.6m	Quartz+carbonate+pyrite band of BIF-hosted ore			2 or 3	3.03	0.02	3.51	0.10	5.44	0.11	1.23	0.02	-1.23	0.11	1446546075	11404473	63574356	228451
QF-4-3_5	MAS-33	FPL-122_634.6m	Quartz+carbonate+pyrite band of BIF-hosted ore			3	1.80	0.01	2.81	0.09	4.70	0.08	0.36	0.01	-0.65	0.08	1420452850	11184812	62386861	224142
QF-4-3_1	MAS-33	FPL-122_634.6m	Quartz+carbonate+pyrite band of BIF-hosted ore			3 or 4	2.53	0.01	3.90	0.09	6.94	0.11	0.53	0.01	-0.48	0.11	1471697468	11596432	64709595	232853
QF-4-3_2	MAS-33	FPL-122_634.6m	Quartz+carbonate+pyrite band of BIF-hosted ore			4	2.59	0.01	3.65	0.07	6.61	0.08	0.72	0.01	-0.33	0.08	1475237859	11626456	64854432	233330
QF-4-3_4	MAS-33	FPL-122_634.6m	Quartz+carbonate+pyrite band of BIF-hosted ore			3 or 4	2.37	0.01	3.58	0.09	5.76	0.09	0.53	0.01	-1.06	0.10	1418482980	11176181	62350070	223952
QF-4-3_6	MAS-33	FPL-122_634.6m	Quartz+carbonate+pyrite band of BIF-hosted ore			4	2.43	0.02	3.58	0.05	6.54	0.08	0.59	0.02	-0.27	0.08	1502265757	11836663	66032785	237461
QF-2-2_30	MAS-33	FPL-122_634.6m	Quartz+carbonate+pyrite band of BIF-hosted ore			3	2.18	0.02	3.35	0.04	5.82	0.10	0.45	0.02	-0.56	0.10	1770860326	13950440	77787928	280008
QF-2-2_3	MAS-33	FPL-122_634.6m	Quartz+carbonate+pyrite band of BIF-hosted ore			3 or 4	2.52	0.01	3.79	0.03	6.74	0.11	0.57	0.01	-0.48	0.10	1620798587	12772300	71225342	256296
QF-2-2_16	MAS-33	FPL-122_634.6m	Quartz+carbonate+pyrite band of BIF-hosted ore			4	1.97	0.02	2.80	0.05	4.71	0.09	0.53	0.02	-0.62	0.10	1612247081	12698301	70782643	254371
QF-2-2_26	MAS-33	FPL-122_634.6m	Quartz+carbonate+pyrite band of BIF-hosted ore			3 or 4	2.77	0.02	3.87	0.08	7.28	0.14	0.78	0.02	-0.08	0.13	1578839368	12447650	69404910	249739
QF-2-2_27	MAS-33	FPL-122_634.6m	Quartz+carbonate+pyrite band of BIF-hosted ore			3 or 4	2.80	0.01	4.13	0.05	7.82	0.09	0.68	0.01	-0.04	0.09	1578198443	12441325	69371618	249883
QF-2-2_29	MAS-33	FPL-122_634.6m	Quartz+carbonate+pyrite band of BIF-hosted ore			3 or 4	1.88	0.02	2.81	0.07	5.34	0.10	0.44	0.02	-0.02	0.10	1573810235	12395361	69106268	248520
QF-3-3_1	MAS-33	FPL-122_634.6m	Pyrite band of BIF-hosted ore			2 or 3	1.80	0.01	2.78	0.03	5.09	0.10	0.38	0.01	-0.19	0.11	1702597405	13408708	74766590	268967
QF-2-5_5	MAS-33	FPL-122_634.6m	Pyrite band of BIF-hosted ore			3 or 4	2.54	0.01	4.12	0.05	7.69	0.11	0.42	0.01	-0.15	0.12	1670940083	13170035	73447350	264668
QF-2-5_6	MAS-33	FPL-122_634.6m	Pyrite band of BIF-hosted ore			3 or 4	2.43	0.01	3.52	0.05	6.35	0.08	0.62	0.01	-0.35	0.08	1659469068	13076114	72903186	262465
QF-2-5_9	MAS-33	FPL-122_634.6m	Pyrite band of BIF-hosted ore			2 or 3	3.18	0.01	4.73	0.03	8.46	0.09	0.75	0.01	-0.54	0.09	1729335195	13636738	76074316	274031
QF-2-5_3	MAS-33	FPL-122_634.6m	Pyrite band of BIF-hosted ore			3	2.25	0.01	3.40	0.04	6.04	0.08	0.50	0.01	-0.43	0.08	1723693779	13579028	75716908	272338
QF-2-5_4	MAS-	FPL-	Pyrite band of BIF-hosted ore			3	2.74	0.02	4.02	0.05	7.39	0.13	0.67	0.02	-0.26	0.13	1730806938	13641808	76068926	273780

Title	Sample Code	Drill Core	Lithology and pyrite occurrence	Zoning type	Zone	Pyrite generation	$\delta^{33}S$/‰	1σ/‰	$\delta^{34}S$/‰	1σ/‰	$\delta^{36}S$/‰	1σ/‰	$\Delta^{33}S$/‰	1σ/‰	$\Delta^{36}S$/‰	1σ/‰	CPS/$^{32}S^-$	CPS/$^{33}S^-$	CPS/$^{34}S^-$	CPS/$^{36}S^-$
	33	122_634.6m																		
QF-2-5_7	MAS-33	FPL-122_634.6m	Pyrite band of BIF-hosted ore			3 or 4	2.11	0.01	3.09	0.05	5.84	0.11	0.52	0.01	-0.04	0.11	1605510613	12646094	70507397	253644
QF-2-1_3	MAS-33	FPL-122_634.6m	Pyrite band of BIF-hosted ore			2 or 3	2.11	0.01	3.16	0.04	5.68	0.11	0.48	0.02	-0.32	0.11	1719358775	13545817	75534193	271638
QF-2-5_8	MAS-33	FPL-122_634.6m	Pyrite band of BIF-hosted ore			3 or 4	2.39	0.01	3.59	0.04	6.70	0.10	0.55	0.01	-0.13	0.10	1696033592	13363727	74525371	268307
QF-2-1_2	MAS-33	FPL-122_634.6m	Pyrite band of BIF-hosted ore			4	2.21	0.02	3.68	0.04	6.12	0.11	0.32	0.02	-0.88	0.12	1615516081	12727397	70990405	255262
QF-2-1_5	MAS-33	FPL-122_634.6m	Pyrite band of BIF-hosted ore			4	2.13	0.01	3.32	0.03	5.75	0.12	0.42	0.01	-0.58	0.12	1646678213	12969597	72325054	260367
QF-2-5_11	MAS-33	FPL-122_634.6m	Pyrite band of BIF-hosted ore			3 or 4	1.44	0.01	2.25	0.04	4.10	0.10	0.28	0.01	-0.18	0.10	1720202380	13540950	75484872	271519
QF-3-3_4	MAS-33	FPL-122_634.6m	Pyrite band of BIF-hosted ore			3 or 4	2.72	0.01	4.08	0.04	6.84	0.08	0.62	0.01	-0.93	0.09	1666929175	13138354	73293351	263689
TE18_3	MAS-44	FPL-122_599.0m	Pyrite band of BIF-hosted ore			3 or 4	2.02	0.02	3.15	0.08	5.55	0.16	0.40	0.02	-0.44	0.16	1516159951	11922208	66461503	226107
MAS-44-1	MAS-44	FPL-122_599.0m	Pyrite band of BIF-hosted ore			3 or 4	2.07	0.01	3.17	0.08	6.28	0.18	0.43	0.01	0.25	0.19	2450011195	19371501	108763638	444106
MAS-44-2	MAS-44	FPL-122_599.0m	Pyrite band of BIF-hosted ore			3 or 4	2.32	0.01	3.34	0.09	6.21	0.14	0.60	0.01	-0.14	0.16	2420635285	19140429	107458634	438591
MAS-44-3	MAS-44	FPL-122_599.0m	Pyrite band of BIF-hosted ore			3 or 4	2.04	0.01	3.04	0.15	5.25	0.24	0.48	0.01	-0.52	0.24	2391698562	18911548	106181344	433539
MAS-44-4	MAS-44	FPL-122_599.0m	Pyrite band of BIF-hosted ore			3 or 4	1.70	0.01	2.30	0.11	3.86	0.24	0.52	0.02	-0.51	0.43	2350432473	18571668	104232689	423955
QF-3-1_4	MAS-50	FPL-122_623.6m	Pyrite band of BIF-hosted ore			2 or 3	2.12	0.01	3.51	0.04	6.34	0.11	0.31	0.01	-0.33	0.11	1755096288	13824702	77122099	277752
QF-3-1_5	MAS-50	FPL-122_623.6m	Pyrite band of BIF-hosted ore			2 or 3	2.08	0.01	3.50	0.05	6.27	0.12	0.28	0.01	-0.40	0.11	1635664676	12885452	71888866	258411
QF-3-2_8_	MAS-50	FPL-122_623.6m	Pyrite band of BIF-hosted ore			3	2.41	0.02	3.39	0.06	6.14	0.11	0.66	0.02	-0.30	0.12	1550440522	12216430	68130756	244894
QF-3-2_9_	MAS-50	FPL-122_623.6m	Pyrite band of BIF-hosted ore			3	2.23	0.02	3.04	0.05	5.75	0.09	0.66	0.02	-0.03	0.09	1558454526	12277533	68465905	246301
QF-3-2_10_	MAS-50	FPL-122_623.6m	Pyrite band of BIF-hosted ore			3	2.20	0.02	3.12	0.05	5.54	0.09	0.59	0.02	-0.39	0.09	1611016137	12692157	70782321	254413
QF-3-1_12_	MAS-50	FPL-122_623.6m	Pyrite band of BIF-hosted ore			3	2.69	0.02	3.39	0.05	6.01	0.09	0.94	0.02	-0.45	0.09	1622182480	12784338	71283608	256094

Title	Sample Code	Drill Core	Lithology and pyrite occurrence	Zoning type	Zone	Pyrite generation	$\delta^{33}S$/‰	1σ/‰	$\delta^{34}S$/‰	1σ/‰	$\delta^{36}S$/‰	1σ/‰	$\Delta^{33}S$/‰	1σ/‰	$\Delta^{36}S$/‰	1σ/‰	CPS/$^{32}S^-$	CPS/$^{33}S^-$	CPS/$^{34}S^-$	CPS/$^{36}S^-$
QF-3-1_9	MAS-50	FPL-122_623.6m	Pyrite band of BIF-hosted ore			3	3.27	0.01	3.97	0.04	6.24	0.12	1.23	0.01	-1.32	0.11	1615744500	12743367	71047657	255495
QF-3-1_3	MAS-50	FPL-122_623.6m	Pyrite band of BIF-hosted ore			3 or 4	2.40	0.02	3.48	0.06	5.89	0.13	0.61	0.02	-0.74	0.12	1582974961	12474576	69580760	250396
QF-3-2_6_	MAS-50	FPL-122_623.6m	Pyrite band of BIF-hosted ore			3 or 4	2.79	0.01	4.16	0.05	7.83	0.09	0.65	0.01	-0.10	0.09	1601624578	12624807	70425867	253698
QF-3-1_11_	MAS-50	FPL-122_623.6m	Pyrite band of BIF-hosted ore			4	2.43	0.01	3.52	0.06	6.52	0.10	0.62	0.01	-0.17	0.10	1575597384	12416581	69256568	249155
QF-3-1_1	MAS-50	FPL-122_623.6m	Pyrite band of BIF-hosted ore			3 or 4	2.23	0.02	3.14	0.07	5.51	0.10	0.62	0.02	-0.46	0.08	1487298090	11717084	65342056	235067
QF-3-1_2	MAS-50	FPL-122_623.6m	Pyrite band of BIF-hosted ore			3 or 4	2.18	0.02	3.01	0.05	5.22	0.11	0.63	0.02	-0.50	0.11	1470416120	11583265	64596729	232281
QF-3-1_8	MAS-50	FPL-122_623.6m	Pyrite band of BIF-hosted ore			4	2.20	0.01	3.08	0.03	5.07	0.10	0.62	0.01	-0.78	0.10	1542599929	12153102	67769845	243748
QF-3-5_2	MAS-50	FPL-122_623.6m	Quartz+carbonate+pyrite band of BIF-hosted ore			2	2.62	0.02	3.33	0.04	5.17	0.10	0.90	0.02	-1.17	0.10	1590712855	12536231	69888125	251286
QF-3-5_5	MAS-50	FPL-122_623.6m	Quartz+carbonate+pyrite band of BIF-hosted ore			2 or 3	2.07	0.02	3.15	0.04	5.18	0.07	0.45	0.02	-0.81	0.07	1664242492	13109886	73119281	262892
QF-3-5_6	MAS-50	FPL-122_623.6m	Quartz+carbonate+pyrite band of BIF-hosted ore			2 or 3	1.81	0.01	2.61	0.03	4.35	0.13	0.46	0.01	-0.61	0.12	1613292224	12704264	70829645	254680
QF-3-4_4	MAS-50	FPL-122_623.6m	Quartz+carbonate+pyrite band of BIF-hosted ore			3	1.80	0.01	2.67	0.04	4.81	0.09	0.43	0.01	-0.26	0.08	1667340195	13130857	73226160	263305
MAS-50-1	MAS-50	FPL-122_623.6m	Quartz+carbonate+pyrite band of BIF-hosted ore			3 or 4	2.44	0.01	3.83	0.07	7.50	0.21	0.46	0.01	0.20	0.17	2236121537	17686515	99340746	405635
QF-3-5_4	MAS-50	FPL-122_623.6m	Quartz+carbonate+pyrite band of BIF-hosted ore			2 or 3	1.59	0.01	2.40	0.05	4.47	0.11	0.35	0.01	-0.10	0.11	1617794731	12737348	71021710	255419
QF-3-4_11	MAS-50	FPL-122_623.6m	Quartz+carbonate+pyrite band of BIF-hosted ore			4	2.18	0.01	3.09	0.05	5.44	0.08	0.59	0.01	-0.44	0.09	1591918545	12540942	69937622	251689
QF-3-5_3	MAS-50	FPL-122_623.6m	Quartz+carbonate+pyrite band of BIF-hosted ore			4	2.33	0.01	3.73	0.06	6.48	0.09	0.41	0.01	-0.62	0.09	1586168003	12498541	69736704	250896
QF-3-4_7	MAS-50	FPL-122_623.6m	Quartz+carbonate+pyrite band of BIF-hosted ore			3	2.19	0.01	2.89	0.05	4.99	0.11	0.70	0.01	-0.52	0.11	1684730047	13273613	73998331	265923
QF-3-4_6						4	2.05	0.01	2.99	0.04	5.33	0.09	0.51	0.01	-0.36	0.09	1633480042	12868052	71758699	258122
QF-3-4_1						2 or 3	1.72	0.01	2.06	0.05	3.57	0.10	0.66	0.01	-0.35	0.10	1529009279	12039800	67090945	241054
QF-3-4_2	MAS-50	FPL-122_623.6m	Quartz+carbonate+pyrite band of BIF-hosted ore			2 or 3	1.99	0.02	2.42	0.05	3.94	0.10	0.75	0.01	-0.66	0.10	1532364225	12069835	67281338	241803
QF-3-4_3						2 or 3	1.91	0.01	2.43	0.05	3.72	0.12	0.66	0.01	-0.91	0.12	1582268230	12462916	69467218	249673

Title	Sample Code	Drill Core	Lithology and pyrite occurrence	Zoning type	Zone	Pyrite generation	$\delta^{33}S$/‰	1σ/‰	$\delta^{34}S$/‰	1σ/‰	$\delta^{36}S$/‰	1σ/‰	$\Delta^{33}S$/‰	1σ/‰	$\Delta^{36}S$/‰	1σ/‰	CPS/$^{32}S^-$	CPS/$^{33}S^-$	CPS/$^{34}S^-$	CPS/$^{36}S^-$
QF-1-1_1	MAS-8	FPL-122_598.0m	Quartz+carbonate+pyrite band of BIF-hosted ore			3	1.96	0.02	2.81	0.05	5.18	0.10	0.52	0.02	-0.17	0.10	1518858161	11971181	66774255	240469
QF-1-1_7	MAS-8	FPL-122_598.0m	Quartz+carbonate+pyrite band of BIF-hosted ore			3	2.16	0.02	3.12	0.03	5.44	0.11	0.56	0.02	-0.50	0.11	1505025917	11862356	66177435	238383
QF-1-1_9	MAS-8	FPL-122_598.0m	Quartz+carbonate+pyrite band of BIF-hosted ore			3	2.44	0.02	3.79	0.02	6.35	0.11	0.49	0.02	-0.87	0.10	1602697286	12634574	70512278	253883
QF-1-1_10	MAS-8	FPL-122_598.0m	Quartz+carbonate+pyrite band of BIF-hosted ore			3	2.17	0.02	3.29	0.03	5.90	0.10	0.48	0.02	-0.36	0.10	1590106787	12535157	69926695	251707
QF-1-4_5	MAS-8	FPL-122_598.0m	Quartz+carbonate+pyrite band of BIF-hosted ore			3	1.54	0.02	2.44	0.04	4.24	0.13	0.28	0.02	-0.41	0.13	1561890265	12303167	68637416	246986
QF-1-4_8	MAS-8	FPL-122_598.0m	Quartz+carbonate+pyrite band of BIF-hosted ore			3	2.44	0.02	3.46	0.07	6.16	0.10	0.65	0.02	-0.43	0.10	1530468213	12067898	67305853	242440
QF-1-4_11	MAS-8	FPL-122_598.0m	Quartz+carbonate+pyrite band of BIF-hosted ore			3	1.92	0.02	2.79	0.04	5.25	0.10	0.49	0.02	-0.06	0.11	1496468467	11793750	65783164	236743
QF-1-1_2	MAS-8	FPL-122_598.0m	Quartz+carbonate+pyrite band of BIF-hosted ore			4	2.41	0.02	3.65	0.05	6.22	0.12	0.53	0.02	-0.72	0.12	1538271698	12129371	67687573	243727
QF-1-1_3	MAS-8	FPL-122_598.0m	Quartz+carbonate+pyrite band of BIF-hosted ore			4	2.22	0.01	3.31	0.03	5.99	0.10	0.52	0.01	-0.31	0.10	1544662340	12175323	67921803	244787
QF-1-1_5	MAS-8	FPL-122_598.0m	Quartz+carbonate+pyrite band of BIF-hosted ore			4	2.37	0.02	3.39	0.04	6.03	0.10	0.63	0.02	-0.42	0.10	1482948134	11691668	65222835	234948
QF-1-1_6	MAS-8	FPL-122_598.0m	Quartz+carbonate+pyrite band of BIF-hosted ore			4	2.33	0.02	3.22	0.07	5.70	0.10	0.67	0.02	-0.44	0.11	1466000368	11557012	64465974	232188
QF-1-1_11	MAS-8	FPL-122_598.0m	Quartz+carbonate+pyrite band of BIF-hosted ore			4	2.28	0.02	3.40	0.04	6.00	0.11	0.53	0.02	-0.48	0.12	1546005138	12187946	67977502	244861
QF-1-1_12	MAS-8	FPL-122_598.0m	Quartz+carbonate+pyrite band of BIF-hosted ore			4	1.68	0.02	2.42	0.04	4.19	0.12	0.44	0.02	-0.40	0.12	1571878573	12386542	69072998	248502
QF-1-1_13	MAS-8	FPL-122_598.0m	Quartz+carbonate+pyrite band of BIF-hosted ore			4	1.82	0.01	2.67	0.05	4.63	0.09	0.44	0.01	-0.46	0.09	1575591817	12416656	69252137	249201
QF-1-4_2	MAS-8	FPL-122_598.0m	Quartz+carbonate+pyrite band of BIF-hosted ore			4	2.29	0.02	3.32	0.05	6.14	0.08	0.58	0.02	-0.18	0.08	1511653751	11917404	66486018	239565
QF-1-4_6	MAS-8	FPL-122_598.0m	Quartz+carbonate+pyrite band of BIF-hosted ore			3	2.53	0.02	3.54	0.06	6.07	0.08	0.70	0.02	-0.67	0.08	1492996665	11771833	65668726	236462
QF-1-4_9	MAS-8	FPL-122_598.0m	Quartz+carbonate+pyrite band of BIF-hosted ore			4	2.23	0.02	3.21	0.08	6.00	0.13	0.58	0.02	-0.10	0.12	1510961942	11912743	66449672	239186
QF-1-2_1	MAS-8	FPL-122_598.0m	Pyrite band of BIF-hosted ore			1a	-0.53	0.02	-6.43	0.05	-14.89	0.11	2.78	0.02	-2.71	0.10	1635526528	12857858	71239071	253366
QF-1-2_11						1a	-1.07	0.01	-7.19	0.03	-16.42	0.09	2.64	0.01	-2.81	0.10	1609003532	12642553	70019759	249039

Title	Sample Code	Drill Core	Lithology and pyrite occurrence	Zoning type	Zone	Pyrite generation	$\delta^{33}S$/‰	1σ/‰	$\delta^{34}S$/‰	1σ/‰	$\delta^{36}S$/‰	1σ/‰	$\Delta^{33}S$/‰	1σ/‰	$\Delta^{36}S$/‰	1σ/‰	CPS/$^{32}S^-$	CPS/$^{33}S^-$	CPS/$^{34}S^-$	CPS/$^{36}S^-$
QF-1-2_2						3	2.04	0.02	2.79	0.05	5.16	0.10	0.61	0.02	-0.14	0.10	1516324303	11952121	66643424	239829
QF-1-2_17						4	2.45	0.02	3.42	0.06	6.51	0.13	0.69	0.02	-0.01	0.14	1511754379	11919585	66479482	239654
QF-1-2_5	MAS-8	FPL-122_598.0m	Pyrite band of BIF-hosted ore			3	2.57	0.01	3.61	0.04	6.49	0.11	0.71	0.01	-0.39	0.11	1542855173	12167330	67888812	244496
QF-1-2_12	MAS-8	FPL-122_598.0m	Pyrite band of BIF-hosted ore			3	2.06	0.01	2.89	0.05	5.10	0.12	0.57	0.01	-0.40	0.12	1517681017	11960860	66712091	240032
QF-1-2_13	MAS-8	FPL-122_598.0m	Pyrite band of BIF-hosted ore			3	2.10	0.02	2.98	0.06	5.40	0.11	0.56	0.02	-0.27	0.11	1495370950	11786836	65738475	236879
QF-1-2_14	MAS-8	FPL-122_598.0m	Pyrite band of BIF-hosted ore			3 or 4	2.37	0.01	3.20	0.02	5.76	0.09	0.72	0.01	-0.33	0.10	1561168507	12308250	68642142	247219
MAS-8.5	MAS-8	FPL-122_598.0m	Pyrite band of BIF-hosted ore			3	2.01	0.01	3.16	0.05	6.12	0.24	0.38	0.01	0.11	0.25	1421590769	11242676	63183439	258024
MAS-8.6	MAS-8	FPL-122_598.0m	Pyrite band of BIF-hosted ore			3	2.05	0.02	3.43	0.09	6.73	0.21	0.28	0.02	0.20	0.22	1370508205	10839473	60928855	248542
MAS-8-8	MAS-8	FPL-122_598.0m	Pyrite band of BIF-hosted ore			3	1.82	0.01	3.05	0.07	5.61	0.16	0.25	0.01	-0.20	0.18	1388879267	10980683	61716660	251643
MAS-8-10	MAS-8	FPL-122_598.0m	Pyrite band of BIF-hosted ore			3	2.22	0.02	3.41	0.07	6.37	0.23	0.47	0.02	-0.12	0.22	1315316571	10404649	58472726	238765
QF-1-2_6	MAS-8	FPL-122_598.0m	Pyrite band of BIF-hosted ore			3 or 4	2.42	0.02	3.65	0.08	6.31	0.06	0.54	0.01	-0.63	0.09	1491491413	11759610	65611664	236290
QF-1-2_7	MAS-8	FPL-122_598.0m	Pyrite band of BIF-hosted ore			4	2.22	0.01	3.21	0.07	5.67	0.10	0.57	0.01	-0.44	0.10	1447390972	11410901	63652366	229166
QF-1-2_9	MAS-8	FPL-122_598.0m	Pyrite band of BIF-hosted ore			3 or 4	2.23	0.02	3.18	0.08	5.59	0.09	0.60	0.02	-0.46	0.10	1482426399	11685825	65181846	234658
QF-1-2_10	MAS-8	FPL-122_598.0m	Pyrite band of BIF-hosted ore			3 or 4	1.94	0.01	2.99	0.06	5.39	0.12	0.40	0.01	-0.30	0.12	1511896431	11915039	66466432	239430
QF-1-2_15	MAS-8	FPL-122_598.0m	Pyrite band of BIF-hosted ore			4	2.21	0.02	2.93	0.05	5.44	0.11	0.70	0.02	-0.13	0.12	1448135010	11415617	63658569	229385
QF-1-2_16	MAS-8	FPL-122_598.0m	Pyrite band of BIF-hosted ore			4	2.30	0.02	3.37	0.06	5.91	0.11	0.57	0.02	-0.49	0.11	1524164313	12015314	67033936	241309
T10-5	MAS-8	FPL-122_598.0m	Pyrite band of BIF-hosted ore			2	1.87	0.01	2.80	0.02	3.95	0.13	0.43	0.01	-1.37	0.14	1516146844	11927498	66790415	227394
T10-6						3	2.26	0.02	3.27	0.05	5.82	0.11	0.58	0.02	-0.40	0.11	1535130940	12082642	67674593	230673
T10-8	MAS-8	FPL-122_598.0m	Pyrite band of BIF-hosted ore			2	2.20	0.02	3.53	0.04	7.88	0.11	0.38	0.02	1.16	0.11	1495792063	11773580	65956911	225129
T10-9						2 or 3	1.91	0.03	3.11	0.07	6.34	0.12	0.31	0.02	0.42	0.12	1514417547	11918381	66765733	227988

Title	Sample Code	Drill Core	Lithology and pyrite occurrence	Zoning type	Zone	Pyrite generation	$\delta^{33}S$/‰	1σ/‰	$\delta^{34}S$/‰	1σ/‰	$\delta^{36}S$/‰	1σ/‰	$\Delta^{33}S$/‰	1σ/‰	$\Delta^{36}S$/‰	1σ/‰	CPS/$^{32}S^-$	CPS/$^{33}S^-$	CPS/$^{34}S^-$	CPS/$^{36}S^-$
T10-11						1a	-0.46	0.02	-5.79	0.06	-14.30	0.14	2.53	0.02	-3.32	0.13	1596326592	12531811	69731302	234843
T10-12	MAS-8	FPL-122_598.0m	Pyrite band of BIF-hosted ore			2	2.05	0.01	3.01	0.07	4.50	0.13	0.50	0.01	-1.23	0.14	1514356180	11918783	66755831	227229
T10-13						3	1.63	0.01	2.39	0.05	4.10	0.12	0.41	0.01	-0.45	0.13	1471982001	11579915	64832539	220862
MAS-8.1	MAS-8	FPL-122_598.0m	Pyrite band of BIF-hosted ore			3	2.74	0.02	4.06	0.08	7.49	0.22	0.65	0.02	-0.23	0.24	1453931262	11504154	64678043	264018
MAS-8.2						4	2.32	0.02	3.68	0.08	6.85	0.15	0.43	0.02	-0.14	0.15	1396478582	11047468	62097040	253393
MAS-8.3	MAS-8	FPL-122_598.0m	Pyrite band of BIF-hosted ore			3	1.76	0.02	2.78	0.07	5.07	0.21	0.33	0.02	-0.22	0.21	1328454855	10503648	59018562	240773
MAS-8.4						4	2.39	0.02	3.81	0.07	6.96	0.17	0.43	0.02	-0.29	0.17	1319887095	10439902	58697885	239829
TE18_7	MAS-26	FPL-120_656.2m	Quartz+carbonate+pyrite veinlet crosscutting BIF			3 or 4	2.83	0.02	3.47	0.09	5.88	0.14	1.04	0.02	-0.72	0.15	1452422212	11433629	63684581	216267
TE18_11	MAS-26	FPL-120_656.2m	Quartz+carbonate+pyrite veinlet crosscutting BIF			3 or 4	3.17	0.02	3.65	0.08	5.90	0.16	1.29	0.02	-1.05	0.15	1527348789	12022981	66961424	227568
TE18_12							2.65	0.02	3.22	0.06	5.34	0.12	0.99	0.02	-0.78	0.13	1523524900	11991316	66788575	226789
MAS-25-2_1	MAS-25	FPL-120_639.2m	Quartz+carbonate+pyrite veinlet crosscutting BIF			3	1.77	0.02	2.27	0.07	3.37	0.24	0.60	0.02	-0.94	0.27	974797645	7706225	43275596	176156
MAS-25-2_3	MAS-25	FPL-120_639.2m	Quartz+carbonate+pyrite veinlet crosscutting BIF			3	2.86	0.02	3.35	0.11	4.45	0.41	1.14	0.02	-1.93	0.37	762013810	6029607	33863858	137804
MAS-25-2_2	MAS-25	FPL-120_639.2m	Quartz+carbonate+pyrite veinlet crosscutting BIF			4	1.68	0.02	2.17	0.09	2.87	0.23	0.57	0.02	-1.25	0.29	889432481	7029420	39482237	161156
MAS-25-1_2						3 or 4	1.81	0.02	2.96	0.09	4.94	0.23	0.29	0.02	-0.69	0.21	1143306785	9037877	50789862	207046
MAS-25-1_1						3 or 4	2.80	0.01	2.81	0.09	3.77	0.26	1.35	0.01	-1.57	0.26	1213495274	9602296	53899943	219644
TE18_4	MAS-25	FPL-120_639.2m	Quartz+carbonate+pyrite veinlet crosscutting BIF			3 or 4	2.75	0.03	2.67	0.07	4.14	0.14	1.37	0.03	-0.95	0.15	1570203902	12361859	68823866	233768
TE18_5						2	3.17	0.02	3.39	0.08	5.51	0.14	1.43	0.02	-0.94	0.13	1539946730	12125535	67507448	229137
TE18_6						3 or 4	3.28	0.02	4.10	0.09	7.43	0.13	1.18	0.02	-0.36	0.14	1573553296	12390518	69030437	234605
TE18_10						3 or 4	2.80	0.03	3.18	0.08	5.21	0.18	1.16	0.02	-0.84	0.18	1539664192	12122141	67513984	229199
LQ-6	LQ	Queimada	Pyrite band of BIF-hosted ore (arsenopyrite-rich)			3	2.39	0.01	3.31	0.12	5.36	0.17	0.68	0.01	-0.94	0.22	2095482070	16570223	93015060	379010
LQ-1						3	1.80	0.01	1.88	0.24	2.78	0.17	0.83	0.01	-0.79	0.17	2247662330	17761440	99598878	405371
LQ-2	LQ	Queimada	Pyrite band of BIF-hosted ore (arsenopyrite-rich)			3	2.63	0.01	3.83	0.11	7.20	0.18	0.66	0.01	-0.09	0.17	2425061473	19183140	107720282	439716
LQ-3						3	2.16	0.01	2.90	0.09	5.13	0.17	0.67	0.01	-0.38	0.20	2238523487	17700795	99351771	404740
LQ-4						3	2.50	0.01	3.57	0.11	6.31	0.17	0.66	0.01	-0.49	0.16	2419686641	19136079	107442256	438550
FLV-167-1	FLV-	FLV-	Pyrite band of BIF-hosted ore			3 or 4	1.31	0.01	1.97	0.09	3.69	0.17	0.30	0.01	-0.06	0.17	2462107785	19446470	109131566	444640

Title	Sample Code	Drill Core	Lithology and pyrite occurrence	Zoning type	Zone	Pyrite generation	$\delta^{33}S$/‰	1σ/‰	$\delta^{34}S$/‰	1σ/‰	$\delta^{36}S$/‰	1σ/‰	$\Delta^{33}S$/‰	1σ/‰	$\Delta^{36}S$/‰	1σ/‰	CPS/$^{32}S^-$	CPS/$^{33}S^-$	CPS/$^{34}S^-$	CPS/$^{36}S^-$
	167	167_225m	(arsenopyrite-rich)																	
FLV-167-2	FLV-167	FLV-167_225m	Pyrite band of BIF-hosted ore (arsenopyrite-rich)			3 or 4	2.04	0.01	3.34	0.12	6.14	0.14	0.32	0.01	-0.22	0.18	2525587105	19969337	112146952	458210
FLV-167-3	FLV-167	FLV-167_225m	Pyrite band of BIF-hosted ore (arsenopyrite-rich)			3 or 4	1.35	0.01	2.03	0.06	4.01	0.17	0.30	0.01	0.14	0.18	2491554768	19686591	110483943	450068
QF-1-3_1	MAS-57	FLU-173	Disseminated fine-grained euhedral to subhedral pyrite in smoky chert-hosted ore			1b	8.33	0.01	6.99	0.02	8.01	0.09	4.74	0.02	-5.31	0.10	1538610497	12201308	67908052	244066
QF-1-3_2	MAS-57	FLU-173	Disseminated fine-grained euhedral to subhedral pyrite in smoky chert-hosted ore			1b	7.90	0.01	6.81	0.03	8.29	0.11	4.40	0.01	-4.69	0.11	1504812981	11929876	66412980	239016
QF-1-3_3	MAS-57	FLU-173	Disseminated fine-grained euhedral to subhedral pyrite in smoky chert-hosted ore			1b	8.43	0.01	7.46	0.05	9.17	0.11	4.60	0.01	-5.04	0.11	1398429584	11091762	61757702	222280
QF-1-3_4	MAS-57	FLU-173	Disseminated fine-grained euhedral to subhedral pyrite in smoky chert-hosted ore			1b	8.58	0.02	6.75	0.06	8.18	0.09	5.11	0.02	-4.69	0.10	1498788856	11889567	66139876	237972
QF-1-3_5	MAS-57	FLU-173	Disseminated fine-grained euhedral to subhedral pyrite in smoky chert-hosted ore			1b	8.31	0.01	6.74	0.05	8.45	0.11	4.85	0.01	-4.39	0.12	1497775849	11879918	66087256	237748
QF-1-3_6	MAS-57	FLU-173	Disseminated fine-grained euhedral to subhedral pyrite in smoky chert-hosted ore			1b	8.42	0.02	6.87	0.07	8.88	0.12	4.88	0.02	-4.22	0.14	1502000462	11912578	66293288	238539
QF-1-3_7	MAS-57	FLU-173	Disseminated fine-grained euhedral to subhedral pyrite in smoky chert-hosted ore			1b	7.91	0.01	6.63	0.06	8.40	0.11	4.50	0.02	-4.24	0.10	1497499500	11871355	66078978	237909
QF-1-3_9	MAS-57	FLU-173	Disseminated fine-grained euhedral to subhedral pyrite in smoky chert-hosted ore			1b	8.32	0.01	6.81	0.04	9.10	0.13	4.81	0.02	-3.87	0.12	1523398000	12081899	67232904	242111
TE18_8	MAS-57	FLU-173	Disseminated fine-grained euhedral to subhedral pyrite in smoky chert-hosted ore			1b	7.75	0.01	6.74	0.06	9.48	0.12	4.29	0.02	-3.35	0.13	1529052069	12097365	67275795	228340
TE18_9	MAS-57	FLU-173	Disseminated fine-grained euhedral to subhedral pyrite in smoky chert-hosted ore			1b	7.81	0.02	6.38	0.04	8.61	0.15	4.52	0.02	-3.55	0.16	1445969813	11444161	63636128	215866
MAS-57-1	MAS-57	FLU-173	Pyrite in smoky chert-hosted ore			3	3.82	0.01	5.24	0.07	9.39	0.20	1.13	0.01	-0.60	0.21	2003181617	15881568	89325268	365342
MAS-57-5	MAS-57	FLU-173	Pyrite in smoky chert-hosted ore			3	3.91	0.01	5.30	0.07	9.34	0.17	1.18	0.01	-0.75	0.18	1955669996	15503849	87215222	356590
MAS-57-3	MAS-	FLU-173	Pyrite in smoky chert-hosted ore			3 or 4	4.02	0.01	5.49	0.09	10.07	0.17	1.20	0.01	-0.38	0.19	2000437097	15863185	89228477	365954

Title	Sample Code	Drill Core	Lithology and pyrite occurrence	Zoning type	Zone	Pyrite generation	$\delta^{33}S$/‰	1σ/‰	$\delta^{34}S$/‰	1σ/‰	$\delta^{36}S$/‰	1σ/‰	$\Delta^{33}S$/‰	1σ/‰	$\Delta^{36}S$/‰	1σ/‰	CPS/$^{32}S^-$	CPS/$^{33}S^-$	CPS/$^{34}S^-$	CPS/$^{36}S^-$
MAS-57-3_3	MAS-57	FLU-173	Pyrite in smoky chert-hosted ore			2	2.56	0.01	3.94	0.06	6.71	0.19	0.53	0.01	-0.80	0.20	1233206228	9756716	54837995	223787
MAS-57-3_7	MAS-57	FLU-173	Pyrite in smoky chert-hosted ore			2	2.64	0.02	3.70	0.11	6.47	0.21	0.74	0.02	-0.57	0.23	1084252986	8579223	48204811	196530
MAS-37-8	MAS-57	FLU-173	Pyrite in smoky chert-hosted ore			3 or 4	2.97	0.01	4.13	0.09	7.37	0.16	0.84	0.01	-0.49	0.18	1884679869	14928357	83949045	343760
MAS-37-1	MAS-57	FLU-173	Pyrite in smoky chert-hosted ore			2	2.37	0.02	3.47	0.09	6.48	0.17	0.59	0.02	-0.11	0.17	1993910232	15784702	88759087	362714
MAS-37-2						3 or 4	3.75	0.01	5.35	0.07	9.87	0.19	1.00	0.01	-0.32	0.22	1966962459	15594148	87723715	359108
MAS-37-5	MAS-57	FLU-173	Pyrite in smoky chert-hosted ore			2	1.26	0.01	1.30	0.08	1.97	0.17	0.59	0.01	-0.50	0.19	1852816695	14651580	82290362	335524
MAS-37-6						3 or 4	2.73	0.01	3.68	0.09	6.60	0.16	0.84	0.01	-0.41	0.17	1831580171	14505774	81555948	333520
MAS-57-3_1						2	2.47	0.03	3.39	0.11	5.69	0.32	0.72	0.03	-0.75	0.32	627573365	4964328	27892896	113596
MAS-57-3_2	MAS-57	FLU-173	Pyrite in smoky chert-hosted ore			2	2.62	0.03	3.27	0.12	5.07	0.47	0.93	0.03	-1.16	0.41	572335544	4527853	25432543	103751
MAS-57-3_4						2	3.26	0.01	4.76	0.07	8.76	0.26	0.81	0.01	-0.31	0.27	1190121581	9422312	52967610	216244
MAS-68-1	MAS-68	FLU-168	Pyrite lamina of banded chlorite-rich ore			3	2.57	0.01	4.01	0.17	7.22	0.18	0.50	0.01	-0.42	0.21	2336898486	18489448	103878610	424698
MAS-68-2	MAS-68	FLU-168	Pyrite lamina of banded chlorite-rich ore			3	1.45	0.01	1.84	0.09	3.54	0.15	0.50	0.01	0.03	0.17	2477137032	19570390	109790046	447187
MAS-62-1	MAS-62	FLU-157_13.60m	Pyrite lamina of banded chlorite-rich ore			3	2.01	0.01	2.93	0.09	5.66	0.17	0.50	0.01	0.08	0.19	2495470657	19729720	110761211	452047
MAS-62-2						3	1.78	0.01	2.52	0.11	4.51	0.17	0.48	0.01	-0.29	0.15	2541018998	20086629	112763571	459903
MAS-62-3	MAS-62	FLU-157_13.60m	Pyrite lamina of banded chlorite-rich ore			4	1.85	0.01	2.68	0.08	4.57	0.19	0.48	0.01	-0.52	0.20	2469058429	19520918	109581583	447033
MAS-62-6	MAS-62	FLU-157_13.60m	Pyrite lamina of banded chlorite-rich ore			4	2.42	0.01	3.73	0.12	6.67	0.21	0.50	0.01	-0.43	0.26	2382861169	18845185	105822998	432256
MAS-62-7	MAS-62	FLU-157_13.60m	Pyrite lamina of banded chlorite-rich ore			3 or 4	1.68	0.01	2.16	0.06	3.68	0.20	0.56	0.01	-0.43	0.21	1676535360	13261393	74519969	303980
MAS-62-4	MAS-62	FLU-157_13.60m	Pyrite lamina of banded chlorite-rich ore			within arsenopyrite, hard to determine which generation	1.92	0.01	2.69	0.14	4.19	0.21	0.54	0.01	-0.93	0.21	2413353539	19072394	107034432	436464
MAS-62-5	MAS-62	FLU-157_13.60m	Pyrite lamina of banded chlorite-rich ore			within arsenopyrite, hard to determine which	2.15	0.01	3.04	0.18	4.64	0.20	0.59	0.01	-1.15	0.20	2439054549	19289187	108306940	441931

Title	Sample Code	Drill Core	Lithology and pyrite occurrence	Zoning type	Zone	Pyrite generation	$\delta^{33}S$/‰	1σ/‰	$\delta^{34}S$/‰	1σ/‰	$\delta^{36}S$/‰	1σ/‰	$\Delta^{33}S$/‰	1σ/‰	$\Delta^{36}S$/‰	1σ/‰	CPS/$^{32}S^-$	CPS/$^{33}S^-$	CPS/$^{34}S^-$	CPS/$^{36}S^-$
						generation														
TE34_MAS-37_5	MAS-37	FPL-122_654.4m	Small euhedral to subhedral pyrite in white veinlet in smoky chert				2.93	0.02	3.34	0.03	5.97	0.14	1.21	0.02	-0.38	0.13	1431430062	11271255	62779148	212959
FPL_1.1	FPL-179	FPL-179_395.0m	Pyrite microcrystal aggregate within the quartz+carbonate+pyrite veinlet in carbonaceous phyllite				5.54	0.02	6.59	0.10	11.24	0.17	2.14	0.02	-1.33	0.16	1161389602	9118852	51113583	173309
FPL_2.11	FPL-179	FPL-179_395.0m	Pyrite microcrystal aggregate within the quartz+carbonate+pyrite veinlet in carbonaceous phyllite				18.24	0.02	15.73	0.05	20.83	0.15	10.17	0.02	-9.28	0.15	1115000584	8868835	49537055	168036
FPL_1.18	FPL-179	FPL-179_395.0m	Pyrite microcrystal aggregate within the quartz+carbonate+pyrite veinlet in carbonaceous phyllite				19.28	0.02	16.19	0.04	21.00	0.13	10.98	0.02	-9.98	0.14	1034718092	8238706	45982732	155979
FPL_2.1	FPL-179	FPL-179_395.0m	Pyrite microcrystal aggregate within the quartz+carbonate+pyrite veinlet in carbonaceous phyllite				16.89	0.11	15.25	0.09	21.09	0.11	9.07	0.11	-8.07	0.12	1068770056	8484520	47406517	160645
FPL_1.22	FPL-179	FPL-179_395.0m	Pyrite microcrystal aggregate within the quartz+carbonate+pyrite veinlet in carbonaceous phyllite				5.65	0.05	6.50	0.06	10.78	0.12	2.31	0.04	-1.61	0.14	1004079629	7885984	44203297	149880
FPL_2.12	FPL-179	FPL-179_395.0m	Pyrite microcrystal aggregate within the quartz+carbonate+pyrite veinlet in carbonaceous phyllite				17.50	0.13	15.47	0.04	21.19	0.14	9.56	0.13	-8.40	0.15	1128636201	8968655	50070258	169878
FPL_2.7	FPL-179	FPL-179_395.0m	Pyrite microcrystal aggregate within the quartz+carbonate+pyrite veinlet in carbonaceous phyllite				7.62	0.05	8.39	0.04	13.34	0.12	3.31	0.05	-2.66	0.12	1080256042	8499895	47615536	161170
FPL_2.8	FPL-179	FPL-179_395.0m	Pyrite microcrystal aggregate within the quartz+carbonate+pyrite veinlet in carbonaceous phyllite				18.75	0.02	15.87	0.08	20.90	0.15	10.60	0.02	-9.48	0.17	1100608162	8755145	48881628	165887
FPL_1.21	FPL-179	FPL-179_395.0m	Pyrite microcrystal aggregate within the quartz+carbonate+pyrite veinlet in carbonaceous phyllite				5.72	0.02	7.09	0.02	12.06	0.13	2.08	0.02	-1.45	0.15	1084479886	8516796	47738330	161811
FPL_1.14	FPL-179	FPL-179_395.0m	Pyrite microcrystal aggregate within the quartz+carbonate+pyrite veinlet in carbonaceous phyllite				4.79	0.02	5.29	0.02	8.72	0.13	2.06	0.02	-1.37	0.12	1108307399	8697919	48727495	165040
MAS-43-4	FPL-179	FPL-179_395.0m	Pyrite microcrystal aggregate within the quartz+carbonate+pyrite veinlet in carbonaceous phyllite				4.90	0.01	5.38	0.07	8.97	0.17	2.13	0.01	-1.28	0.19	1613957079	12809095	71974375	294511
MAS-43-5	FPL-179	FPL-179_395.0m	Pyrite microcrystal aggregate within the quartz+carbonate+pyrite veinlet in carbonaceous phyllite				11.84	0.12	12.89	0.12	20.59	0.18	5.22	0.12	-4.03	0.16	1716241014	13710710	77095968	316736
MAS-43-8	FPL-179	FPL-179_395.0m	Pyrite microcrystal aggregate within the quartz+carbonate+pyrite veinlet in				18.56	0.02	15.70	0.07	20.60	0.16	10.51	0.02	-9.45	0.18	1724891086	13874852	77706622	318290

Title	Sample Code	Drill Core	Lithology and pyrite occurrence	Zoning type	Zone	Pyrite generation	$\delta^{33}S$/‰	1σ/‰	$\delta^{34}S$/‰	1σ/‰	$\delta^{36}S$/‰	1σ/‰	$\Delta^{33}S$/‰	1σ/‰	$\Delta^{36}S$/‰	1σ/‰	CPS/$^{32}S^-$	CPS/$^{33}S^-$	CPS/$^{34}S^-$	CPS/$^{36}S^-$
			carbonaceous phyllite																	
MAS-43-13	FPL-179	FPL-179_395.0m	Pyrite microcrystal aggregate within the quartz+carbonate+pyrite veinlet in carbonaceous phyllite				10.21	0.03	10.41	0.08	16.40	0.23	4.87	0.04	-3.47	0.18	1720266546	13725519	77100272	316365
FPL_1.23	FPL-179	FPL-179_395.0m	Recrystalized microcrystal pyrite aggregate within the matrix of carbonaceous phyllite				5.95	0.02	7.51	0.03	12.16	0.19	2.09	0.02	-2.16	0.19	1106011367	8691631	48745010	165260
MAS-43-1	FPL-179	FPL-179_395.0m	Recrystalized microcrystal pyrite aggregate within the matrix of carbonaceous phyllite				5.51	0.01	6.70	0.21	10.79	0.19	2.06	0.01	-1.97	0.27	2279669649	18083221	101532157	414986
MAS-43-2	FPL-179	FPL-179_395.0m	Recrystalized microcrystal pyrite aggregate within the matrix of carbonaceous phyllite				6.57	0.01	8.79	0.08	15.59	0.17	2.06	0.01	-1.18	0.18	2140093778	16997879	95561699	392047
TE36_6.1	FPL-179	FPL-179_395.0m	Recrystalized microcrystal pyrite aggregate within the matrix of carbonaceous phyllite				6.50	0.02	7.91	0.03	13.51	0.13	2.44	0.02	-1.56	0.14	1637987561	12936465	72092650	245713
TE36_6.2	FPL-179	FPL-179_395.0m	Recrystalized microcrystal pyrite aggregate within the matrix of carbonaceous phyllite				6.28	0.02	7.72	0.03	13.09	0.12	2.31	0.02	-1.63	0.14	1626047240	12841827	71586593	243878
TE38_10.1	FPL-179	FPL-179_395.0m	Recrystalized microcrystal pyrite aggregate within the matrix of carbonaceous phyllite				5.92	0.02	7.35	0.05	12.63	0.14	2.15	0.02	-1.38	0.14	1631805202	12887686	71862659	244689
TE38_10.2	FPL-179	FPL-179_395.0m	Recrystalized microcrystal pyrite aggregate within the matrix of carbonaceous phyllite				6.72	0.01	8.51	0.02	14.65	0.15	2.34	0.02	-1.57	0.17	1628156568	12861787	71703812	244189
MAS-43-2-1	MAS-43	FPL-122_560.4m	Recrystalized microcrystal pyrite aggregate within the matrix of carbonaceous phyllite				4.49	0.01	5.57	0.15	9.25	0.20	1.63	0.02	-1.36	0.23	1111675760	8819285	49588428	202826
QF-4-1_4	MAS-49B	FPL-128_561.4m	Medium to coarse euhedral to subhedral pyrite grain within the quartz+carbonate+pyrite veinlet in carbonaceous phyllite				5.95	0.01	8.90	0.07	16.47	0.10	1.38	0.01	-0.51	0.10	1419280021	11222244	62713623	226633
QF-4-1_5	MAS-49B	FPL-128_561.4m	Medium to coarse euhedral to subhedral pyrite grain within the quartz+carbonate+pyrite veinlet in carbonaceous phyllite				5.75	0.01	8.51	0.09	16.04	0.11	1.37	0.02	-0.19	0.11	1417554417	11207066	62614950	226192
QF-4-1_8	MAS-49B	FPL-128_561.4m	Medium to coarse euhedral to subhedral pyrite grain within the quartz+carbonate+pyrite veinlet in carbonaceous phyllite				5.63	0.01	8.40	0.06	15.47	0.11	1.31	0.01	-0.55	0.11	1530052469	12093815	67569366	243848
QF-4-1_9	MAS-49B	FPL-128_561.4m	Medium to coarse euhedral to subhedral pyrite grain within the quartz+carbonate+pyrite veinlet in				6.24	0.02	9.50	0.06	17.43	0.08	1.36	0.02	-0.69	0.08	1552337649	12276216	68624991	248118

Title	Sample Code	Drill Core	Lithology and pyrite occurrence	Zoning type	Zone	Pyrite generation	$\delta^{33}S$/‰	1σ/‰	$\delta^{34}S$/‰	1σ/‰	$\delta^{36}S$/‰	1σ/‰	$\Delta^{33}S$/‰	1σ/‰	$\Delta^{36}S$/‰	1σ/‰	CPS/$^{32}S^-$	CPS/$^{33}S^-$	CPS/$^{34}S^-$	CPS/$^{36}S^-$
			carbonaceous phyllite																	
QF-4-1_10	MAS-49B	FPL-128_561.4m	Medium to coarse euhedral to subhedral pyrite grain within the quartz+carbonate+pyrite veinlet in carbonaceous phyllite				5.19	0.01	7.43	0.06	13.60	0.12	1.37	0.02	-0.57	0.12	1531875354	12103000	67593764	243999
QF-4-1_11	MAS-49B	FPL-128_561.4m	Medium to coarse euhedral to subhedral pyrite grain within the quartz+carbonate+pyrite veinlet in carbonaceous phyllite				5.25	0.01	7.57	0.06	13.87	0.10	1.36	0.01	-0.55	0.10	1551926128	12262562	68486114	246900
QF-4-1_3_	MAS-49B	FPL-128_561.4m	Medium to coarse euhedral to subhedral pyrite grain within the quartz+carbonate+pyrite veinlet in carbonaceous phyllite				5.98	0.02	8.93	0.07	16.47	0.11	1.39	0.02	-0.56	0.12	1431775048	11321422	63269614	228712
QF-4-2_1	MAS-49B	FPL-128_561.4m	Medium to coarse euhedral to subhedral pyrite grain within the quartz+carbonate+pyrite veinlet in carbonaceous phyllite				4.79	0.02	6.75	0.09	12.22	0.09	1.32	0.02	-0.66	0.09	1390782172	10984609	61330473	221332
QF-4-2_4	MAS-49B	FPL-128_561.4m	Medium to coarse euhedral to subhedral pyrite grain within the quartz+carbonate+pyrite veinlet in carbonaceous phyllite				5.02	0.02	7.13	0.08	13.11	0.11	1.36	0.02	-0.49	0.12	1348519918	10653112	59477269	214558
QF-4-2_5	MAS-49B	FPL-128_561.4m	Medium to coarse euhedral to subhedral pyrite grain within the quartz+carbonate+pyrite veinlet in carbonaceous phyllite				5.13	0.01	7.31	0.08	13.54	0.08	1.37	0.01	-0.39	0.08	1395051110	11021426	61544302	221972
QF-4-2_8	MAS-49B	FPL-128_561.4m	Medium to coarse euhedral to subhedral pyrite grain within the quartz+carbonate+pyrite veinlet in carbonaceous phyllite				5.08	0.02	7.53	0.08	13.03	0.09	1.20	0.01	-1.34	0.09	1334261094	10540507	58870459	212370
QF-4-2_9	MAS-49B	FPL-128_561.4m	Medium to coarse euhedral to subhedral pyrite grain within the quartz+carbonate+pyrite veinlet in carbonaceous phyllite				4.99	0.01	7.15	0.06	12.85	0.13	1.32	0.02	-0.77	0.12	1465567328	11576610	64644205	233182
QF-4-2_10	MAS-49B	FPL-128_561.4m	Medium to coarse euhedral to subhedral pyrite grain within the quartz+carbonate+pyrite veinlet in carbonaceous phyllite				4.91	0.02	7.07	0.06	12.22	0.12	1.28	0.02	-1.25	0.12	1202964183	9501197	53058332	191266
TE34_MAS-49B_11	MAS-49B	FPL-128_561.4m	Medium to coarse euhedral to subhedral pyrite grain within the quartz+carbonate+pyrite veinlet in carbonaceous phyllite				5.50	0.02	7.98	0.04	14.97	0.14	1.40	0.02	-0.24	0.14	1588873998	12542292	69998585	238868
TE34_MAS-49_17	MAS-49B	FPL-128_561.4m	Medium to coarse euhedral to subhedral pyrite grain within the quartz+carbonate+pyrite veinlet in				4.91	0.02	6.90	0.04	12.28	0.16	1.37	0.03	-0.86	0.16	1501334112	11846000	66083935	225133

Title	Sample Code	Drill Core	Lithology and pyrite occurrence	Zoning type	Zone	Pyrite generation	$\delta^{33}S$/‰	1σ/‰	$\delta^{34}S$/‰	1σ/‰	$\delta^{36}S$/‰	1σ/‰	$\Delta^{33}S$/‰	1σ/‰	$\Delta^{36}S$/‰	1σ/‰	CPS/$^{32}S^-$	CPS/$^{33}S^-$	CPS/$^{34}S^-$	CPS/$^{36}S^-$
			carbonaceous phyllite																	
TE34_MAS-49_12	MAS-49B	FPL-128_561.4m	Medium to coarse euhedral to subhedral pyrite grain within the quartz+carbonate+pyrite veinlet in carbonaceous phyllite				5.70	0.02	8.45	0.04	15.60	0.15	1.36	0.02	-0.50	0.16	1463326009	11549893	64483842	220079
TE34_MAS-49_18	MAS-49B	FPL-128_561.4m	Medium to coarse euhedral to subhedral pyrite grain within the quartz+carbonate+pyrite veinlet in carbonaceous phyllite				4.85	0.02	6.88	0.05	12.69	0.14	1.31	0.02	-0.43	0.16	1597875958	12607574	70336252	239764
QF-2-3_1	MAS-46	FPL-122_514.6m	Porphyroblastic pyrite in micaceous phyllite				4.45	0.01	4.50	0.04	7.01	0.11	2.13	0.01	-1.55	0.11	1676014595	13233535	73701951	265128
QF-2-3_2	MAS-46	FPL-122_514.6m	Porphyroblastic pyrite in micaceous phyllite				4.61	0.01	4.84	0.03	7.48	0.10	2.12	0.01	-1.73	0.10	1683993873	13299084	74084543	266524
QF-2-3_4	MAS-46	FPL-122_514.6m	Porphyroblastic pyrite in micaceous phyllite				4.75	0.01	5.16	0.03	8.00	0.08	2.10	0.01	-1.83	0.09	1711977977	13519751	75324740	271243
QF-2-3_5	MAS-46	FPL-122_514.6m	Porphyroblastic pyrite in micaceous phyllite				4.36	0.02	4.34	0.05	6.77	0.10	2.13	0.02	-1.49	0.10	1686221827	13312524	74129606	266640
QF-2-3_7	MAS-46	FPL-122_514.6m	Porphyroblastic pyrite in micaceous phyllite				4.28	0.01	4.17	0.04	6.29	0.09	2.14	0.01	-1.66	0.09	1690710187	13346429	74332317	267237
QF-2-4_1	MAS-46	FPL-122_514.6m	Porphyroblastic pyrite in micaceous phyllite				3.13	0.01	2.03	0.05	2.61	0.11	2.08	0.01	-1.25	0.10	1674204022	13201485	73447480	263846
QF-2-4_6	MAS-46	FPL-122_514.6m	Porphyroblastic pyrite in micaceous phyllite				4.86	0.01	5.25	0.03	8.33	0.09	2.15	0.01	-1.67	0.10	1686984609	13323895	74244276	267147
QF-2-4_5	MAS-46	FPL-122_514.6m	Porphyroblastic pyrite in micaceous phyllite				4.80	0.01	5.21	0.04	8.29	0.07	2.12	0.01	-1.63	0.07	1708436592	13493552	75202549	270423
MAS_18_1	MAS-18	FPL-120_694.3m	Porphyroblastic pyrite in micaceous phyllite				4.48	0.06	4.85	0.12	8.00	0.20	1.98	0.05	-1.23	0.20	1717711867	13659651	76621069	257005
MAS_18_2	MAS-18	FPL-120_694.3m	Porphyroblastic pyrite in micaceous phyllite				3.60	0.02	2.95	0.09	3.74	0.15	2.09	0.02	-1.87	0.17	1670484634	13270470	74337973	249396
MAS_18_3	MAS-18	FPL-120_694.3m	Porphyroblastic pyrite in micaceous phyllite				2.11	0.05	-1.45	0.07	-5.51	0.24	2.86	0.05	-2.75	0.29	1174320183	9309524	52001428	172920
MAS_18_4	MAS-18	FPL-120_694.3m	Porphyroblastic pyrite in micaceous phyllite				-0.45	0.02	-4.91	0.26	-12.94	0.28	2.08	0.03	-3.63	0.27	1222480243	9668350	53949635	178953
MAS_18_5	MAS-18	FPL-120_694.3m	Porphyroblastic pyrite in micaceous phyllite				0.89	0.03	-3.32	0.10	-8.84	0.28	2.60	0.03	-2.54	0.29	1208503134	9566019	53388863	177382
MAS_18_6	MAS-18	FPL-120_694.3m	Porphyroblastic pyrite in micaceous phyllite				4.26	0.03	4.45	0.08	6.51	0.26	1.96	0.03	-1.97	0.22	1696737086	13492306	75639620	253870
MAS_18_7	MAS-	FPL-	Porphyroblastic pyrite in micaceous				3.70	0.04	3.79	0.08	5.98	0.22	1.75	0.04	-1.24	0.26	1713035588	13604365	76272863	255553

Title	Sample Code	Drill Core	Lithology and pyrite occurrence	Zoning type	Zone	Pyrite generation	$\delta^{33}S$/‰	1σ/‰	$\delta^{34}S$/‰	1σ/‰	$\delta^{36}S$/‰	1σ/‰	$\Delta^{33}S$/‰	1σ/‰	$\Delta^{36}S$/‰	1σ/‰	CPS/$^{32}S^-$	CPS/$^{33}S^-$	CPS/$^{34}S^-$	CPS/$^{36}S^-$
	18	120_694.3m	phyllite																	
MAS_18_8	MAS-18	FPL-120_694.3m	Porphyroblastic pyrite in micaceous phyllite				4.67	0.02	5.28	0.17	8.26	0.19	1.95	0.02	-1.79	0.21	1727282496	13725781	76939365	257669
Porphyroblast_1	MAS-48	FPL-122_396.2m	Porphyroblastic pyrite in micaceous phyllite				2.92	0.01	2.95	0.14	4.53	0.17	1.40	0.01	-1.08	0.18	2386143777	18882443	105901677	431186
Porphyroblast_2	MAS-48	FPL-122_396.2m	Porphyroblastic pyrite in micaceous phyllite				3.62	0.01	4.26	0.09	7.03	0.20	1.43	0.01	-1.08	0.20	2430647790	19243600	107979388	439814
Porphyroblast_4	MAS-48	FPL-122_396.2m	Porphyroblastic pyrite in micaceous phyllite				3.75	0.01	4.56	0.09	7.76	0.16	1.41	0.01	-0.92	0.16	2411694520	19094380	107149433	437513
T10-1						Core	6.81	0.01	6.54	0.06	9.30	0.10	3.45	0.01	-3.16	0.10	1448889354	11456666	64091906	218567
T10-2	MAS-47	FPL-122_527.8m	Porphyroblastic pyrite in micaceous phyllite			Mantle 1	5.49	0.03	4.31	0.05	5.70	0.10	3.28	0.02	-2.50	0.11	1469461285	11605017	64859525	220749
T10-4						Mantle 2	4.78	0.02	3.51	0.04	1.81	0.10	2.98	0.02	-4.86	0.11	1415600012	11172778	62426558	212003
T10-3						Rim	5.14	0.03	4.33	0.08	4.71	0.15	2.91	0.02	-3.53	0.15	1455125925	11487872	64230666	218641
TE18_2	MAS-40	FOA-11_92.4m	Euhedral to subhedral pyrite in metabasalt				1.52	0.03	1.94	0.09	3.43	0.12	0.52	0.03	-0.26	0.11	1524350927	11985188	66752200	226338
TE34_MAS-40_8	MAS-40	FOA-11_92.4m	Euhedral to subhedral pyrite in metabasalt				1.70	0.02	2.22	0.03	4.00	0.12	0.56	0.02	-0.23	0.12	1589371062	12497869	69620451	236362
TE34_MAS-40_7	MAS-40	FOA-11_92.4m	Euhedral to subhedral pyrite in metabasalt				2.18	0.02	2.87	0.04	5.00	0.14	0.70	0.02	-0.47	0.15	1530839521	12043260	67103114	227973
TE34_MAS-40_6	MAS-40	FOA-11_92.4m	Euhedral to subhedral pyrite in metabasalt				1.88	0.02	2.34	0.03	3.94	0.16	0.67	0.02	-0.52	0.15	1455968972	11450311	63786336	216655
Altered_basalt_1-1	MAS-40	FOA-11_92.4m	Euhedral to subhedral pyrite in metabasalt				2.33	0.01	3.29	0.03	6.07	0.21	0.63	0.01	-0.18	0.21	2399010528	18988521	106644280	436062
Altered_basalt_1-2	MAS-40	FOA-11_92.4m	Euhedral to subhedral pyrite in metabasalt				1.82	0.01	2.45	0.07	4.13	0.18	0.56	0.01	-0.53	0.22	2396701428	18961216	106463431	434104
Altered_basalt_2-1	MAS-40	FOA-11_92.4m	Euhedral to subhedral pyrite in metabasalt				1.67	0.01	2.23	0.04	3.69	0.19	0.52	0.01	-0.55	0.19	2321242636	18357238	103055760	420085
Altered_basalt_2-2	MAS-40	FOA-11_92.4m	Euhedral to subhedral pyrite in metabasalt				1.64	0.01	2.11	0.09	3.57	0.17	0.55	0.01	-0.43	0.18	2382448812	18849350	105826969	431960
TE34_MAS-31_3	MAS-31	FPL-122_113.7m	Euhedral to subhedral pyrite in dolerite dyke				0.65	0.02	0.97	0.04	1.75	0.16	0.15	0.02	-0.10	0.16	1481108405	11631144	64791722	219719
TE34_MAS-31_4	MAS-31	FPL-122_113.7m	Euhedral to subhedral pyrite in dolerite dyke				0.52	0.02	0.72	0.03	1.25	0.18	0.16	0.02	-0.11	0.17	1516828640	11911124	66346990	225065
Dyke_1-2	MAS-31	FPL-122_113.7m	Euhedral to subhedral pyrite in dolerite dyke				0.78	0.01	1.09	0.07	2.21	0.18	0.22	0.01	0.14	0.19	2343832359	18524614	103983505	423726

Title	Sample Code	Drill Core	Lithology and pyrite occurrence	Zoning type	Zone	Pyrite generation	$\delta^{33}S$/‰	1σ/‰	$\delta^{34}S$/‰	1σ/‰	$\delta^{36}S$/‰	1σ/‰	$\Delta^{33}S$/‰	1σ/‰	$\Delta^{36}S$/‰	1σ/‰	CPS/$^{32}S^-$	CPS/$^{33}S^-$	CPS/$^{34}S^-$	CPS/$^{36}S^-$
Dyke_2-1	MAS-31	FPL-122_113.7m	Euhedral to subhedral pyrite in dolerite dyke				0.76	0.01	1.09	0.07	2.01	0.19	0.20	0.01	-0.06	0.20	2422847005	19145978	107476134	438586
Dyke_2-2	MAS-31	FPL-122_113.7m	Euhedral to subhedral pyrite in dolerite dyke				0.22	0.01	0.07	0.11	0.17	0.18	0.18	0.01	0.04	0.18	2437837143	19260151	108069898	440332
RUTTAN_7.1							0.79	0.01	1.39	0.06	2.81	0.09	0.07	0.01	0.18	0.09	1483290815	11668547	65054736	233388
RUTTAN_7.2							0.68	0.01	1.40	0.06	2.58	0.09	-0.04	0.01	-0.09	0.09	1474719073	11599758	64674815	232202
RUTTAN_7.4							0.67	0.01	1.37	0.08	2.64	0.09	-0.04	0.02	0.03	0.09	1501488354	11810509	65856093	236516
RUTTAN_7.5							0.61	0.01	1.33	0.06	2.52	0.10	-0.07	0.01	0.00	0.10	1500720722	11802884	65811730	236331
RUTTAN_7.6							0.72	0.01	1.31	0.07	2.43	0.08	0.04	0.01	-0.07	0.08	1474185815	11594459	64645966	232113
RUTTAN_8.1							0.44	0.01	0.91	0.07	1.69	0.12	-0.03	0.01	-0.04	0.12	1373637651	10801732	60210889	216136
RUTTAN_8.2							0.44	0.01	0.80	0.05	1.47	0.08	0.02	0.01	-0.06	0.08	1392730636	10951165	61040784	219042
RUTTAN_8.3							0.42	0.01	0.86	0.07	1.44	0.08	-0.02	0.02	-0.18	0.08	1360135150	10696667	59616911	213872
RUTTAN_3.12							0.80	0.01	1.43	0.06	2.95	0.12	0.07	0.01	0.22	0.12	1629374014	12816003	71450694	256996
BALMAT_5.3							7.74	0.01	15.11	0.06	28.91	0.09	-0.01	0.01	0.00	0.09	1517929940	12022915	67488570	245220
BALMAT_5.4							7.78	0.01	15.15	0.02	29.13	0.10	0.01	0.01	0.15	0.11	1799079881	14251263	79980208	290761
BALMAT_5.5							7.55	0.02	14.61	0.03	28.22	0.11	0.05	0.02	0.28	0.12	1512079934	11976888	67201700	244101
BALMAT_5.6							7.58	0.01	14.84	0.05	28.43	0.10	-0.04	0.01	0.04	0.10	1503559153	11908606	66835248	243017
BALMAT_3.8							7.51	0.02	14.56	0.07	28.17	0.10	0.04	0.02	0.32	0.10	1608406731	12738962	71466957	259855
RUTTAN_1.1							0.43	0.01	0.84	0.04	1.84	0.07	0.00	0.01	0.24	0.07	1568223062	12331888	68719248	246845
RUTTAN_1.2							0.56	0.02	1.05	0.04	2.07	0.11	0.02	0.02	0.07	0.11	1577709964	12407589	69134889	248252
RUTTAN_1.3							0.56	0.01	1.08	0.04	2.25	0.10	0.00	0.02	0.19	0.10	1588788760	12493997	69634547	250302
RUTTAN_1.4							0.61	0.01	1.11	0.05	1.97	0.09	0.03	0.01	-0.15	0.09	1630251528	12821314	71451676	256564
RUTTAN_1.5							0.56	0.01	1.06	0.04	2.18	0.08	0.02	0.01	0.16	0.08	1625731877	12784706	71243209	255790
RUTTAN_1.6							0.60	0.01	1.17	0.06	2.07	0.10	0.00	0.01	-0.15	0.08	1647771174	12960540	72227359	259343
RUTTAN_1.7							0.65	0.02	1.29	0.03	2.25	0.09	-0.02	0.02	-0.21	0.10	1647397280	12956262	72216602	259480
RUTTAN_2.1							0.77	0.01	1.53	0.04	3.03	0.13	-0.02	0.01	0.11	0.13	1632179246	12839454	71555599	257166
RUTTAN_2.2							0.57	0.01	1.05	0.04	2.29	0.11	0.03	0.01	0.29	0.10	1688051447	13276693	73982472	265869
RUTTAN_2.3							0.70	0.01	1.38	0.04	2.46	0.09	-0.01	0.01	-0.15	0.09	1692104128	13310504	74174605	266396

Title	Sample Code	Drill Core	Lithology and pyrite occurrence	Zoning type	Zone	Pyrite generation	$\delta^{33}S$/‰	1σ/‰	$\delta^{34}S$/‰	1σ/‰	$\delta^{36}S$/‰	1σ/‰	$\Delta^{33}S$/‰	1σ/‰	$\Delta^{36}S$/‰	1σ/‰	CPS/$^{32}S^-$	CPS/$^{33}S^-$	CPS/$^{34}S^-$	CPS/$^{36}S^-$
RUTTAN_2.4							0.79	0.02	1.63	0.05	2.69	0.12	-0.05	0.02	-0.40	0.11	1649254554	12973918	72319836	259654
BALMAT_1.1							7.59	0.01	14.78	0.06	28.30	0.10	0.00	0.02	0.04	0.10	1556315273	12324669	69139402	251429
BALMAT_1.2							7.54	0.02	14.75	0.06	28.23	0.13	-0.03	0.02	0.02	0.12	1568102096	12418766	69646564	253369
BALMAT_1.3							7.58	0.01	14.70	0.06	28.14	0.10	0.03	0.01	0.02	0.11	1603796897	12700527	71244359	258906
BALMAT_1.4							7.71	0.02	15.04	0.04	28.75	0.09	-0.01	0.02	-0.01	0.10	1654101786	13102579	73499273	267132
BALMAT_1.5							7.58	0.01	14.70	0.04	28.31	0.09	0.04	0.02	0.19	0.09	1604462871	12706586	71268509	258879
BALMAT_1.6							7.60	0.02	14.81	0.03	28.19	0.09	0.00	0.02	-0.13	0.10	1616134095	12798228	71799024	260933
Ruttan_1							0.54	0.02	1.08	0.07	2.03	0.15	-0.02	0.02	-0.03	0.15	1542742570	12120185	67517202	228693
Ruttan_2							0.63	0.03	1.16	0.06	2.49	0.14	0.03	0.03	0.28	0.15	1499399311	11771459	65573773	222037
Ruttan_3							0.65	0.02	1.27	0.04	2.39	0.14	0.00	0.02	-0.02	0.14	1568585835	12323159	68643644	232675
Ruttan_4							0.66	0.02	1.33	0.07	2.66	0.19	-0.03	0.02	0.14	0.17	1559022241	12247658	68240192	231607
Ruttan_5							0.72	0.02	1.33	0.06	2.47	0.13	0.04	0.02	-0.06	0.15	1598725999	12558297	69948133	237123
Ruttan_6							0.51	0.02	1.03	0.02	1.65	0.14	-0.02	0.02	-0.31	0.13	1565365949	12292676	68463330	232117
Balmat_1							7.61	0.02	14.95	0.06	28.90	0.15	-0.06	0.02	0.31	0.15	1562020561	12352380	69267244	237909
Balmat_2							7.72	0.02	15.01	0.06	28.70	0.15	0.01	0.02	-0.02	0.17	1579654600	12495330	70055191	240112
Balmat_3							7.56	0.01	14.85	0.06	28.52	0.15	-0.05	0.02	0.12	0.15	1583596075	12523797	70234546	241118
Ruttan-3.1							0.59	0.01	1.04	0.13	2.14	0.16	0.06	0.01	0.17	0.20	2394487779	18904209	106082104	431751
Ruttan-3.2							0.71	0.01	1.26	0.10	2.81	0.18	0.06	0.01	0.42	0.17	2376948227	18767841	105312036	428916
Ruttan-3.3							0.60	0.01	1.10	0.11	1.93	0.19	0.04	0.01	-0.17	0.22	2405762836	18993374	106572533	434642
Ruttan-3.4							0.70	0.01	1.29	0.08	2.20	0.21	0.04	0.01	-0.24	0.21	2441695878	19281040	108217126	441934
Ruttan-3.5							0.66	0.01	1.30	0.09	2.31	0.16	-0.01	0.01	-0.17	0.16	2409965652	19028089	106793845	434672
Ruttan-3.6							0.74	0.01	1.41	0.09	2.68	0.13	0.01	0.01	0.00	0.15	2466631871	19477619	109309419	445273
Ruttan-4.1							0.64	0.01	1.33	0.07	2.92	0.15	-0.04	0.01	0.40	0.16	2518452394	19882439	111585252	454621
Ruttan-4.2							0.56	0.01	1.17	0.12	2.69	0.18	-0.04	0.01	0.47	0.19	2488441169	19648135	110265119	449031
Ruttan-4.3							0.42	0.01	0.89	0.18	1.43	0.21	-0.04	0.01	-0.27	0.22	2428547344	19170535	107556759	437979
Balmat-3.1							7.88	0.01	15.28	0.11	29.07	0.19	0.03	0.01	-0.18	0.22	2327221063	18509209	104562453	431046
Balmat-3.2							7.90	0.01	15.41	0.09	30.32	0.16	-0.01	0.01	0.84	0.17	2387136010	18985456	107270200	443070

Title	Sample Code	Drill Core	Lithology and pyrite occurrence	Zoning type	Zone	Pyrite generation	$\delta^{33}S$/‰	1σ/‰	$\delta^{34}S$/‰	1σ/‰	$\delta^{36}S$/‰	1σ/‰	$\Delta^{33}S$/‰	1σ/‰	$\Delta^{36}S$/‰	1σ/‰	CPS/$^{32}S^-$	CPS/$^{33}S^-$	CPS/$^{34}S^-$	CPS/$^{36}S^-$
Balmat-3.3							7.85	0.01	15.39	0.11	29.21	0.20	-0.04	0.01	-0.23	0.20	2366071005	18818890	106343584	438926
Balmat-4.1							7.76	0.01	15.22	0.09	29.20	0.15	-0.05	0.01	0.08	0.16	2497996573	19862513	112236199	463026
Balmat-4.2							7.98	0.01	15.65	0.15	29.62	0.15	-0.05	0.01	-0.32	0.23	2430979551	19333850	109255120	450997
RUTTAN_3.1							0.56	0.02	1.02	0.02	1.87	0.11	0.03	0.02	-0.06	0.11	1615373572	12705284	70811740	254394
RUTTAN_3.2							0.64	0.02	1.23	0.04	2.26	0.11	0.00	0.01	-0.07	0.10	1585175601	12468287	69500652	249732
RUTTAN_3.3							0.64	0.01	1.27	0.05	2.30	0.11	-0.02	0.01	-0.11	0.10	1583574282	12456110	69436641	249482
RUTTAN_3.4							0.62	0.01	1.27	0.03	2.37	0.08	-0.03	0.01	-0.05	0.08	1632354326	12840156	71588239	257126
RUTTAN_3.5							0.66	0.01	1.36	0.04	2.23	0.10	-0.04	0.01	-0.35	0.09	1624830398	12780482	71266530	255973
RUTTAN_3.6							0.60	0.01	1.20	0.04	2.32	0.09	-0.02	0.01	0.04	0.09	1616992130	12719594	70896105	254803
RUTTAN_3.7							0.65	0.01	1.13	0.05	2.29	0.09	0.07	0.01	0.14	0.10	1652852918	13002170	72474545	260436
RUTTAN_3.8							0.67	0.02	1.26	0.05	2.48	0.10	0.02	0.02	0.08	0.10	1679451567	13210534	73664955	264762
RUTTAN_3.9							0.65	0.01	1.30	0.03	2.49	0.11	-0.02	0.01	0.02	0.11	1687898536	13277086	74027565	266072
RUTTAN_3.10							0.59	0.03	1.06	0.04	2.12	0.09	0.04	0.02	0.10	0.09	1659472295	13051955	72760611	261459
RUTTAN_3.11							0.53	0.01	1.10	0.03	2.36	0.10	-0.04	0.01	0.26	0.11	1668575088	13122714	73150568	262824
BALMAT_3.1							7.56	0.01	14.65	0.05	28.06	0.09	0.04	0.01	0.04	0.09	1584685541	12552031	70418263	256022
BALMAT_3.2							7.58	0.01	14.70	0.04	27.99	0.11	0.04	0.01	-0.12	0.12	1573207814	12460482	69902959	254188
BALMAT_3.3							7.56	0.02	14.92	0.04	27.84	0.09	-0.09	0.02	-0.70	0.09	1598368399	12660589	71049298	258262
BALMAT_3.4							7.58	0.02	14.88	0.05	28.23	0.09	-0.06	0.02	-0.24	0.09	1617868657	12814567	71898925	261292
BALMAT_3.5							7.47	0.01	14.61	0.04	27.88	0.08	-0.02	0.01	-0.06	0.08	1660561721	13151789	73791904	268351
BALMAT_3.6							7.44	0.01	14.54	0.04	27.86	0.09	-0.02	0.01	0.06	0.09	1666038532	13194729	74030639	269068
RUTTAN-1.1							0.37	0.02	0.81	0.06	1.45	0.13	-0.05	0.02	-0.09	0.11	1561756332	12287911	68513530	246289
RUTTAN-1.2							0.55	0.02	1.03	0.03	1.78	0.10	0.03	0.01	-0.17	0.11	1608412546	12658628	70575708	253632
RUTTAN-1.3							0.56	0.01	1.13	0.04	1.81	0.11	-0.02	0.01	-0.33	0.10	1597227736	12568451	70077939	251841
RUTTAN_1.4							0.53	0.01	1.10	0.03	2.00	0.10	-0.03	0.01	-0.08	0.11	1571565863	12368055	68952754	247896
RUTTAN_1.5							0.56	0.01	1.07	0.05	1.94	0.11	0.00	0.01	-0.10	0.12	1534632433	12076571	67330902	242115
RUTTAN_1.6							0.59	0.01	1.16	0.04	2.48	0.11	-0.01	0.01	0.28	0.11	1508620208	11872851	66203283	238111
RUTTAN_1.7							0.70	0.02	1.32	0.05	2.42	0.09	0.02	0.01	-0.09	0.10	1531147489	12050799	67190129	241721

Title	Sample Code	Drill Core	Lithology and pyrite occurrence	Zoning type	Zone	Pyrite generation	$\delta^{33}S$/‰	1σ/‰	$\delta^{34}S$/‰	1σ/‰	$\delta^{36}S$/‰	1σ/‰	$\Delta^{33}S$/‰	1σ/‰	$\Delta^{36}S$/‰	1σ/‰	CPS/$^{32}S^-$	CPS/$^{33}S^-$	CPS/$^{34}S^-$	CPS/$^{36}S^-$
RUTTAN_1.8							0.65	0.02	1.25	0.03	2.38	0.10	0.00	0.02	0.00	0.10	1552791387	12221299	68136166	244975
RUTTAN_2.1							0.71	0.02	1.42	0.04	2.70	0.09	-0.02	0.02	0.00	0.10	1545912280	12168082	67860593	244065
RUTTAN_2.2							0.68	0.01	1.34	0.06	2.67	0.10	0.00	0.02	0.13	0.11	1546820899	12173890	67892929	243973
RUTTAN_2.3							0.78	0.02	1.45	0.05	2.76	0.10	0.04	0.02	0.01	0.10	1524916595	12004518	66940937	240798
RUTTAN_2.4							0.67	0.02	1.34	0.05	2.61	0.13	-0.02	0.02	0.07	0.12	1529805225	12040092	67146322	241550
RUTTAN_2.5							0.65	0.02	1.25	0.05	2.47	0.12	0.00	0.02	0.09	0.12	1541050318	12128079	67613343	243364
RUTTAN_2.6							0.66	0.01	1.15	0.04	2.47	0.12	0.07	0.01	0.29	0.12	1544884822	12158423	67786136	243738
BALMAT-1.1							7.33	0.01	14.42	0.06	27.47	0.10	-0.07	0.01	-0.11	0.10	1546827140	12256322	68774777	250173
BALMAT-1.2							7.16	0.02	14.10	0.06	26.96	0.10	-0.08	0.02	0.00	0.11	1544504869	12236047	68650131	249740
BALMAT-1.3							7.25	0.02	14.18	0.06	27.05	0.12	-0.02	0.02	-0.06	0.12	1494923988	11843413	66454949	241682
BALMAT_1.4							7.15	0.01	14.00	0.05	26.76	0.12	-0.03	0.02	-0.02	0.13	1483383726	11751268	65927910	239750
BALMAT_1.5							7.24	0.02	14.07	0.04	26.86	0.11	0.02	0.02	-0.04	0.11	1484198179	11757320	65977230	239919
BALMAT_1.6							7.42	0.01	14.57	0.06	27.90	0.12	-0.06	0.01	0.04	0.12	1517719315	12027066	67498845	245687
BALMAT_1.7							7.19	0.01	14.07	0.05	26.66	0.17	-0.03	0.01	-0.24	0.12	1481597941	11738941	65863961	239546
Ruttan-11.1							0.66	0.02	1.11	0.05	2.02	0.15	0.09	0.02	-0.09	0.17	1346155840	10631326	59703004	243520
Ruttan-11.2							0.78	0.02	1.27	0.06	2.62	0.18	0.13	0.02	0.20	0.20	1345265185	10623725	59672439	242879
Ruttan-11.3							0.55	0.01	1.21	0.08	2.31	0.22	-0.08	0.01	0.01	0.22	1258616392	9937865	55825812	227349
Ruttan-11.4							0.49	0.01	1.21	0.08	2.17	0.21	-0.14	0.01	-0.12	0.22	1230343409	9714607	54571161	221971
Balmat-11.1							8.32	0.01	15.57	0.07	29.90	0.22	0.34	0.02	0.12	0.25	1375846982	10949120	61901726	255733
Balmat-11.2							7.74	0.02	15.43	0.07	29.41	0.18	-0.18	0.02	-0.12	0.19	1255065333	9981170	56457724	232926
Ruttan_10.1							0.72	0.02	1.33	0.04	2.28	0.14	0.03	0.02	-0.25	0.14	1480748112	11636409	65141618	221477
Ruttan_10.2							0.75	0.02	1.61	0.04	3.03	0.11	-0.08	0.02	-0.02	0.10	1506532353	11840518	66304832	225970
Ruttan_10.3							0.56	0.01	0.94	0.05	1.86	0.11	0.08	0.01	0.07	0.11	1470451049	11555692	64666570	220176
Ruttan_10.4							0.42	0.02	0.79	0.03	1.47	0.11	0.01	0.02	-0.04	0.11	1445892081	11358495	63571601	216077
Ruttan_10.5							0.53	0.02	1.19	0.04	2.62	0.11	-0.08	0.02	0.36	0.12	1437761526	11297030	63243551	215521
Ruttan_10.6							0.73	0.02	1.34	0.05	2.43	0.15	0.04	0.02	-0.13	0.17	1441590453	11328525	63425259	215930
Balmat_10.1							8.10	0.02	15.82	0.05	30.23	0.11	-0.01	0.02	-0.03	0.11	1504377414	11910309	67140647	231443

Title	Sample Code	Drill Core	Lithology and pyrite occurrence	Zoning type	Zone	Pyrite generation	$\delta^{33}S$/‰	1σ/‰	$\delta^{34}S$/‰	1σ/‰	$\delta^{36}S$/‰	1σ/‰	$\Delta^{33}S$/‰	1σ/‰	$\Delta^{36}S$/‰	1σ/‰	CPS/$^{32}S^-$	CPS/$^{33}S^-$	CPS/$^{34}S^-$	CPS/$^{36}S^-$
Balmat_10.2							7.75	0.02	15.07	0.04	28.86	0.09	0.01	0.02	0.03	0.11	1481756785	11728786	66090975	227767
Balmat_10.3							7.87	0.01	15.26	0.05	28.74	0.13	0.04	0.01	-0.45	0.13	1452518937	11497338	64794535	223050
Ruttan-6.1							0.59	0.02	1.12	0.08	2.32	0.22	0.02	0.02	0.18	0.21	1291606834	10197682	57274449	233520
Ruttan-6.2							0.55	0.02	1.04	0.08	2.01	0.19	0.02	0.02	0.03	0.20	1236682335	9764933	54836770	223131
Ruttan-6.3							0.62	0.01	1.25	0.08	2.47	0.24	-0.02	0.01	0.10	0.22	1136499389	8974153	50402351	205195
Ruttan-6.4							0.57	0.02	1.12	0.09	2.22	0.19	-0.01	0.02	0.10	0.19	1130853227	8929755	50147510	204224
Ruttan-6.5							0.72	0.03	1.36	0.12	2.40	0.32	0.02	0.03	-0.18	0.31	1011582186	7988593	44867595	182641
Ruttan-6.6							0.65	0.02	1.32	0.13	2.27	0.26	-0.03	0.02	-0.23	0.27	988050594	7800707	43821700	178459
Balmat-6.1							7.46	0.01	14.76	0.08	27.87	0.21	-0.11	0.01	-0.36	0.22	1197043951	9517544	53803856	221678
Balmat-6.2							7.65	0.01	15.02	0.09	28.62	0.26	-0.06	0.02	-0.11	0.28	1056275542	8398258	47487755	195982
Balmat-6.3							7.68	0.02	15.44	0.11	28.87	0.23	-0.25	0.01	-0.67	0.23	1004484263	7989104	45178676	186389
Ruttan-5.1							0.59	0.02	1.10	0.08	2.39	0.18	0.03	0.02	0.29	0.20	1923131361	15200193	85408072	348779
Ruttan-5.2							0.54	0.01	1.00	0.09	2.31	0.20	0.02	0.02	0.41	0.21	1866180779	14746059	82865709	338244
Ruttan-5.3							0.56	0.01	1.17	0.11	2.08	0.19	-0.04	0.01	-0.14	0.21	1838702348	14531788	81661466	333723
Ruttan-5.4							0.61	0.01	1.24	0.10	2.24	0.13	-0.02	0.01	-0.12	0.16	1879884576	14855436	83497657	340584
Ruttan-5.6							0.62	0.01	1.35	0.14	2.57	0.21	-0.07	0.01	0.01	0.20	1570005277	12406637	69741154	284481
Ruttan-5.8							0.57	0.02	1.04	0.15	1.95	0.20	0.04	0.02	-0.03	0.21	967585249	7646248	42964922	175314
Balmat-5.1							7.69	0.01	15.11	0.08	29.50	0.17	-0.06	0.01	0.60	0.19	1989704273	15835168	89597489	370542
Balmat-5.2							7.78	0.01	15.24	0.10	29.53	0.21	-0.04	0.01	0.37	0.23	1933342045	15387675	87065812	360337
Balmat-5.3							7.96	0.01	15.52	0.13	29.65	0.17	-0.01	0.01	-0.04	0.16	1690328977	13453960	76142999	314708
Balmat-5.4							7.75	0.02	14.94	0.12	27.31	0.22	0.08	0.02	-1.26	0.24	989860917	7877490	44565378	183827
Ruttan_3.1							0.73	0.02	1.47	0.05	2.74	0.12	-0.03	0.02	-0.06	0.12	936955767	7324765	41047222	138734
Ruttan_3.2							0.52	0.03	1.00	0.14	1.84	0.17	0.01	0.03	-0.07	0.18	883684097	6905244	38685928	130648
Ruttan_3.3							0.77	0.02	1.43	0.03	2.56	0.13	0.04	0.02	-0.16	0.14	1028528751	8042025	45053644	152492
Ruttan_3.4							0.59	0.02	1.31	0.02	2.64	0.14	-0.09	0.02	0.16	0.14	1061777208	8299337	46504576	157293
Ruttan_4.1							0.63	0.02	1.27	0.04	2.60	0.13	-0.02	0.02	0.19	0.12	1022140376	7990485	44760594	151344
Ruttan_4.2							0.63	0.02	1.22	0.09	2.16	0.14	0.00	0.02	-0.16	0.13	1029092279	8041404	45055601	152101

Title	Sample Code	Drill Core	Lithology and pyrite occurrence	Zoning type	Zone	Pyrite generation	$\delta^{33}S$/‰	1σ/‰	$\delta^{34}S$/‰	1σ/‰	$\delta^{36}S$/‰	1σ/‰	$\Delta^{33}S$/‰	1σ/‰	$\Delta^{36}S$/‰	1σ/‰	CPS/$^{32}S^-$	CPS/$^{33}S^-$	CPS/$^{34}S^-$	CPS/$^{36}S^-$
Ruttan_4.3							0.62	0.02	1.15	0.06	2.45	0.14	0.03	0.02	0.27	0.16	1067927882	8344890	46743895	158319
Ruttan_4.4							0.60	0.02	1.27	0.07	2.24	0.14	-0.05	0.02	-0.18	0.16	1059036257	8275650	46365202	156655
Ruttan_4.5							0.54	0.02	0.88	0.04	1.88	0.15	0.09	0.02	0.21	0.16	1024161027	8002940	44825134	151417
Ruttan_4.6							0.55	0.02	1.02	0.08	1.71	0.16	0.03	0.02	-0.22	0.16	944657455	7382158	41358428	139699
Balmat_3.1							7.46	0.03	14.24	0.08	26.84	0.16	0.15	0.03	-0.38	0.16	894512457	7038297	39685212	135559
Balmat_3.2							7.40	0.02	14.52	0.11	27.64	0.13	-0.05	0.02	-0.14	0.13	1051134461	8269463	46629052	159356
Balmat_4.1							7.83	0.02	15.16	0.06	28.66	0.14	0.05	0.02	-0.35	0.14	1102054520	8676761	48942460	167538
Balmat_4.2							7.64	0.03	14.94	0.05	28.49	0.12	-0.03	0.03	-0.08	0.13	1055308148	8306662	46847941	160208
Ruttan_1							0.58	0.02	1.14	0.03	2.30	0.14	0.00	0.02	0.14	0.15	1602307876	12584332	70099496	238046
Ruttan_2							0.48	0.02	0.95	0.09	1.74	0.17	-0.01	0.02	-0.07	0.17	1500973792	11788587	65654909	222584
Ruttan_3							0.73	0.01	1.35	0.06	2.53	0.14	0.03	0.02	-0.03	0.14	1525841827	11986571	66777708	226465
Ruttan_4							0.68	0.03	1.32	0.04	2.31	0.16	0.00	0.03	-0.21	0.17	1516107513	11901441	66317893	224930
Ruttan_5							0.62	0.02	1.20	0.05	2.30	0.13	0.00	0.02	0.01	0.14	1541425206	12105793	67437167	228630
Ruttan_6							0.62	0.02	1.24	0.05	2.50	0.14	-0.02	0.02	0.15	0.16	1561790924	12266723	68329091	231412
Balmat_1							7.98	0.02	15.51	0.05	29.82	0.14	0.03	0.02	0.15	0.14	1542005725	12196707	68400774	234710
Balmat_2							7.97	0.02	15.50	0.10	29.57	0.17	0.02	0.03	-0.09	0.15	1526247575	12070998	67725290	232699
Balmat_3							7.90	0.02	15.44	0.06	29.28	0.14	-0.02	0.03	-0.26	0.14	1522824139	12042917	67553768	232008
Ruttan_3.1							0.75	0.03	1.24	0.08	2.60	0.18	0.11	0.02	0.24	0.16	1666440035	13200683	74036809	248041
Ruttan_3.2							0.65	0.02	1.33	0.13	2.86	0.25	-0.03	0.02	0.34	0.24	1669452867	13221750	74113524	247908
Ruttan_3.3							0.60	0.02	1.29	0.09	2.70	0.23	-0.06	0.02	0.25	0.23	1574085424	12461371	69839333	233194
Ruttan_3.5							0.85	0.02	1.81	0.15	3.31	0.20	-0.08	0.02	-0.12	0.21	942325288	7459963	41831635	139832
Ruttan_3.6							0.87	0.04	1.69	0.17	2.82	0.38	-0.01	0.04	-0.40	0.26	1017141835	8057735	45196787	151257
Balmat_3.1							7.40	0.03	14.40	0.09	27.31	0.18	0.01	0.02	-0.23	0.20	1610303074	12834466	72395184	245631
Balmat_3.2							7.26	0.02	14.19	0.09	26.92	0.23	-0.03	0.02	-0.22	0.25	1519585778	12112568	68336598	231270
Balmat_3.3							7.97	0.03	15.79	0.14	29.96	0.33	-0.13	0.03	-0.26	0.32	980105448	7818888	44163046	149636
Ruttan_1							0.49	0.02	0.99	0.05	2.01	0.12	-0.02	0.02	0.12	0.13	1579105616	12406192	69110610	234252
Ruttan_2							0.56	0.02	1.18	0.04	2.49	0.13	-0.05	0.02	0.24	0.14	1547330609	12150032	67693147	229633

Title	Sample Code	Drill Core	Lithology and pyrite occurrence	Zoning type	Zone	Pyrite generation	$\delta^{33}S$/‰	1σ/‰	$\delta^{34}S$/‰	1σ/‰	$\delta^{36}S$/‰	1σ/‰	$\Delta^{33}S$/‰	1σ/‰	$\Delta^{36}S$/‰	1σ/‰	CPS/$^{32}S^-$	CPS/$^{33}S^-$	CPS/$^{34}S^-$	CPS/$^{36}S^-$
Ruttan_3							0.62	0.03	1.21	0.04	2.06	0.13	0.00	0.03	-0.25	0.13	1593334940	12516332	69722187	236553
Ruttan_4							0.72	0.01	1.27	0.03	2.28	0.13	0.06	0.01	-0.13	0.13	1598368278	12555503	69944824	237168
Ruttan_5							0.71	0.02	1.33	0.04	2.67	0.13	0.02	0.02	0.15	0.13	1591083113	12498792	69641536	235976
Ruttan_6							0.61	0.01	1.22	0.04	2.18	0.14	-0.01	0.01	-0.13	0.16	1587509574	12470454	69478261	235460
Balmat_1							7.68	0.02	15.11	0.02	28.62	0.18	-0.07	0.02	-0.29	0.21	1580219815	12499663	70105446	241190
Balmat_2							7.69	0.02	14.98	0.06	28.17	0.15	0.00	0.02	-0.49	0.16	1580818131	12505858	70139033	240579
Balmat_3							7.65	0.02	15.07	0.05	28.51	0.16	-0.08	0.02	-0.31	0.16	1626521501	12867370	72173935	247629
Ruttan-4.5							0.49	0.02	0.92	0.05	1.54	0.18	0.01	0.02	-0.21	0.19	1689436307	13349469	75001563	305898
Ruttan-4.6							0.46	0.01	0.95	0.05	1.97	0.20	-0.03	0.01	0.17	0.20	1680204378	13274299	74593767	304597
Ruttan-4.7							0.79	0.01	1.50	0.06	2.76	0.14	0.02	0.01	-0.09	0.14	1891925265	14954167	84040679	342997
Ruttan-4.8							0.73	0.01	1.44	0.06	2.86	0.19	-0.01	0.01	0.13	0.20	1847161226	14599074	82049308	334928
Balmat-4.3							7.76	0.01	15.15	0.05	28.82	0.18	-0.01	0.01	-0.15	0.18	1685623986	13415133	75897123	313132
Balmat-4.4							7.64	0.01	15.05	0.05	29.17	0.19	-0.08	0.02	0.39	0.18	1887515040	15019525	84977573	350802
Ruttan-2.1							0.99	0.01	1.77	0.04	3.79	0.20	0.08	0.01	0.42	0.20	2513729975	19869238	111569168	454913
Ruttan-2.2							0.89	0.01	1.67	0.07	3.47	0.12	0.03	0.01	0.29	0.17	2509256759	19833339	111395138	454819
Ruttan-2.3							0.77	0.01	1.39	0.09	2.78	0.23	0.06	0.01	0.14	0.22	2458427239	19426247	109050390	445368
Ruttan-2.4							0.91	0.01	1.66	0.10	3.29	0.20	0.06	0.01	0.13	0.22	2495201350	19724692	110770879	452140
Ruttan-2.5							1.00	0.01	2.01	0.04	4.24	0.18	-0.04	0.01	0.40	0.18	2504933748	19798505	111195196	453875
Ruttan-2.6							0.92	0.01	1.68	0.08	3.73	0.19	0.05	0.01	0.53	0.18	2493216414	19705785	110651887	451604
Ruttan-2.7							1.01	0.01	1.94	0.04	4.14	0.17	0.01	0.01	0.46	0.18	2483885024	19633746	110262552	449795
Ruttan-2.8							0.99	0.01	1.97	0.04	4.04	0.16	-0.02	0.01	0.29	0.15	2486984067	19657629	110403845	451049
Ruttan-2.9							0.84	0.01	1.71	0.07	3.42	0.21	-0.04	0.01	0.17	0.19	2474358579	19557271	109820670	448085
Ruttan-2.10							0.83	0.01	1.79	0.09	3.13	0.13	-0.09	0.01	-0.27	0.16	2498870263	19749621	110928264	453079
Balmat-2.1							8.17	0.01	15.81	0.04	30.73	0.16	0.06	0.01	0.49	0.20	2491496957	19834614	112133771	463671
Balmat-2.2							7.99	0.01	15.49	0.07	29.64	0.17	0.04	0.01	0.00	0.18	2471835460	19673195	111206478	459854
Balmat-2.3							8.02	0.01	15.65	0.08	30.30	0.18	-0.01	0.01	0.36	0.21	2458231067	19569321	110636654	457117
Balmat-2.4							7.91	0.01	15.54	0.10	30.08	0.18	-0.06	0.01	0.35	0.18	2520490169	20062409	113431311	468439

Title	Sample Code	Drill Core	Lithology and pyrite occurrence	Zoning type	Zone	Pyrite generation	$\delta^{33}S$/‰	1σ/‰	$\delta^{34}S$/‰	1σ/‰	$\delta^{36}S$/‰	1σ/‰	$\Delta^{33}S$/‰	1σ/‰	$\Delta^{36}S$/‰	1σ/‰	CPS/$^{32}S^-$	CPS/$^{33}S^-$	CPS/$^{34}S^-$	CPS/$^{36}S^-$
Balmat-2.5							7.91	0.01	15.53	0.08	29.99	0.18	-0.06	0.01	0.28	0.18	2548657275	20288171	114697061	473822
TE29_1.1	MAS-8	FPL-122_598.0m	Pyrite band of BIF-hosted ore	C	1	1a	-0.89	0.03	-7.16	0.12			2.81	0.04			587474965	4610872	25518018	
TE29_1.2					2	2	2.49	0.06	3.57	0.07			0.65	0.06			563897055	4439564	24745346	
TE29_1.3					3	3	1.84	0.03	2.37	0.06			0.62	0.03			563818477	4436645	24719226	
TE29_1.4					4	4	2.54	0.04	3.50	0.07			0.74	0.04			562447561	4428850	24684276	
T11_4	MAS-8	FPL-122_598.0m	Pyrite band of BIF-hosted ore	C	1	1a	-1.22	0.03	-7.01	0.13			2.40	0.03			507807231	3977571	22097760	
T11_5					2	2	2.24	0.04	3.24	0.14			0.58	0.04			489029955	3843526	21499775	
T11_6					3	3	1.98	0.03	2.93	0.15			0.47	0.04			478649879	3761194	21038008	
T11_7					4	4	2.33	0.04	3.35	0.14			0.61	0.04			469599266	3691056	20648693	
T28_3.13	MAS-8	FPL-122_598.0m	Pyrite band of BIF-hosted ore	C	1	1a	-0.42	0.06	-6.46	0.33			2.91	0.06			582778065	4566683	25259460	
T28_3.14					2	2	1.58	0.06	0.78	0.25			1.18	0.05			580954149	4558259	25340048	
TE28_3.14'					2	2	1.43	0.04	2.34	0.11			0.23	0.04			1021298554	8006739	44693122	
T28_3.15					3	3	2.76	0.05	4.16	0.10			0.61	0.06			573103832	4507211	25116268	
T28_3.16					4	4	3.29	0.03	4.51	0.17			0.97	0.03			546240494	4298436	23948730	
T-1_19	MAS-8	FPL-122_598.0m	Pyrite band of BIF-hosted ore	B	1	2	0.88	0.05	0.73	0.15			0.51	0.05			425410985	3338295	18655711	
T-1_18					2	3	1.72	0.03	2.41	0.09			0.48	0.04			418061049	3283136	18363997	
T-1_17					3	4	2.31	0.04	3.40	0.12			0.56	0.04			429243283	3373080	18870621	
T28_3.1	MAS-8	FPL-122_598.0m	Pyrite band of BIF-hosted ore	C	1	1a	0.09	0.04	-3.50	0.14			1.90	0.04			592569356	4650767	25799279	
T28_3.2					3	3	1.79	0.04	2.92	0.09			0.28	0.04			555848807	4370538	24352439	
T28_3.3					4	4	2.99	0.07	4.54	0.13			0.66	0.08			531773848	4184038	23329879	
T28_3.4	MAS-8	FPL-122_598.0m	Pyrite band of BIF-hosted ore	B	1	2	1.90	0.05	3.71	0.09			-0.01	0.05			513935778	4039310	22523464	
T28_3.5					2	3	1.90	0.08	3.44	0.11			0.13	0.10			479977621	3770316	21023338	
T28_3.6					3	4	3.27	0.07	5.31	0.09			0.54	0.08			506029872	3981726	22203485	
T-1_8	MAS-8	FPL-122_598.0m	Pyrite band of BIF-hosted ore	C	1	1a	-0.12	0.04	-6.10	0.24			3.02	0.05			525113412	4117237	22868763	
T-1_9					3	3	2.41	0.05	2.89	0.18			0.92	0.06			488087799	3837509	21452370	

Title	Sample Code	Drill Core	Lithology and pyrite occurrence	Zoning type	Zone	Pyrite generation	$\delta^{33}S$/‰	1σ/‰	$\delta^{34}S$/‰	1σ/‰	$\delta^{36}S$/‰	1σ/‰	$\Delta^{33}S$/‰	1σ/‰	$\Delta^{36}S$/‰	1σ/‰	CPS/$^{32}S^-$	CPS/$^{33}S^-$	CPS/$^{34}S^-$	CPS/$^{36}S^-$
T-1_10					4	4	3.32	0.04	4.18	0.10			1.17	0.03			486716714	3829007	21417199	
T-1_11					1	2	2.50	0.05	3.57	0.15			0.67	0.04			463314347	3644291	20381470	
T-1_12	MAS-8	FPL-122_598.0m	Pyrite band of BIF-hosted ore	B	2	3	1.69	0.04	2.58	0.13			0.37	0.04			446233915	3506525	19606633	
T-1_13					3	4	2.35	0.04	3.53	0.09			0.53	0.04			445621921	3503737	19598974	
T11_1					1	2	2.26	0.04	3.81	0.16			0.30	0.03			519489458	4083554	22856711	
T11_2	MAS-8	FPL-122_598.0m	Pyrite band of BIF-hosted ore	B	2	3	2.20	0.05	3.04	0.18			0.63	0.05			514909717	4046517	22635722	
T11_3					3	4	2.72	0.05	4.02	0.13			0.65	0.05			516547544	4062903	22730614	
T10_9					1	2	1.43	0.04	2.48	0.05			0.16	0.05			557332703	4377688	24487991	
T10_10	MAS-8	FPL-122_598.0m	Pyrite band of BIF-hosted ore	B	1	2	1.82	0.04	2.98	0.09			0.28	0.04			521143318	4095551	22909006	
T10_11					2	3	2.15	0.03	3.56	0.10			0.32	0.04			509568758	4006279	22412967	
TE28_3.10					1	2	1.71	0.05	2.11	0.08			0.63	0.05			563035869	4429810	24669380	
TE28_3.11	MAS-8	FPL-122_598.0m	Pyrite band of BIF-hosted ore	B	2	3	1.65	0.07	2.13	0.13			0.56	0.07			540108289	4252472	23697690	
T28_3.13					3	4	1.89	0.09	3.33	0.16			0.18	0.10			472833590	3721754	20743419	
TE28_3.12'					3	4	2.37	0.02	3.45	0.08			0.60	0.02			1024961606	8041129	44897443	
TE29_1.9					2	2	1.83	0.11	2.91	0.08			0.33	0.11			528028077	4155583	23161325	
TE29_1.10	MAS-8	FPL-122_598.0m	Pyrite band of BIF-hosted ore	C	3	3	2.18	0.09	2.94	0.13			0.67	0.10			528673646	4163317	23197848	
TE29_1.11					4	4	2.42	0.05	3.69	0.04			0.52	0.05			532607425	4192758	23378118	
TE29_1.5					1	2	1.02	0.03	1.28	0.21			0.36	0.03			927254953	7264662	40516364	
TE29_1.6	MAS-8	FPL-122_598.0m	Pyrite band of BIF-hosted ore	B	2	3	1.66	0.03	2.51	0.07			0.37	0.03			948393114	7434631	41511635	
TE29_1.7					3	4	1.96	0.03	3.10	0.15			0.37	0.03			983401888	7709591	43034595	
TE29_1.5-					1	2	1.15	0.03	1.49	0.14			0.38	0.03			917438601	7186365	40076416	
TE29_1.6-	MAS-8	FPL-122_598.0m	Pyrite band of BIF-hosted ore	B	2	3	1.28	0.02	1.74	0.14			0.38	0.02			1014606796	7954289	44393337	
TE29_1.7-					3	4	2.08	0.05	2.87	0.24			0.61	0.05			1010713469	7925890	44252898	
T-1_6	MAS-8	FPL-122_598.0m	Pyrite band of BIF-hosted ore	A	1	3	2.25	0.07	2.59	0.25			0.92	0.07			489639520	3847787	21516969	
T-1_7					2	4	3.19	0.05	3.69	0.22			1.29	0.05			481099838	3785085	21163468	
T10_3	MAS-33	FPL-122_634.6m	Pyrite band of BIF-hosted ore	C	1	1a	-0.91	0.04	-6.24	0.31			2.31	0.04			471953768	3699278	20555558	
T10_4					2	2	1.98	0.05	3.20	0.15			0.33	0.05			433033990	3403422	19033818	

Title	Sample Code	Drill Core	Lithology and pyrite occurrence	Zoning type	Zone	Pyrite generation	$\delta^{33}S$/‰	1σ/‰	$\delta^{34}S$/‰	1σ/‰	$\delta^{36}S$/‰	1σ/‰	$\Delta^{33}S$/‰	1σ/‰	$\Delta^{36}S$/‰	1σ/‰	CPS/$^{32}S^-$	CPS/$^{33}S^-$	CPS/$^{34}S^-$	CPS/$^{36}S^-$
T10_5					3	3	1.05	0.05	1.66	0.11			0.19	0.05			493307236	3872402	21651362	
T10_6					4	4	2.23	0.06	3.88	0.12			0.23	0.06			469937401	3695491	20673936	
T10_1					1	1a	0.42	0.05	-4.33	0.08			2.65	0.05			454583110	3567449	19839286	
T10_2	MAS-33	FPL-122_634.6m	Pyrite band of BIF-hosted ore	C	2	2	2.88	0.05	3.74	0.10			0.96	0.06			429473905	3378365	18890807	
T10_7					3	3	1.76	0.06	2.83	0.10			0.30	0.07			484394665	3805366	21284928	
T-1_1					1	1a	0.36	0.04	-1.97	0.17			1.37	0.05			489425709	3840154	21405668	
T-1_2					2	2	2.15	0.04	3.19	0.09			0.51	0.04			451138875	3545251	19836371	
T-1_3	LQ	Queimada	Pyrite band of BIF-hosted ore (arsenopyrite-rich)	C	3	3	2.81	0.04	3.96	0.10			0.77	0.04			458489656	3605894	20170850	
T-1_4					3	3	2.90	0.05	4.09	0.11			0.79	0.05			476300162	3745569	20960825	
T-1_5					4	4	3.34	0.04	4.88	0.11			0.83	0.04			460498924	3623334	20279596	
TE45_Z3.6					1	2	1.33	0.08	1.71	0.12			0.45	0.11			743958327	5830022	32398840	
TE45_Z3.3					1	2	2.25	0.07	2.77	0.08			0.82	0.06			716196415	5621953	31330867	
TE45_Z3.2	LQ	Queimada	Pyrite band of BIF-hosted ore (arsenopyrite-rich)	B	2	3	2.14	0.09	3.37	0.11			0.40	0.09			777733268	6103355	33982393	
TE45_Z3.4					2	3	2.49	0.10	3.46	0.10			0.71	0.11			855861222	6713465	37390452	
TE45_Z3.5					2	3	3.23	0.10	4.99	0.08			0.67	0.09			735429610	5772381	32228599	
TE45_Z3.1					3	4	3.72	0.07	5.58	0.03			0.85	0.07			687444490	5399268	30113334	
TE45_Z1.3					1	2	2.43	0.08	3.29	0.03			0.74	0.07			820266537	6441137	35910240	
TE45_9_25_1.5	LQ	Queimada	Pyrite band of BIF-hosted ore (arsenopyrite-rich)	B	1	2	2.42	0.07	3.27	0.05			0.74	0.07			539167078	4241795	23634080	
TE45_Z1.2					2	3	2.90	0.07	4.03	0.03			0.83	0.07			760536258	5973306	33315550	
TE45_Z1.1					3	4	2.13	0.15	2.62	0.12			0.79	0.13			849198682	6667004	37084477	
TE45_Z7.3					1	2	3.14	0.08	4.30	0.03			0.93	0.08			747983547	5880590	32774559	
TE45_Z7.1	LQ	Queimada	Pyrite band of BIF-hosted ore (arsenopyrite-rich)	B	2	3	3.00	0.08	4.31	0.02			0.78	0.08			726186687	5700311	31780277	
TE45_Z7.2					3	4	2.75	0.11	4.12	0.05			0.64	0.11			838292127	6585302	36683669	
TE45_4.2					1	2	1.86	0.04	1.70	0.11			0.99	0.04			541683535	4257725	23690963	
TE45_4.3	LQ	Queimada	Pyrite band of BIF-hosted ore (arsenopyrite-rich)	B	2	3	2.96	0.05	4.01	0.04			0.90	0.05			570152953	4489290	25023280	
TE45_4.1					3	4	3.05	0.03	4.41	0.05			0.78	0.03			542562699	4271407	23816034	
T28_3.23	FLV-	FLV-	Pyrite band of BIF-hosted ore	C	1	1a	1.06	0.07	-2.53	0.13			2.36	0.07			600120220	4714978	26154228	

Title	Sample Code	Drill Core	Lithology and pyrite occurrence	Zoning type	Zone	Pyrite generation	$\delta^{33}S$/‰	1σ/‰	$\delta^{34}S$/‰	1σ/‰	$\delta^{36}S$/‰	1σ/‰	$\Delta^{33}S$/‰	1σ/‰	$\Delta^{36}S$/‰	1σ/‰	CPS/$^{32}S^-$	CPS/$^{33}S^-$	CPS/$^{34}S^-$	CPS/$^{36}S^-$
T28_3.23'	167	167_225m	(arsenopyrite-rich)		1	1a	0.53	0.05	-3.03	0.04			2.09	0.05			565240494	4437666	24616692	
T28_3.24					2	2	2.93	0.05	4.09	0.07			0.82	0.05			572001557	4502095	25085379	
T28_3.24'					2	2	2.17	0.03	2.93	0.12			0.66	0.04			551352663	4334881	24142477	
T28_3.25					3	3	1.09	0.04	1.69	0.07			0.22	0.05			535825537	4209219	23448930	
T28_3.26					4	4	2.31	0.03	3.75	0.10			0.38	0.03			506296527	3981999	22195083	
TE28_3.26'					4	4	1.87	0.05	2.87	0.20			0.39	0.05			1046434067	8204461	45812658	
TE28_2.61					1	1a	-1.09	0.02	-5.17	0.14			1.57	0.02			1005534554	7859716	43642546	
TE28_2.62	FLV-167	FLV-167_225m	Pyrite band of BIF-hosted ore (arsenopyrite-rich)	C	2	2	1.63	0.04	1.61	0.18			0.80	0.04			980760041	7688209	42887178	
TE28_2.63					3	3	1.69	0.03	2.47	0.13			0.42	0.03			968611948	7592959	42371052	
TE28_2.64					4	4	1.92	0.04	3.11	0.08			0.32	0.04			983423806	7712534	43076436	
TE45_57_2.1					1	1b	8.47	0.08	3.80	0.02			6.52	0.07			566170830	4480953	24824759	
TE45_57_2.4					1	1b	8.40	0.03	2.77	0.14			6.98	0.03			565053804	4473921	24780503	
TE45_57_2.2	MAS-57	FLU-173	Pyrite in smoky chert-hosted ore	F	2	2	3.09	0.08	4.86	0.13			0.58	0.08			575986723	4532155	25275349	
TE45_57_2.3					3	3	2.40	0.04	3.51	0.03			0.59	0.03			598781036	4710527	26253351	
TE45_57_2.5					3	3	4.52	0.04	5.87	0.04			1.50	0.04			598361868	4717210	26300179	
TE45_57_1.1					1	1b	6.40	0.09	1.89	0.03			5.43	0.09			668911571	5280160	29247886	
TE45_57_1.2	MAS-57	FLU-173	Pyrite in smoky chert-hosted ore	F	2	2	2.03	0.10	3.25	0.05			0.36	0.10			763449558	5988642	33378196	
TE45_57_1.3					3	3	3.11	0.10	4.14	0.03			0.98	0.09			698097885	5482884	30577249	
TE48-3_1					orange core	1b	6.62	0.06	3.71	0.08			4.71	0.06			553012209	4349311	24287876	
TE48_3.1					blue	2	2.86	0.07	3.20	0.10			1.21	0.07			383935486	3010039	16848423	
TE48_3.3	MAS-25	FPL-120_639.2m	Pyrite lamina of sulphidized BIF	D	blue	2	3.37	0.07	3.29	0.04			1.68	0.07			388381397	3043984	17035769	
TE48-3_2					blue	2	2.25	0.05	3.04	0.11			0.69	0.05			551804752	4322454	24218719	
TE48-3_3					blue	2	3.16	0.05	2.91	0.07			1.66	0.05			550476588	4315224	24155533	
TE48-1.2					orange core	1b	9.88	0.06	6.75	0.07			6.41	0.07			384512710	3033798	16913358	
TE48-1.1	MAS-25	FPL-120_639.2m	Pyrite lamina of sulphidized BIF	D	blue	2	3.48	0.06	3.75	0.06			1.55	0.06			379130021	2972482	16630685	
TE48-1.3					orange	2	3.70	0.08	3.93	0.11			1.68	0.08			402535667	3158234	17678285	

Title	Sample Code	Drill Core	Lithology and pyrite occurrence	Zoning type	Zone	Pyrite generation	$\delta^{33}S$/‰	1σ/‰	$\delta^{34}S$/‰	1σ/‰	$\delta^{36}S$/‰	1σ/‰	$\Delta^{33}S$/‰	1σ/‰	$\Delta^{36}S$/‰	1σ/‰	CPS/$^{32}S^-$	CPS/$^{33}S^-$	CPS/$^{34}S^-$	CPS/$^{36}S^-$
TE48_5.1					blue	2	3.36	0.06	3.26	0.10			1.69	0.07			552919307	4335215	24260016	
TE48_5.2	MAS-25	FPL-120_639.2m	Pyrite lamina of sulphidized BIF	D/E	blue	2	2.49	0.04	3.55	0.07			0.66	0.04			583309425	4568210	25618839	
TE48_5.3					orange	2	4.13	0.03	4.23	0.10			1.95	0.03			592224857	4644791	26019120	
TE48-1.4	MAS-25	FPL-120_639.2m	Pyrite lamina of sulphidized BIF	D	orange core	1b	9.70	0.08	5.70	0.07			6.77	0.07			361552919	2852785	15900786	
TE48-1.5					blue	2	2.78	0.05	4.11	0.07			0.66	0.05			372342830	2917335	16346812	
TE48-4.1	MAS-25	FPL-120_639.2m	Pyrite lamina of sulphidized BIF	E	orange	2	3.44	0.15	3.94	0.05			1.41	0.13			393372164	3082159	17256196	
TE48-4.2					blue	2	3.54	0.05	4.01	0.06			1.48	0.05			404438505	3171136	17752598	
TE48-4.3	MAS-25	FPL-120_639.2m	Pyrite lamina of sulphidized BIF	D	orange core	1b	8.46	0.08	4.44	0.04			6.18	0.08			386697684	3046660	16966498	
TE48_4.1					blue	2	3.50	0.05	3.62	0.08			1.64	0.06			597821565	4688562	26257726	
TE48-2.2					orange core	1b	8.45	0.08	5.54	0.05			5.60	0.09			354011257	2788457	15559977	
TE48-2.1	MAS-25	FPL-120_639.2m	Pyrite lamina of sulphidized BIF	D	blue	2	3.53	0.06	3.89	0.10			1.53	0.06			386929043	3034961	16986529	
TE48-17_1					orange	2	3.92	0.06	4.09	0.11			1.82	0.05			565050627	4430075	24820587	
TE48-17_2					orange	2	3.43	0.04	3.28	0.10			1.74	0.04			545132997	4272849	23929275	
TE48_1	MAS-57	FLU-173	Pyrite in smoky chert-hosted ore	G	blue	2	2.22	0.07	3.16	0.08			0.59	0.06			548628401	4297138	24081630	
TE48_2					orange	2	3.63	0.11	3.93	0.05			1.61	0.10			558752321	4382348	24551425	
TE48_10.1	MAS-57	FLU-173	Pyrite in smoky chert-hosted ore	G	orange	2	3.54	0.06	3.78	0.12			1.59	0.06			529770468	4151969	23261767	
TE48_10.2					blue	2	2.37	0.05	3.49	0.11			0.58	0.06			526440668	4122505	23110728	
TE9_A	FPL-179	FPL-179_395.0m	Pyrite microcrystal aggregate within the quartz+carbonate+pyrite veinlet in carbonaceous phyllite				13.18	0.12	12.68	0.17			6.67	0.13			689367586	5461405	30336670	
TE9_B	FPL-179	FPL-179_395.0m	Pyrite microcrystal aggregate within the quartz+carbonate+pyrite veinlet in carbonaceous phyllite				13.25	0.12	11.03	0.05			7.59	0.12			770184534	6106847	33936402	
TE9_C	FPL-179	FPL-179_395.0m	Pyrite microcrystal aggregate within the quartz+carbonate+pyrite veinlet in carbonaceous phyllite				11.52	0.36	14.21	0.23			4.23	0.39			769322274	6085257	33872738	
TE9_D	FPL-179	FPL-179_395.0m	Pyrite microcrystal aggregate within the quartz+carbonate+pyrite veinlet in carbonaceous phyllite				7.96	0.13	9.98	0.21			2.83	0.15			816150060	6448798	36044439	
TE9_E	FPL-	FPL-	Pyrite microcrystal aggregate within the quartz+carbonate+pyrite veinlet in				14.34	0.23	14.69	0.06			6.81	0.21			869564211	6905311	38467902	

Title	Sample Code	Drill Core	Lithology and pyrite occurrence	Zoning type	Zone	Pyrite generation	$\delta^{33}S$/‰	1σ/‰	$\delta^{34}S$/‰	1σ/‰	$\delta^{36}S$/‰	1σ/‰	$\Delta^{33}S$/‰	1σ/‰	$\Delta^{36}S$/‰	1σ/‰	CPS/$^{32}S^-$	CPS/$^{33}S^-$	CPS/$^{34}S^-$	CPS/$^{36}S^-$
	179	179_395.0m	carbonaceous phyllite																	
TE9_F	FPL-179	FPL-179_395.0m	Pyrite microcrystal aggregate within the quartz+carbonate+pyrite veinlet in carbonaceous phyllite				2.46	0.20	5.56	0.18			-0.40	0.17			873053061	6849972	38231277	
TE9_G	FPL-179	FPL-179_395.0m	Pyrite microcrystal aggregate within the quartz+carbonate+pyrite veinlet in carbonaceous phyllite				8.85	0.12	10.18	0.09			3.62	0.11			797761826	6313378	35203675	
TE9_I	FPL-179	FPL-179_395.0m	Pyrite microcrystal aggregate within the quartz+carbonate+pyrite veinlet in carbonaceous phyllite				5.02	0.10	6.18	0.02			1.84	0.10			815735267	6424590	35812337	
TE9_F'	FPL-179	FPL-179_395.0m	Pyrite microcrystal aggregate within the quartz+carbonate+pyrite veinlet in carbonaceous phyllite				17.82	0.07	14.58	0.11			10.34	0.07			761776059	6068427	33639759	
Ruttan_1							0.68	0.08	1.16	0.13			0.08	0.08			504472310	3965388	22089987	
Ruttan_2							0.78	0.03	1.35	0.06			0.09	0.03			515695348	4053894	22581539	
Ruttan_4							0.81	0.05	1.50	0.06			0.04	0.05			514767600	4047314	22547634	
Ruttan_5							0.86	0.04	1.51	0.05			0.09	0.05			509359771	4005192	22311122	
Balmat_1							7.66	0.07	14.62	0.08			0.15	0.08			532201333	4212696	23617431	
Balmat_2							8.04	0.05	15.24	0.05			0.21	0.05			562876600	4456980	24993838	
Ruttan_11.1							0.37	0.05	0.76	0.16			-0.02	0.05			458101386	3593466	20093527	
Ruttan_11.2							0.54	0.05	1.14	0.10			-0.05	0.05			453936371	3562342	19914822	
Ruttan_11.3							1.17	0.04	1.90	0.10			0.20	0.04			479069900	3762222	21035671	
Ruttan_11.4							0.90	0.03	1.52	0.10			0.11	0.03			467041360	3666830	20498391	
Ruttan_11.5							0.44	0.04	1.06	0.09			-0.10	0.05			441247207	3461765	19352725	
Ruttan_11.6							0.30	0.04	0.82	0.04			-0.12	0.04			451381573	3542208	19797003	
Balmat_11.1							7.84	0.04	15.41	0.10			-0.06	0.04			473805991	3745395	21086070	
Balmat_11.2							7.17	0.05	14.34	0.08			-0.19	0.05			465756705	3678875	20704487	
Ruttan_1							0.97	0.04	1.73	0.09			0.08	0.05			574345094	4510501	25123734	
Ruttan_2							0.89	0.06	1.88	0.05			-0.08	0.06			582121708	4572629	25481208	
Ruttan_3							0.46	0.07	1.46	0.08			-0.29	0.09			535054678	4200705	23411132	
Ruttan_4							0.56	0.12	1.41	0.20			-0.17	0.12			503961479	3957331	22047633	

Title	Sample Code	Drill Core	Lithology and pyrite occurrence	Zoning type	Zone	Pyrite generation	$\delta^{33}S$/‰	1σ/‰	$\delta^{34}S$/‰	1σ/‰	$\delta^{36}S$/‰	1σ/‰	$\Delta^{33}S$/‰	1σ/‰	$\Delta^{36}S$/‰	1σ/‰	CPS/$^{32}S^-$	CPS/$^{33}S^-$	CPS/$^{34}S^-$	CPS/$^{36}S^-$
Ruttan_5							1.02	0.09	2.05	0.16			-0.04	0.09			550556768	4324068	24089314	
Ruttan_8							0.27	0.07	0.46	0.11			0.03	0.06			544251143	4272522	23787296	
Balmat_1							7.26	0.08	15.09	0.14			-0.48	0.09			515506536	4077668	22877766	
Balmat_2							8.77	0.08	16.86	0.09			0.13	0.07			556270990	4401394	24691756	
Balmat_3							6.77	0.08	13.44	0.14			-0.13	0.09			484045770	3823948	21421393	
Ruttan_29.1							0.73	0.04	1.39	0.15			0.01	0.04			970018468	7598580	42402047	
Ruttan_29.2							0.79	0.05	1.49	0.13			0.02	0.05			960331612	7519295	41937564	
Ruttan_29.3							0.61	0.04	1.15	0.07			0.02	0.04			955996642	7486670	41768860	
Ruttan_29.4							0.69	0.03	1.31	0.17			0.01	0.03			958662533	7505852	41864167	
Ruttan_29.5							0.51	0.02	1.05	0.14			-0.03	0.02			913808366	7157317	39932154	
Ruttan_29.6							0.38	0.04	0.81	0.14			-0.04	0.04			877177238	6871052	38338583	
Balmat_29.1							7.59	0.02	14.83	0.19			-0.02	0.02			929382925	7329548	41158557	
Balmat_29.2							7.46	0.02	14.67	0.15			-0.07	0.02			950610753	7494832	42091972	
Ruttan_1.1							0.95	0.03	1.84	0.03			0.00	0.03			413989321	3249212	18178096	
Ruttan_1.2							0.49	0.05	0.95	0.15			0.00	0.05			467316901	3666248	20499760	
Ruttan_1.3							0.78	0.05	1.53	0.15			0.00	0.05			475152072	3728423	20855016	
Ruttan_1.4							0.82	0.04	1.38	0.13			0.11	0.03			470095129	3689826	20631759	
Ruttan_1.5							0.85	0.03	1.46	0.13			0.10	0.04			454489682	3567028	19944074	
Ruttan1.6							0.26	0.04	0.60	0.13			-0.05	0.04			452541508	3548938	19840989	
Ruttan1.7							0.21	0.03	0.70	0.11			-0.16	0.03			444007216	3483026	19468660	
Ruttan1.8							0.74	0.04	1.28	0.08			0.08	0.04			474328658	3721939	20814056	
Ruttan1.9							0.62	0.03	1.18	0.08			0.01	0.03			447757087	3513407	19644377	
Ruttan1.10							0.47	0.05	1.08	0.05			-0.08	0.05			454433560	3564778	19936734	
Balmat_1.1							8.12	0.03	15.63	0.08			0.10	0.03			482926403	3818451	21495224	
Balmat_1.2							7.86	0.03	15.33	0.07			0.00	0.03			467225677	3692379	20792225	
Balmat_1.3							7.76	0.07	15.45	0.11			-0.17	0.06			464621865	3671408	20675283	
Balmat_1.4							7.68	0.06	15.01	0.13			-0.02	0.06			486497889	3843955	21642764	

Title	Sample Code	Drill Core	Lithology and pyrite occurrence	Zoning type	Zone	Pyrite generation	$\delta^{33}S$/‰	1σ/‰	$\delta^{34}S$/‰	1σ/‰	$\delta^{36}S$/‰	1σ/‰	$\Delta^{33}S$/‰	1σ/‰	$\Delta^{36}S$/‰	1σ/‰	CPS/$^{32}S^-$	CPS/$^{33}S^-$	CPS/$^{34}S^-$	CPS/$^{36}S^-$
Ruttan_10.1							0.44	0.06	1.12	0.08			-0.14	0.06			478430111	3752993	20991039	
Ruttan_10.2							1.25	0.05	1.99	0.08			0.22	0.06			473740832	3720132	20804276	
Ruttan_10.4							0.05	0.04	0.38	0.12			-0.14	0.04			478165950	3750718	20960656	
Ruttan_10.5							0.49	0.05	1.18	0.12			-0.12	0.05			482375938	3786364	21164541	
Ruttan_10.6							0.39	0.05	1.15	0.11			-0.20	0.05			487589751	3827221	21394221	
Balmat_10.1							8.05	0.05	15.03	0.14			0.34	0.04			494331510	3909112	21994433	
Balmat_10.2							7.75	0.06	15.49	0.13			-0.20	0.05			504470711	3988146	22452601	
Ruttan_1							0.92	0.06	1.44	0.06			0.17	0.07			827360151	6490950	36184154	
Ruttan_2							0.35	0.09	1.05	0.16			-0.19	0.11			855671515	6708195	37318402	
Ruttan_3							1.16	0.07	1.73	0.05			0.27	0.07			780463891	6116007	34025689	
Ruttan_4							0.80	0.09	1.75	0.05			-0.10	0.09			751746521	5884906	32752926	
Ruttan_5							0.45	0.07	0.62	0.22			0.13	0.08			790658989	6188562	34460085	
Ruttan_7							0.95	0.09	1.96	0.03			-0.06	0.08			727007778	5697447	31754374	
Ruttan_8							0.32	0.08	0.42	0.08			0.10	0.09			764830936	5984376	33335738	
Ruttan_9							1.03	0.06	1.58	0.11			0.21	0.07			758960108	5937949	33033977	
Ruttan_10							0.61	0.08	1.31	0.23			-0.06	0.09			731332667	5723784	31867956	
Ruttan_11							0.60	0.09	1.24	0.21			-0.03	0.10			882944061	6927656	38603693	
Ruttan_12							0.94	0.09	1.72	0.04			0.06	0.09			842751030	6603198	36807917	
Ruttan_13							0.24	0.12	0.61	0.12			-0.07	0.12			831168539	6502859	36226235	
Ruttan_14							0.75	0.07	1.43	0.06			0.02	0.07			728554802	5704986	31754546	
Ruttan_16							0.79	0.07	1.62	0.04			-0.05	0.07			754532984	5917638	32969986	
Ruttan_17							0.87	0.10	1.72	0.06			-0.02	0.09			714569651	5604892	31214621	
Balmat_1							8.36	0.06	16.23	0.07			0.03	0.06			781312565	6167197	34623955	
Balmat_2							8.12	0.10	15.89	0.07			-0.04	0.11			802500316	6340871	35594922	
Balmat_3							7.72	0.08	14.78	0.07			0.14	0.08			845724069	6677134	37456230	
Balmat_4							7.46	0.14	14.20	0.07			0.17	0.11			856819432	6761268	37917572	
Balmat_5							7.79	0.11	15.24	0.16			-0.03	0.10			774914813	6112956	34271388	

Title	Sample Code	Drill Core	Lithology and pyrite occurrence	Zoning type	Zone	Pyrite generation	$\delta^{33}S$/‰	1σ/‰	$\delta^{34}S$/‰	1σ/‰	$\delta^{36}S$/‰	1σ/‰	$\Delta^{33}S$/‰	1σ/‰	$\Delta^{36}S$/‰	1σ/‰	CPS/$^{32}S^-$	CPS/$^{33}S^-$	CPS/$^{34}S^-$	CPS/$^{36}S^-$
Balmat_6							7.38	0.07	14.67	0.15			-0.15	0.09			791275353	6242652	34972749	
Ruttan_1							0.46	0.06	1.24	0.19			-0.17	0.08			530931598	4168603	23224614	
Ruttan_2							0.49	0.06	1.35	0.07			-0.21	0.05			531679224	4174120	23267236	
Ruttan_3							0.67	0.04	1.54	0.10			-0.12	0.03			531754616	4176088	23272380	
Ruttan_3							0.92	0.04	1.57	0.05			0.11	0.04			547375240	4298638	23942711	
Ruttan_4							0.81	0.06	1.20	0.05			0.19	0.05			578254298	4543376	25297147	
Ruttan_5							0.64	0.04	1.04	0.06			0.10	0.05			559921034	4397155	24484286	
Ruttan_6							0.34	0.05	0.57	0.06			0.05	0.06			534115093	4193458	23350287	
Ruttan_7							0.83	0.03	1.31	0.03			0.15	0.04			578545474	4543997	25303009	
Ruttan_8							0.63	0.04	1.14	0.03			0.04	0.04			549342848	4314618	24031189	
Ruttan_9							0.39	0.08	1.04	0.18			-0.15	0.09			541705695	4251062	23692650	
Balmat_1							8.35	0.09	16.62	0.15			-0.17	0.10			542017411	4287304	24072637	
Balmat_2							7.66	0.03	14.83	0.24			0.05	0.03			812370510	6424978	36033756	
Balmat_3							7.93	0.03	15.51	0.04			-0.03	0.03			553236677	4374608	24543039	
Balmat_4							7.25	0.05	14.96	0.09			-0.42	0.04			529337494	4183683	23468660	
Ruttan_1							0.63	0.04	0.89	0.03			0.17	0.04			548048976	4284400	24007531	
Ruttan_2							0.16	0.08	0.58	0.18			-0.14	0.08			519513593	4060253	22732921	
Ruttan_3							0.85	0.06	1.38	0.09			0.14	0.06			557406199	4356567	24405045	
Ruttan_4							0.94	0.07	1.29	0.08			0.28	0.07			548931696	4291803	24055079	
Ruttan_5							0.21	0.06	0.91	0.05			-0.26	0.07			573520859	4482950	25128257	
Ruttan_6							0.74	0.07	1.36	0.07			0.05	0.06			565172187	4418436	24770130	
Ruttan_8							0.50	0.05	1.04	0.08			-0.03	0.05			566428376	4427858	24812730	
Ruttan_11							0.37	0.06	0.72	0.05			0.00	0.06			551130052	4308682	24140839	
Ruttan_12							0.34	0.04	0.79	0.05			-0.06	0.05			555114895	4337142	24316526	
Balmat_1							7.83	0.08	15.08	0.05			0.09	0.09			575638296	4535275	25575000	
Balmat_2							8.21	0.05	15.26	0.09			0.38	0.06			563575436	4440251	25036326	
Balmat_3							8.04	0.06	15.13	0.11			0.28	0.06			567094894	4467098	25201173	

Title	Sample Code	Drill Core	Lithology and pyrite occurrence	Zoning type	Zone	Pyrite generation	$\delta^{33}S$/‰	1σ/‰	$\delta^{34}S$/‰	1σ/‰	$\delta^{36}S$/‰	1σ/‰	$\Delta^{33}S$/‰	1σ/‰	$\Delta^{36}S$/‰	1σ/‰	CPS/$^{32}S^-$	CPS/$^{33}S^-$	CPS/$^{34}S^-$	CPS/$^{36}S^-$
Balmat_4							8.23	0.06	15.43	0.09			0.32	0.06			553580053	4360335	24604920	
Ruttan_9.1							0.81	0.06	1.38	0.04			0.10	0.07			369192009	2885987	16158605	
Ruttan_9.2							0.64	0.05	1.24	0.08			0.00	0.05			386310807	3021190	16901825	
Ruttan_9.1							0.53	0.06	1.06	0.21			-0.02	0.06			394357076	3085180	17267636	
Ruttan_9.2							0.44	0.07	0.70	0.12			0.08	0.07			399138095	3122152	17473086	
Ruttan_9.4							0.90	0.04	1.52	0.04			0.11	0.05			387653074	3030602	16970934	
Ruttan_9.5							0.86	0.05	1.43	0.04			0.13	0.06			391419671	3061102	17138168	
Ruttan_9.6							0.57	0.05	1.09	0.05			0.01	0.05			382589823	2991031	16735924	
Ruttan_9.7							0.75	0.05	1.57	0.10			-0.06	0.06			398167820	3114892	17440424	
Ruttan_9.8							0.85	0.06	1.67	0.08			-0.01	0.06			386936653	3026700	16937775	
Ruttan_9.9							0.73	0.07	1.36	0.08			0.03	0.07			396448452	3100735	17352213	
Ruttan_9.10							0.94	0.04	2.06	0.08			-0.12	0.04			395946507	3098404	17349162	
Ruttan_9.11							0.78	0.06	1.68	0.11			-0.09	0.06			392644322	3071752	17196704	
Ruttan_9.12							0.59	0.08	1.38	0.10			-0.12	0.08			376164616	2942337	16466283	
Ruttan_9.13							0.38	0.07	1.17	0.14			-0.22	0.05			391041907	3058451	17115821	
Balmat_9.1							7.39	0.08	14.23	0.08			0.09	0.07			379628685	2988821	16825014	
Balmat_9.1							7.34	0.05	14.40	0.10			-0.05	0.05			385290326	3033612	17092673	
Balmat_9.2							7.33	0.05	14.15	0.35			0.07	0.05			625824846	4922716	27719868	
Balmat_9.3							7.52	0.05	14.48	0.12			0.09	0.06			380524836	2997150	16876052	
Balmat_9.4							7.15	0.07	14.09	0.13			-0.09	0.07			382113033	3009108	16948805	
Balmat_9.5							7.39	0.07	14.44	0.16			-0.02	0.07			377790502	2975211	16754504	
Balmat_9.6							6.99	0.06	13.97	0.16			-0.18	0.07			382222201	3009398	16949691	
Ruttan_2							0.70	0.13	1.31	0.02			0.02	0.10			756098922	5922997	32967888	
Ruttan_3							0.86	0.09	1.52	0.03			0.07	0.09			819305782	6424289	35804727	
Ruttan_4							0.04	0.06	0.61	0.03			-0.27	0.07			797198435	6245427	34763850	
Ruttan_5							0.66	0.10	1.71	0.06			-0.22	0.11			766179989	6003851	33473473	
Ruttan_6							0.69	0.07	1.24	0.03			0.05	0.07			754943099	5919347	32941312	

Title	Sample Code	Drill Core	Lithology and pyrite occurrence	Zoning type	Zone	Pyrite generation	$\delta^{33}S$/‰	1σ/‰	$\delta^{34}S$/‰	1σ/‰	$\delta^{36}S$/‰	1σ/‰	$\Delta^{33}S$/‰	1σ/‰	$\Delta^{36}S$/‰	1σ/‰	CPS/$^{32}S^-$	CPS/$^{33}S^-$	CPS/$^{34}S^-$	CPS/$^{36}S^-$
Ruttan_7							0.55	0.08	1.05	0.06			0.01	0.08			810752402	6357495	35423838	
Balmat_1							7.74	0.07	15.51	0.10			-0.22	0.07			759491902	5992463	33605094	
Balmat_2							7.99	0.06	15.64	0.03			-0.03	0.06			836141424	6599436	37093283	
Balmat_3							8.06	0.07	15.99	0.04			-0.14	0.08			793469739	6266712	35190065	

Table 6.7 Results of semi-quantitative determination of gold abundance in each growth zone of zoned pyrite.

Title	Spot	Sample code	Drill core	Lithology and pyrite occurrence	Zoning type	Growth zone	Pyrite generation	CPS($^{133}Cs^{32}S_2^-$)	CPS($^{197}Au^-$)	1000×CPS($^{133}Cs^{32}S_2^-$)/CPS($^{197}Au^-$)
TE28_3.1_1	Big	MAS-8	FPL-122_598.0m	Pyrite band of BIF-hosted ore	C	1	1a	3697.76	6.56	1.77
TE28_3.1_1"						1	1a	2672.38	2.16	0.81
TE28_3.1_2						3	3	3662.16	10.99	3.00
TE28_3.1_5						3	3	2678.26	16.93	6.32
TE28_3.1_6						3	3	2659.39	13.82	5.20
TE28_3.1_2'						3	3	2622.50	9.21	3.51
TE28_3.1_4						3	3	2756.92	24.76	8.98
TE28_3.1_3						4	4	3313.97	3.48	1.05
TE28_3.1_3'						4	4	2571.93	1.46	0.57
TE28_3.1_7						4	4	2626.44	1.44	0.55
TE28_4.4_1	Big	MAS-8	FPL-122_598.0m	Pyrite band of BIF-hosted ore	B	1	2	4217.47	461.77	109.49
TE28_4.4_1'						1	2	3376.68	234.33	69.40
TE28_4.4_2'						2	3	3246.72	39.52	12.17
TE28_4.4_2						2	3	4294.09	39.13	9.11
TE28_4.4_3						3	4	4257.52	2.54	0.60
TE28_4.4_4						3	4	4628.78	4.03	0.87
TE28_4.4_4'						3	4	3213.00	2.73	0.85
TE28_4.4_3'						3	4	3155.50	1.77	0.56
TE28_3.16_1	Big	MAS-8	FPL-122_598.0m	Pyrite band of BIF-hosted ore	C	1	1a	4244.77	52.81	12.44
TE28_3.16_2'						2	2	3344.70	76.43	22.85
TE28_3.16_2						2	2	3896.64	100.52	25.80
TE28_3.16_3						3	3	4119.66	60.60	14.71
TE28_3.16_3'						3	3	3152.95	35.92	11.39
TE28_3.16_4						4	4	4090.49	11.92	2.91
TE28_3.16_4'						4	4	3102.73	4.02	1.30
TE28_3.5_2	Big	MAS-8	FPL-122_598.0m	Pyrite band of BIF-hosted ore	B	1	2	3582.33	185.80	51.87

Title	Spot	Sample code	Drill core	Lithology and pyrite occurrence	Zoning type	Growth zone	Pyrite generation	CPS($^{133}Cs^{32}S_2^-$)	CPS($^{197}Au^-$)	1000×CPS($^{133}Cs^{32}S_2^-$)/CPS($^{197}Au^-$)
TE28_3.5_2'						1	2	3293.83	209.86	63.71
TE28_3.5_1'						2	3	3215.88	6.24	1.94
TE28_3.5_1						2	3	3527.15	17.31	4.91
TE28_3.5_3						3	4	4239.30	5.57	1.31
TE28_3.5_3'						3	4	2928.29	2.35	0.80
TE29_2.2_1						1	2	4424.22	205.40	46.43
TE29_2.2_1'						1	2	3187.21	77.87	24.43
TE29_2.2_2	Big	MAS-8	FPL-122_598.0m	Pyrite band of BIF-hosted ore	B	2	3	4399.83	35.16	7.99
TE29_2.2_2'						2	3	3154.64	11.66	3.70
TE29_2.2_3						3	4	4261.84	9.37	2.20
TE29_2.2_3'						3	4	3016.85	2.42	0.80
TE29_1.1_1						1	1a	4187.87	39.75	9.49
TE29_1.1_2'						2	2	3248.01	98.10	30.20
TE29_1.1_3	Big	MAS-8	FPL-122_598.0m	Pyrite band of BIF-hosted ore	C	3	3	4109.16	25.41	6.18
TE29_1.1_3'						3	3	3171.24	20.49	6.46
TE29_1.1_4						4	4	3908.63	7.02	1.80
TE29_1.1_4'						4	4	3054.92	1.87	0.61
TE29_2.4_3						3	3	3895.66	31.80	8.16
TE29_2.4_3'	Big	MAS-8	FPL-122_598.0m	Pyrite band of BIF-hosted ore	C	3	3	3074.62	5.22	1.70
TE29_2.4_4						4	4	4057.18	1.32	0.32
TE29_2.4_4'						4	4	3063.19	2.02	0.66
TE28_2.6_1						1	1a	4333.65	11.15	2.57
TE28_2.6_3	Big	FLV-167	FLV-167_225m	Pyrite band of BIF-hosted ore (arsenopyrite-rich)	C	3	3	4273.40	100.12	23.43
TE28_2.6_4						4	4	4288.52	2.31	0.54
TE28_3.23_3						3	3	3831.88	182.89	47.73
TE28_3.23_4	Big	FLV-167	FLV-167_225m	Pyrite band of BIF-hosted ore (arsenopyrite-rich)	C	4	4	4354.37	5.10	1.17
TE28_3.23_4-						4	4	3684.51	15.27	4.15

Title	Spot	Sample code	Drill core	Lithology and pyrite occurrence	Zoning type	Growth zone	Pyrite generation	CPS($^{133}Cs^{32}S_2^-$)	CPS($^{197}Au^-$)	1000×CPS($^{133}Cs^{32}S_2^-$)/CPS($^{197}Au^-$)
TE48_28_3.1_1						1	1a	3400.38	5.47	1.61
TE48_28_3.1_1'						1	1a	3370.21	8.00	2.37
TE48_28_3.1_1"						1	1a	3281.56	3.46	1.05
TE48_28_3.1_2						2	2	2797.81	54.48	19.47
TE48_28_3.1_2'						2	2	3687.22	118.98	32.27
TE48_28_3.1_3	Small	MAS-8	FPL-122_598.0m	Pyrite band of BIF-hosted ore	C	3	3	3864.88	26.37	6.82
TE48_28_3.1_4						3	3	3331.21	31.80	9.55
TE48_28_3.1_3'						3	3	3442.72	25.54	7.42
TE48_28_3.1_5						3	3	3434.87	14.38	4.19
TE48_28_3.1_5'						3	3	3523.71	58.19	16.51
TE48_28_3.1_5"						3	3	3522.07	83.19	23.62
TE48_28_3.1_6						4	4	3340.08	2.34	0.70
TE48_29_1.1_1.1						1	1a	1874.22	23.22	12.39
TE48_29_1.1_1.1'						1	1a	2297.27	21.41	9.32
TE48_29_1.1_1.1"						1	1a	2254.68	32.04	14.21
TE48_29_1.1_1.2	Small	MAS-8	FPL-122_598.0m	Pyrite band of BIF-hosted ore	C	2	2	4416.63	292.95	66.33
TE48_29_1.1_1.2'						2	2	2312.92	74.74	32.32
TE48_29_1.1_1.3						3	3	2359.95	54.45	23.07
TE48_29_1.1_1.3'						3	3	2438.05	19.95	8.18
TE48_29_1.1_1.4						4	4	2065.64	0.73	0.35
TE48_29_1.1_2.4						1	2	2182.91	46.53	21.31
TE48_29_1.1_2.5	Small	MAS-8	FPL-122_598.0m	Pyrite band of BIF-hosted ore	B	2	3	1951.95	11.53	5.91
TE48_29_1.1_2.6'						3	4	1806.75	1.55	0.86
TE48_28_3.15_1						1	1a	2961.11	14.00	4.73
TE48_28_3.15_2	Small	MAS-8	FPL-122_598.0m	Pyrite band of BIF-hosted ore	C	2	2	5849.65	93.07	15.91
TE48_28_3.15_2'						2	2	3249.76	33.07	10.18
TE48_28_3.15_3						3	3	3279.08	29.97	9.14

Title	Spot	Sample code	Drill core	Lithology and pyrite occurrence	Zoning type	Growth zone	Pyrite generation	CPS($^{133}Cs^{32}S_2^-$)	CPS($^{197}Au^-$)	1000×CPS($^{133}Cs^{32}S_2^-$)/CPS($^{197}Au^-$)
TE48_28_3.15_4						4	4	3341.45	7.77	2.32
TE48_28_3.15_4'						4	4	3265.47	1.83	0.56
TE48_29_2.4_1						2	2	4452.42	70.56	15.85
TE48_29_2.4_3	Small	MAS-8	FPL-122_598.0m	Pyrite band of BIF-hosted ore	C	3	3	2537.08	7.83	3.09
TE48_29_2.4_4						4	4	2521.46	5.30	2.10
TE48_57_1.1						1	1b	2407.48	50.88	21.14
TE48_57_1.9						1	1b	1512.46	47.29	31.26
TE48_57_1.2						1	1b	1544.65	1.05	0.68
TE48_57_1.3						1	1b	1937.17	1.65	0.85
TE48_57_1.4	Small	MAS-57	FLU-173	Pyrite grains in smoky chert-hosted ore	F	2	2	2181.83	223.70	102.53
TE48_57_1.8						2	2	1419.00	223.68	157.63
TE48_57_1.5						3	3	2481.32	2.54	1.02
TE48_57_1.6						3	3	2337.74	2.74	1.17
TE48_57_1.7						3	3	1432.14	0.86	0.60
TE48_57_2.1						1	1b	3359.66	107.08	31.87
TE48_57_2.2	Small	MAS-57	FLU-173	Pyrite grains in smoky chert-hosted ore	F	2	2	2741.51	239.08	87.21
TE48_57_2.3						3	3	1126.01	39.32	34.92
TE48_57_2.4						3	3	1393.64	3.43	2.46
TE48_28_2.6_1						1	1a	3352.55	4.56	1.36
TE48_28_2.6_2						2	2	5116.59	480.01	93.81
TE48_28_2.6_2'	Small	FLV-167	FLV-167_225m	Pyrite band of BIF-hosted ore (arsenopyrite-rich)	C	2	2	3250.24	972.20	299.12
TE48_28_2.6_3						3	3	3044.90	33.02	10.84
TE48_28_2.6_3'						3	3	3091.32	27.09	8.76
TE48_28_2.6_4						4	4	2950.23	3.10	1.05
TE48_28_3.26_1						1	1a	2177.28	80.33	36.89
TE48_28_3.26_2	Small	FLV-167	FLV-167_225m	Pyrite band of BIF-hosted ore (arsenopyrite-rich)	C	2	2	4554.05	337.12	74.03
TE48_28_3.26_3						3	3	2919.71	129.78	44.45

Title	Spot	Sample code	Drill core	Lithology and pyrite occurrence	Zoning type	Growth zone	Pyrite generation	CPS($^{133}Cs^{32}S_2^-$)	CPS($^{197}Au^-$)	1000×CPS($^{133}Cs^{32}S_2^-$)/CPS(197Au$^-$)
TE48_28_3.26_4						4	4	2823.73	1.78	0.63
TE48-3_2						orange	1b	359.00	0.53	1.46
TE48-3_1	Small	MAS-25	FPL-120_639.2m	Pyrite lamina of sulfidized BIF	D	blue	2	456.91	16.38	35.84
TE48-3_3'						blue	2	342.40	5.64	16.46
TE48-2.2_2						orange	1b	501.26	1.13	2.24
TE48-2.2_1	Small	MAS-25	FPL-120_639.2m	Pyrite lamina of sulfidized BIF	D	blue	2	294.00	8.78	29.85
TE48-2.2_3						orange	2	1017.03	4.58	4.50
TE48-4.2_2	Small	MAS-25	FPL-120_639.2m	Pyrite lamina of sulfidized BIF	D	orange	1b	402.25	1.45	3.60
TE48-4.2_1						blue	2	353.10	11.69	33.10
TE48-4.1_1						blue	2	388.80	13.71	35.27
TE48-4.1_2	Small	MAS-25	FPL-120_639.2m	Pyrite lamina of sulfidized BIF	E	orange	2	343.45	3.94	11.46
TE48-4.1_4						orange	2	395.40	3.59	9.07
TE48-17.1						orange	1b	374.54	0.57	1.51
TE48-17.3	Small	MAS-25	FPL-120_639.2m	Pyrite lamina of sulfidized BIF	D	blue	2	392.85	10.41	26.50
TE48-17.5						orange	2	264.80	1.16	4.39
TE48_57_1.1						blue	2	1939.09	49.68	25.62
TE48_57_1.2	Small	MAS-57	FLU-173	Pyrite grain in smoky chert-hosted ore	G	blue	2	1937.79	22.28	11.50
TE48_57_1.3						orange	2	2328.88	2.00	0.86
TE48_57_1.4						orange	2	1950.06	1.56	0.80
TE48_57_10.1						blue	2	1405.83	20.59	14.64
TE48_57_10.3	Small	MAS-57	FLU-173	Pyrite grain in smoky chert-hosted ore	G	orange	2	1665.96	1.28	0.77
TE48_57_10.4						orange	2	1650.42	0.23	0.14
TE48_57_10.5						orange	2	1815.69	1.61	0.89

Table 6.8 Results of semi-quantitative determination of the abundance of selenium and molybdenum in each growth zone of zoned pyrite.

Title	Sample code	Drill core	Lithology and pyrite occurrence	Zoning type	Growth zone	Pyrite generation	CPS($^{80}Se^-$)	CPS($^{98}Mo^{32}S^-$)	CPS($^{54}Fe^{32}S^-$)	1000×CPS($^{80}Se^-$)/CPS($^{54}Fe^{32}S^-$)	1000×CPS($^{98}Mo^{32}S^-$)/CPS($^{54}Fe^{32}S^-$)
TE28_3.1_1	MAS-8	FPL-122_598.0m	Pyrite band of BIF-hosted ore	C	1	1a	3151.17	138.13	214565.34	14.69	0.64
TE28_3.1_2					1	1a	3013.08	117.40	249000.13	12.10	0.47
TE28_3.1_3					3	3	58.58	56.40	107308.62	0.55	0.53
TE28_3.1_3-TE28_3.1_4					3	3	100.47	176.97	280264.64	0.36	0.63
					3	3	383.73	168.00	196028.20	1.96	0.86
TE28_3.1_5					4	4	169.15	128.87	112207.73	1.51	1.15
TE28_3.1_6					4	4	98.95	119.70	109047.05	0.91	1.10
TE28_3.1_6-TE28_9_1					4	4	184.00	184.10	209784.48	0.88	0.88
					4	4	36.40	49.63	32767.19	1.11	1.51
TE28_9_1-					4	4	41.40	33.80	42950.44	0.96	0.79
TE28_9_1--					4	4	219.47	115.20	226266.54	0.97	0.51
TE28_9_2					3	3	124.60	135.65	283683.98	0.44	0.48
TE28_9_2-TE28_9_3					3	3	191.25	243.90	385277.29	0.50	0.63
					2	2	184.90	274.24	262190.63	0.71	1.05
TE28_9_4					1	1a	1218.29	339.04	282764.25	4.31	1.20
TE28_3.16_1-TE28_3.16_2					4	4	1.94	258.13	256670.77	0.01	1.01
					4	4	272.38	256.65	281768.36	0.97	0.91
TE28_3.16_3					3	3	80.58	182.80	178158.83	0.45	1.03
					2	2	122.95	232.40	203427.23	0.60	1.14

Title	Sample code	Drill core	Lithology and pyrite occurrence	Zoning type	Growth zone	Pyrite generation	CPS($^{80}Se^-$)	CPS($^{98}Mo^{32}S^-$)	CPS($^{54}Fe^{32}S^-$)	1000×CPS($^{80}Se^-$)/CPS($^{54}Fe^{32}S^-$)	1000×CPS($^{98}Mo^{32}S^-$)/CPS($^{54}Fe^{32}S^-$)
TE28_3.16_4	MAS-8	FPL-122_598.0m	Pyrite band of BIF-hosted ore	C	1	1a	313.17	218.00	121032.66	2.59	1.80
TE28_2.6_1					4	4	79.22	224.43	186577.98	0.42	1.20
TE28_2.6_2					3	3	174.70	114.30	181747.08	0.96	0.63
TE28_2.6_2-TE28_2.6_4					3	3	304.00	220.67	289189.60	1.05	0.76
					1	1a	161.70	133.05	118418.57	1.37	1.12
TE28_2.6_4-TE28_2.6_5					1	1a	261.05	212.35	210986.95	1.24	1.01
					1	1a	121.93	148.23	134007.68	0.91	1.11
TE28_3.23_1					4	4	59.80	93.57	99796.79	0.60	0.94
TE28_3.23_2					3	3	99.50	207.00	182996.51	0.54	1.13
TE28_3.23_3					2	2	240.53	74.05	172701.59	1.39	0.43
TE28_3.23_3-TE28_3.23_3'					2	2	178.75	162.40	109962.62	1.63	1.48
					2	2	61.60	124.30	131554.99	0.47	0.94
TE28_3.23_4					1	1a	1563.41	66.13	122039.66	12.81	0.54
TE29_1.1_1					4	4	469.23	264.78	322438.65	1.46	0.82
TE29_1.1_2					4	4	228.00	281.90	200349.31	1.14	1.41
TE29_1.1_3					3	3	55.50	149.10	167967.86	0.33	0.89
TE29_1.1_3-TE29_1.1_8					3	3	71.05	128.80	331311.69	0.21	0.39
					3	3	75.52	277.77	268931.61	0.28	1.03

Title	Sample code	Drill core	Lithology and pyrite occurrence	Zoning type	Growth zone	Pyrite generation	CPS($^{80}Se^{-}$)	CPS($^{98}Mo^{32}S^{-}$)	CPS($^{54}Fe^{32}S^{-}$)	1000×CPS($^{80}Se^{-}$)/CPS($^{54}Fe^{32}S^{-}$)	1000×CPS($^{98}Mo^{32}S^{-}$)/CPS($^{54}Fe^{32}S^{-}$)
TE29_1.1_4					2	2	1019.63	252.25	280210.82	3.64	0.90
TE29_1.1_7					2	2	359.15	97.80	140635.64	2.55	0.70
TE29_1.1_9					2	2	985.79	167.23	187885.35	5.25	0.89
TE29_1.1_5					1	1a	2332.65	191.30	274704.08	8.49	0.70
TE29_1.1_6					1	1a	1416.37	607.48	258602.52	5.48	2.35
TE29_4_1					4	4	233.45	269.80	236261.73	0.99	1.14
TE29_4_2					3	3	129.80	189.43	269225.86	0.48	0.70
TE29_4_3	MAS-8	FPL-122_598.0m	Pyrite band of BIF-hosted ore	C	2	2	539.68	194.00	181137.47	2.98	1.07
TE29_4_4					1	1a	583.66	139.90	365830.47	1.60	0.38
TE29_4_6					1	1a	1354.65	374.70	296135.00	4.57	1.27
TE48_1.1_1					3	3	334.82	259.30	246856.35	1.36	1.05
TE48_1.1_1					3	3	340.50	138.60	229698.01	1.48	0.60
TE48_1.1_1	MAS-57	FLU-173	Pyrite grain in smoky chert-hosted ore	F	3	3	194.47	184.63	174111.30	1.12	1.06
TE48_1.1_3					2	2	125.50	166.10	193617.61	0.65	0.86
TE48_1.1_4					1	1b	387.99	478.14	221946.17	1.75	2.15
TE48_3-1					blue	2	254.09	237.30	307138.19	0.83	0.77
TE48_3-4					blue	2	183.77	110.27	134241.32	1.37	0.82
TE48_3-5	MAS-25	FPL-120_639.2m	Pyrite lamina of sulfidized BIF	D	blue	2	210.45	149.00	178446.50	1.18	0.83
TE48_3-2					orange	1b	244.30	48.70	93305.56	2.62	0.52
TE48_3-2-					orange	1b	609.71	83.20	235493.44	2.59	0.35
TE48_2_1	MAS-25	FPL-120_639.2m	Pyrite lamina of sulfidized BIF	D	blue	2	185.30	149.30	219553.13	0.84	0.68
TE48_2_3					orange	2	643.61	165.10	258711.55	2.49	0.64
TE48_4.1_1					blue	2	115.55	101.37	143015.75	0.81	0.71
TE48_4.1_4	MAS-25	FPL-120_639.2m	Pyrite lamina of sulfidized BIF	E	orange	2	671.78	204.30	241793.53	2.78	0.84
TE48_4.1_5					blue	2	279.45	372.95	357200.30	0.78	1.04
TE48_57.3	MAS-57	FLU-173	Disseminated fine-grained euhedral to subhedral pyrite in smoky chert-hosted ore			1b	591.93	163.70	130165.43	4.55	1.26

Title	Sample code	Drill core	Lithology and pyrite occurrence	Zoning type	Growth zone	Pyrite generation	CPS($^{80}Se^-$)	CPS($^{98}Mo^{32}S^-$)	CPS($^{54}Fe^{32}S^-$)	1000×CPS($^{80}Se^-$)/CPS($^{54}Fe^{32}S^-$)	1000×CPS($^{98}Mo^{32}S^-$)/CPS($^{54}Fe^{32}S^-$)
TE48_57.4	MAS-57	FLU-173	Disseminated fine-grained euhedral to subhedral pyrite in smoky chert-hosted ore			1b	550.21	133.60	186300.89	2.95	0.72
TE48_57.5	MAS-57	FLU-173	Disseminated fine-grained euhedral to subhedral pyrite in smoky chert-hosted ore			1b	1202.42	170.80	156767.01	7.67	1.09

Chapter 7 Concluding Remarks

1 Summary of the results

Some important data of the multiple sulphur isotopic composition of pyrite in Archean records have been obtained through the five studies of this thesis.

(1) **Chapter 2:** The $\Delta^{33}S$ measured in pyrite of 3.2-2.72 Ga metasedimentary rocks from the Pilbara Craton, Western Australia ranges from -2.40‰ to 0.79‰. Such a range characterized by larger magnitude of the minimum negative $\Delta^{33}S$ than that of the maximum positive $\Delta^{33}S$ is inconsistent with any experiment of producing S-MIF conducted so far. All of the sulphur-bearing products (elemental sulphur and sulphate) in these experiments show much larger maximum positive $\Delta^{33}S$. The pyrite with more negative $\Delta^{36}S/\Delta^{33}S$ shows deviation trends approximately parallel to the mass dependent biological fractionation in the $\Delta^{33}S$-$\Delta^{36}S$ plot or hydrothermal overprints and modifications mineragraphically.

(2) **Chapter 3:** Two generations of pyrite are revealed in the 3.49 Ga Dresser Formation. The first generation is $\delta^{34}S$- and $\Delta^{33}S$-positive, while the second generation is $\delta^{34}S$- and $\Delta^{33}S$-negative. The pyrite that is associated with barite and has considerably negative $\delta^{34}S$ is $\Delta^{33}S$-negative. The pyrite with depleted ^{34}S shows no clear biological fractionations from the associated barite in the $\Delta^{33}S$-$\Delta^{36}S$ plot.

(3) **Chapter 4:** Two generations of pyrite are revealed in each of the typical Archean shale samples. Each generation of pyrite has two types of morphology (nodule and disseminated grain in the shale matrix). The multiple sulphur isotopic compositions of nodular pyrite and disseminated pyrite of each generation are similar, and the sign of $\Delta^{33}S$ is the same.

(4) **Chapter 5:** The products of the desulphidized initial pyrite (both Ruttan pyrite and the Neoarchean pyrite) at 675 °C and sulphidized metal iron by the released sulphur are both pyrrhotite. The $\delta^{34}S$ range of products expands compared with that of the starting pyrite, and the mean $\delta^{34}S$ increases or decreases by sub-permil to several permil. The $\Delta^{33}S$ of initial pyrite and both products is relatively constant. The $\Delta^{36}S$ range of products from the

Neoarchean pyrite is narrowed compared with that of initial pyrite, while the $\Delta^{36}S$ range of products from Ruttan pyrite stays constant. The fractionation in $\Delta^{33}S$ and $\Delta^{36}S$ between both Ruttan pyrite and the Neoarchean pyrite and products is slight (0.1 to 0.2‰).

(5) **Chapter 6:** Four generations of pyrite are revealed in the ores of the Lamego gold deposit. Generation one has low to moderate gold abundance, and is subdivided into 1a and 1b. Generation 1a shows negative $\delta^{34}S$ and moderate magnitudes of positive $\Delta^{33}S$, while generation 1b displays positive $\delta^{34}S$ and large magnitudes of positive $\Delta^{33}S$. The sulphur isotopic compositions of generation two to four pyrite are similar, and the majority has small positive $\delta^{34}S$ and $\Delta^{33}S$. Generation two is characterized by oscillatory zoning and the highest gold abundance, whereas generation three and four contain much less gold, particularly generation four. Most of generation 1 pyrite has higher selenium abundance than the other generations.

2 Implications

Based on the results listed above, implications on methods (1 and 2), constraints on some problems of S-MIF in the Archean (3, 4, and 5), and the application of multiple sulphur isotopes to tracing the sulphur sources of Archean gold deposits (6 and 7) have been acquired.

(1) A key finding of this thesis is that it is necessary to establish the pyrite generation prior to the in-situ measurement for multiple sulphur isotopic composition, since it is common for individual pyrite grains to preserve multiple generations of pyrite as a result of complex geological history of the metasedimentary rocks. Without a clear knowledge of the pyrite generation, the sampling of in-situ analysis (i.e., the bombardment of primary beam on the pyrite grain surface) can involve multiple generations of pyrite. As a result, the data are essentially the compositions of mixed sulphur components, and thus provide incorrect information and lead to misinterpretations. Sodium hypochlorite etching combined with BSE imaging is useful and effective in revealing the internal textures of pyrite, based on which the pyrite generation can be clarified. Many previous studies have simply used reflected light

microscopy in the characterization of grain-boundary textures and have effectively not constrained the pyrite petrogenesis.

(2) With a well-established pyrite generation, it is essential to combine big-spot with small-spot analyses due to the variable size of each pyrite grain or different growth zone of individual grains, particularly for nodular pyrite and zoned pyrite. While the small-spot analysis limits the amount of $^{36}S^-$ that can be collected, the association of $\Delta^{33}S$ between small-spot and big-spot analyses provides strong mineralogical context.

(3) **Chapter 2:** The maximum magnitude of $\Delta^{33}S$ is not so small as reported in previous studies. Additionally, many important samples of deep marine depositional environments have not been sampled and measured so far due to poor or no geological preservations. As such, larger magnitudes of $\Delta^{33}S$ is possibly to be discovered. The deviations of $\Delta^{36}S/\Delta^{33}S$ from ARA are caused by post-diagenetic biological or hydrothermal modifications rather than different photochemical processes of producing S-MIF in the atmosphere. Therefore, the conclusion of a compositionally different atmosphere from 3.2 Ga to 2.72 Ga needs to be reassessed.

(4) **Chapter 3:** Previous in-situ analyses for triple sulphur isotopic compositions of microscopic pyrite within barite suggest elemental sulphur disproportionation as the earliest sulphur-involving metabolism, based on positive $\Delta^{33}S$ associated with significantly negative $\delta^{34}S$. However, this study reveals negative $\Delta^{33}S$ of the pyrite with considerably negative $\delta^{34}S$, suggesting sulphate reduction rather than elemental sulphur disproportionation for the earliest sulphur metabolism on the Earth. Nevertheless, the correspondence between $\Delta^{33}S$ sign and sulphur metabolism type needs further confirmation due to the complicated formation processes of pyrite. Additionally, it still cannot be concluded whether the sulphur of the pyrite with depleted ^{34}S is of biological origin.

(5) **Chapter 4:** Previous studies show morphology dependence of the $\Delta^{33}S$ sign of pyrite. However, the results of this study indicate that the sign of $\Delta^{33}S$ is independent of pyrite morphology (nodule or disseminated grain). Elemental sulphur and sulphate (SO_2 photolysis

products in the atmosphere) with positive and negative $\Delta^{33}S$, respectively have no preservation preferences. Nodular pyrite is derived from coalescence of disseminated pyrite grains. Later generation of pyrite overprints on earlier pyrite nodules as rims, and also occur as disseminated grains in the shale matrix.

(6) **Chapter 5:** The fractionations in $\delta^{34}S$ can be induced by matrix effect and mass dependent fractionation. The slight fractionations in $\Delta^{33}S$ and $\Delta^{36}S$ during the desulphidation of pyrite to pyrrhotite can be attributed to analytical uncertainty and kinetic mass dependent fractionations. Due to the sensitivity of $\delta^{34}S$ on redox state, $\Delta^{33}S$ can provide additional significant constraints on the sulphur sources of Archean ore deposits.

(7) **Chapter 6:** The extensive S-MIF in the four generations of pyrite suggests that the hydrothermal fluids can be metamorphic fluids, metamorphic fluids reacted with surrounding rocks, and magmatic fluids mixed with metamorphic fluids and/or interacted with wall rocks. The metamorphic fluids are derived from devolatilization of the underlying strata, in the case of Lamego, it is the Nova Lima Group of the Rio das Velhas Supergroup as well as the basement. The sulphur sources revealed here for the Lamego gold deposit are consistent with the majority of previous studies, i.e., S-MIF is pervasive in ore-related pyrite of Archean gold deposits. The sulphur is probably from multiple sources, one of which should be Archean metasedimentary rocks.

3 Future work

Although some results and implications have been gained from the studies of this thesis, some basics still need to be established and more samples need to be measured. The specific future work needed is as follows:

(1) Investigation into the sulphur isotope fractionation during abiological reduction of barite under hydrothermal conditions. This work is needed because the most important evidence supporting the earliest sulphur-involving metabolisms on the Earth is the ^{34}S-depleted pyrite. However, as the results of Chapter 3 show, $\Delta^{33}S$ and $\Delta^{36}S$ do not support biological origin. Therefore, it is necessary to investigate whether abiological reduction of barite can produce

considerably ^{34}S-depleted pyrite under the physico-chemical conditions associated with the Dresser Formation.

(2) Previous studies have proposed two contrasting mechanisms of producing the oscillatory zoning in pyrite, i.e., it is produced in one single flow or repeated flows of hydrothermal fluids. Experiments need to be conducted to test which mechanism is more likely.

(3) The partition coefficients of redox-sensitive elements between pyrite and hydrothermal fluids under different redox state need to be experimentally established. This work is needed because many studies related to trace element of pyrite have applied these redox-sensitive elements to address the associated redox states. Nevertheless, how these widely considered redox-sensitive elements act towards redox state change has not been investigated in detail. Thus, in order to consolidate the reasonability of these redox-sensitive elements in the aspects of revealing redox state change, laboratory experimental work with these trace elements and with redox state as the main variable is necessary.

(4) Many more fresh drill core samples of deep marine depositional environments of 3.2-2.72 Ga from the Pilbara Craton and other parts of the world need to be measured, although it is challenging to obtain such samples.